

**Molecular roles of IDRs in a germ granule-associated
DDX3 RNA helicase**

Dissertation
zur Erlangung des
Doktorgrades der Naturwissenschaften (Dr. rer. nat.)

der

Naturwissenschaftlichen Fakultät I – Biowissenschaften –
der Martin-Luther-Universität
Halle-Wittenberg,
vorgelegt

von

Herrn Oleksandr Sorokin

Datum der Verteidigung der Dissertation: 15.12.2023

Gutachter:

1. Prof. Dr. Jochen Balbach
2. Prof. Dr. Christian R. Eckmann
3. Dr. Mandy Jeske

Summary

RNA-binding proteins are important regulators of RNA biogenesis and guide cellular activities of all RNA species. RNA helicases represent a unique class of RNA-binding proteins and introduce changes to RNA structure to influence cytoplasmic mRNA fates, such as RNA localization or translation. By unwinding double-stranded secondary elements in an ATP-dependent manner, DEAD-box (DDX) RNA helicases became in recent years a focus of intense research, as they are also prevalent components of RNA granules, such as stress granules or germ granules. Especially members of DDX3 RNA helicases were found in isolation to form liquid-liquid phase separated (LLPS) droplets *in vitro*, making them a paradigm for studying RNA granule integrity. Although, collective evidence from various organisms suggests that DDX3 proteins are important in many cell types for normal physiology and animal development, their cellular roles as posttranscriptional regulators and molecular modulators of RNA granule dynamics are still poorly understood.

This work investigated the biophysical properties and molecular functions of the *C. elegans* DDX3 ortholog LAF-1, with a particular focus on its role as a germ (P) granule component. In addition to IDR-truncated structural variants, wild-type and genetically defined mutant proteins of recombinant LAF-1 were analysed for their enzymatic capabilities to disentangle cellular RNA substrates in a newly established bulk RNA helicase assay. This panel of experiments document that both, the N-terminal RGG IDR and C-terminal GQ IDR, are essential for helicase activity, and that LAF-1 acts as a dimer, providing explanations to the peculiar phenotypes observed in heterozygote animals. In experiments aimed at discovering regulators of LLPS droplet formation, ATP and especially eIF4E translation initiation factors were found to have a negative impact, while RNA had a positive influence. LLPS was mediated by the RGG IDR and required its full length, because a newly discovered endogenous isoform designated LAF-1S, which is enriched in early embryos and lacks ~33.5% of the N-terminal IDR failed to support droplet formation *in vitro*. This panel of experiments was complimented with immunopurifications of LAF-1 from embryonic material to better describe processes that depend on LAF-1 *in vivo*. Factors associated with translation elongation were among the most enriched proteins. In summary, the collective findings of this work are relevant and extendable to all DDX3 RNA helicases and provide a framework for how their RNA-binding and helicase activity might be coupled to IDR-mediated liquid-liquid phase separation, underlying RNA granule dynamics to release stored mRNAs for subsequent translation.

Zusammenfassung

RNA-bindende Proteine sind wichtige Regulatoren der RNA-Biogenese und steuern die zellulären Aktivitäten aller RNA-Arten. RNA-Helikasen stellen eine einzigartige Klasse von RNA-bindenden Proteinen dar und führen Veränderungen in der RNA-Struktur ein, um das Schicksal zytoplasmatischer mRNA zu beeinflussen, wie z. B. die RNA Lokalisierung oder Translation. Indem sie doppelsträngige Sekundärelemente ATP-abhängig auflösen, sind DEAD-Box (DDX) RNA-Helikasen in den letzten Jahren in den Mittelpunkt intensiver Forschung gerückt, da sie auch gängige Bestandteile von RNA-Granula sind, wie z.B. von Stress- oder Keimgranula. Insbesondere Mitglieder der DDX3-RNA-Helikasen wurden gefunden in Lösung sich in eine separate Phasen abzutrennen (LLPS) und *in vitro* Tröpfchen zu bilden, was sie zu einem Paradigma für die Untersuchung der Integrität von RNA-Granula macht. Obwohl kollektive Beweise aus verschiedenen Organismen darauf hindeuten, dass DDX3-Proteine in vielen Zelltypen für die normale Physiologie und die Entwicklung von Tieren wichtig sind, ist ihre zelluläre Rolle als posttranskriptionelle Regulatoren und molekulare Modulatoren der RNA-Granular-Dynamik noch immer unzureichend verstanden.

In dieser Arbeit wurden die biophysikalischen Eigenschaften und molekularen Funktionen des DDX3-Orthologen Proteins LAF-1 aus *C. elegans* untersucht. Ein besonderes Augenmerk wurde dabei auf dessen Rolle als Bestandteil von Keimzell (P)-Granula gelegt. Zusätzlich zu den IDR-Strukturvarianten wurden Wildtyp- und genetisch definierte Mutantenproteine von rekombinantem LAF-1 auf ihre enzymatischen Fähigkeiten zur Entwindung zellulärer RNA-Substrate in einem neu etablierten Helikasetest basierend auf Gesamt-RNA untersucht. Diese Versuchsreihe belegte, dass sowohl die N-terminale RGG IDR als auch die C-terminale GQ IDR für die Helikaseaktivität notwendig sind und dass LAF-1 als Dimer agiert, was eine Erklärung für die besonderen Phänotypen liefert, die bei heterozygoten Tieren beobachtet werden. In Experimenten, die darauf abzielten, Regulatoren der LLPS-Tropfenbildung zu entdecken, wurde festgestellt, dass ATP und insbesondere eIF4E-Translationsinitiationsfaktoren einen negativen Einfluss haben, während RNA einen positiven Einfluss hat. LLPS wurde durch die RGG IDR vermittelt und erforderte deren volle Länge, da eine neu entdeckte endogene Isoform mit der Bezeichnung LAF-1S, die in frühen Embryonen angereichert ist und der ~33,5 % der N-terminalen IDR fehlen, die Tröpfchenbildung *in vitro* nicht unterstützte. Diese Reihe von Experimenten wurde durch Immunaufreinigungen von LAF-1 aus embryonalem Material ergänzt, um Prozesse, die *in vivo* von LAF-1 abhängen, besser zu beschreiben. Zu den am stärksten angereicherten Proteinen gehörten Faktoren, die

mit dem Prozess der Translation in Verbindung stehen. Zusammenfassend wurden in dieser Arbeit wichtige Erkenntnisse gewonnen die für alle DDX3-RNA-Helikasen relevant und anwendbar sind. Sie bieten einen Rahmen dafür, wie RNA-Bindung und Helikaseaktivität mit der IDR-vermittelten Flüssig-Flüssig-Phasentrennung gekoppelt sein könnte, um sowohl die Dynamik der RNA-Granula zu beeinflussen und gespeicherte mRNAs für die anschließende Translation ins Zytosol freizusetzen.

Table of contents

| | |
|--|-----------|
| Summary..... | 3 |
| Zusammenfassung..... | 4 |
| Lists of abbreviations..... | 9 |
| 1. Introduction..... | 11 |
| 1.1. Structure of DDX3 RNA helicases | 12 |
| 1.2. DDX3 proteins as posttranscriptional RNA regulators | 18 |
| 1.3 <i>C. elegans</i> germline development and P granules | 20 |
| 1.4. Research aim..... | 25 |
| 2. Materials and Methods..... | 26 |
| 2.1. Materials | 26 |
| 2.2. Solutions | 27 |
| 2.3. Methods..... | 29 |
| 2.3.1. SDS-polyacrylamide gel electrophoresis | 29 |
| 2.3.2. Western blot..... | 29 |
| 2.3.3. Isoelectric focusing in 2-D electrophoresis..... | 30 |
| 2.3.4. Protein precipitation with TCA..... | 31 |
| 2.3.5. Expression of recombinant proteins..... | 32 |
| 2.3.6. Purification of recombinant LAF-1 proteins..... | 33 |
| 2.3.7. Recombinant inclusion body washing | 34 |
| 2.3.8. Purification of recombinant IFE-x proteins | 35 |
| 2.3.9. Immunoblot affinity purification of anti-LAF-1 polyclonal rabbit sera | 36 |
| 2.3.10. LAF-1 immunoprecipitation | 38 |
| 2.3.11. Total RNA extraction (Trizol method) | 38 |
| 2.3.12. Agarose gel electrophoresis in TBE buffer system..... | 39 |
| 2.3.13. RNA helicase assay..... | 40 |
| 2.3.14. Polymerase chain reaction (PCR) | 41 |

| | |
|--|-----------|
| 2.3.15. Plasmid vector cloning..... | 42 |
| 2.3.16. RNAi feeding | 43 |
| 2.3.17. Embryo extraction..... | 44 |
| 2.3.18. Differential interference contrast microscopy | 45 |
| 2.3.19. LC-MS/MS of <i>C. elegans</i> samples | 46 |
| 2.3.20. Small-angle X-ray scattering | 48 |
| 2.3.21. Phylogenetic analysis..... | 48 |
| 3. Results | 49 |
| 3.1. Identification of LAF-1 short isoform (LAF-1S)..... | 49 |
| 3.1.1. Defining the epitope of monoclonal anti-LAF-1 antibody mAb BW75..... | 50 |
| 3.1.2. LAF-1S is expressed during embryogenesis..... | 53 |
| 3.2. Purification of recombinant LAF-1 proteins..... | 56 |
| 3.3. Studying LAF-1L phase separation by DIC microscopy..... | 61 |
| 3.4. LAF-1 LLPS in presence of potential binding partners..... | 68 |
| 3.4.1. LAF-1S LLPS differs from LAF-1L and influences LAF-1L LLPS..... | 68 |
| 3.4.2. LAF-1L LLPS is suppressed by eIF4E proteins | 75 |
| 3.4.3. Purification of <i>C. elegans</i> IFE proteins..... | 75 |
| 3.4.4. IFE proteins affect LAF-1L LLPS | 77 |
| 3.4.5. LAF-1 LLPS in presence of total <i>C. elegans</i> RNA. | 79 |
| 3.5. LAF-1L isomerisation SAXS studies | 84 |
| 3.6. Enzymatic profile studies of LAF-1 helicase activity..... | 88 |
| 3.6.1. Setting up a bulk RNA helicase assay | 88 |
| 3.6.2. LAF-1L is an ATP-dependent RNA helicase | 93 |
| 3.6.3. Genetically identified mutant LAF-1 proteins lack RNA helicase activity and interfere with wild-type LAF-1..... | 94 |
| 3.6.4. mAb BW75 compromises LAF-1 activity..... | 97 |
| 3.6.5. Contribution of either IDR to LAF-1L helicase activity | 99 |

| | |
|--|------------|
| 3.7. Attempts to identify components of LAF-1 RNPs | 105 |
| 3.7.1. Immunoblot affinity purification of anti-LAF-1 polyclonal rabbit sera | 105 |
| 3.7.2. LC-MS/MS of <i>C. elegans</i> embryo samples | 107 |
| 3.7.3. LAF-1 immunoprecipitation experiments..... | 109 |
| 4. Discussion..... | 116 |
| 4.1. LAF-1 activity is represented by two protein isoforms | 116 |
| 4.2. RNA-helicase activity is the essential function of LAF-1 | 118 |
| 4.3. LAF-1 LLPS behaviour depends on molecular environment | 121 |
| 4.4. LAF-1 as a P granule component and potential translational regulator..... | 126 |
| 5. Appendixes..... | 131 |
| 5.1. List of equipment | 131 |
| 5.2. List of FPLC columns and matrixes | 131 |
| 5.3. List of chemicals and materials..... | 132 |
| 5.4. List of kits | 134 |
| 5.5. List of enzymes | 134 |
| 5.6. List of enzymatic buffers and its components | 134 |
| 5.7. List of antibodies..... | 134 |
| 5.8. List of primers..... | 135 |
| 5.9. List of primer combinations to clone new LAF-1 expression plasmids | 136 |
| 5.10. List of primer combinations to clone IFE-x expression constructs | 136 |
| 5.11. List of <i>C. elegans</i> strains..... | 136 |
| 5.12. LC-MS/MS results of 42 selected protein markers of embryonic stage..... | 137 |
| 6. References..... | 138 |
| Acknowledgement..... | 151 |
| Eidesstattliche Erklärung..... | 152 |
| Curriculum vitae..... | 153 |

Lists of abbreviations

| | |
|----------|---|
| aa | Amino acid |
| ACN | Acetonitrile |
| AGC | Automatic gain control |
| ATP | Adenosine triphosphate |
| BSA | Bovine serum albumin |
| CAA | 2-chloroacetamide |
| CFP | Cyan fluorescent protein |
| CHAPS | 3-[(3-cholamidopropyl)dimethylammonio]-1-propanesulfonate |
| DMP | Dimethyl pimelimidate |
| DNA | Deoxyribonucleic acid |
| dNTP | Deoxynucleoside triphosphate |
| dsRNA | Double-stranded RNA |
| DTT | Dithiothreitol |
| EDTA | Ethylenediaminetetraacetic acid |
| EGTA | Ethylene glycol-bis(β -aminoethyl ether)- <i>N,N,N',N'</i> -tetraacetic acid |
| FA | Formic acid |
| FDR | False discovery rate |
| GRAVY | Grand average of hydropathicity |
| GST | Glutathione S-transferase |
| iBAQ | Intensity based absolute quantification |
| IEF | Isoelectric focusing |
| IMAC | Immobilized metal affinity chromatography |
| IP | Immunoprecipitation |
| IPTG | Isopropylthio- β -galactosid |
| LB | Lysogeny broth |
| LC-MS/MS | Liquid chromatography (LC)-coupled tandem mass spectrometry (MS) |
| LLPS | Liquid-liquid phase separation |
| mAb | Monoclonal antibody |
| MBP | Maltose-binding protein |
| MCS | Multiple cloning site |
| NGM | Nematode growth media |
| ORF | Open reading frame |
| pAb | Polyclonal antibodies |
| PAGE | Polyacrylamide gel electrophoresis |
| PBS | Phosphate-buffered saline |
| PCR | Polymerase chain reaction |
| PVDF | Polyvinylidene fluoride |

| | |
|-------|--|
| RNA | Ribonucleic acid |
| RNAi | RNA interference |
| RNP | Ribonucleoprotein |
| RPS | Rotation per second |
| SAXS | Small-angle X-ray scattering |
| SDS | Sodium dodecyl sulfate |
| SEC | Size exclusion chromatography |
| SOC | Super optimal broth with catabolite repression |
| TCA | Trichloroacetic acid |
| TCEP | Tris(2-carboxyethyl)phosphine |
| TEMED | Tetramethylethylenediamine |
| TFA | Trifluoroacetic acid |
| Tris | Tris(hydroxymethyl)aminomethane |
| WB | Western blot |
| WT | Wild type |

1. Introduction

RNA molecules are born in the nucleus, in a process termed transcription. Immediately thereafter, RNA-binding proteins (RBPs) will associate with these transcripts to form RNA-protein (RNP) complexes to assist in their further biogenesis and subsequent cellular activities as matured molecules belonging to functional classes, such as ribosomal RNAs or messenger RNAs. During an RNA's life time, its two and three-dimensional structure remains dynamically influenced by RBPs. Furthermore, numerous RNP components will be exchanged, depending on the RNPs function(s). All these dynamical rearrangements are subject to activity control and represent important life time events of RNA molecules.

Among the many diverse RNA-binding proteins, RNA helicases stand out as a ubiquitous class of modelers of RNA structure and cellular activities. RNA helicases are typically endowed with an RNA-induced ATP hydrolysis activity that enables them to unwind RNA duplexes *in vitro*, however, it appears that catalysis is not a prerequisite for all their *in vivo* functions. Nonetheless, RNA helicases typically assist RNA dynamics and restructurings of RNP folds or components. As such RNA helicases are a large group of RBPs, classified into six different protein superfamilies, and connected to essentially all steps of nuclear RNA processing and cytoplasmic posttranscriptional processes that influence RNA fates, encompassing RNA storage, translation and RNA stability. Despite their evolutionary conservation, surprisingly little is still known about molecular and cellular roles of most RNA helicases.

A particular subcellular behaviour of RNP dynamics to agglomerate in larger RNP granules became in recent years a centre of intense research. RNP granules are non-membrane encased microscopically visible sites of RNP agglomeration, subject to growth and dissolution. At the cellular level, the dynamics of these processes are influenced by the physiological or developmental states of a cell. At the molecular level, the dynamics are suggested to be influenced by flexible protein regions that do not have a predefined stable three-dimensional fold, but rather exist in alternative folds and are therefore termed intrinsically disordered regions (IDRs). The contribution of IDRs to RNA granule dynamics is exemplified by human pathophysiological conditions linked to several mutant RBPs that display altered RNA granule dynamics. As RNA helicases are integral parts of RNA granules, their combined catalytic activities and flexible protein regions may be important pivots for RNA granule dynamics.

1.1. Structure of DDX3 RNA helicases

DDX3 proteins represent a subfamily of the DEAD-box RNA helicase family, named after the conserved DEAD (asp-glu-ala-asp) motif embedded in an evolutionary conserved helicase domain of a stereotypical fold (Linder et al., 1989). Common to superfamily 2 (SF2) helicases (Fairman-Williams et al., 2010), their enzymatic ATP binding and ATP hydrolysis domain comprises a Walker A and Walker B motif, two RecA-like folds linked via a short flexible peptide loop (domain 1 and domain 2 in Figure 1A). In addition, they share a set of short peptide stretches that are spread across the central folded helicase core assisting its RNA-induced ATPase activities (Figure 1A) (Cordin et al., 2006; Linder & Jankowsky, 2011).

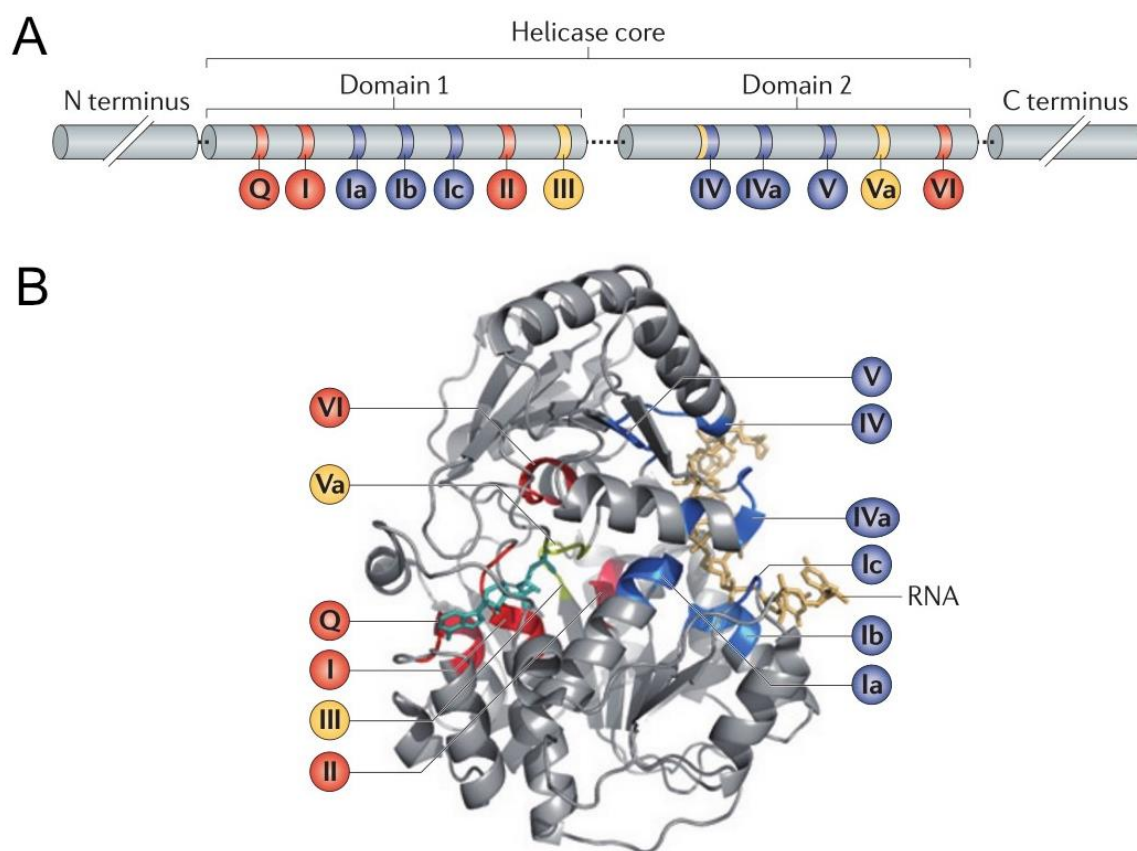


Figure 1. DEAD-box RNA helicases have a stereotypical polypeptide structure.

A. Schematic cartoon image of evolutionary conserved sequences of an universal DEAD-box protein. Two RecA-like domains 1 and 2 are flanked by variable N- and C-terminal extensions. Motifs II and III correspond to DEAD and SAT peptide sequences, respectively.

B. Tertiary structures of the translation initiation factor eIF4AIII DEAD-box RNA helicase in presence of RNA. Motifs in red have ATP affinity, in blue bind to RNA, in yellow have both specificities. (Adapted and modified from Linder & Jankowsky, 2011)

Originally, DEAD-box helicases had seven specific motifs named I, Ia, II (DEAD), III (SAT), IV, V, and VI (Lane, 1988), but were later further extended by motifs Q, Ib, Ic, IVa, and Va (Cordin et al., 2004; Montpetit et al., 2011; Sengoku et al., 2006). All motifs are located on the inner surfaces of the helicase core, where both ATP and RNA binding occur, as shown in Figure 1B (Linder & Jankowsky, 2011). Next to their classification via particular sequence differences among their helicase core, DEAD-box proteins are distinguished from each other via additional sequence elements that either form ordered structural units (i.e. protein domains) or remain unordered, such as intrinsically disordered regions (Cordin et al., 2006).

DEAD-box proteins are widely abundant among most prokaryotes and eukaryotes (Rocak & Linder, 2004) and have been connected to essentially all steps of RNA metabolism of different transcript classes, encompassing all aspects of an RNA's life cycle, from RNA transcription to RNA processing, nuclear export, localization, decay and translational regulation, as depicted in Figure 2 (Iost et al., 1999; Jarmoskaite & Russell, 2011; Linder, 2006). Although DDX proteins comprise a conserved class of distinct RBPs, e.g. the human genome encodes for up to 37 different DDX proteins and homologs of most are present also in the nematode genome of *C. elegans* (Consortium, 1998), still little is known about their mechanistic and biological roles in regulating animal physiology or development.

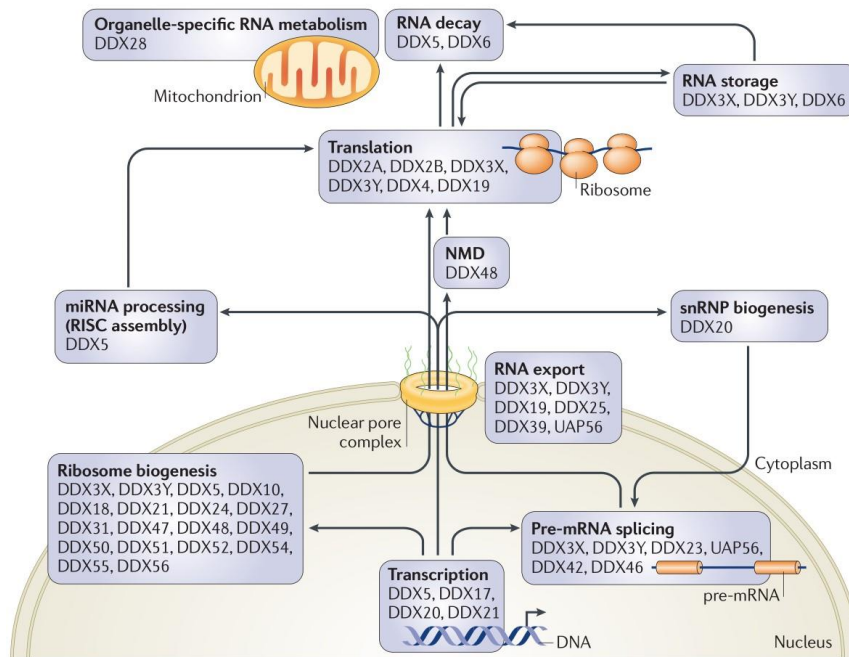


Figure 2. DEAD-box helicases assist RNA during entire lifecycle.

Schematic cartoon image summarising functions of DEAD-box RNA helicases from different organisms. (Adapted and modified from Linder & Jankowsky, 2011)

DDX3 RNA helicases were first discovered in the baker yeast (*Saccharomyces cerevisiae* Ded1p) and subsequently in multicellular eukaryotes, at first as a maternally localized mRNA in frog oocytes (*Xenopus laevis* An3) (Gururajan et al., 1991). Subsequently, at least one member of the DDX3 subfamily were identified in most common eukaryotic model organisms, including the genetic model systems *Drosophila melanogaster* (fly Belle) and *Caenorhabditis elegans* (LAF-1 and VBH-1) (Figure 3A) (Hubert & Anderson, 2009; Johnstone et al., 2005). Interestingly, mammalian genomes possess two DDX3 RNA helicase-encoding loci, one on either allosome, giving rise to nearly identical paralogous proteins, DDX3X and DDX3Y (Abdelhaleem, 2005). On the contrary, nematodes possess two genetic loci encoding two different paralogous on autosomes, LAF-1 and VBH-1, whereby according to its protein domain structure, LAF-1 is more similar to human DDX3 than VBH-1 (Figure 3B) (Kim & Myong, 2016). Although initially identified by genetic mutations in model systems (Chuang & Li, 2004; Goodwin et al., 1997; Johnstone et al., 2005), most investigations on DDX3 RNA helicases focused on mammalian cell culture models due to its prevalent connections to the immune system, cancer biogenesis, neurogenesis and autism-related intellectual disability disorders (Lennox et al., 2020; Samir et al., 2019; Snijders Blok et al., 2015).

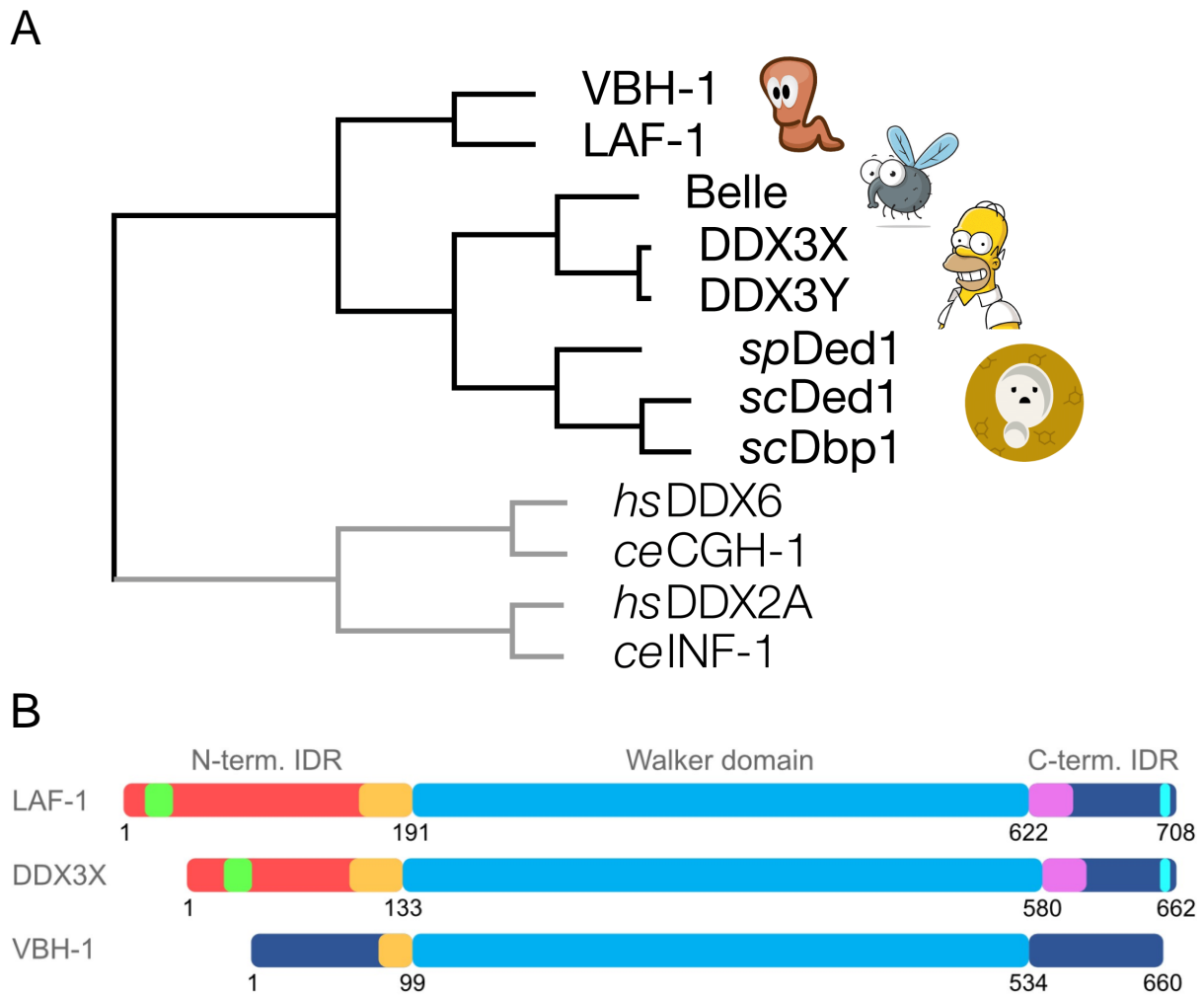


Figure 3. Evolutional relations of DDX3 protein family members.

A. Phylogenetic tree of given DDX3 protein family members from indicated species and selected DDX6 and DDX2 (eIF4E) proteins as outgroups. Letters in parentheses indicate species as follows: *ce*–*Caenorhabditis elegans*, *hs*–*Homo sapiens*, *sc*–*Saccharomyces cerevisiae* and *sp*–*Saccharomyces pombe*.

B. Stick diagram of human and nematode DDX3 paralogs with indicated protein domains and motifs specific to these RNA helicases. Red – N-terminus RGG/RG-rich IDR, Blue – folded Walker domain, Ultramarine – C-terminus GQ/GS/Q-rich IDR, Magenta – C-terminus extension, Orange – N-terminus extension, Green – initiation factor binding motif, Cyan – WW motif. IDR boundaries were assigned according to AlphaFold.

Somatic roles of DDX3 have been characterized based on the broad phenotypes induced by disruption of its zygotic gene function. In humans, for instance, a functional defect in DDX3X protein leads to the genetic neurodevelopmental disorder known as "DDX3X syndrome", predicted to be the cause of 1-3% of all unexplained developmental delays and/or intellectual disabilities in females (Nicola et al., 2019; Snijders Blok et al., 2015). Genetic screening revealed that in most cases, the syndrome is caused by a heterozygous *de novo* DDX3X pathogenic variant identified in females, and it may be caused by a hemizygous

DDX3X pathogenic variant in males (Nicola et al., 2019). Affected individuals experience intellectual disability, autism spectrum disorder, language delays, attention-deficit/hyperactivity disorder, and various medical comorbidities (Levy et al., 2023), significantly impacting their quality of life. Furthermore, many *de novo* missense and nonsense mutations in DDX3X, are a leading cause of cancers, such as medulloblastomas and natural killer/T-cell lymphoma (Jiang et al., 2015; Jones, 2012; Valentin-Vega et al., 2016).

Germline roles of DDX3 have been primarily revealed in genetic animal models, such as flies and nematodes. Functional reduction of Belle, the sole DDX3 protein in *D. melanogaster*, causes early larval arrest, spermatogenesis defects, and a reduction in female fertility due to pathological mRNA metabolism (Johnstone et al., 2005). One of the earliest phenotypes connected to germ cell development of DDX3 deficiency was described in *C. elegans*, where the *laf-1* gene is required for male fate choice of larval germ cells in XX hermaphrodites and for overall male fate development in XO males (Goodwin et al., 1997). Several missense *laf-1* mutations were identified in a genetic suppression screen of forced sperm production in *fem-3* gain-of-function XX hermaphrodites, reverting their continued sperm production to oogenesis, producing again self-fertile animals. Here, the female sex determination gene *tra-2*, a molecular opponent of *fem-3*, has been suggested to be posttranscriptionally downregulated by LAF-1 to achieve the natural sperm-to-oocyte switch in adult hermaphrodites (Goodwin et al., 1997; Hubert & Anderson, 2009). In addition to this sex determination defect in heterozygotes, homozygote *laf-1* alleles produce either dead embryos or developmentally arrested larvae. Although not yet further investigated, both name-giving phenotypes, *lethal and feminization (laf)*, are connected to RNA helicase activity, as all three cloned *laf-1* alleles exchange amino acids in the helicase core (Hubert & Anderson, 2009). Combined with data of vertebrates, DDX3s are essential for embryogenesis probably in all metazoans, suggesting basic contributions to RNA regulation in cells of both somatic and germline tissues.

While the role of DDX3 in RNA metabolism has been clearly highlighted in multiple organisms, the molecular mechanisms of how DDX3 binds RNA and unwinds RNA duplexes remain controversial. Two alternative structural principles of quaternary RNA helicase organization have been proposed, namely acting as dimeric or trimeric DDX3 protomers to melt dsRNA substrates (Epling et al., 2015; Floor et al., 2016; Putnam et al., 2015; Song & Ji, 2019). Certainly, this difference might rely on evolutionary adaptations between the two studied DDX3 representatives, yeast Ded1p and human DDX3, or the offered artificial RNA

substrates (Sharma et al., 2017; Song & Ji, 2019). However, it may also be explained by the use of truncated polypeptide sequences that were trimmed to the helicase core, extended bit-by-bit to include some flanking sequences (termed N- and C-terminal extensions, see also Figure 3B) to regain *in vitro* RNA helicase activity (Epling et al., 2015; Floor et al., 2016; Kim & Myong, 2016; Langdon et al., 2018). The derived crystal structures of DDX3 fragments led initially to a trimer model (Figure 4A) that was recently revised to a potential dimer model (Figure 4B), in which each DDX3 protomer binds via its helicase core to one strand of an RNA duplex to splay them apart, upon simultaneous release of ADP, inorganic phosphate and the unwound RNA substrate (Song & Ji, 2019).

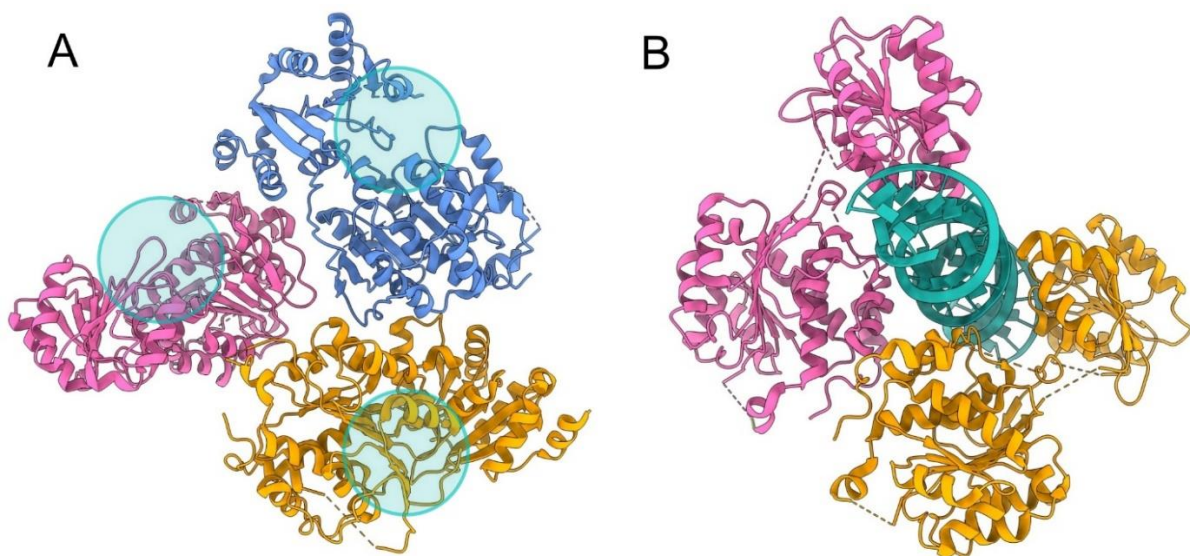


Figure 4. X-ray crystallography suggests both dimer and trimer DDX3 complexes.

A. Schematic image of the 5E7J crystal structure of the human DDX3X RNA helicase trimer protein complex at 2.2 Å (Floor et al., 2016). Pink, orange and blue proteins represent the 132-607 residues of the individual DDX3X monomers' folded domains. Green circles mark DDX3X RNA-binding sites. Dashed lines represent unresolved fragments of DDX3X structure.

B. Schematic image of the 6O5F crystal structure of the human DDX3X RNA helicase dimer protein in complex with a synthetic 20 nucleotides double-helix RNA (green) at 2.5 Å (Song & Ji, 2019). Each protomer (orange and pink) represent the 132-607 residues of the individual DDX3X monomers' folded domains. Dashed lines represent unresolved fragments of DDX3X structure.

Surprisingly, potential functional contributions of the N- and C-terminal IDRs to the enzymatic role of DDX3 remained largely unexplored, and only few experiments were conducted with full-length proteins. Using FRET-based methods, the N-terminal RGG IDR within full-length LAF-1 has been suggested to serve as both an interface for interprotein interactions of DDX3 RNA helicase dimers and an RNA recognition domain (Kim & Myong,

2016). Additionally, the N-terminal RGG IDR has been shown to be an essential and sufficient domain for liquid-liquid phase separation (LLPS) of DDX3 *in vitro* and to maintain integrity of RNA granules *in vivo* (Elbaum-Garfinkle et al., 2015; Saito et al., 2019; Valentin-Vega et al., 2016). Genetic experiments in flies further suggested an essential role of the N-terminal RGG-IDR for Belle's *in vivo* functions (Liao et al., 2019). However, the C-terminal IDR of DDX3 subfamily members has received much less attention, and its functions remain poorly understood.

1.2. DDX3 proteins as posttranscriptional RNA regulators

Across animals, DDX3 proteins appear to be involved in almost all steps of RNA metabolism and even in genome stability. Although at steady state localized to the cytoplasm, nuclear DDX3 has been suggested to regulate transcription and pre-mRNA splicing (Botlagunta et al., 2008; Chao et al., 2006; Merz et al., 2007; Schroder et al., 2008; Soulat et al., 2008). Consistent with a conserved nuclear export signal (NES) present at its very N-terminus (Figure 3B), DDX3 has also been implicated in assisting nuclear export of RNAs to the cytoplasm, thereby accompanying RNA transcripts for a long period in their life cycle (Lai et al., 2008; Yedavalli et al., 2004). Interestingly, monomeric DDX3X was recently shown to possess RNaseH2-like activity, initiating ribonucleotide excision repair reactions in cooperation with several different DNA polymerases to prevent genetic instability (Riva et al., 2020). Further combined with human DDX3's contributions in assisting viral propagation (Angus et al., 2010; Han & Yang, 2020; Mamiya & Worman, 1999; Yedavalli et al., 2004), all these findings suggest a wide variety of cellular functions for nuclear DDX3.

By contrast, as a predominantly to the cytoplasm localized protein, DDX3 emerged as a global regulator of protein synthesis across species. Although initially implicated in mRNA-specific translational control, global analysis techniques in different human cell types revealed a larger spectrum of bound mRNAs that depend on DDX3 presence for efficient translation (Calviello et al., 2021; Valentin-Vega et al., 2016; Venkataramanan et al., 2021). As general dsRNA-binding proteins, DDX3 RNA helicases appear not to bind sequence specifically, instead, they accumulate on mRNAs with highly structured 5' untranslated regions (UTRs). Intriguingly, DDX3 directly contact also a specific helix of the 18S RNA located near the mRNA entry channel of the 40S ribosomal subunit to perhaps further assist translation initiation (Calviello et al., 2021; Geissler et al., 2012; Oh et al., 2016; Venkataramanan et al.,

2021). However, DDX3 in human cells, Belle in flies and LAF-1 in *C. elegans*, have also been connected to translational repression of specific mRNAs, using a yet unknown mechanism (Goodwin et al., 1997; Gotze et al., 2017; Ihry et al., 2012; Shih et al., 2008; Yarunin et al., 2011). Next to translational initiation also translational elongation has been put forward as a potential role of DDX3 in protozoa (Padmanabhan et al., 2021), arguing that either species-specific adaptations within the DDX3 polypeptide have evolved or unique co-factors exist that influence DDX3 activities in how protein synthesis is promoted, or even repressed.

Translation of most eukaryotic mRNAs relies on the scanning mechanism, which is initiated once the 43S preinitiation complex (PIC) assembled on the mRNA near its 5' end (Hinnebusch, 2014). The PIC is composed of the GTP-charged eukaryotic translation initiation factor 2 (eIF2) that in turn is bound to a Methionyl-initiator tRNA, including a few other eIFs (Pelletier & Sonenberg, 2019). PIC's recruitment to an mRNA is facilitated by the cytoplasmic cap-binding complex, a heterodimer of the cap-binding protein eIF4E and eIF4G, a rather large protein orchestrating 3' end connections and interactions with PIC (Gebauer & Hentze, 2004). Once in place, PIC scans the mRNA's 5' UTR for an start codon triplet (typically AUG). To overcome structural RNA folds, this process is assisted by the prototypical DEAD box helicase family members of eIF4A-type DDX2 RNA helicases (Schuller & Green, 2018). In a later step of translation initiation and after AUG recognition, PIC is remodelled by the activity of associated eIFs to an 48S complex that is eventually joined by the large 60S ribosomal subunit to initiate polypeptide synthesis (Hinnebusch, 2014). Elongation proceeds progressively until a stop codon defines the end of the translated open reading frame (ORF) and induces termination to disassemble and recycle the ribosome (Hellen, 2018).

To a large extent, translational control homes in onto the initiation process (Gebauer & Hentze, 2004). Moreover, 5'UTRs may contain stem loop structures as well as decoy AUGs that define short upstream open reading frames, both negatively influencing productive ribosome formation (Hinnebusch et al., 2016). Interestingly, species-specific adaptations shape and expand the options on how translational control can be exerted at the mechanistic level (Gebauer & Hentze, 2004). For example, unlike many eukaryotic models, *Caenorhabditis elegans* mRNAs carry next to mono-methyl caps at their 5' end, primarily three-methyl cap structures, due to the dominating process of *trans*-splicing (Lasda & Blumenthal, 2011). As a consequence, several eIF4E orthologs (termed IFE proteins) are expressed that recognize either both cap structures equally well or with a preference for one or the other (Keiper et al., 2000; Miyoshi et al., 2002). An additional consequence of *trans*-splicing is that many mRNAs have

a very short 5'UTR sequence. Nonetheless, there are examples of long 5'UTRs and translational control is a heavily exploited mechanism in *C. elegans* germ cells to manipulate developmental fate decisions of germ cells.

How DDX3 RNA helicases act as translational regulators is still unclear. In all tested organisms, a functional ATPase activity was essential for *in vivo* functions (Chao et al., 2006; Goodwin et al., 1997; Johnstone et al., 2005; Padmanabhan et al., 2021). But tethering studies of *Drosophila* DDX3/Belle to a reporter mRNA substrate in germ cells, suggested also a requirement of the N-terminal RGG IDR but not the C-terminal IDR in promoting translation of the encoded reporter protein (Liao & Regev, 2021). As suggested also for human DDX3 (Chen et al., 2018; Shih et al., 2012), this stimulatory effect of the N-terminal IDR may rely on its embedded eIF4E-binding motif, yet a single missense mutation within this motif designed to weaken Belle's affinity to eIF4E was found to broadly complement *in vivo* functions of *belle* null mutants (Liao & Regev, 2021). Therefore, it remains controversial for which purpose and to which extent either IDR contributes to cellular functions of DDX3 proteins.

Global translational repression is linked to a restructuring of cytoplasm, leading to an agglomeration of RNPs into larger assemblies of RNA granules (Khong & Parker, 2020). As part of an inducible and reversible cellular stress response pathway, these so called stress granules tightly package mRNA molecules and shield them from ribosome assembly (Protter & Parker, 2016). Cancer-associated ATPase mutations of DDX3 drive stress granule formation, consistent with reducing target-encoded protein expression (Shih et al., 2012; Valentin-Vega et al., 2016). In this respect, the N-terminal RGG IDR was found to be crucial for promoting DDX3 localization to stress granules. Furthermore, acetylation of several lysins in the IDR suppressed stress granule enrichment, implying that posttranslational modifications of the N-terminal IDR might serve as a regulatory dial for subcellular spatiotemporal dynamics of DDX3 RNA helicases (Saito et al., 2019).

1.3 *C. elegans* germline development and P granules

Caenorhabditis elegans is a small nematode that lives in the soil and is found in a broad range of areas around the globe. It was originally introduced as a genetic model organism for behavioural studies (Argon & Ward, 1980; Brenner, 1973, 1974). However, due to its short lifecycle, a high brood size, its simple anatomy, rich in morphological detail and full-body transparency throughout its lifetime, paired with a wide array of forward and reverse genetic

tools, *C. elegans* has been adapted for research beyond neurobiology, reaching from obesity, aging, toxicology, immunology, stem cell biology to many other medically relevant research fields (Hunt, 2017; Marsh & May, 2012; Shen, Yue, & Park, 2018; Shen, Yue, Zheng, et al., 2018; Watts & Ristow, 2017).

In laboratory conditions, *C. elegans* is fed on agar plates with *E. coli* (Frezal & Felix, 2015). This technicality is exploited in the reverse genetic technique of RNA interference (RNAi) by feeding dsRNA-producing bacteria to animals, thereby causing a specific knockdown in gene expression activity, affecting fed animals and their progeny (Kamath et al., 2003). Modern genome editing techniques, such as CRISPR/Cas-mediated genome engineering, have by now replaced non-targeted EMS-induced mutations at genomic loci (Kutscher & Shaham, 2014). While biochemistry is not the major strength of this model system, a few aspects make it possible to perform biochemical experiments. Worms can be grown in large numbers, and they can be reasonably synchronized according to developmental stages. It is also possible to enrich for early embryonic stages due to the many chitin layers protecting embryos from aggressive chemicals that otherwise disintegrate larvae or adults, such as NaOH and hypochlorite (Khan & Mcfadden, 1980). Lastly, all germ cells together represent about two thirds of an animal's body mass, making especially germ cell-enriched proteins a good source for biochemical experiments. However, higher developmental resolution can only be achieved on a one-by-once case with the help of high-powered microscopes to follow individual proteins by immunostaining of fixed samples or by life-cell microscopy of proteins fused to fluorescent proteins.

The full lifecycle of *C. elegans* usually takes only about 3 days with a progressive increase in size from embryogenesis through four larval stages to adulthood (Figure 5). In parallel, sex-specific reproductive organs are formed to house the developing germline tissue. Self-fertilizing hermaphrodites (XX) dominate the population and produce during their last larval stage a defined number of sperm, before switching to oocyte production. On the contrary, males (XO) are rare in the population due to spontaneous chromosomal non-disjunction (0.1%) in the meiotic hermaphrodite germ line, and they only produce sperm throughout their life time. While hermaphroditic individuals produce genetically almost identical progeny during self-fertilization, male nematodes are able to introduce genetic diversity into the population upon crossing with hermaphrodites, leading also to a temporal increase of males in a given population (Byerly et al., 1976).

Especially germline development is well documented and heavily investigated in *C. elegans* (Hubbard & Greenstein, 2005). It begins in embryonic lineages and continues with germline stem cell expansion in larvae to finally end with gamete production in adults (Figure 5). Next to a detailed characterization at the histological level during every lifecycle stage, distinct molecular regulatory mechanisms are emerging and posttranscriptional RNA regulation has been identified as a dominating theme to guide essentially all aspects of germ cell biology (Albarqi & Ryder, 2022). Next to RNA helicases, such as LAF-1, many other evolutionary conserved RNA regulators, including RBPs and RNA modifying enzymes, were identified and characterized in this context. Together they influence the sexual fate of germ cells as well as their differentiation programs, and maintain germ cell identity (Kimble & Crittenden, 2007).

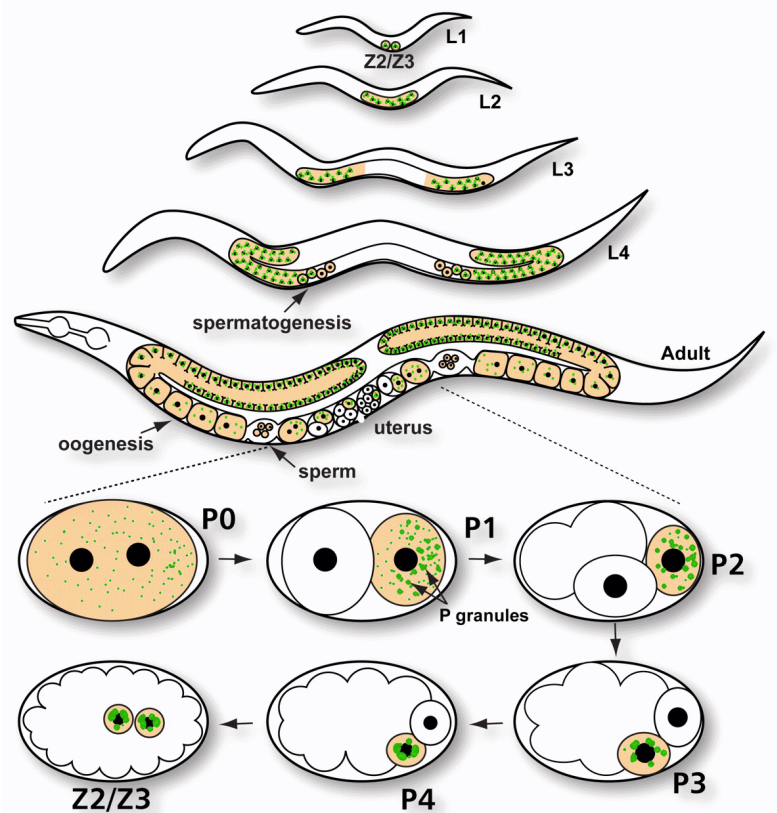


Figure 5. *C. elegans* germ line development during a hermaphrodite's life cycle.

In this scheme, germ cells are highlighted in orange and germ (P) granules labelled in green colour. Z2/Z2 – germ cell precursors, borne in the embryo; L1-L4 – four distinct larval stages, separated by a moulting event; P0-P4 – P lineage of germ cell blastomeres. Note, P granules are primarily perinuclear. Only in later stages of oogenesis and very early P cells, P granules are detached from the outer nuclear membrane to be only cytosolic. (Adapted from Updike & Strome, 2009).

C. elegans also became one of the first organisms in which germ (P) granules were microscopically identified and described (Strome & Wood, 1982; Wolf et al., 1983). P granules are markers of germ cells and represent cytoplasmic RNA granules that strictly correlate with germ cell fate (Figure 5). During the first cell division of the zygote (i.e. the fertilized oocyte), this P0 cell gives rise to two distinct cell types, the somatic blastomer AB and the germline precursor P1, by asymmetrically segregating cytoplasmic soma-determining components and P granules to either sister cell, respectively (Figure 5). This process is started by an initial disassembly of all P granules present across the zygotic cytosol and a subsequent localized reassembly of P granules in the future P1 sister cytoplasm prior to cytokinesis that separates the two sister cells (Brangwynne et al., 2009). In four additional asymmetric divisions until the P4 stage, only one cell maintains P granules, until a symmetric division gives rise to two equal sisters, Z2 and Z3. These two primordial germ cells postembryonically develop further into over a thousand germ cells colonizing the gonads of adult organisms (Figure 5). These cell cycle-coupled events of reiterative P granule dissolution and condensation nicely demonstrate the many dynamic changes that P granules undergo during germline development (Phillips & Updike, 2022). One driver of these fluidic behaviours of phase separations, later dubbed liquid-liquid phase separation (LLPS), has been suggested to rely on weak affinities among its protein and RNA components that collectively support agglomeration and dispersal (Mittag & Parker, 2018). In particular, intrinsically disordered proteins and IDRs of protein components are seen as molecular hubs of P granule fluidics and more generally all RNA granules (Smith et al., 2016) (Protter et al., 2018; Smith et al., 2016).

Next to RNA, many RBPs and RNA-modifying enzymes are components of P granules. This includes members of the *C. elegans* specific PGL (*P-granule abnormality*) protein family of PGL-1 and PGL-3, as well as four evolutionary conserved GLH (*Germline Helicase*) proteins (Updike & Strome, 2010). Both PGL proteins are RBPs containing RGG-rich regions to contact RNA non-specifically (Chong et al., 2018). GLH-1 to GLH-4 are DDX4 RNA helicases of the VASA protein family (Kuznicki et al., 2000). Besides being together essential molecules to germline development, both protein families are almost exclusively expressed in germ cells and highly enriched in P granules, making them popular markers of germ cell fate in *C. elegans* (Kuznicki et al., 2000; Orsborn et al., 2007; Spike et al., 2008). This is in contrast to LAF-1 DDX3, which is strongly present in the cytosol next to its enrichment in P granules (Elbaum-Garfinkle et al., 2015), presumably dynamically exchanging between both the soluble (cytosolic) and liquid-liquid phase separated (P granule) state. In favour of this working

hypothesis are the observations that a reduction of LAF-1 protein levels affect P granule identity; PGL-1 becomes cytosolic instead of remaining in the granular phase (Elbaum-Garfinkle et al., 2015). As early germline development in the embryo happens in the absence of transcriptional activity and some maternal mRNAs are enriched in P granules, these RNA granules can be envisioned as developmental RNA storage organelles that protect and maintain mRNA molecules for translation at subsequent P lineage stages. How mRNAs or as such mRNPs are integrated or discharged from P granules remains to be investigated.

1.4. Research aim

This study aims to understand the molecular functions and biophysical properties of the *C. elegans* DDX3 ortholog LAF-1 and its intrinsically disordered regions (IDRs). An extension of both objectives is the determination of the contributions of the folded and disordered domains of LAF-1 to germline development and their participation in germ granules.

The genetic locus *laf-1* is predicted to produce two alternative transcripts encoding two potential DDX3-type RNA helicases that differ in their N-terminal RGG IDR. To clarify *laf-1*'s expression activity throughout the nematode's lifecycle and its full coding potential at the protein level, a monoclonal antibody will be characterized in its ability to serve as a tool for discriminating and characterizing both protein isoforms. Furthermore, polyclonal antibodies will be purified as additional LAF-1-specific tools.

Next, the newly identified LAF-1 isoforms will be examined for their RNA-induced enzymatic helicase activity and abilities to induce liquid-liquid phase separation (LLPS) *in vitro*. By setting up a bulk RNA helicase assay of total RNA from *C. elegans*, these experiments are expected to clarify the contribution of the folded core domain and terminal IDRs to RNA helicase activity of LAF-1. In parallel, a second set of *in vitro* experiments is designed to examine the effects of the previously genetically identified missense mutations within the helicase core domains of LAF-1. By combining mutated or IDR-truncated LAF-1 with full-length wild-type proteins, new insights regarding the controversial oligomer structure of DDX3 proteins are expected. Together, these data points will be important to understand the molecular features that, on the one hand disrupt germline sex determination and spermatogenesis in *laf-1* heterozygote mutants, and on the other hand induce severe larval arrest phenotypes in *laf-1* homozygotes. Lastly, the LLPS abilities of LAF-1 isoforms will be investigated in dependence on RNA and all five *C. elegans* eIF4E orthologs as potential regulators of LAF-1 activity. Together with biophysical structural analysis tools (SAXS), these experiments are expected to clarify LAF-1's localization potential to enrich in P granules and act as a potential RNA regulator of stored mRNAs during maternal germline development.

In a last step to accomplish the established aims, unknown LAF-1 interaction partners that assist LAF-1 in germline development will be identified by combining immunoprecipitation with mass spectrometric identification. After validation, the most prominent candidates will be in future experiments used for LLPS and enzymatic studies to reveal potential *in vivo* molecular consequences of such interactions.

2. Materials and Methods

2.1. Materials

Software

- Affinity Designer (1.10.5.1342)
- Affinity Photo (1.10.5.1342)
- ChromeLab (6.1)
- ChimeraX (1.3)
- GCUA (http://gcu.schoedl.de/sequential_v2.html/)
- Image Studio LI-COR Edition (5.2.5)
- ImageJ (1.53t)
- Microsoft Office Standard 2019
- MUSCLE (<https://www.ebi.ac.uk/Tools/msa/muscle/>)
- Simple Phylogeny (https://www.ebi.ac.uk/Tools/phylogeny/simple_phylogeny)
- SnapGene (2.7.3)
- The Leica Application Suite X (LAS X) (3.7.3.23245)
- Visual Molecular Dynamics (VMD) (1.9.4)
- Visual Studio Community 2019 (3.3.2185.63263)

Solid and liquid media

- LB media: 1% tryptone 0.5% yeast extract, 0.5% NaCl. Autoclaved.
- LB agar media: 1% tryptone 0.5% yeast extract, 0.5% NaCl, 0.5% agar. Autoclaved.
- SOC media: 2% tryptone, 0.5% yeast extract, 0.05% NaCl, 20 mM glucose, 25 mM KCl, 10 mM MgCl₂. Medium was autoclaved after pH adjustment to ~7.0.
- NGM: 0.3% NaCl, 0.25% peptone, 2% agar, 0.0005% cholesterol, 1mM CaCl₂, 1 mM MgSO₄, 25 mM PBS pH 6.0. NaCl, peptone and agar mixture solution was autoclaved in final volume before composition adjustment.

Bacterial strains

- OP50 (feeding strain): uracil auxotroph *E. coli* strain used as a food supply for *Caenorhabditis elegans* laboratory maintenance on agar plate.
- DH5 α (cloning strain): *E. coli* [*F*⁻ *endA1 glnV44 thi-1 recA1 relA1 gyrA96 deoR nupG purB20 ϕ 80dlacZ Δ M15 Δ (lacZYA-argF) U169, hsdR17(rK-mK+), λ -]*
- XL1-Blue (cloning strain): *E. coli* [*endA1 gyrA96(nalR) thi-1 recA1 relA1 lac glnV44 F'*:*:Tn10 proAB+ lacIq Δ (lacZ)M15] hsdR17(rK- mK+)]*

- BL21-CodonPlus (DE3)-RIL (protein expressing strain): *E. coli* [*B F⁻ ompT hsdS(rB - mB -) dcm⁺ Tetr gal λ(DE3) endA Hte [argU ileY leuW Camr]*]
- HT115(DE3) (Bacteria-mediated RNAi strain): *E. coli* [*F⁻, mcrA, mcrB, IN(rrnD-rrnE)1, rnc14::Tn10(DE3 lysogen: lacUV5 promoter -T7 polymerase)*]

2.2. Solutions

Proteins

- Stacking gel stock: 150 mM Tris-HCl pH 6.8, 5% acrylamide/bis (19:1), 0.1 % SDS.
- SDS (Tris/Glycine/SDS) running buffer (10x): 25 mM Tris-HCl pH 8.3, 192 mM glycine, 0.1% SDS.
- SDS sample buffer (4x): 250 mM Tris-HCl pH 6.8, 8% SDS, 40% glycerol, 0.02% bromophenol blue, 5% 2-mercaptoethanol.
- Coomassie Brilliant Blue gel staining solution: 0.1% Coomassie Brilliant Blue R-250 Dye, 10% acetic acid, 50% ethanol.
- Blotting buffer (10x): 25 mM Tris-HCl pH 8.3, 192 mM glycine.
- PBS pH 7.4 (1x): 2.7 mM KCl, 137 mM NaCl, 2 mM KH₂PO₄, 10 mM Na₂HPO₄.
- 1 M PBS pH 6.0: 138.1 mM Na₂HPO₄, 861.9 mM KH₂PO₄.
- PBS-T: 0.05% Tween-20 in PBS pH 7.4.
- Blocking solution: 5% skimmed milk powder in PBS-T.
- Antibody incubation buffer: 0.5% skimmed milk powder in PBS-T.
- Stripping solution: 2% acetic acid, 0.5% SDS.
- Isoelectric focusing sample buffer: 8M urea, 1% CHAPS, 25 mM DTT, 0.5% HPE IPG strip buffer.
- IP buffer: B70 buffer with EDTA-free protease inhibitor cocktail, 1 U/μL Ribolock RNase inhibitor and 25 μg/mL cycloheximide.
- Equilibration base buffer: 6M urea, 2% SDS, 50 mM Tris-HCl pH 8.8, 50% glycerol.
- LAF-1L lysis buffer: 50 mM Tris-HCl pH 7.4, 500 mM NaCl, 0.1% Triton X-100, 10% glycerol, 20 mM imidazole, 1x EDTA-free protease inhibitor cocktail, lysozyme 0.25 mg/mL.
- LAF-1L washing buffer: 50 mM Tris-HCl pH 7.4, 650 mM NaCl, 0.1% Triton X-100, 10% glycerol, 40 mM imidazole.
- LAF-1L elution buffer: 50 mM Tris-HCl pH 7.4, 650 mM NaCl, 0.1% Triton X-100, 10% glycerol, 300 mM imidazole.

- LAF-1L rebuffing solution: 50 mM Tris-HCl pH 7.4, 1000 mM NaCl, 0.1% Triton X-100, 10% glycerol.
- LAF-1S lysis buffer: PBS pH 7.4, 25 mM Tris-HCl pH 7.4, additional 150 mM NaCl, 10 mM MgCl₂, 0.1% NP-40, 10% glycerol, 20 mM imidazole, 1x EDTA-free protease inhibitor cocktail, lysozyme 0.25 mg/mL.
- LAF-1S washing buffer: PBS pH 7.4, 25 mM Tris-HCl pH 7.4, additional 250 mM NaCl, 10 mM MgCl₂, 0.1% NP-40, 10% glycerol, 40 mM imidazole.
- LAF-1S elution buffer: PBS pH 7.4, 25 mM Tris-HCl pH 7.4, additional 250 mM NaCl, 10 mM MgCl₂, 0.1% NP-40, 10% glycerol, 300 mM imidazole.
- IFE-x lysis buffer: 50 mM Tris-HCl pH 7.4, 250 mM NaCl, 10 mM imidazole, 1x EDTA-free protease inhibitor cocktail, lysozyme 0.25 mg/mL.
- IFE-x washing buffer: 50 mM Tris-HCl pH 7.4, 250 mM NaCl, 30 mM imidazole.
- IFE-x elution buffer: 50 mM Tris-HCl pH 7.4, 300 mM NaCl, 250 mM imidazole.
- IFE-x denaturing buffer: 50 mM Tris-HCl pH 7.4, 8M urea, 20 mM imidazole.
- IFE-x rebuffing solution: 50 mM Tris-HCl pH 7.4, 250 mM NaCl, 10% glycerol.
- Borate buffer: 200 mM sodium borate pH 9.0.
- Ethanolamine buffer: 200 mM ethanolamine pH 8.0.
- Acidic antibody elution buffer: 100 mM glycine-HCl pH 2.4.
- Basic antibody elution buffer: 100 mM ethanolamine pH 11.5.
- High salt antibody elution buffer: 50 mM Tris-HCl pH 7.4, 3 M MgCl₂.

Nucleic acids

- TBE (Tris/Borate/EDTA) running buffer (5x): 0.445 M Tris-borate pH 8.2 – 8.4, 0.01 M EDTA.
- RNA gel loading buffer (2X): 95% formamide, 0.025% SDS, 0.05% Orange G, 0.025% ethidium bromide, 0.5 mM EDTA.
- DNA gel loading buffer (6X): 60% v/v glycerol, 20 mM Tris-HCl pH 7.4, 60 mM EDTA, 0.48% SDS, 0.03% xylene cyanol, 0.03% bromophenol blue, 0.12% Orange G.
- Trizol reagent: 9.5% guanidinium thiocyanate, 3.1% ammonium thiocyanate, 105 mM sodium acetate solution pH 5.0, 48% v/v aqua-phenol, 2.5 mM EDTA (pH 8.0), 2.5 mM EGTA in RNase-free dH₂O.

2.3. Methods

2.3.1. SDS-polyacrylamide gel electrophoresis

SDS-polyacrylamide gel electrophoresis (SDS-PAGE) according to Laemmli system was performed using the Mini-PROTEAN (BioRad) electrophoresis apparatus (Laemmli, 1970). A 10% resolving gel was made by combining 1.75 mL of distilled water, 1.88 mL of 1M Tris-HCl pH8.8, 1.25 mL of 40% acrylamide/bis solution (19:1), and 50 μ L of 10% SDS. Polymerization was initiated by adding 40 μ L of TEMED and 10 μ L of 10% ammonium persulfate to the resolving solution. After brief pipetting, the solution was immediately poured into a Mini-PROTEAN cell casting module. The solution was gently covered with 100% isopropanol to form an even surface on the resolving gel. After solidification, the isopropanol was removed and any leftovers were washed out with dH₂O. A 1.5 mL of 8% acrylamide stacking gel stock solution was mixed with 15 μ L of APS and 1.5 μ L of TEMED, poured on top of the stacking gel, and a comb inserted. After full polymerization of the stacking gel, the casting cell was transferred into a Mini-PROTEAN apparatus (BioRad) with 1x Tris/Glycine/SDS running buffer. After comb removal, protein samples in SDS sample buffer were loaded into sample pockets, next to 3 μ L prestained protein ladder (Thermo Fisher), and run for 1.5 hours at 25 mA per gel with a maximum electric potential of 200 V.

For visual analysis of protein composition, post-run gels were stained with Coomassie Brilliant Blue gel staining solution for 30-40 minutes at room temperature with gentle shaking. After the staining procedure, the gel background was decolorized with hot water washing under slow agitation. The water was changed every hour until the gel was fully clarified. A digital image was obtained using a scanner or camera.

2.3.2. Western blot

Western blot protein transfer and immobilization on a nitrocellulose membrane were performed using the Mini-Trans-Blot apparatus (BioRad). The nitrocellulose membrane and filter papers were briefly soaked in blotting buffer and assembled into a sandwich with an SDS-polyacrylamide gel overlaid with a nitrocellulose membrane inside and two layers of soaked filter paper outside. The sandwich was placed into the system filled with blotting buffer according to transfer polarity. The western blot was run for 2.5 hours on ice at 400 mA with a maximum electric potential of 180 V. After the transfer, the membrane was extracted from the

sandwich and gently cleaned from any gel residue with a clean paper towel. Then, the membrane was briefly washed twice in PBS-T and blocked by a 15-minute incubation in blocking buffer to prevent nonspecific protein sorption during further steps. After blocking, the membrane was washed twice for 10 minutes with PBS-T.

The blotted protein membrane was incubated overnight at +4 °C in primary antibodies diluted in antibody incubation buffer with constant cavitation. Subsequently, the membrane was washed three times for 5 minutes each with PBS-T on a benchtop rocking platform shaker. To visualize the primary antibody, the membrane was incubated with fluorescent-coupled secondary antibodies in antibody incubation buffer for 2.5 hours at room temperature. Afterward, the membrane was briefly washed three times with PBS-T and visualized with the help of the Odyssey XF Imaging System. The measuring channels were selected and adjusted according to the secondary antibodies' fluorescent dyes and signal intensities. The membranes could be stored in PBS-T buffer at +4 °C for further reprobing. All primary antibodies used for western blotting are summarized in Appendix List 5.7.

The membrane could be reprobed with antibodies after the stripping procedure. To do so, the membrane was washed twice for 5 minutes in PBS-T. After transferring the membrane to a hermetic container, it was covered with at least 5 mm of stripping solution and placed into a +55 °C water bath for 1 hour. After stripping, the membrane was washed three times in PBS-T for 15 minutes on a rocking shaker. The membrane was then reprobed immediately or stored at +4 °C for later use. Before antibody treatment, it was reblocked according to the procedure above.

2.3.3. Isoelectric focusing in 2-D electrophoresis

Isoelectric focusing (IEF) was used to separate proteins based on their individual isoelectric points (pI). IPG BlueStrip 7 cm stripes (SERVA) with a linear pH gradient in the range of 3.0-10.0 were used. Total protein was solubilized in isoelectric focusing sample buffer, and the protein concentration and buffer volume were adjusted according to the strip size and the manufacturer's instruction manual. To remove insoluble impurities, the sample was centrifuged at maximum speed in a 5417R centrifuge with F-45-30-11 rotor (Eppendorf) for 5 minutes at room temperature. The supernatant was then evenly transferred onto the strip holder cuvette surface. The strip was placed on the transferred sample without air bubbles, according to the strip holder's polarity. A thin layer of HPE IPG Overlay mineral oil (SERVA) was

applied to cover the strip to prevent sample evaporation. The holder was then closed and installed into an isoelectric focusing apparatus (Amersham), according to the system polarity.

First, the strip was rehydrated at +20 °C for 7 hours. The isoelectric focusing procedure was designed according to the strip manufacturer's instruction manual and is presented in List 1. The maximum current was restricted to 70 μ A/strip and 110 μ A/strip for 7 cm and 11 cm strips, respectively.

| Order | Step | Voltage (V) | Duration (hours) |
|-------|-------------|-------------|------------------|
| 1 | Step-n-Hold | 150 | 1 |
| 2 | Step-n-Hold | 300 | 1 |
| 3 | Gradient | 1000 | 1 |
| 4 | Gradient | 3000 | 2 |
| 5 | Step-n-Hold | 3000 | 2 |

Table 1. Isoelectric focusing program for 2-D electrophoresis.

The focused strip was carefully cleaned of mineral oil with a paper towel. To equilibrate the strip, it was incubated in a 15 mL centrifugation tube containing 5 mL of equilibration buffer with 2% DTT under constant rocking for 10 minutes. After that, 125 mg of iodoacetamide were added, and the tube was gently shaken until the iodoacetamide dissolved completely. The strip was then briefly washed in PBS and wiped to remove excess liquid. Next, it was placed on top of an SDS-polyacrylamide gel and immobilized by covering it with 1% agarose in 1x Tris/Glycine/SDS running buffer. Further steps of SDS-PAGE, western blotting transfer, and immunodetection were performed according to the corresponding chapters.

2.3.4. Protein precipitation with TCA

Protein solution was mixed with a 100% TCA solution in a 1:5 ratio. After incubation for 1 hour at room temperature or overnight at +4 °C, the solution was centrifuged at maximum speed using an F-45-30-11 rotor in a 5417R centrifuge (Eppendorf) for 10 minutes. The supernatant was discarded, and the pellet was resuspended in 500 μ L of 100% acetone to remove any remaining TCA. Pellets were ground into a fine powder using a plastic pipette tip. The emulsions were centrifuged for 5 minutes at top speed at room temperature. Pellets were washed two more times with pure acetone. After the final discard of acetone, each pellet was air dried until all remaining acetone evaporated. Protein pellets were then dissolved in SDS

sample buffer. To speed up the protein dissolving process, a brief heating to +80 °C and sonication in an RK100H ultrasonic bath (Sonorex) was used. The buffer volume was adjusted based on the size of the pellet and the experimental requirements. Typically, pellet did not exceed 10% of the sample volume.

2.3.5. Expression of recombinant proteins

25 ng of pET-28b+ plasmid encoding the protein of interest was gently mixed with 30 µL of chemically competent BL21-CodonPlus (DE3)-RIL *E. coli* strain kept on ice and incubated for 30 minutes. Afterwards, the bacteria were transformed by heat shocking procedure at +42 °C for 40 seconds, followed by a 30 second incubation on ice. After transformation, 300 µL of SOC media was added for bacterial recovery and antibiotic resistance development. The bacterial culture was incubated at +37 °C with shaking at 300 rpm for 40 minutes. The entire culture was evenly spread on a 10 cm kanamycin and chloramphenicol LB agar plate for double antibiotic selection. The plate was incubated for 8-12 hours at +37 °C until independent colonies became visible. One clone was picked and further cultivated overnight in 3 mL of LB media with kanamycin under 180 rpm rotation at +37 °C.

Next, a 5L-Erlenmeyer media flask with a vent cap was filled with 1L of sterile LB media with kanamycin. The media was inoculated with the full volume of the overnight culture and incubated at +37 °C with 180 rpm shaking until the OD600 value equalled ~0.5. Thereafter, the media was cooled on ice for 20 minutes. Protein expression was induced by adding 0.5 mL of 1 M IPTG solution to the cooled media. The induced culture was shaken at 180 rpm overnight at +16 °C to express protein. The induction time did not exceed 12 hours.

The overnight culture was cooled on ice for 1 hour and concentrated into pellets by portioned centrifugation in 50 mL centrifuge tubes at 10,000 rpm for 10 minutes at +4 °C in an Allegra X-30R centrifuge with C0650 rotor (Beckman-Coulter). The pellets were united and stored at -20 °C until further purification.

2.3.6. Purification of recombinant LAF-1 proteins

An induced pellet, generated from 1 L of media (Chapter 2.3.5), was fully resuspended on ice in 40 mL of LAF-1L lysis buffer. The resuspended bacteria were then sonicated using a Sonopuls GM70 ultrasonic disruptor (Bandelin). To prevent overheating, the emulsion was kept on ice during the entire procedure. Three cycles were done in total, with each cycle taking 4 minutes at 50% pulse and time settings, followed by a 1-minute pause between cycles. After sonication, the lysate was centrifuged for 20 minutes at 10,000 rpm at +4 °C in an Allegra X-30R centrifuge with C0650 rotor to purify the solution from insoluble bacterial leftovers. The supernatant was then filtered through a 0.45-micron syringe PVDF-Filter into a clean tube and kept on ice until further purification.

A 1 mL Ni-charged IMAC column was installed on an NGC chromatography system (BioRad) and equilibrated with LAF-1L lysis buffer until the conductivity, 280 nm, 260 nm, and pH curves plateaued. For the entire purification, the flow rate was set to 1 mL/min, and the LAF-1L lysis buffer was used as a blank value for all sensors. The pressure limits were set according to the column manual guidelines, and the chromatography system and column were kept at room temperature. During the load of filtered supernatant in the column, the lysate remained in an ice bath. After the load, the column was washed with 5 column volumes (CV) of LAF-1L lysis buffer and 10 CV of LAF-1L washing buffer. The bound protein was eluted by 5-7 CV of elution buffer until the sensors graphs plateaued. The total elution volume was fractionated to 1 mL and collected with the help of an automated NGC fraction collector (BioRad). Valid fractions were selected based on SDS-PAGE stained with Coomassie.

Due to the high aggregation and phase-separation potency of the recombinant LAF-1L protein, it cannot be stored at a high concentration unfrozen even for a short period of time. To prevent immediate loss of protein, it was diluted with LAF-1L elution buffer without imidazole 2-3 times until the final NaCl concentration reached 1 M and the turbidity disappeared. The approximate concentration at which the protein remains stable enough for enzymatic assays or rebuffing is around 1.5 mg/mL. Protein aliquots were flash frozen in liquid nitrogen and stored at -80°C. Protein stability was the biggest concern during further research. The reduction of salt or glycerol concentration leads to the intensification of the phase-separation process with further protein aggregation, even at lower protein concentrations.

Size exclusion chromatography (SEC) was performed with a 0.5 mL ice-malted aliquot against LAF-1L rebuffing solution. The total protein load for a single purification was in the

range of 1.5-2.0 mg. The flow speed was set to 1 mL/min according to the manufacturer's recommendation. After rebuffing, protein samples were stored at +4°C for no longer than overnight and were diluted to the final salt concentration right before the assay of interest.

The recombinant LAF-1S induction, freezing, and IMAC purification procedures were identical to LAF-1L with the LAF-1S set of lysis, wash, and elution buffers. For both IMAC and SEC, similar prepacked columns from Bio-Rad and Cytiva (Appendix List 5.2) were used. No significant difference was observed under the same buffer and running conditions.

2.3.7. Recombinant inclusion body washing

Inclusion bodies were extracted from either frozen *E. coli* pellets or intact bacteria. To reduce the content of cellular leftovers, pellets were resolubilized in a 50 mL centrifugation tube containing 500 mM NaCl with 1% Triton X-100 and sonicated on ice with the help of an ultrasonic disruptor for 4 min at 50% intensity and cycle settings. It is recommended to maintain a pellet-to-solution ratio of at least 1:7. Sonicated inclusion bodies were pelleted at +4 °C and 10,000 rpm in an Allegra X-30R centrifuge with a C0650 rotor (Beckman Coulter). Afterwards, the supernatant was discarded, and the pellet was resolubilized, sonicated, and pelleted under the same conditions. The minimum number of cycles is 4, but additional washing steps could be done in case of high contaminant content. Pellet colour and texture were used as approximate quality control parameters. Cleaned inclusion bodies have an even light-to-dark grey colour, while dirty pellets have an uneven dark yellow or olive colour. Clean inclusion bodies should easily emulsify in aqueous solution after brief vortexing. If inclusion bodies precipitate into a thick pellet or form visible particles, additional wash steps were conducted. Purified inclusion bodies were washed in distilled water three times, as described above. Finally, the pellet was aliquoted and stored at -20 °C in a minimal liquid volume (typically 100-200 µL). Alternatively, pellets were air-dried or dehydrated with acetone and stored as a dry powder at +4 °C. Inclusion bodies were used as an antigen for antibody induction and purification, as well as control samples for western blot and SDS-PAGE.

2.3.8. Purification of recombinant IFE-x proteins

IFE-1, IFE-3, and IFE-4 proteins were purified in native conditions, while IFE-2 and IFE-5 were chemically denatured and refolded on the IMAC column. Purification in native conditions was done by IMAC affinity purification and SEC, similar to the LAF-1 purification procedure (Chapter 2.3.6), with a different subset of buffers. For bacterial pellet resuspension, ultrasonic lysis and column binding were used with IFE-x lysis buffer. IMAC washing and elution steps were utilized with IFE-x washing buffer and IFE-x elution buffer, respectively. SEC rebuffing was done with IFE-x rebuffing solution.

Due to zero yield of soluble recombinant IFE-2 and IFE-5 proteins from the bacterial culture, a refolding protocol was developed and implemented. Because of the high protein content of the target protein in inclusion bodies, the primary LB bacterial culture was downscaled to 150 mL for a single purification. Inclusion bodies were prepared according to Chapter 2.3.7. Washed inclusion bodies were transferred into a 50 mL centrifuge tube and resuspended in 40 mL of IFE-x denaturing buffer. To increase the solubilizing surface of the inclusion bodies, the protein mixture was sonicated by Sonopuls GM70 ultrasonic disruptor (Bandelin) for 5 minutes with 25% pulse and time settings. To prevent overheating, the emulsion was kept on ice during the entire procedure. Five cycles were done in total with a 1-minute pause between sonications. Further denaturing was done overnight at +4 °C under constant rotation. Insoluble leftovers were precipitated by centrifugation in an Allegra X-30R centrifuge with C0650 rotor (Beckman Coulter) for 20 minutes at +4 °C temperature and 10,000 rpm rotation speed. The supernatant was transferred into a new 50 mL centrifuge tube and kept on ice until further refolding steps.

IFE-x refolding was done with the help of a 1 mL EconoFit Profinity IMAC column (Cytiva) installed on an NGC chromatography system with an NGC fraction collector (BioRad). The system was washed and equilibrated with IFE-x lysis buffer at a 1 mL/min flow rate. Background values were blanked after reaching plateau values of conductivity, 260 nm, 280 nm, and pH meter sensors. Maximum pressure restrictions were set to 42 psi, according to the column manual guideline. The chromatography system and column were kept at room temperature. After calibration was done, the system was rebuffed with 10 CV of IFE-x denaturing buffer at 0.5 mL/min flow rate. The full volume of denatured protein solution was loaded into the system at the same flow speed. Unbound protein was washed off by 10 CV of IFE-x denaturing buffer. The IFE-x protein refolding procedure was performed by a steady

gradient replacement of IFE-x denaturing buffer from 100 to 0% by IFE-x lysis buffer in a 100 mL volume at 0.25 mL/min flow rate at room temperature. All solutions had room temperature during the entire procedure.

After each sample was loaded, the column was washed with 5 CV of lysis buffer and 10 CV of washing buffer. The bound protein was then eluted with 5-7 CV of elution buffer until the sensor graphs plateaued. The elution volume was fractionated to 1 mL and collected using an automated NGC fraction collector (BioRad). Valid fractions were selected based on SDS-PAGE stained with Coomassie after each purification. Further SEC was performed with IFE-x rebuffing solution according to the LAF-1L SEC protocol. The eluted protein was then concentrated or diluted to 1 mg/mL and aliquoted into 100 μ L of protein solution in 1.5 mL centrifugation tubes. These aliquots were flash frozen in liquid nitrogen and stored at -80°C .

2.3.9. Immunoblot affinity purification of anti-LAF-1 polyclonal rabbit sera

Polyclonal rabbit serum had been previously generated by triple induction of New Zealand white rabbits with 0.1% SDS in PBS resolubilized MBP-tagged (N-terminus) recombinant LAF-1 and complete Freund's adjuvant (Szczepaniak 2021). Animal maintenance, inductions, and bleedings were outsourced to the antibody facility at MPI-CBG. Blood serum was used as an input material for further polyclonal antibody (pAb) purification.

Initially, 1 mg of 6xHis-tagged (N-terminus) recombinant LAF-1 washed inclusion bodies were resolubilized in 250 μ L of SDS sample buffer by continuous 1-minute $+90^{\circ}\text{C}$ incubations and brief vortexing until maximal resolubilisation of inclusion bodies for at least 5 times. Insoluble leftovers were spun down at 14,000 rpm in 5417R centrifuge with F-45-30-11 rotor (Eppendorf) for 5 minutes at room temperature. The full supernatant volume was loaded onto a 10% gel and run according to the SDS-PAGE Chapter (2.3.1). To get the entire recombinant LAF-1 protein band (76.3 kDa), a 55 to 100 kDa gel fragment was cut out using the prestained marker as a size reference. The cut piece was transferred onto a nitrocellulose membrane, according to the above-mentioned Western blotting parameters (Chapter 2.3.2), with the only exception in the membrane blocking procedure. For pAb purification, 25% horse serum diluted with PBS-T was used as a blocking solution with the same incubation time. It is recommended to make several strips at once to increase purification yield. Strips could be stored for 1 month in PBS-T with 1 mM NaN_3 at $+4^{\circ}\text{C}$.

One mL of rabbit serum was diluted 1:10 with 25% horse serum in PBS-T in a 15 mL centrifuge tube. During the whole purification process, the serum was kept on ice or in a cold room. Afterward, the serum was centrifuged for 10 minutes at 4000 rpm at +4°C in a 5810R benchtop centrifuge with an A-4-62 swing bucket rotor with a 15 mL tube adaptor (Eppendorf). The supernatant was transferred into a fresh 50 mL centrifuge tube that already contained strips with blotted recombinant LAF-1. Further incubation under constant agitation lasted for 3 hours. To track antibody leftovers in the serum, aliquots were taken before and after membrane incubation. Thereafter, the diluted serum was transferred into a fresh tube and stored at -20°C. Strips were washed 3 times with 30 mL of PBS-T for 5 minutes with shaking. The first elution was done by 1-minute incubation of 1.5 mL of acidic antibody elution buffer with strips on a shaker. The acidic eluate was transferred into a 2 mL tube with 200 µL of 1 M Tris-HCl pH 8.8, to immediately neutralize the acidic pH. Strips were washed with 30 mL PBS-T for 5 minutes. The second elution buffer was 1.5 mL of basic antibody elution buffer under the same conditions. The eluate was transferred into a 2 mL tube with 200 µL of 1 M Tris-HCl pH 6.8. For the last elution step, strips were incubated with 1.5 mL of high salt elution buffer under the same conditions. The eluate was transferred into a fresh 2 mL tube. Strips were washed 3 times with 30 mL of PBS-T and stored at +4°C in PBS-T with 1 mM NaN₃. Strips could be reprobed and reused several times. All three elution fractions were twice dialyzed in 10K MWCO dialysis cassettes (Thermo Fisher). The first dialysis was performed in 1 L of 2x PBS with 25% glycerol with magnet mixing for 2 hours in a cold room. The second dialysis was done overnight in the same conditions in 600 mL of 2x PBS with 50% glycerol. Rebuffered samples were quantified by 280 nm absorbance with the help of a microvolume spectrometer and tested in Western blot assay with 1 to 125 ng range of recombinant LAF-1 (recombinant positive control), 200 ng of total embryo lysate protein (wildtype positive control), 200 ng of total *E. coli* lysate protein (typical immunogenic negative control), 125 ng BSA (negative control with high protein density band), and a prestained protein marker. Based on the background intensity and specificity, samples were combined to achieve the best specificity to volume ratio. The combined antibodies were stored at -20°C until further usage. Rabbit sera are an unreproducible source of pAb that varies in quantity, affinity, and specificity. This is why every serum should be tested individually to get an optimal final polyclonal pool. Additionally, antibodies could be concentrated with a centrifugal concentrator, such as Vivaspin 2 PES (Sartorius) prior to dialysis.

2.3.10. LAF-1 immunoprecipitation

The LAF-1 protein was precipitated from both adult worms or embryonic lysates. To do so, 10 μL of washed protein G magnetic beads (Dynabeads, ThermoFisher) were incubated with 2.5–3.0 μg of mouse mAbs in 1 mL of B70 buffer. The incubation lasted overnight in a cold room under constant rotation. The incubated beads were then washed twice with B70 buffer. To preserve the protein G/antibody complex, the proteins were crosslinked with DMP. First, the magnetic beads were washed twice with 500 μL of borate buffer. Then, the beads were incubated for 2 hours with 500 μL of borate buffer with 2.6% DMP at room temperature under constant rotation. Afterward, the crosslinked beads were washed two times with 500 μL ethanolamine buffer and incubated for 1 hour in 500 μL of ethanolamine buffer with 0.01% Triton X-100 at the same conditions to block all remaining DMP. After additional double washes with 500 μL of B70, the beads were stored at +4 $^{\circ}\text{C}$ for no longer than two days.

The *C. elegans* lysate was prepared by grinding frozen pearls of worms or embryos in IP buffer placed in a 10 mL grinding jar (Retsch) using a MM301 mixer mill (Retsch). For a single IP reaction, the equivalent of approximately 150-200 adult worms or 10,000-12,000 ≤ 128 -cell stage embryos were used. The grinding mixture was kept frozen by liquid nitrogen. After 10 seconds of grinding at 30 RPS, the ice powder was transferred into a microcentrifugation tube and centrifuged in a 5417R centrifuge with F-45-30-11 rotor (Eppendorf) at maximum speed for 15 minutes at +4 $^{\circ}\text{C}$. To precipitate LAF-1, the lysate supernatant was incubated with beads for 2 hours in a cold room under constant rotation. The incubated beads were then washed three times for 5 minutes with IP buffer on the rotor. The elution method was selected based on further procedures.

2.3.11. Total RNA extraction (Trizol method)

80-100 adult worms were placed on the bottom of a 1.5 mL centrifuge tube and flash frozen in liquid nitrogen. 200 μL of Trizol reagent were added to frozen pellet and mixture was immediately placed into a thermal shaker for 15 minutes at +65 $^{\circ}\text{C}$ with 700 rpm shaking. To separate phases, the mixture was combined with 40 μL chloroform and intensively vortexed for 30 seconds. After an incubation at room temperature for 3 minutes, it was centrifuged at 14,000 rpm in 5417R centrifuge with F-45-30-11 rotor (Eppendorf) at +4 $^{\circ}\text{C}$. Supernatant was carefully transferred into a fresh 1.5 mL tube without any impurities from middle or bottom phases. Combined with equal volume of isopropanol, supernatant was intensively vortexed for

30 seconds and incubated at room temperature for 10 minutes. To precipitate RNA, mixture was centrifuged at same conditions and supernatant was discarded. The pellet was washed with 1 mL of 75% ethanol and gently inverted several times. Additional centrifugation was applied at same conditions as before with further supernatant discard. Pellet was airdried at room temperature till significant (but not absolute) reduction of liquid. The resuspension volume depends on pellet size which varies between batches. As a rule of thumb, 20 μ L of DEPC-treated dH₂O was added for a primary dilution. RNA concentration and purity were checked by microvolume spectrometer absorption ratio at 260/280 nm. Pure RNA without significant protein contamination is expected to be >1.8. If a lower value was achieved, purification with Trizol was repeated. After adjustment of final concentration to 350 ng/ μ L, RNA was aliquoted and stored at -20 °C. As an addition quality control, agarose gel electrophoresis was performed. The final yield of total RNA from 200 adult worms is approximately 1 μ g. For unclear reasons, some batches could not be used for RNA heat-aggregation due to formation of over-entangled RNA particles. Which is why heat-aggregation efficiency of every batch was checked before each helicase assay.

2.3.12. Agarose gel electrophoresis in TBE buffer system

Agarose gel electrophoresis was utilized to separate DNA fragments based on their polynucleotide chain size and total RNA quantification in the helicase assay. To prepare the gel, 50 mL of 0.5-2.0% agarose was boiled in 1x TBE until it completely dissolved. Ethidium bromide at a concentration of approximately 1 μ g/mL was added to the melted agarose solution and mixed thoroughly. The final solution was poured into a horizontal gel chamber pre-installed in a custom-made casting frame. The final height of the agarose gel was at least 0.8 cm. A comb was placed into the chamber sockets while the agarose remained melted. After the gel thickened, it was positioned in the running chamber and covered with TBE solution according to the chamber markings. Once the comb was removed, 5 μ L of DNA marker (1 kb Plus DNA Ladder) and samples resuspended in 1-2x DNA gel loading buffer samples were loaded into the gel pockets. Electrophoresis voltage was set to 10 V/cm, and the runtime was selected based on the sample DNA size and further assays.

2.3.13. RNA helicase assay

A modified helicase assay was used for quantification of RNA helicase activity of recombinant LAF-1 variants (Van Treeck et al., 2018). To produce dsRNA substrate, purified total RNA was aggregated by heating 250 ng/ μ L RNA in 25 mM Tris-HCl pH 7.4 and 20 mM MgCl₂ to +95 °C for 10 minutes. Afterwards, this solution was cooled to +20 °C with constant reduction of temperature at 20 °C/min rate. The temperature gradient was done with a T100 PCR thermal cycler (BioRad). To remove nonaggregated RNA molecules, samples were centrifuged in Allegra X-30R centrifuge, equipped with a F2402H rotor and PCR tube sockets (Beckman Coulter) at 18,000 rpm at +4 °C temperature for 15 minutes. Supernatant was gently removed from the tube with a pipette. It was essential not to disturb the aggregated RNA pellet, otherwise a fraction of it might be accidentally discarded. Aggregated RNA should be prepared directly before use and not stored for a long time or be frozen. Depending on the assay, further dilutions were carried out in resuspension buffer. In this work, RNA from the same stock was used for each individual experiment. In certain cases, uneven distribution of aggregated RNA among aliquots was observed.

To perform a helicase assay, 50 ng/ μ L of aggregated RNA was combined in a PCR tube with 25 mM ATP, 5 mM MgCl₂ in 25 mM Tris-HCl pH 7.4, and target concentration of recombinant LAF-1. The final volume of experimental mixture per tube was 5 μ L. For characterizing kinetic properties, the concentration of recombinant LAF-1 helicase ranged from 0 to 5 μ M while for quality tests, typically a concentration of 5 μ M was used. The final fraction of recombinant protein mixture never exceeded 10%. Samples were incubated for 1 h at +25 °C and centrifuged in Allegra X-30R centrifuge, equipped with a F2402H rotor and PCR tube sockets (Beckman Coulter) at 18,000 rpm and +4 °C temperature for 15 minutes. Whereas supernatant was transferred into a clean tube, pellet was resuspended in 5 μ L volume of 25 mM Tris-HCl pH 7.4. Both pellet and supernatant were mixed with 5 μ L of RNA gel loading buffer. Samples were incubated at +95 °C for 10 minutes. After a short spinning step, heat-treated samples were separated in 12 cm 2% agarose gel for 20 minutes at 20 V/cm (Chapter 2.3.12). RNA distribution was identified by ultraviolet fluorescence of ethidium bromide, using a digital camera-based gel documentation system (Vilber Lourmat). Individual sample signals were quantified with the help of ImageJ software. To generate a positive control of single stranded untangled RNA, aggregated RNA was heat treated for 10 minutes at +95 °C and kept on ice. This procedure unwinds aggregated RNA imitating helicase activity. As a

negative control, heat resolubilized aggregated RNA was used. To control absence of RNAses and RNA substrate condition, a nonaggregated RNA aliquot should be loaded on a gel.

2.3.14. Polymerase chain reaction (PCR)

The PCR technique was used for cloning, quality analysis, and genotyping of *E. coli* colonies or *C. elegans* strains. The principle of the reaction is based on the ability of high-temperature stable DNA-dependent DNA-polymerase to attach deoxynucleotide triphosphates (dNTPs) to the 3'-end of a DNA oligomer (i.e., primer) that is hybridized to the target DNA sequence in a complementary manner. Each primer is oriented with its 3'-end in the direction of synthesis, and its sequence is primarily chosen based on the expected product and uniqueness in the templating DNA matrix. The typical composition of the reaction mixture includes Mg- or Mn-containing buffer, dNTPs, 10-100 ng matrix DNA, two primers, and polymerase mixed in PCR-tubes. The reaction takes place in three steps multiple times with pre-set time duration and temperature that are controlled by a PCR-cycler. The first step is the denaturing of double-stranded DNA, which is typically a short (10-30 seconds) +95 °C incubation. The second step is annealing, which is the hybridization of primers to single-stranded matrix DNA. The annealing temperature and duration depend on the size, primer structure, and DNA-polymerase type. The last step is the extension of the primer in the 3'-direction by a thermostable DNA-dependent DNA-polymerase, if possible, with high proof-reading activity. The extension time is set based on polymerase efficiency and expected DNA product size, while temperature is determined by protein structure and enzymatic profile. Each PCR cycle doubles DNA product under perfect conditions. The number of cycles depends on the purpose of PCR and further matrix usage. The main reason is an increase in the error frequency in DNA product after the ~20th cycle, which is critical for DNA cloning. In this research, home-made Taq-polymerase was used for analytical PCR, while Q5 (NEB) and Phusion (NEB) were used for cloning. All primers are summarized in Appendix List 5.10.

2.3.15. Plasmid vector cloning

In this work, plasmid cloning was primarily used for the creation of protein expression vectors. For new gene expression vectors, the insert was made from cDNA synthesized by RT-PCR. The cDNA was analysed for codon composition and *E. coli* expression accordance with the help of the GCUA online tool. Codons that were atypical for the *E. coli* expression system were replaced with appropriate sequences using PCR. Sticky ends for site-specific cloning were implemented by a PCR reaction with further restriction digest of integrated restriction sites in extension sequences. pET-28b+ was a major His-tagged protein expression vector due to its high reliability and an available restriction enzyme library that covered most of the restriction digest sequences in the vector backbone and MCS. Typically, two different restriction enzymes were used to digest extended PCR products and the plasmid's MCS. Digested DNA was run on a 1% agarose gel and extracted using a gel clean-up kit according to the manual procedure (Promega). DNA concentrations were quantified with a microvolume spectrometer Colibri (Berthold). Sticky-end ligation reactions were carried out in a 20 μ L volume with a final concentration of 50 ng of backbone DNA, 50 ng of insert DNA, 1x T4 DNA ligase reaction buffer, and 25 units of T4 DNA ligase (NEB). The molar concentration ratio of vector to insert was kept at 1:4 or 1:5. The ligation mixture was incubated overnight at +16 °C or for 1 hour at room temperature.

Twenty-five percent of the ligated mixture was used for a 35-40 second heat shock transformation at +42 °C of 30 μ L chemically competent DH5 α or XL1-Blue *E. coli* strains. As control samples, transformations of digested insert, digested backbone, and pure competent cells were used. Alternatively, the plasmid could be transformed into electrocompetent cells by electroporation. To do so, the cryostock of electrocompetent cells was diluted 1:5 with ice-cold dH₂O. 100 μ L of diluted competent cells were transferred into chilled electroporation cuvettes and resuspended with the ligated DNA aliquot. Electroporation was performed in an electroporator at 2500 V.

To express plasmid-encoded antibiotic resistance, *E. coli* samples were gently resuspended in 150 μ L of SOC media and incubated at +37 °C for 40 minutes with shaking right after the heat shock on a thermoshaker (Eppendorf). Afterwards, recovered bacteria were plated on a petri dish with LB-agar containing the appropriate plasmid resistance-encoded antibiotic and grown overnight at +37 °C. To extract enough plasmid for sequencing, individual colonies were cultivated in 10 mL LB media with an antibiotic and processed according to the

miniprep DNA purification kit (Promega). Further selection of correct clones was done based on sequencing results. DNA sequencing was outsourced to Microsynth Seqlab GmbH. Sequencing data processing and construct designs were done with the help of SnapGene software. The appropriate clone was retransformed and cultivated in 10 mL of media with an antibiotic to obtain enough plasmid for transformation into an *E. coli* strain for protein expression. For cryopreservation, 500 μ L of bacterial cultures were mixed with an equal volume of 50% glycerol and placed at -80 °C in 1.5 mL cryotubes.

Deletions and mutations in already existing full-length expression constructs were also introduced by PCR reaction. After PCR clean-up kit purification (Promega), DNA was 5'-phosphorylated by T4 polynucleotide kinase (PNK) in presence of T4 DNA ligase (NEB). Synchronous phosphorylation and ligations could be achieved due to high similarity of T4 PNK and T4 ligase buffers and active temperatures. The final volume of reaction mixture was 10 μ L consisting of 75 ng of DNA, 3 mM additional ATP, 1x T4 PNK buffer with 10 U of T4 DNA ligase and 10 U PNK. Each mixture was incubated at +37 °C for 1 h extended overnight at +16 °C. Further transformation and clone selection were made identically to above described cDNA-based cloning procedures. See appendix for enzymes (List 5.5), buffers (List 5.6), and primer combinations for all generated plasmids (Lists 5.9 and 5.10).

2.3.16. RNAi feeding

Previously published experiments were used as a reference for *C. elegans*-specific RNAi feeding experiments (Kamath et al., 2003). The RNA interference plasmid was generated by blunt end ligation cloning of 1-990 nucleotides of *laf-1* ORF into the pL4440 plasmid (Szczepaniak 2021). This construct, also designated as the *laf-1*(5') RNAi clone, was confirmed by restriction digest and sequencing prior to transformation into the HT115(DE3) *E. coli* strain. Ampicillin and tetracycline were used as selective antibiotics. An isolated bacterial colony was then grown overnight in 2 mL of LB with carbenicillin at +37 °C with shaking at 180 rpm. Twenty mL of fresh LB with carbenicillin were inoculated with the overnight culture and grown until OD600 ~0.5 under the same conditions. Afterwards, the culture was centrifuged for 10 min at 4000 rpm in the 5810R benchtop centrifuge with the A-4-62 swing bucket rotor.

The pellet was washed twice with 4 mL of fresh LB with centrifugations between, resolubilized in 2 mL of fresh LB, and evenly dropped and dried onto RNAi plates in sterile

conditions. Current calculations were based on 2x10 cm or 4x6 cm plates and were adjusted proportionally to the experimental scale. RNAi plates are based on the standard NGM recipe with an extra 1 mM IPTG and 100 µg/mL carbenicillin added to the liquid and autoclaved agar mixture. Spotted plates were left overnight at room temperature to synthesize enough siRNA. Plates were prepared freshly before the experiment and stored no longer than two days at +4 °C in emergency cases. Typically, hatched L1 worms (Chapter 2.3.17) were transferred from empty plates onto RNAi plates.

2.3.17. Embryo extraction

The extraction technique is based on the aggressive chemical dissolution of worms, while embryos remain resistant due to a natural thick chitin layer. Adult worms that had just started laying embryos were collected as the input material by manual picking or M9 wash off in a 15 mL centrifuge tube. To minimize bacterial contamination, each worm pellet was washed 4-5 times with 10 volumes of M9 using a 5810R benchtop centrifuge with an A-4-62 swing bucket rotor with a 15 mL tube adaptor (Eppendorf) for 1 minute at 1000 rpm at +4 °C. The number of wash steps was increased for samples with remaining bacterial turbidity. Worms may have been separated into several tubes to keep the final volume of the worm pellet below 1 mL per tube.

Each aliquot was diluted with M9 to a final volume of 8 centrifuged pellets. To start embryo extraction, 1 volume of 4 M NaOH and 1 volume of 6-14% sodium hypochlorite aqueous solution were added to the resuspended worm pellet of equal volume. The closed tube was vigorously shaken for 3-4 minutes. To avoid lethal embryo damage, samples should be examined every 20-30 seconds. As a rule of thumb, samples should not contain any visible worms or their leftovers, and clean extracted embryos should have a light caramel or white colour. In case darker layers remained, the bleaching step was extended until they disappeared. After collecting embryos by centrifugation, the supernatant was discarded, and the embryos were briefly washed once in 0.05% Tween-20 in M9 and pelleted by centrifugation to stop further chemical damage.

Afterwards, the embryos were continuously washed 5 more times with pure M9 buffer. Clean embryos were incubated in a small volume of M9 solution overnight (approximately 3 mL) at room temperature with gentle shaking at a rocker (IKA) to obtain hatched starved L1 worms. Alternatively, embryos were frozen immediately in liquid nitrogen and stored at -80

°C for biochemical experiments. In the latter case, a small fraction of embryos was left to hatch on an empty NGM plate as a quality control. Overexposure to aggressive solution or leftovers accumulated in worm leftovers potentially causes death of embryos or hatched L1 worms. The approximate yield of an embryo extraction was 4-8% from input biomass.

2.3.18. Differential interference contrast microscopy

Differential interference contrast (DIC) microscopy was used to document the liquid-liquid phase separation (LLPS) properties of recombinant proteins and to characterize the morphology of *C. elegans* worms and embryos. Both oil and non-oil DIC immersive microscopy were used during the research. DIC was preferred to brightfield microscopy due to better contrasting of LLPS droplets and a broader monochromatic shade diapason, which made it more descriptive and easier for further in silico analysis.

Recombinant protein samples were generated by placing an 8-10 µL drop between a standard cover and slide glass. The typical incubation time for recombinant protein samples was 5 minutes at room temperature. Incubation was performed between glass slides to minimize evaporation and preserve possible sub-products like protein aggregates or liquid-liquid phase separated droplets that could be sensitive to additional pipetting; nail polish was applied to slide corners to stabilize this sandwich.

Organismal DIC imaging was also carried out on glass slides, but to prevent redundant mechanical stress, organisms were placed onto an agar pad before final microscopy slide assembly. An agar pad was made by dropping a melted 1% agar drop onto the centre of a +70 °C preheated base glass slide. The adjustment of the final pad thickness was done by placing two tape pieces aside the slide centre before covering the agar drop with a second +70 °C preheated glass slide, which is the final acceptor of the agar pad. Afterwards, the agar sandwich was left at room temperature to cool down. Cooled glasses were carefully disassembled to keep the agar pad on the top glass slide. To paralyze *C. elegans* for constant body positioning, worms were incubated with 1 mM sodium azide in M9 solution during microscopy in an 8 µL drop on the microscopy cover slide. Subsequently, the cover slide with organisms in the drop was stuck to the agar pad on the slide glass and fixed with small drops of nail polish in the cover slide corners. The sample was used after a brief drying of the polish.

To minimize the software processing impact on image consistency, brightness, image sharpness, resolution, and preferable composition were adjusted primarily by hardware setups and native microscopy software during the image take. In case of high homogeneity of the sample, small artifacts were added to the composition to double-check the correctness of the focal plane.

2.3.19. LC-MS/MS of *C. elegans* samples

LC-MS/MS analyses and all primary data processing were performed in the laboratory of Carla Schmidt from Interdisciplinary Research Center HALOmem (Institute of Biochemistry, Martin Luther University, Halle-Wittenberg). For each single LC-MS/MS analysis, 10,000-12,000 cryopreserved embryos (Chapter 2.3.17) or immunoprecipitated samples from the above-mentioned biomass (Chapter 2.3.10) were used. Biological samples were lysed by resuspension in four volumes of TFA and incubation at room temperature for 2-3 minutes until complete lysis. Subsequently, 10 volumes (corresponding to the amount of TFA used for cell lysis) of 2 M Tris and 1.1 volume of 29 mM TCEP and 37 mM CAA were added to the lysis solution and incubated for 5 minutes at +95 °C. The cell lysate was diluted 1:5 with distilled water and further mixed with trypsin (Promega) at a 50:1 protein-to-enzyme molar ratio. The total protein amount was approximated based on the input material after cell lysis. Tryptic hydrolysis was performed overnight at +37 °C and 600 rpm cavitation in a thermomixer. Subsequently, peptides were desalted using peptide desalting spin columns (#89852, Thermo Fisher) according to manufacturer's guidelines. Eluted peptides were dried in a vacuum centrifuge.

The tryptic peptides were dissolved in 2% ACN and 0.1% FA. The peptides were separated using a Dionex-UltiMate 3000 RSLCnano System (Thermo Fisher) coupled with a Q Exactive Plus Hybrid Quadrupole-Orbitrap mass spectrometer (Thermo Fisher). The mobile phase A contained 0.1% FA, while mobile phase B was composed of 80% ACN and 0.1% FA. The peptides were first desalted using a trap column (μ -Precolumn C18 Acclaim PepMap 100, C18, 300 μ m I.D., particle size 5 μ m; Thermo Fisher) at a flow rate of 10 μ L/min, and then separated on an analytical C18 capillary column (50 cm, HPLC column Acclaim PepMap 100, C18, 75 μ m I.D., particle size 3 μ m; Thermo Fisher) at a flow rate of 300 nL/min.

For proteome analysis, a gradient of 4–90% mobile phase B was used over 152 minutes, and the peptides were directly eluted into the mass spectrometer. The mass spectrometric

settings were as follows: the spray voltage was set to 2.8 kV, the capillary temperature was +275°C, and the mass spectrometer was operated in positive ion mode. For the survey full scans in the orbitrap, a resolution of 70,000, an automatic gain control (AGC) target of 3e6, a maximum injection time of 80 ms, and a scan range of 350 to 1600 m/z were used. Fragmentation of the 20 most intense ions within charge states of 2+ to 7+ was performed in the HCD cell using a normalised collisional energy of 30%. The MS/MS spectra were acquired with a resolution of 17,500, an AGC target of 1e5, a maximum injection time of 150 ms, and a fixed first mass set to 105 m/z. Previously selected ions were dynamically excluded for 30 s. The lock mass option was active at m/z 445.120025.

The raw proteomic data from 4 biological replicates of each sample were searched against the *C. elegans* Uniprot database (Proteome ID: UP000001940, 9K entries, version date: November 2019) using MaxQuant (version 1.6.17.0). Standard software settings were employed, including fixed modification with carbamidomethyl (cysteine), variable modifications with oxidation (methionine) and acetylation (protein N-terminus), 2 maximum missed cleavage sites, 7 amino acid residues minimum peptide length, 6,000 Da maximum peptide mass, 0.01 peptide and 0.01 protein False Discovery Rates, and trypsin/P enzyme (cleavage C-terminal of lysine or arginine, even when the C-terminal amino acid is proline). The iBAQ, MaxQuant LFQ, and 'match between runs' options were enabled.

Quantification of global protein abundance was performed using the Perseus software (<https://maxquant.net/perseus/>). Images were generated in RStudio (version 1.2.1335) using R language (version 4.0.2). Typical protein contaminants, decoy database hits, and proteins identified with only one peptide were omitted. To identify the significance of expressed protein between conditions (early/late etc.), a two-sided t-test was employed. P-values were corrected according to Benjamini and Hochberg (Benjamini & Hochberg, 1995). Depending on the condition, different cut-offs for fold-change and p-values were used for comparison. Excel and CSV datasheets containing MS results were processed using custom scripts in Python3 or C++.

2.3.20. Small-angle X-ray scattering

Small-angle X-ray scattering (SAXS) analysis and primary data processing were performed in collaboration with Maria Ott, (Institute of Biochemistry, Martin Luther University, Halle-Wittenberg). SAXS is based on capability of sample particles to introduce X-rays scattering. Scattered angles are fingerprint that depends on sample particles sizes and densities. Average working sample particle size varies from 1 to 100 nm. In biological studies, SAXS is typically used for investigation of protein complexes.

Experiments were done using a SAXSLAB laboratory setup (Retro-F) equipped with an AXO microfocus X-ray source and AXO multilayer X-ray optic (AXO Dresden GmbH, Dresden, Germany) together with monochromator for Cu-K α radiation ($\lambda=0.154$ nm). 2D scattering patterns were measured using two-dimensional detector (PILATUS3 R 300 K; DECTRIS, Baden, Switzerland). Liquid samples were placed into 1 mm outer diameter refillable capillaries (BioSAS JSP stage, SAXSLAB/Xenocs SAS, Grenoble, France). The intensities were angular-averaged and plotted versus the scattering angle q .

Both LAF-1L and RNA samples or supplemented with IFE-proteins were dissolved in LAF-1L elution buffer and incubated for 5 minutes at room temperature before the measurement. System configuration and measuring time were adjusted for each sample individually. Since X-ray scattering frequency depends on sample concentration, samples were diluted as little as possible.

2.3.21. Phylogenetic analysis

To reveal evolutionary relationships among DDX3 orthologous, a multiple sequence alignment was generated with MUSCLE using the following peptide sequences derived from the Uniprot database (<https://www.uniprot.org/>): [*Drosophila melanogaster*] Belle_Q9VHP0; [*Caenorhabditis elegans*] LAF-1_D0PV95-1, VBH-1_Q65XX1; INF-1_P27639; CGH-1_Q95YF3; [*Homo sapiens*] DDX3X_O00571, DDX3Y_O15523, DDX6_P26196, DDX2A_P60842; [*Saccharomyces cerevisiae*] Ded1_P06634, Dbp1_P24784; [*Schizosaccharomyces pombe*] Ded1_O13370. A Phylogram was generated with Simple Phylogeny, employing the Clustering method UPGMA and keeping distance correction ON. The tree is displayed in Chapter 1, Figure 3A).

3. Results

3.1. Identification of LAF-1 short isoform (LAF-1S)

Based on previous RNA sequencing data deposited on WormBase (release WS289), the genetic locus of *laf-1* expresses two alternative transcripts, termed *laf-1L* and *laf-1S* (Figure 6A). Whereas LAF-1L protein corresponds to previously termed full length LAF-1 (Hubert & Anderson, 2009), the short isoform (LAF-1S) lacks amino acids 41 to 105, due to elimination of a corresponding exonic sequence that otherwise remains in the common precursor transcript to produce LAF-1L. Consequently, removal of the alternative intron 1 during pre-mRNA splicing (Figure 6A) truncates the RGG IDR of LAF-1S by ~33.5%, leaving other evolutionary conserved protein sequences intact (Figure 6B). As the N-terminal IDR of LAF-1L is known to be responsible for LLPS *in vitro* (Elbaum-Garfinkle et al., 2015), it was important to investigate whether a second isoform with potentially different LLPS properties may be expressed *in vivo*.

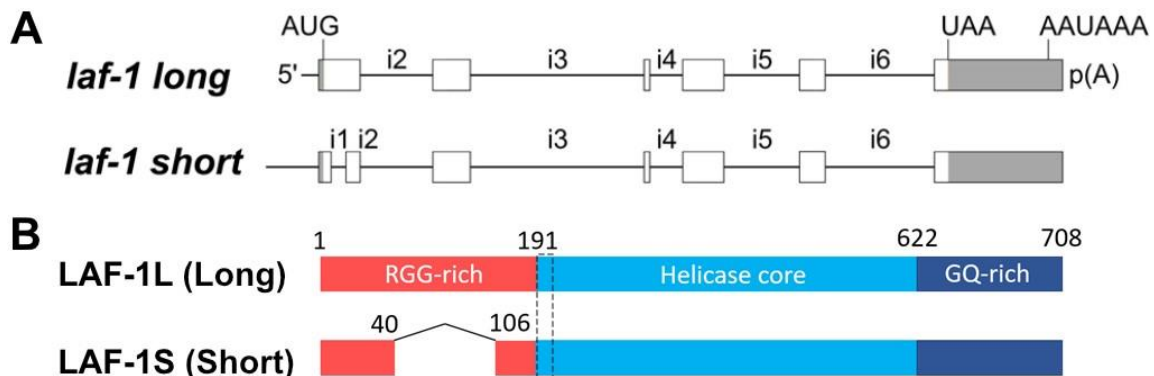


Figure 6. *laf-1* locus generates two products.

A. Precursor mRNA transcripts of *laf-1* prior to mRNA splicing. Boxes represent exons; introns (i); grey, untranslated sequences; white, open reading frame (ORF); p(A) indicates the poly(A)-tail. Note, Exon 1 of *laf-1 long* pre-mRNA is alternatively spliced into *laf-1 short* transcript. Therefore, numbers of introns represent all possible ones.

B. Stick diagrams of corresponding LAF-1 protein sequences. Unstructured and structured protein domain boundaries were deduced from PONDR and AlphaFold predictions, as well as a multiple protein alignment, composed of yeast Ded1p, human DDX3X and DDX1, frog An3, fly Belle and nematode LAF-1: Intrinsically disordered region (IDR) rich in RGG (red) or GQ (ultramarine) amino acids; helicase domain (blue); and in this work coarsely-mapped mAb BW75 epitope region (red+20 amino acids). Note, LAF-1S lacks 65 aa of the RGG-IDR of LAF-1L but shares most of the coarsely mapped epitope for mAb BW75. This work fine-mapped the epitope of mAb BW75 to the beginning of the helicase core (dotted line, see main text).

3.1.1. Defining the epitope of monoclonal anti-LAF-1 antibody mAb BW75

To gain evidence for LAF-1S expression at the protein level, the already existing monoclonal anti-LAF-1 antibody mAb B75 needed to be more carefully epitope mapped, utilizing western blot (WB) analyses. Previous work provided a rough epitope mapping of this mAb to overlap with amino acids 1-221 of LAF-1L (Szczepaniak 2021), encompassing the entire RGG-IDR of LAF-1L (Figure 6B). Therefore, a series of bacterial expression constructs in the pET28+ backbone were generated by PCR-mediated blunt-end cloning (Chapter 2.3.15) to produce individual deletions of ~50aa within the amino-terminal region of an otherwise N-terminal 6xHis tagged LAF-1L isoform (Figure 7A). As subsequent expression optimisations showed that an N-terminal His-tag enhances LAF-1L protein's aggregation potency (Chapter 3.2), abundantly enriched inclusion bodies were extracted, washed and resolubilised in SDS-SB. Eventually, 300 ng of each truncated LAF-1L isoform was resuspended in 10 μ L of 2x SDS-SB and subjected to WB analysis (Figure 7B).

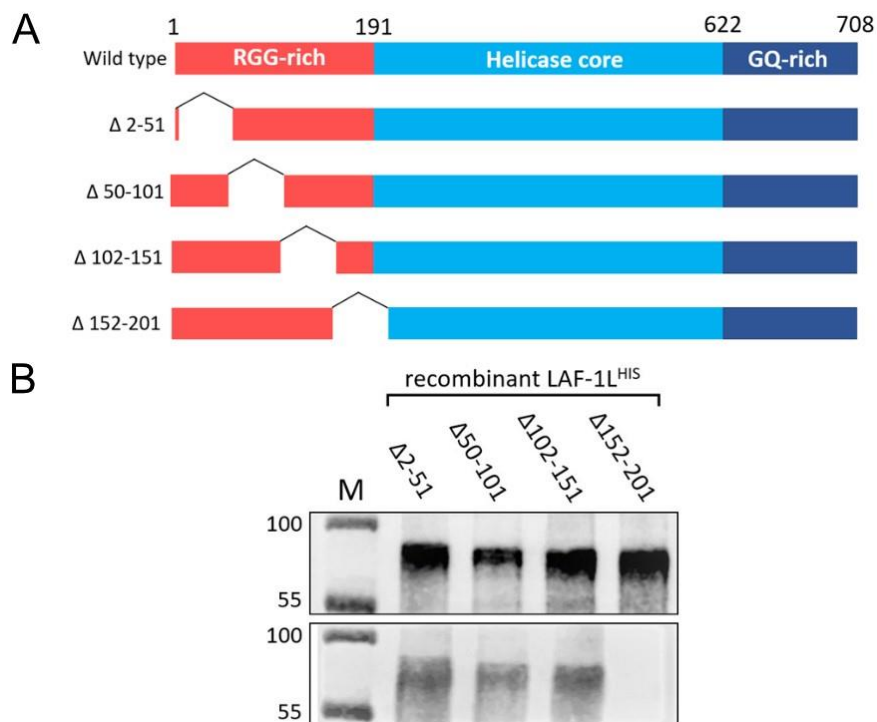


Figure 7. RGG IDR deletions were generated to identify the binding site of mAb BW75.

A. Schematic illustration of LAF-1L isoforms produced for epitope mapping via Western blotting (WB) analysis. The delta range (Δ) indicates the amino acids missing in each recombinant LAF-1L::6xHis isoform; FL designates full-length protein.

B. Monochrome fluorescence images of a single WB nitrocellulose membrane. (Top) Probed with immunopurified polyclonal rabbit serum 32978 and IRDye 800CW goat anti-rabbit IgG secondary antibody (1:1000). (Bottom) Probed with mAb BW75 and IRDye 800CW goat anti-mouse IgG secondary antibody (1:1000). M – 3 μ L of PageRuler protein ladder (Thermo Scientific), with molecular weights assigned in kDa. n = 3.

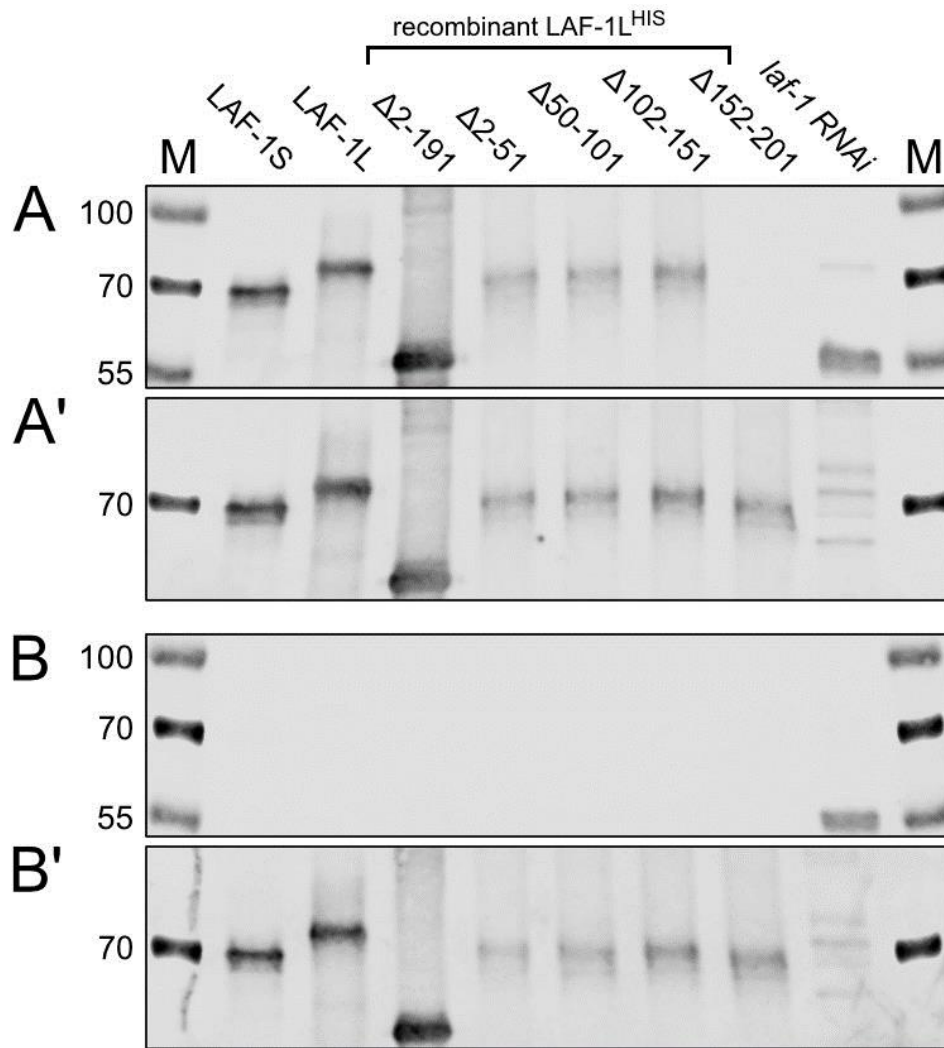


Figure 8. mAb BW75 recognition of LAF-1 depends on aa residues 192 to 201.

Monochrome fluorescence images of WB nitrocellulose membranes. Samples: M – 3 μ L of PageRuler protein ladder (Thermo Scientific), with molecular weights assigned in kDa; LAF-1S – recombinant LAF-1S::6xHis; LAF-1L – recombinant LAF-1L::6xHis; Delta range samples (Δ) represent recombinant LAF-1L::6xHis with missing amino acid sequences as labelled; *laf-1* RNAi – 300 worms exposed to *laf-1* dsRNA-producing *E.coli* (Chapter 2.3.16). 70 kDa marker band signal was captured by 600 nm filter channel. n = 3.

A. Blotted nitrocellulose membrane probed with two mAbs: anti-LAF-1 BW75 and anti-Tubulin, which detects both tubulin subunits at ~55kDa and IRDye 680CW goat anti-mouse IgG (1:1000) secondary antibody.

A'. Membrane from figure A probed with affinity-purified rabbit 32978 pAb and detected with IRDye 800CW goat anti-rabbit IgG (1:1000) secondary antibody. Note, pAb crossreacts with all used recombinant LAF-1 isofoms and shows some background bandsin worm extracts.

B. Blotted nitrocellulose membrane probed with the unrelated monoclonal antibody BF30, later used immunoprecipitaiton experiments, anti-Tubulin mAb and IRDye 680CW goat anti-mouse IgG (1:1000) secondary antibody.

B'. Membrane from figure B probed with affinity-purified rabbit 32978 pAb, and IRDye 800CW goat anti-rabbit IgG (1:1000) secondary antibody.

To further clarify the exact position of the mAb BW75 epitope, LAF-1L Δ RGG (Δ 2-191) was generated as an additional expression construct, which according to AlphaFold structure prediction lacks the entire N-terminal unstructured region and begins with the structured part of LAF-1 RNA helicase (Figure 6B). Interestingly, subsequent immune detections showed that mAb BW75 is capable of recognizing the Δ RGG LAF-1L recombinant protein, whereas the Δ 152-201 isoform remained unrecognized (Figure 8A and 8A'), suggesting that mAb BW75 binds most efficiently to LAF-1 polypeptide between the 192nd and 201st residue. As this short peptide is already part of the structured domain, this data indicates that the previous statement of BW75 binding the RGG IDR was incorrect. Furthermore, by comparing these 11 amino acids of LAF-1 to the correspondingly aligned protein sequence of the second DDX3 variant of *C. elegans*, VBH-1, no strong sequence resemblance can be detected (Figure 9), arguing that a cross-reactivity of BW75 to VBH-1 is rather unlikely, which is consistent with previously reported data (Szczepaniak 2021). However, discontinuous epitopes were not considered in current research. Foremost and consistent with a specific detection of both LAF-1 isoforms, His-tag purified LAF-1S and LAF-1L proteins (see detailed below) were equally well detected in these Western blots (Figure 8A), given that equal amounts of recombinant proteins were loaded on the gel.

| | | | | | | | |
|-------|-----|---------------------|------------|------------|-----|----|-------|
| LAF-1 | 181 | SRGTSKWENRG | ARDERIEQEL | FSGQLSGINF | 211 | | |
| VBH-1 | 89 | NNGAESNQWGGAPAEYSES | NLFHRTD | SGINF | 119 | | |
| | | * | ** | * | * | ** | ***** |

Figure 9. Sequence similarity differs between LAF-1 and VBH-1 at the deduced anti-LAF-1 BW75 binding site.

Extracted amino acid sequence alignment of LAF-1 and VBH-1, encompassing the mapped anti-LAF-1 BW75 mAb binding site (orange). Asterisks (*) in bottom row below aligned sequences highlight identical amino acids. Note, GINF is part of the conserved ATP-binding loop, as determined for human DDX3 (Epling et al., 2015).

3.1.2. LAF-1S is expressed during embryogenesis

The biggest challenge in Western blot detection of LAF-1S in worm extracts was to find conditions sufficient to resolve LAF-1L (76.3 kDa) and LAF-1S (69.9 kDa). A series of attempts to identify LAF-1S with 10% and 12% SDS-PAGE with triple extension of runtime failed (Chapter 3.2). Moreover, extended runtime induced smearing of proteins making any further differentiation of LAF-1 isoforms impossible. Sufficient resolution was obtained using 8% SDS-PAGE under normal runtime parameters on ice. While purified recombinant His-tagged LAF-1 short and long proteins showed a discernible size difference and upshift compared to endogenous LAF-1 isoforms, worm extracts of LAF-1S only (EV1280) and LAF-1L only (EV1324) strains displayed less significant LAF-1 isoform resolution (Figure 10), most likely induced through effects by other proteins present in a protein extract. Therefore, recombinant proteins and *laf-1* RNAi knockdown samples were taken as a control of antibody specificity in these experiments, and the running behaviour of LAF-1 isoforms was primarily juggled by comparison to EV1280 and EV1324 worm extracts.

In several repetitions, only early embryonic stage (≤ 128 -cell stage) samples revealed two distinct bands corresponding to the molecular weights of LAF-1L and LAF-1S (Figure 10). However, both bands of wild-type animals are slightly upshifted, when compared to mutant animals expressing isoform specific LAF-1 proteins. By contrast, wild-type L1-enriched early larval stages, hatched from bleach-synchronized embryos appeared to contain predominantly only one band, which is similar in size to LAF-1L (Figure 10). Also, adult stages of hermaphrodites lacked detectable LAF-1S and appeared to be enriched in LAF-1L. RNAi-treated counterparts document antibody specificity, as the LAF-1L signal is strongly reduced in age-matched animals (Figure 10). Furthermore, adult male samples contained predominantly a LAF-1L-sized band (Figure 10), indicating that there is no overt sex-specific isoform expression difference in nematodes. Together this data suggests that LAF-1L is the prevailing isoform in most developmental stages and that LAF-1S abundance enriches detectably during early embryogenesis only.

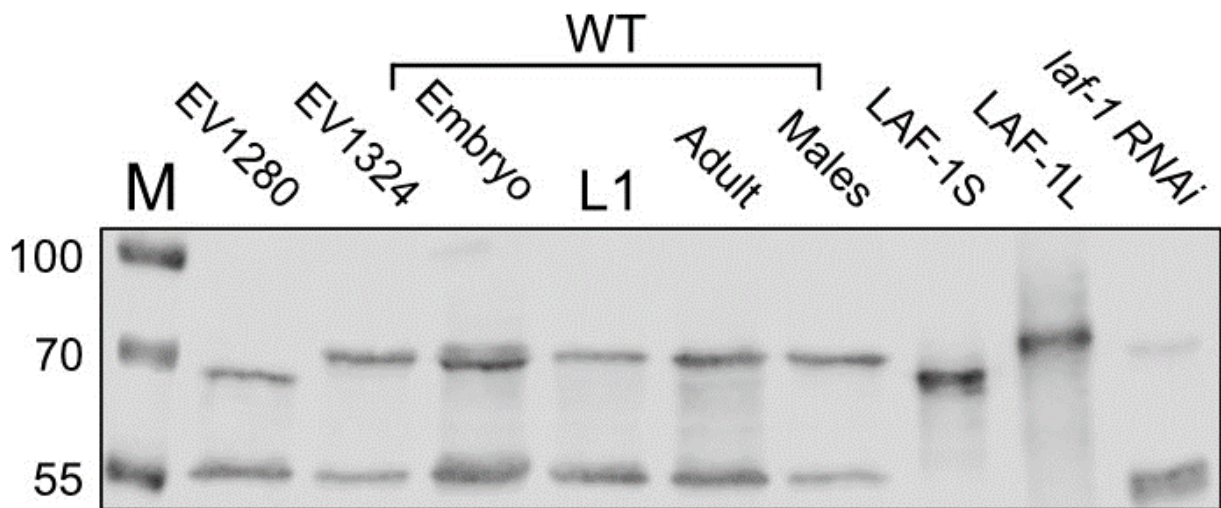


Figure 10. LAF-1S expression is apparent during early embryonic development.

Monochrome fluorescence image of a typical WB nitrocellulose membrane, initially probed with anti-LAF-1 mAb BW75 and anti-Tubulin mAb antibodies, followed by secondary antibody IRDye 680CW goat anti-mouse IgG (1:1000). Samples: M – 3 μ L of PageRuler protein ladder (Thermo Scientific), with molecular weights assigned in kDa. Worm protein extracts: EV1280 – 100 adult hermaphrodites of a strain that expresses LAF-1S only; EV1324 – 100 adult hermaphrodites of a strain that expresses LAF-1L only; Embryo – 1500 early embryonic stages of the N2 wild-type strain, L1 – 500 synchronized larval stage L1 animals, Adult – 100 hand-picked N2 adult hermaphrodites, Males – 200 hand-picked N2 adult males; LAF-1S – recombinant LAF-1S::6xHis; LAF-1L – recombinant LAF-1L::6xHis; *laf-1* RNAi – 300 adult hermaphrodites exposed to *laf-1* RNAi bacterial feeding culture (Chapter 2.3.16). Of note, 70 kDa marker band signal was captured by 600 nm filter channel. n = 3.

Due to obvious resolution limitations in the available WB setup, additional attempts were made to validate the presence of LAF-1S in early stage embryonic samples, exploiting the technique of 2D gel electrophoresis. A partial truncation of the RGG IDR causes a loss of 10 positively and 8 negatively charged amino acid residues, leading to a change in the theoretical isoelectric point (pI) among LAF-1 isoforms: LAF-1S shifts from a pI value of 6.60 for LAF-1L to 6.42. To take advantage of both mass and charge differences, standard 1D SDS-PAGE western blots were therefore extended with isoelectric focusing (IEF). Moreover, in this 2D gel electrophoresis setup, VBH-1, the second DDX3 protein family member of *C. elegans*, has a theoretical pI value of 8.42, clearly distinguishing it from both LAF-1 isoforms. Embryonic input was increased from average 1500 for WB assay to 4500 embryos because of loss during grinding and rehydration of IEF strips. Smaller quantities did not show any significant signal. Finally, embryos were resuspended in 250 μ L isoelectric focusing sample buffer, frozen in liquid nitrogen and grinded with a mixer mill (Retsch) at top speed for 30 seconds. Such adaptations to the standard procedure (Chapter 2.3.3) were necessary to disrupt embryonic thick chitin layer that prevented protein extraction.

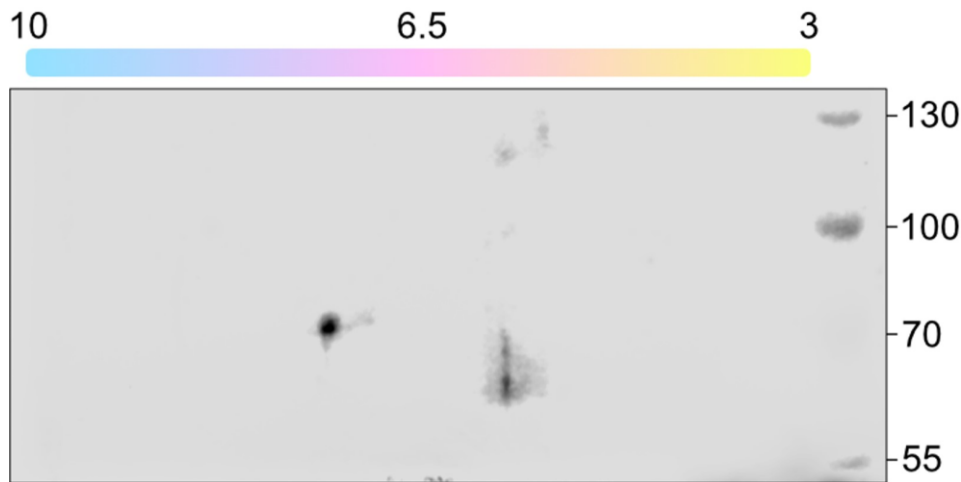


Figure 11. Isoelectric focusing confirmed LAF-1S isoform in early stage embryos.

Monochrome fluorescence image of a WB nitrocellulose membrane probed with anti-LAF-1 mAb BW75 and IRDye 680CW goat anti-mouse IgG secondary antibody (1:1000). Protein extract of 4500 early embryonic N2 stages were initially isoelectrically focused and subsequently resolved through 8% SDS-PAGE. Molecular weight marker bands (right side in kDa): 3 μ L of PageRuler protein ladder (Thermo Scientific), 70 kDa marker band signal was captured by 600 nm filter channel. Top scalebar represents pH gradient across 7 cm pH 3-10 IFE strip (SERVA), the inferred pI value of 6.5 represents its arithmetic middle. $n > 2$. Note, LAF-1S (pI \sim 6.4) migrates as a non-homogeneous upsmeared spot.

Two distinct signal spots were detected on two independent WB assays of isoelectrically focused protein lysates from wild-type early embryos (Figure 11). Both major signals correlate well in mass and theoretical pI values to LAF-1L (MW=76.3, pI=6.60) and LAF-1S (MW=69.9, pI=6.42). While the signal for LAF-1L is a focused single dot, the signal for LAF-1S smears across a size range of \sim 6-8 kDa (Figure 11), suggesting potential—yet non-clarified—posttranslational modifications. Additional major signals at different pI values were not discovered in this setup, such for VBH-1, arguing WB detection specificity. As both LAF-1 isoforms appear equal in signal strength, it appears that LAF-1S is indeed most abundant in early stages of embryogenesis and LAF-1L prevails in all other developmental stages. While the biological roles of either LAF-1 isoform remains unclear, these data argue that the molecular difference between both LAF-1 isoforms, which is restricted to the RGG-IDR of DDX3, is likely to affect the physiochemical properties of either LAF-1 isoform *in vitro* and maybe also impinge on its molecular activity as a DDX3 RNA helicase.

3.2. Purification of recombinant LAF-1 proteins

To study LAF-1 activities in *in vitro* assays, recombinant LAF-1 variants were purified from bacteria. By the time this experimental workflow began, a codon optimized LAF-1L construct for *E. coli* expression had been available (Elbaum-Garfinkle et al., 2015). This construct in the pET-28b+ vector backbone encoded the full-length *laf-1L* ORF sequence fused in frame to a C-terminal 6xHis Tag. Due to its many arginine codons, BL21-CodonPlus (DE3)-RIL *E. coli* cells were chosen as the preferred expression host for all expression studies. Initially, both lysis and wash buffers contained 50 mM Tris-HCl pH 7.4 with 300 mM NaCl and 10% glycerol, and the elution buffer was additionally supplemented with 300 mM of imidazole, recommended by the manufacturer of the IMAC column (Appendix List 5.2). In pilot experiments to adjust expression and purification conditions, the culture volume of induction was downscaled to 250 mL LB media, a range of IPTG concentrations for expression induction was tested, and recombinant protein yield was surveyed by Coomassie-stained SDS-PAGE of TCA-precipitated *E. coli*-induced samples.

Results showed that 1.0 mM and 0.5 mM final IPTG concentrations did not yield any differences in protein yield, while 0.25 mM had a ~30% reduction after overnight incubation at +25 °C (Figure 12). Therefore, 0.5 mM final IPTG concentration was selected as the standard for all inductions of recombinant LAF-1L variants. However, in two attempts, little to no protein was eluted after IMAC chromatography, with a total yield of only 0.1 mg of protein in 2 mL of elution buffer. Subsequent SEC rebuffing in imidazole-free lysis buffer led to a total on-column aggregation of recombinant protein. Hence, further optimizations were required to obtain sufficient protein amounts.

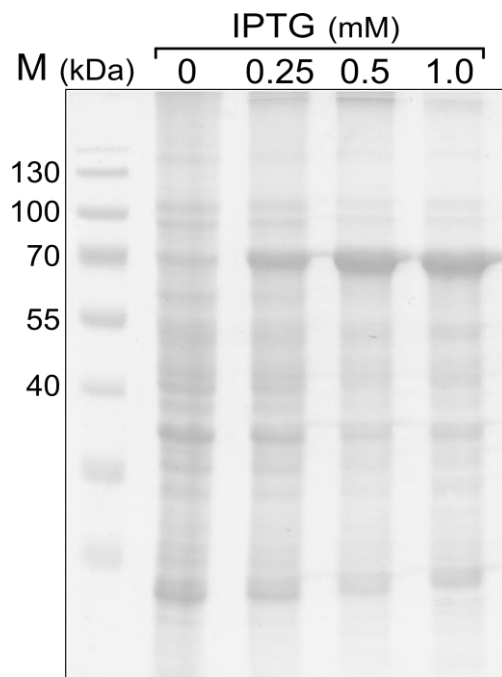


Figure 12. Recombinant LAF-1L expression depends on IPTG concentration induction.

Monochrome digital scan of a 1 mm Coomassie-stained 12% SDS-PAGE gel with a 10-well comb. Samples: M – 3 μ L of PageRuler protein ladder (Thermo Scientific) with molecular weights assigned in kDa. Numeric values represent the concentration of IPTG in mM units used for overnight induction at +25°C of a BL21(DE3)-RIL *E. coli* expression strain transformed with pET-28b+ encoding C-terminally 6xHis-tagged full-length LAF-1L.

At first, several overnight incubation temperatures were tested at +12, +16, +20 and +25 °C. Although +16 °C had a lower total expression rate compared to higher temperatures, the soluble fraction was the highest of the four temperatures, which allowed a total yield of ~0.35 mg in 1-1.2 mL from 250 mL of initial LB culture volume. Experiments with HEPES, MOPS, and PBS buffer systems in the 6.2 – 8.0 pH range and Tris-HCl buffer systems in the 6.8 – 8.4 pH range showed that Tris-HCl pH 7.4 is the most optimal buffer system. Additionally, different induction time frames in the range of 2-12 hours with 2-hour steps were tested. However, after 8 hours of incubation at +16 °C, the fraction of soluble protein did not increase and a significant fraction (~50%) of expressed protein was identified to be sequestered in inclusion bodies. Due to experimental flow timings, overnight incubation was selected to fit best the combined expression and purification procedure of two working days. Moreover, long-term storage of bacterial pellet at -80 °C was found not to affect the final protein solubility.

As a precaution, the provided expression plasmid was resequenced to exclude potential amino acid deviations. Subsequent sequence analysis identified a single nucleotide mutation in the main open reading frame. The second nucleotide of the 477th codon of *laf-1* was modified

from guanine to alanine, leading to an exchange of a wild-type glycine residue to glutamic acid in the recombinant protein. This E477G mutation was reversed to wild type by PCR-mediated site-directed mutagenesis, using primers CE06903 and CE06904 on the pET-28b+ construct (Appendix List 5.9). The corrected 6xHis::LAF-1L(WT) plasmid was sequence verified, transformed into BL21(DE3)-RIL *E. coli* expression strain, and the purification procedure was repeated under the same conditions as outlined above. Unfortunately, the new construct had insignificantly better solubility, with a final yield of 0.6 mg of recombinant protein from 250 mL of *E. coli* culture and a stable concentration in the range of 0.2-0.3 mg/mL. Most importantly, SEC caused massive protein aggregation and the column matrix became blocked. No soluble protein could be eluted.

Next, a new LAF-1 expression construct was generated by Gibson assembly to move the His-tag to the C-terminus. The CE06351 and CE06352 primer pair with pETMM41 encoding a MBP::LAF-1 fusion protein were used for insert generation through PCR amplification. pET-28b+ was selected as the backbone of the new construct. Both insert and backbone were digested by HindIII-HF and NcoI-HF restriction enzymes, purified through gel extraction, and ligated through sticky ends with the help of the Gibson assembly kit according to the manufacturer's recommendations. After sequence confirmation, the plasmid was retransformed into the bacterial expression strain and protein expression induced. The new construct had a similar total yield, but the fraction of soluble protein doubled, which is why it was used for all further expressions and cloning of other LAF-1L derivatives.

Based on the high stability of the recombinant protein in bacterial lysate and its instant aggregation upon dilution to less than 6-7 mg/mL of total protein, it was hypothesised that anionic, cationic, and hydrophobic lysate components may positively impact on recombinant LAF-1 stability. Therefore, the protein purification strategy was focused on adjusting NaCl and Triton X-100 concentrations as typical ion donors and hydrophobicity modulators of buffer solutions. A broad range of concentrations for both components were tested, and after multiple attempts, the largest chromatography peak volume and moderate aggregation potency were achieved in 50 mM Tris-HCl pH 7.4, 500 mM NaCl, 0.1% Triton X-100, and 10% glycerol. To reduce proteolytic degradation, 1x EDTA-free protease inhibitor cocktail was added. *E. coli* lysis was boosted with the help of 0.25 mg/mL of lysozyme, freshly added before ultrasonic disruption of bacterial emulsion. As a final adjustment of the LAF-1L lysis buffer, 20 mM imidazole was added to reduce unspecific binding and enhanced the final purity of eluted proteins. Based on this lysis buffer, wash and elution buffers were developed without lysozyme

and protease inhibitor cocktail but containing 40 mM and 300 mM of imidazole, respectively. Single-step IMAC purification yields varied in the range of 2.5-3.0 mg of pure protein from 1 L of LB media with 95-97% purity of recombinant LAF-1L, as judged by Coomassie-stained SDS-PAGE gel (Figure 13A). Even though an additional washing step had a minor reduction effect on protein yield, which was typically in the range of 1-1.3 mg per 1 L of induced bacterial culture, it allowed for the elimination of previously visible impurity bands at ~25 kDa and ~65 kDa on Coomassie-stained SDS-PAGE.

A series of tests showed that a combination of 1M NaCl and 300 mM imidazole prevented recombinant LAF-1L from liquid-liquid phase separation *in vitro* and contributed to LAF-1L stability during further freeze-melt cycles. SEC against the LAF-1L rebuffering solution led to partial protein aggregation and loss of 10-15% of input material.

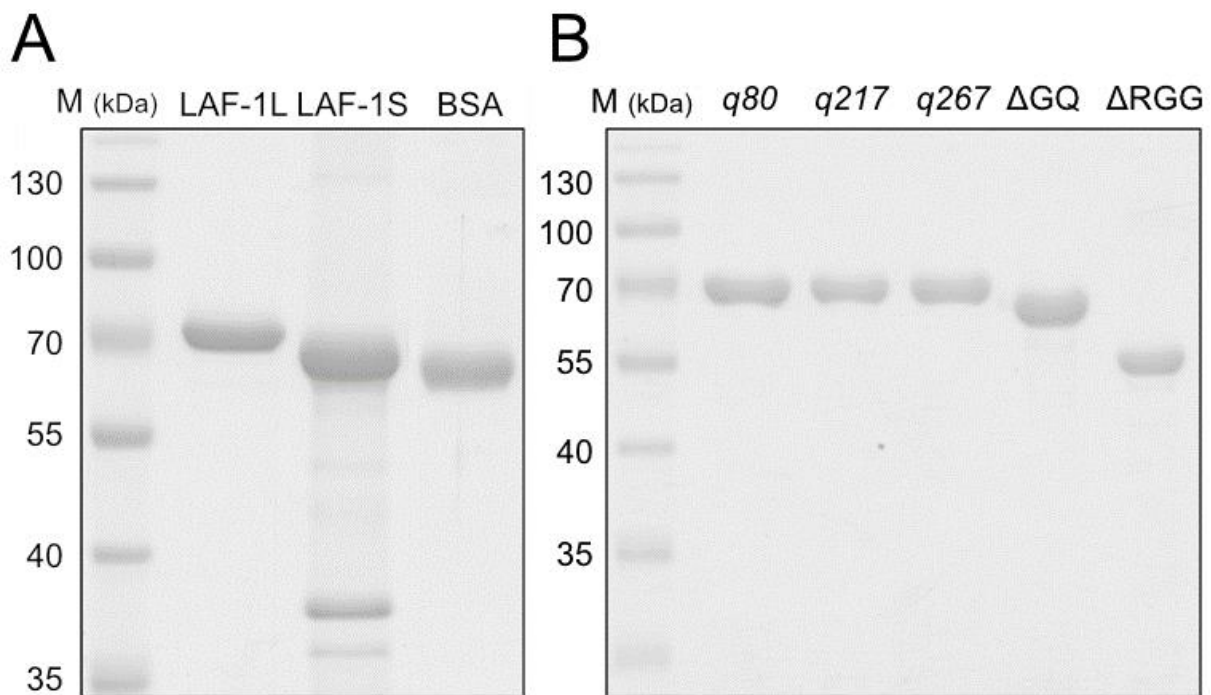


Figure 13. Recombinant LAF-1 proteins were purified to homogeneity.

Monochrome digital scan of 1 mm Coomassie-stained 12% SDS-PAGE with 10-well comb. Samples: M – 3 μ L of PageRuler protein ladder (Thermo Scientific), molecular weight assigned in kDa; and following LAF-1 derivatives:

A. LAF-1L – 3 μ g of recombinant LAF-1L::6xHis; 4 μ g of recombinant LAF-1S::6xHis; 3 μ g of BSA calibration standard (Thermo Scientific);

B. q80 – LAF-1L::6xHis R426C; q217 – LAF-1L::6xHis M430I; q267 – LAF-1L::6xHis T434I; Δ GQ – LAF-1L::6xHis Δ 623-708; Δ RGG – LAF-1L::6xHis Δ 2-191. 3 μ g of each recombinant LAF-1L::6xHis mutant was loaded.

With the presented optimized purification strategy in place, several additional LAF-1 expression constructs were generated with the help of PCR cloning to purify mutant LAF-1L derivatives (summarized in Appendix 5.9). All constructs were validated with the help of multisite restriction digest, confirmed by sequencing, and subjected to expression tests in small scale. These included, three genetically identified single amino acid mutants of LAF-1L, *q80* (R426C), *q217* (M430I), and *q267* (T434I), as well as the N- or C-terminal IDR deleted Δ RGG (Δ 2-191) and Δ GQ (Δ 623-708) derivatives, respectively. All His-tagged proteins were purified under conditions identical to those of the WT recombinant full-length LAF-1L protein. While the total yield, purity, and LLPS behaviour of the single-point mutated proteins were similar to the WT variant, Δ GQ had a lower yield of approximately 0.7 mg from 1 L of induced LB culture with around 80% purity (Figure 13B).

Furthermore, a recombinant LAF-1S::6xHis expression vector was cloned from the pET-28b+ LAF-1L::6xHis. After sequencing and preliminary expression validation with the help of immunodetection of an induced bacterial aliquot, 1L of culture was processed using the same method as the LAF-1L purification protocol. However, after IMAC elution the total yield was just 700 μ g in 3 mL, which is 4-5 times lower than the identical outcome for LAF-1L. Hence, the presumed significant impact of N-terminus LAF-1 IDR truncation on *in vitro* solubility properties required modification of the ongoing strategy. Multiple attempts to adjust concentrations of Triton X-100 (0.05-2.0%), glycerol (10-30%) and NaCl (50-1000 mM) did not give any significant improvement. However, a switch of detergents from Triton X-100 to NP-40 and a combination of phosphate and Tris buffer systems improved yields. This breakthrough was based on brute force checks of different buffer conditions and several lucky mistakes made during buffer mixings.

The final composition of LAF-1S lysis buffer became 2x PBS pH 7.4, 25 mM Tris-HCl pH 7.4, additional 150 mM NaCl, 10 mM $MgCl_2$, 0.1% NP-40, 10% glycerol, 20 mM imidazole, supplemented with 1x EDTA-free protease inhibitor cocktail and 0.25 mg/mL lysozyme as standard components for the bacterial lysis buffer. Single-step IMAC purification yields varied in range from 1.1-1.4 mg of pure protein from 1 L of LB media with 80-85% purity of recombinant LAF-1S, as judged by Coomassie-stained SDS-PAGE analyses (see an example in Figure 13A). Unfortunately, unified purification buffers for LAF-1L and LAF-1S recombinant proteins were not discovered.

Next, wash and elution buffers were designed similarly to the LAF-1L purification strategy by increasing NaCl concentration by 100 mM and removing the EDTA-free protease inhibitor cocktail and lysozyme. In addition, imidazole concentrations were increased to 40 mM and 300 mM, respectively. The final yield of LAF-1S::6xHis was 2.1 mg in 2 mL from 1 L of LB bacterial culture with over 85% purity. Aliquots were stable after freezing-thawing in the elution buffer at ~1.2 mg/mL protein concentration. Any further SEC and dialysis attempts led to massive aggregation of recombinant LAF-1S.

A similar approach was applied for Δ RGG (Δ 2-191) LAF-1 variant as it also had a predicted compromised LLPS behaviour due to lack of RGG IDR. Following optimised LAF-1S purification conditions, obtained purity was close to 70-80% with final yield of 0.6 mg. Protein was concentrated to ~1.2 mg/mL using a Vivaspin 2 centrifugal concentrator (Sartorius) and flash frozen. Several attempts to adjust buffer condition similarly to LAF-1S didn't give any improvement neither in purity nor in yield. Since this protein was purified primarily for antibody mapping and RNA helicase assay, an absolute purity was deemed not essential. Additionally, by the time Δ RGG mutant had been purified significant time concerns needed to be taken into account to complete this work. Interestingly both LAF-1S and LAF-1 Δ RGG were mostly contaminated with presumably proteolysis products even though full-length LAF-1L didn't experience such impact from *E. coli* expression host (compare in Figure 13, A to B).

3.3. Studying LAF-1L phase separation by DIC microscopy

Interestingly, just 2-3 minutes past an IMAC column purification cycle, recombinant LAF-1L protein elution fractions became turbid at room temperature (Figure 14A). Gently shaking of the tube reduced the cloudiness for approximately 15 seconds. A similar behaviour was observed during the optimization runs of the lysis buffer, but unlike the optimized purifications, the turbidity persisted for less than 5 minutes, and the protein fraction always ended up being aggregated in visible white flakes on the bottom of a tube. Conversely, optimized buffer allowed for the preservation of the turbidity state for at least 3 hours with 0.5 mg/mL (6.5 μ M) protein concentration at +4 °C. After being kept on ice for 1 hour, minor LAF-1L aggregates began to appear and increased over the following 2 hours, until none of the soluble protein remained. Normally, protein sample turbidity develops due to protein aggregate formation, but the reversible reduction of sample murkiness after NaCl concentration increase

up to 1000 mM suggested a different nature of this phenomenon. To investigate this protein behaviour in solution, freshly IMAC-eluted LAF-1L protein cloudy samples were scrutinized using Differential Interference Contrast (DIC) microscopy, revealing a high abundance of spherical droplets ranging in size from ~ 0.5 to $5 \mu\text{m}$ (Figure 14B). The droplets exhibited uniform distribution within the sample, irrespective of their sizes. Constant droplet migration and high aggregation potential within the microscopy sample impeded reproducible investigation of droplets interaction behaviour.

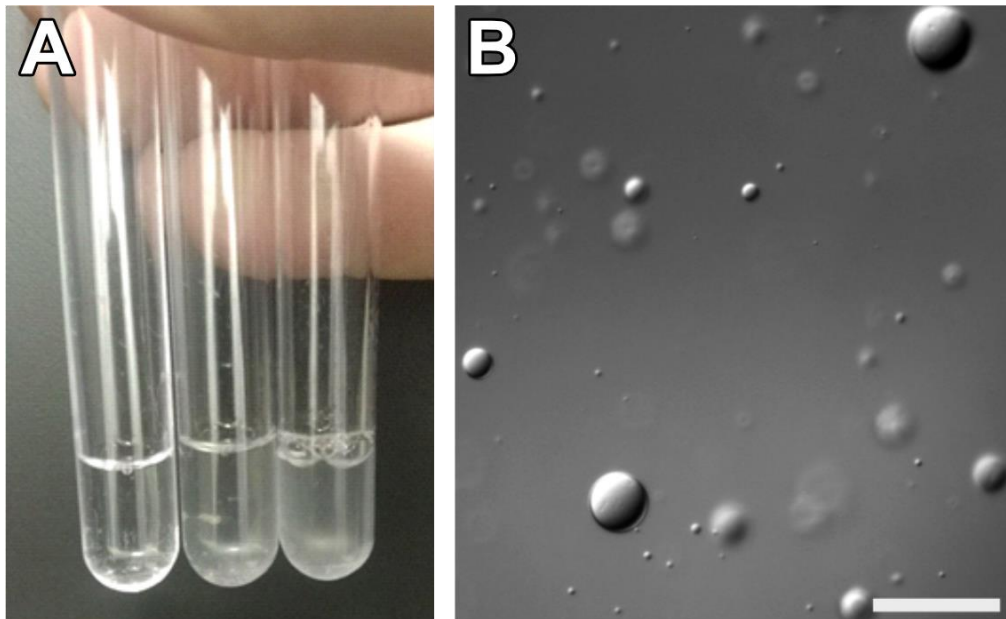


Figure 14. Recombinant LAF-1L protein starts to LLPS immediately after IMAC elution.

A. Image displays freshly eluted recombinant LAF-1L protein fractions following IMAC purification. The left tube contains the LAF-1L elution buffer, the central tube contains the second IMAC elution fraction with a LAF-1L concentration of 0.6 mg/mL , and the right tube contains the first IMAC elution fraction with a LAF-1L concentration of 1.3 mg/mL .

B. A representative DIC microscopy image that demonstrates LLPS of recombinant LAF-1L protein in LAF-1L elution buffer with a protein concentration of approximately 1.3 mg/mL . The scale bar represents $10 \mu\text{m}$. The experiment was conducted at room temperature.

Performing a full purification cycle of recombinant LAF-1L for each DIC microscopy assay had an adverse impact on reproducibility and experimental workflow due to protein purification time concerns. Therefore, further adjustments of the buffer composition were deemed necessary. After recombinant LAF-1L elution, a series of NaCl and Triton X-100 adjustments revealed that increasing the NaCl concentration to 1M and adjusting protein concentration to approximately 1.5 mg/mL ($\sim 20 \mu\text{M}$) on the slide suppressed LAF-1L LLPS and enabled maintenance of a stable protein cryostock. Further dilution of LAF-1L protein to

lower NaCl concentrations resulted in the recovery of LAF-1L LLPS droplet formation, as documented with DIC microscopy. After IMAC elution at 500 mM NaCl, recombinant LAF-1 protein exhibited intense LLPS droplet formation during the first few minutes, followed by almost complete protein aggregation (around 80%) after 15 minutes of incubation at room temperature. In contrast, a similar protein sample with adjusted concentration of NaCl to 1M showed minor LLPS droplet formation and only slight aggregation (around 10-15%) at same conditions (Figure 15). The similarity in the quantities of LAF-1L droplets and aggregates may be attributed to the reversible transition of soluble protein into LLPS droplets, which then irreversibly aggregate (Figure 15). After establishing cryostock preservation conditions for recombinant LAF-1L protein, further investigations were conducted to describe droplet formation and possible interactions among them.

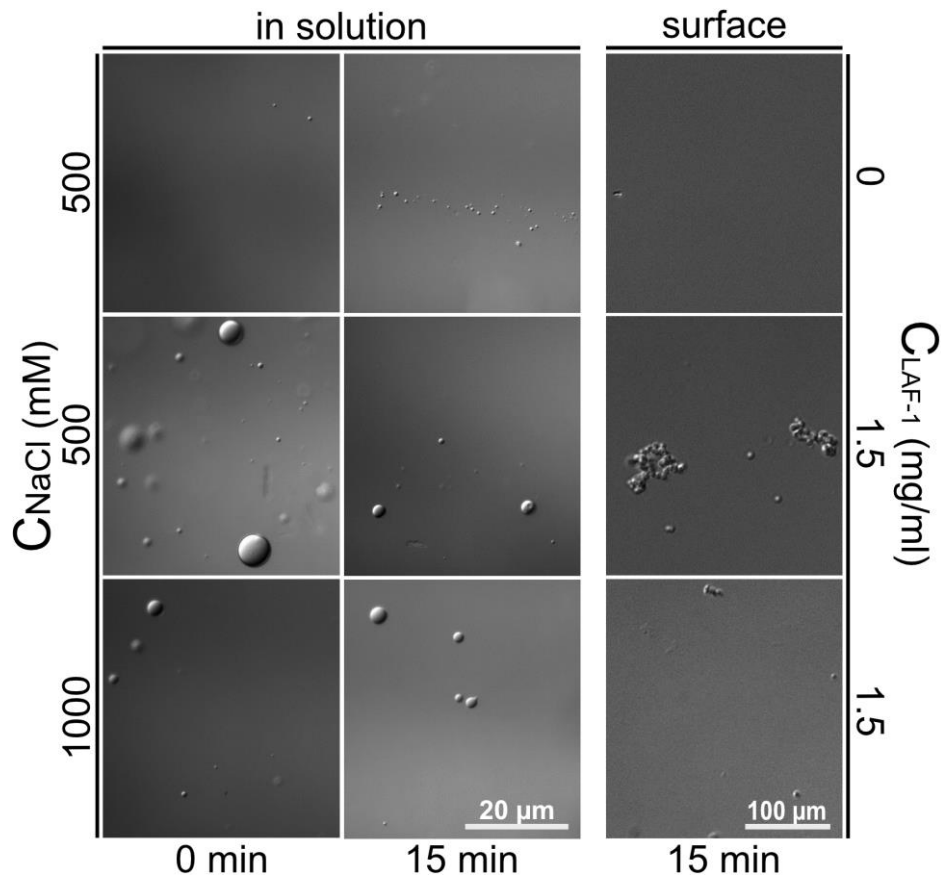


Figure 15. In low salt buffer, recombinant LAF-1L droplets transform into protein aggregates. An increase of buffer salt concentration dissociates LLPS droplets and prevents further aggregation of LAF-1L.

DIC microscopy images of freshly titrated recombinant LAF-1L in rebuffing solution, to varying protein and salt concentrations at room temperature. The 20 μm scalebar images were captured from a middle plane. The 100 μm scalebar images focus on the surface plane of the same glass slide.

Firstly, interactions between already assembled droplets in close proximity were studied. As previously shown in Figure 14B, recombinant LAF-1L protein samples contain a population of droplets evenly distributed in LAF-1L elution buffer. For DIC microscopy, samples of recombinant LAF-1L were diluted to 500 mM NaCl and a protein concentration of 1.0 mg/mL, incubated for 15 minutes at room temperature, and immediately documented (Figure 16). As the droplets rapidly migrated on the slide throughout the imaging procedure, all snapshots were taken with a 3-second delay to manually track and refocus on the protein droplet population. The sizes of recombinant LAF-1L droplets varied in the range of 1 to 80 μm , which was significantly larger than in unincubated samples (compare images in Figure 16 to Figure 14B).

Most protein droplets assembled into a spherical shape after each fusion event and during growth. It is conceivable to hypothesize that the observed behaviour of recombinant LAF-1L protein droplets could result in further assembly of a single massive final droplet, provided the physical behaviour remains constant. However, experimental data show that the droplet diameter decreased in proportion to the growth of protein aggregates until complete disassembly of all droplets, as seen in Figure 15. Interestingly, after a sudden increase in NaCl concentration to 1M, droplets have been observed to diffuse but this had no effect on aggregates (Figure 15).

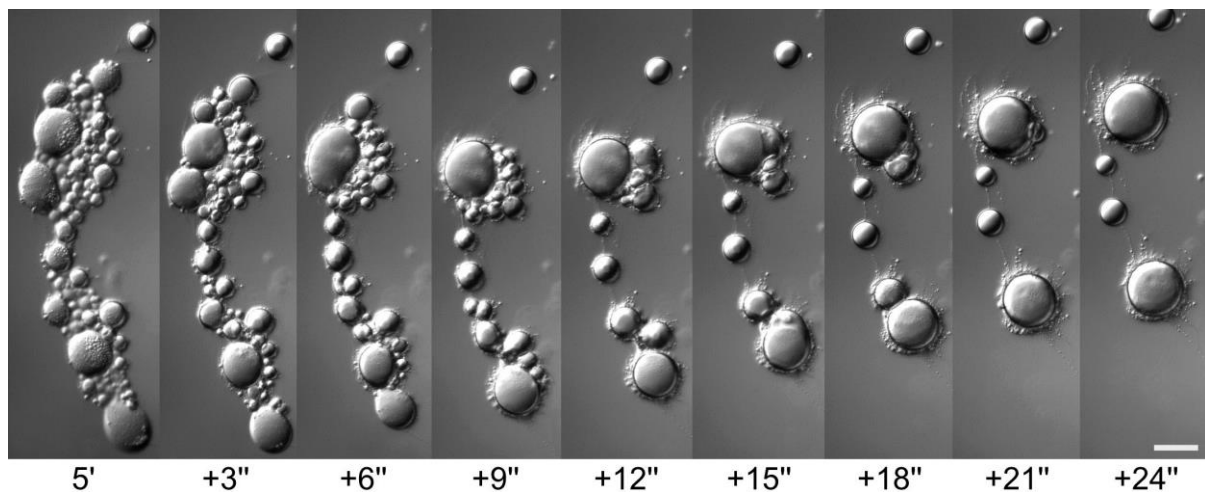


Figure 16. Smaller LAF-1L protein droplets fuse over time into bigger units.

This series of DIC microscopy images documents sequential stages of recombinant LAF-1L protein undergoing liquid-liquid phase separation (LLPS) at a protein concentration of 1.0 mg/mL (13 μM) in LAF-1L elution buffer with 500 mM NaCl. The experiment was conducted after an initial 10 minutes incubation at room temperature. The time interval between each still frame is 3 seconds. Scale bar, 50 μm .

The second question under consideration was the formation of new protein droplets after the primary droplet pool had already been established. Due to the restrictions of the optical plane and the high morphological similarity between young droplets and air bubbles occasionally appearing in the buffer, individual droplets in isolation were not considered. All droplets with a diameter of $\leq 3 \mu\text{m}$ were noted as early-stage, while mature droplets were judged by a diameter $\geq 50 \mu\text{m}$.

The largest accumulation of young droplets ($\geq 80\%$) was visible in close proximity to mature droplets, forming patterns similar to flame tongues (Figure 17). Further observation showed a brief increase in the size of early-stage droplets, along with their integration into the nearest mature droplet. However, none of the observed young droplets exhibited a size increment of more than $\sim 6 \mu\text{m}$. The current behaviour can be described as a dynamically equilibrated system that maintains its state through the constant association and dissociation of recombinant LAF-1L protein molecules with mature droplets, presumably mediated at large by the RGG IDR as previously suggested (Elbaum-Garfinkle et al., 2015). The current equilibrium state indicates the end of the droplet growth phase and further transformation of LLPS droplets into an aggregated state.

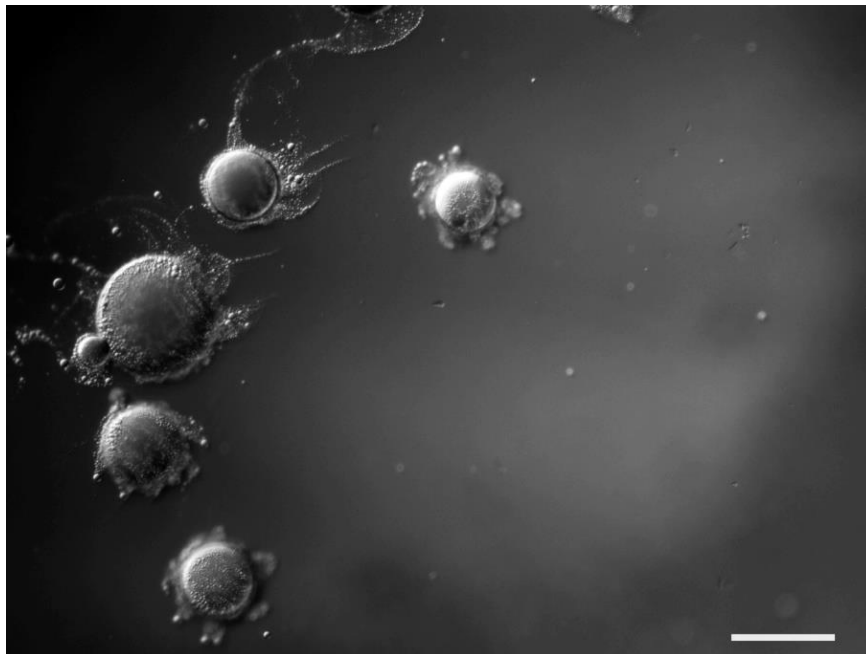


Figure 17. Big LLPS droplets of recombinant LAF-1L appear to induce condensation of smaller droplets in their close proximity.

DIC microscopy image of 1 mg/mL (13 μM) recombinant LAF-1L protein in LAF-1L elution buffer with 500 mM NaCl at room temperature after 10 minutes of incubation. Dilution from 1000 mM to 500 mM NaCl was immediately before incubation and imaging. Scale bar, 100 μm .

During optimization of the purification procedure to produce recombinant LAF-1S, none of the above mentioned LLPS features of LAF-1L droplets were observed. Instead, tempering with salt concentrations of soluble purified LAF-1S in LAF-1S elution buffer lead primarily to aggregate formation. Therefore, further attempts to discover buffer conditions that may trigger the formation of recombinant LAF-1S LLPS droplets were not conducted due to the high aggregation potency and significant loss of purified recombinant protein after each attempt. Although LAF-1S droplets were not discovered during this research, the shortened N-terminal RGG IDR of LAF-1S may still potentially contribute to or even induce LLPS to form recombinant protein droplets under optimal buffer conditions.

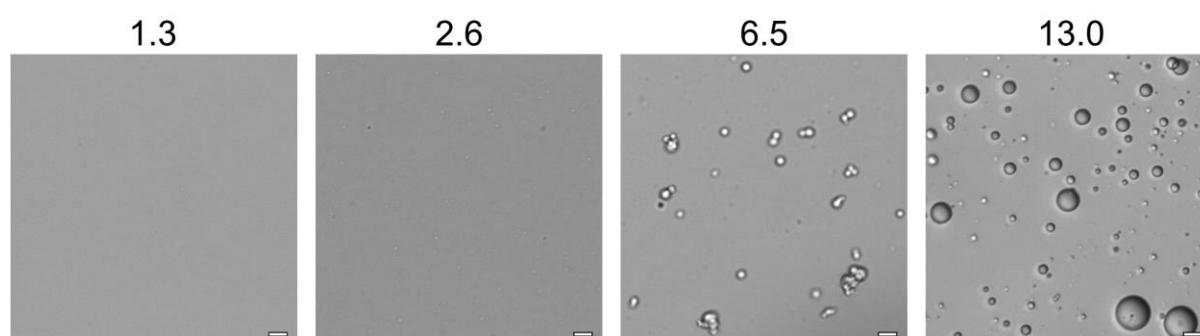


Figure 18. The LLPS of LAF-1L is primarily driven by protein concentration.

DIC microscopy of 0.1 mg/mL (1.3 μ M) to 1 mg/mL (13 μ M) recombinant LAF-1L protein in LAF-1L elution buffer with 500 mM NaCl at room temperature after 5 minutes of incubation. Dilution from 1000 mM to 500 mM NaCl was carried out immediately before incubation and imaging. Scale bar, 10 μ m.

The droplets of recombinant LAF-1L protein samples exhibited significant variation in size and growth rate across a concentration range spanning from 2.6 μ M to 13.0 μ M (Figures 18 and 19). The average droplet diameter for samples incubated at 13 μ M protein concentration for 5 minutes at room temperature was 19 ± 4 μ m ($n=30$). Samples containing 6.5 μ M LAF-1L protein under the same conditions had a diameter of 4 ± 2 μ m ($n=30$). Even after 30 minutes of incubation at room temperature, DIC microscopy imaging of 1.3 μ M did not reveal any visible droplets while 2.6 μ M LAF-1L samples contained barely visible droplets with ~ 1 μ m diameter ($n=30$) (Figure 19). Precise quantification of 2.6 μ M samples was not possible because of poor visibility of droplets and low image resolution. This behaviour of recombinant LAF-1L protein suggests that droplet formation occurs in a concentration-dependent manner and requires at least 2.6 μ M protein concentration under the tested conditions (Figures 18 and 19). Further increases in LAF-1L protein concentration had a growth rate similar to linear progression under tested conditions (Figure 20).

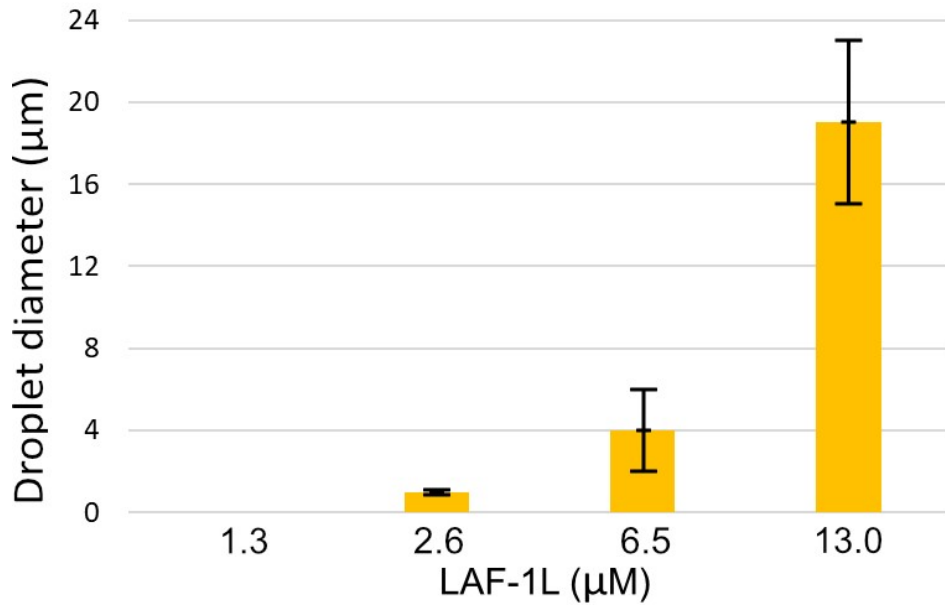


Figure 19. Average LAF-1L LLPS droplet size depends on protein concentration.

Bar graph represents average sizes of recombinant LAF-1L protein droplets in LAF-1L elution buffer with 500 mM NaCl after 5 minutes incubation at room temperature. Values of LAF-1L droplet diameters were obtained by processing DIC microscopy images (examples given in Figure 18) with ImageJ software. Averages and standard deviation values were calculated by Python3 custom script. n=30 each.

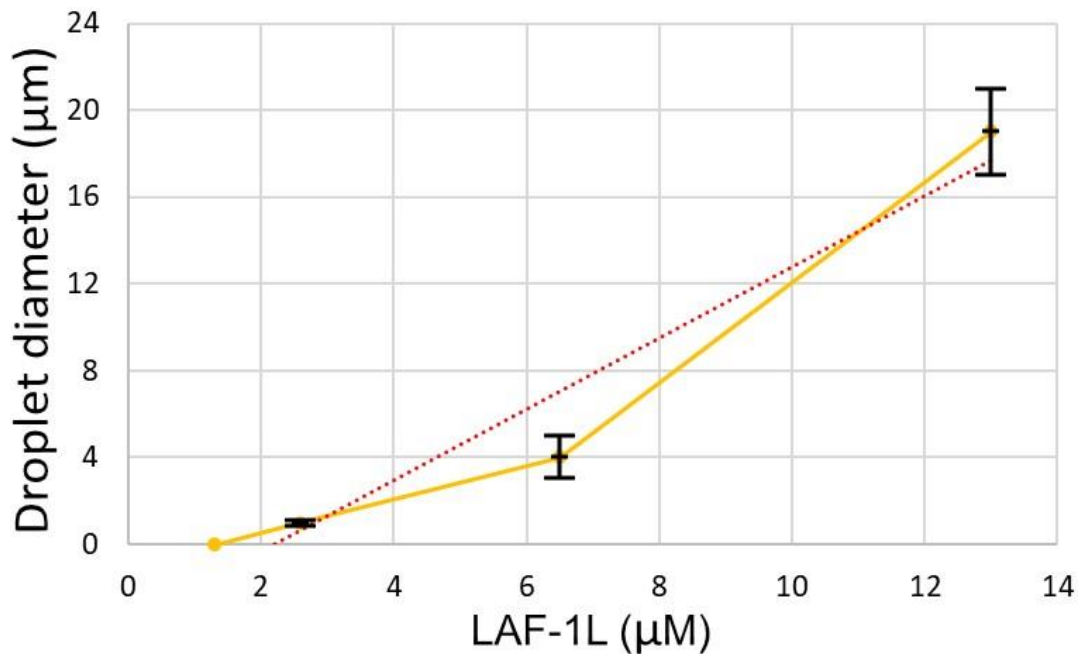


Figure 20. LAF-1L droplet size correlates with recombinant protein concentration in a manner similar to linear growth.

The red curve represents a linear progression based on a concentration-dependent droplet size increase curve with respect to recombinant LAF-1L amounts that are based on average values taken from Figure 19. $R^2=0.94$.

3.4. LAF-1 LLPS in presence of potential binding partners

Further research workflow focused on droplet integrity in the presence of non-interacting proteins and potentially specific binders to LAF-1L. As a presumed negative protein control in binding to LAF-1, BSA was selected since it is a typical globular protein not present in *C. elegans*. So far, the only identified LAF-1L binding partner was LAF-1L itself forming a dimer on RNA, independent of its N-terminal RGG IDR (Kim & Myong, 2016). This interaction occurred during the formation of an RNA-helicase dimer complex or a higher-order functional unit.

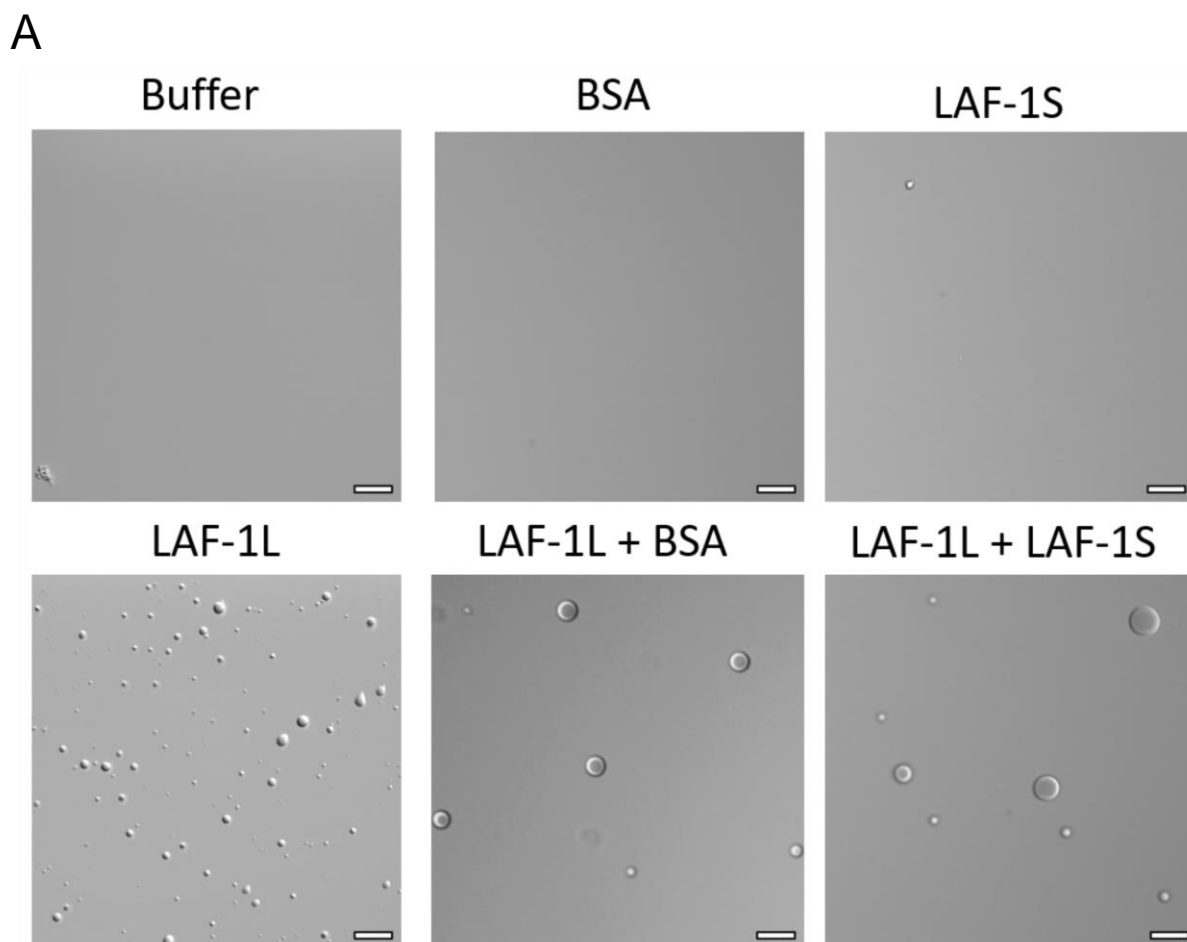
Therefore, one priority goal was to investigate a physical interaction with potential LAF-1L binding proteins through interference with recombinant LAF-1L LLPS in forming droplets. Potential physical protein interactors of LAF-1L are the LAF-1S isoform and, based on previous published data on DDX3 proteins (Shih et al., 2008), *C. elegans* variants of mammalian eIF4E, which altogether are five IFE orthologous proteins (IFE-1 to IFE-5). The hypothesis of protein-protein interaction between LAF-1L and LAF-1S isoforms was based on the published crystal structure of DDX3X (human DDX3 ortholog), which demonstrated RNA-helicase dimer bound to double-helix RNA molecule (Song & Ji, 2019). Dimer formation occurs through folded Walker domains of either DDX3X protomer (see also Figure 4B). Since LAF-1L and LAF-1S have presumed identical folded core helicase domains, a similar complex is likely to form between the two protein isoforms.

3.4.1. LAF-1S LLPS differs from LAF-1L and influences LAF-1L LLPS

DIC microscopy imaging confirmed that neither BSA nor recombinant LAF-1S proteins were able to form LLPS droplets in 50% LAF-1S elution buffer and 50% LAF-1L elution buffer with 500 mM NaCl at room temperature (Figures 21 and 22). Such buffer conditions were on the one hand the consequence of mixing purified proteins in their storage buffers, and on the other hand a compromise to guarantee that both recombinant LAF-1L and LAF-1S have low aggregation potential during samples preparation for DIC microscopy. Also for this reason, investigated protein concentrations were reduced to 6.5 μ M due to high abundance of LAF-1L protein aggregates in higher concentrated samples. After 5 minutes of incubation, stable LLPS droplet formation was clearly visible by eye in all samples that contained recombinant LAF-1L protein. Once LAF-1L droplets reached their average

maximum size, they were able to maintain their size in a dynamic equilibrium for a brief period of time (approximately up to 15 minutes) before aggregation began to occur.

Whereas the average diameter (values are rounded to integers) of 6.5 μM LAF-1L only droplets was 3 ± 1 μm ($n=30$), addition of 6.5 μM BSA or 6.5 μM LAF-1S enhanced droplet diameters to 5 ± 3 μm ($n=30$) and 6 ± 4 μm ($n=30$), respectively (Figures 21 and 22A). Moreover, DIC microscopy identified 441 ± 108 droplets (dr.) per 1 mm^2 (dr./ mm^2) abundance for LAF-1 only, while LAF-1L in presence of BSA had only 76 ± 18 dr./ mm^2 (Figures 21 and 22B). LAF-1S had a similar effect to BSA by reducing droplet abundance to 81 ± 27 dr./ mm^2 (Figures 21 and 22B). It is worthwhile to mention that these datapoints were generated based on manual calculation of droplet number on $1/9^{\text{th}}$ of a 1 mm^2 surface area of a single DIC microscopy image, equalling roughly the size of the CCD camera chip on the DIC microscope. Assuming equal distribution on a glass slide, obtained numbers were then multiplied by 9 to reach a more understandable surface area. Such calculations were performed on four individual images taken from different regions of the same slide. Taken together, the high similarity between recombinant LAF-1S and BSA proteins in their effects on LAF-1L droplets suggests unspecific droplet growth by addition of different proteins. These changes may be simply be the consequence of an additional selective pressure on LAF-1L droplet formation through higher protein content in the buffer, similar to a molecular crowding situation.



B

| Sample (6.5 μM each) | LAF-1L | LAF-1L + BSA | LAF-1L + LAF-1S |
|--|--------|--------------|-----------------|
| Av. diameter (μm) | 3 | 5 | 6 |
| Av. abundance (dr./ mm^2) | 441 | 76 | 81 |
| Av. volume (μm^3) | 14.14 | 65.45 | 113.10 |
| Av dr. density ($\mu\text{m}^3/\text{mm}^2$) | 6236 | 4712 | 9161 |

Figure 21. BSA or LAF-1S has minor impact on LAF-1L LLPS droplet morphology.

A. This series of DIC microscopy images represents presence/absence of LLPS droplets of individual proteins and their mixtures. Each final protein concentration was 6.5 μM in a buffer mixture that is composed of 50% LAF-1S elution buffer and 50% LAF-1L elution buffer with 500 mM NaCl (Buffer) after 5 minutes incubation at room temperature. The scale bar represents 10 μm . Note, irregularly shaped objects in pictures without droplets were intentionally taken and represent the occasional dirt flake on top of the glass slide.

B. Summary of droplet metrics as quantified by DIC microscopy. Av. – Average; dr. – droplet.

As BSA and LAF-1S had comparable effects on LAF-1L droplets and no protein-specific patterns were identified, potential droplet composition changes were investigated based on comparisons of total droplet volumes (Figures 21B and 22C). Given the observed roundness of droplet morphology in a given optical plane, it was assumed that droplets mostly have spherical shape (Figure 21A). Volume of sphere can be calculated by formula $V = \pi \cdot \varnothing^3 / 6$, where V is a sphere volume, \varnothing is a sphere diameter and π is a mathematical constant (~3.14159). Afterwards, an average density was calculated by multiplication of average droplet volume on droplet abundancy (Figure 21B). The average volume was rounded to a second digit to the right of the separator and calculated density is given per optical section (Figure 22C).

Even though BSA and LAF-1S had a similar effect on LAF-1L droplets morphology, comparison of average values showed that BSA sample has 25.5% reduction in average droplets density, meanwhile presence of LAF-1S induced 44.9% increase (Figure 22C). These datapoints suggest that LAF-1S but not BSA may co-LLPS with LAF-1L under tested conditions, indicating a specific affinity between LAF-1 proteins. Nonetheless, presented model relies on a series of assumptions and generalizations that introduce multiple numerical errors likely distorting the final result and, therefore, cannot be used to argue a final conclusion. This is why, additional studies were conducted to investigate a possible integration of LAF-1S into LAF-1L droplets.

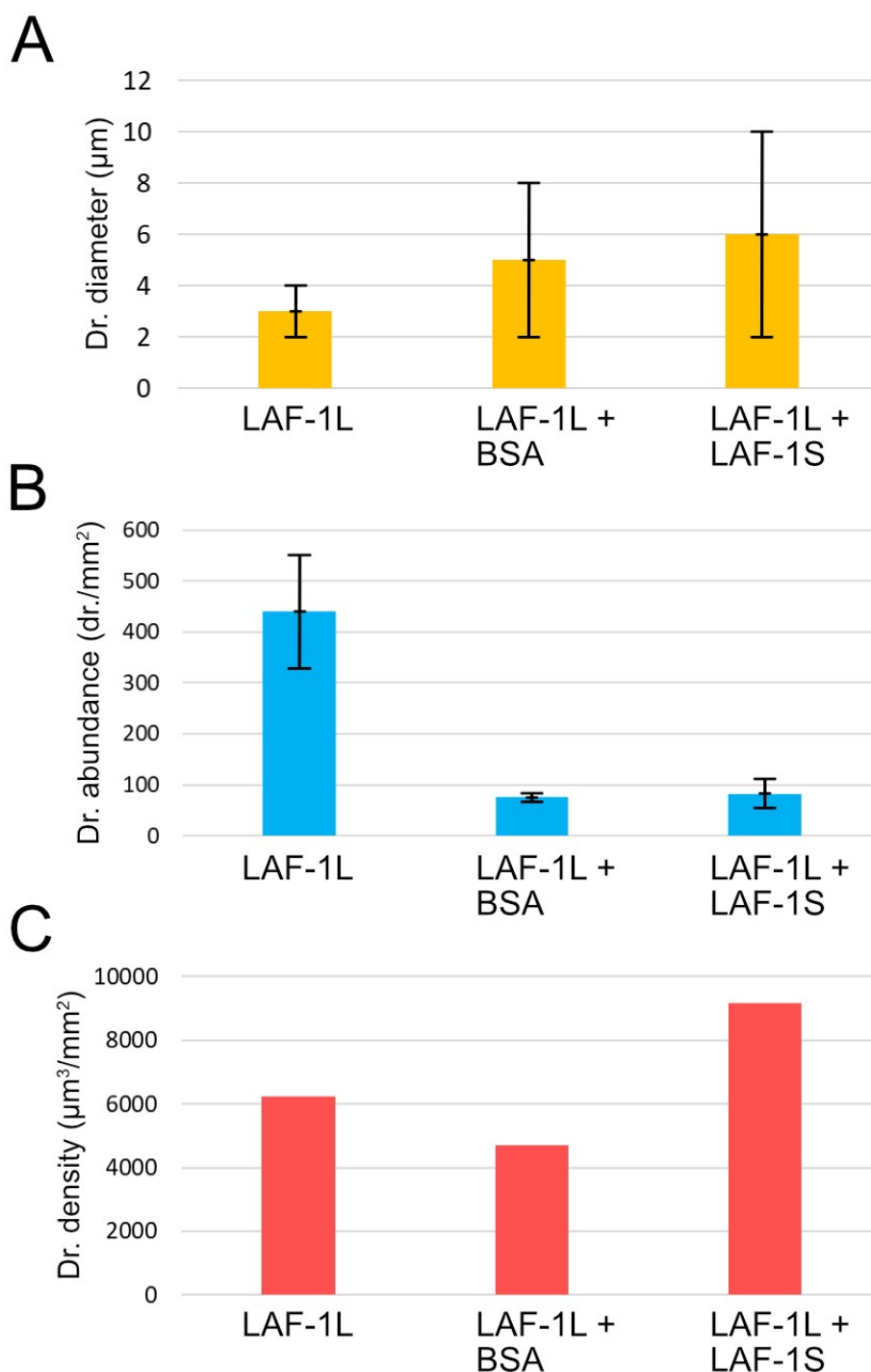


Figure 22. BSA and LAF-1S have a minor impact on LAF-1L LLPS droplet morphology.

Protein concentration and buffer compositions as in Figure 23. Values of droplet (n) diameters and abundance were obtained by processing four separate DIC microscopy images from a single glass slide with ImageJ software. Average values and standard deviations were calculated by Python3 custom script; numbers are in Figure 21B.

A. Droplet (Dr.) diameter values.

B. Droplet abundance.

C. Average droplet density as calculated by multiplication of average value of droplet diameter by average droplet abundance for each sample.

The new strategy relied on the hypothesis that during the accumulation of fluorescently labelled protein in LAF-1L droplets, an intensification of the fluorophore signal in recombinant LAF-1L droplets might be visualized. VRDye 490 (LI-COR) was selected as the fluorescent agent because it could be detected under the CFP (cyan fluorescent protein) filter of the DM6 B fluorescence microscope (Leica), which was previously used in the DIC microscopy assay. Furthermore, the VRDye 490 labelling kit (LI-COR) was commercially available and had already been tested during this research work.

The major difficulty in the VRDye 490 labelling procedure is its narrow range of buffer components, as neither free amino groups nor detergents are compatible with its crosslinking chemistry. That's why the 1 mL stock solution of approximately 17 μM (approximately 1.2 mg/mL) purified recombinant LAF-1S had to be first rebuffered into PBS buffer through a dialysis procedure with the help of the Slide-A-Lyzer cassette (ThermoFisher). Dialysis was performed in two steps. First, the cassette was placed into 1L of PBS solution for 2 hours at a temperature of +4 °C with constant mixing. Afterwards, the solution was replaced with an equal volume of fresh PBS and incubated overnight under the same conditions. As expected from previous LAF-1S purifications (Chapter 3.2), most of the recombinant LAF-1S had aggregated during the dialysis procedure. The final outcome was 1.2 mL of approximately 4.2 μM (approximately 0.3 mg/mL) of rebuffered LAF-1S protein in PBS. In parallel, a BSA stock solution (2.0 mg/mL, ThermoFisher) was directly diluted to 1 mL in PBS with a protein concentration of 15 μM (1 mg/mL). Both LAF-1S and BSA solutions were labelled and desalted according to the manufacturer's guidelines and concentrated to a volume of 1 mL using a Vivaspin 2 centrifugal concentrator (Sartorius) at 3000 rpm at +4°C in a 5810R benchtop centrifuge with an A-4-62 swing bucket rotor with a 15 mL tube adaptor (Eppendorf). During the labelling procedure, LAF-1S had partially aggregated, which is why the final protein concentration was further reduced to 3.52 μM (0.25 mg/mL). Additional attempts to increase the labelled LAF-1S concentration failed and ended in protein aggregation. Preliminary experiments showed that 3.5 μM of BSA and LAF-1S overexposed the CFP channel, which is why the concentration of both proteins was reduced to 1.4 μM (~0.1 mg/mL). The LAF-1L concentration was not changed and remained at 6.5 μM (0.5 mg/mL).

Combined DIC and fluorescent microscopy examination showed that BSA and LAF-1S were not able to undergo LLPS themselves (Figure 23). Furthermore, only LAF-1S but not BSA was capable of intensifying the fluorophore signal in LAF-1L droplets (Figure 23). This observation suggests that LAF-1S is capable of undergoing LLPS under the examined

conditions, provided LAF-1L droplets are present. Inclusion of LAF-1S into LAF-1 droplets may either rely on potential dimerization via the Walker domains or might be mediated by the RGG IDR, which is known to be the major structure during LLPS of LAF-1L (Elbaum-Garfinkle et al., 2015). Apparently, LAF-1S has a sufficient size to undergo LLPS together with LAF-1L without disassembling LAF-1 droplets. However, LAF-1S itself has insufficient RGG IDR size to induce LLPS under the tested conditions. Even though the current research highlights LAF-1L LLPS, a precise adjustment of LAF-1S buffer conditions is likely to trigger *in vitro* droplet formation of recombinant LAF-1S.

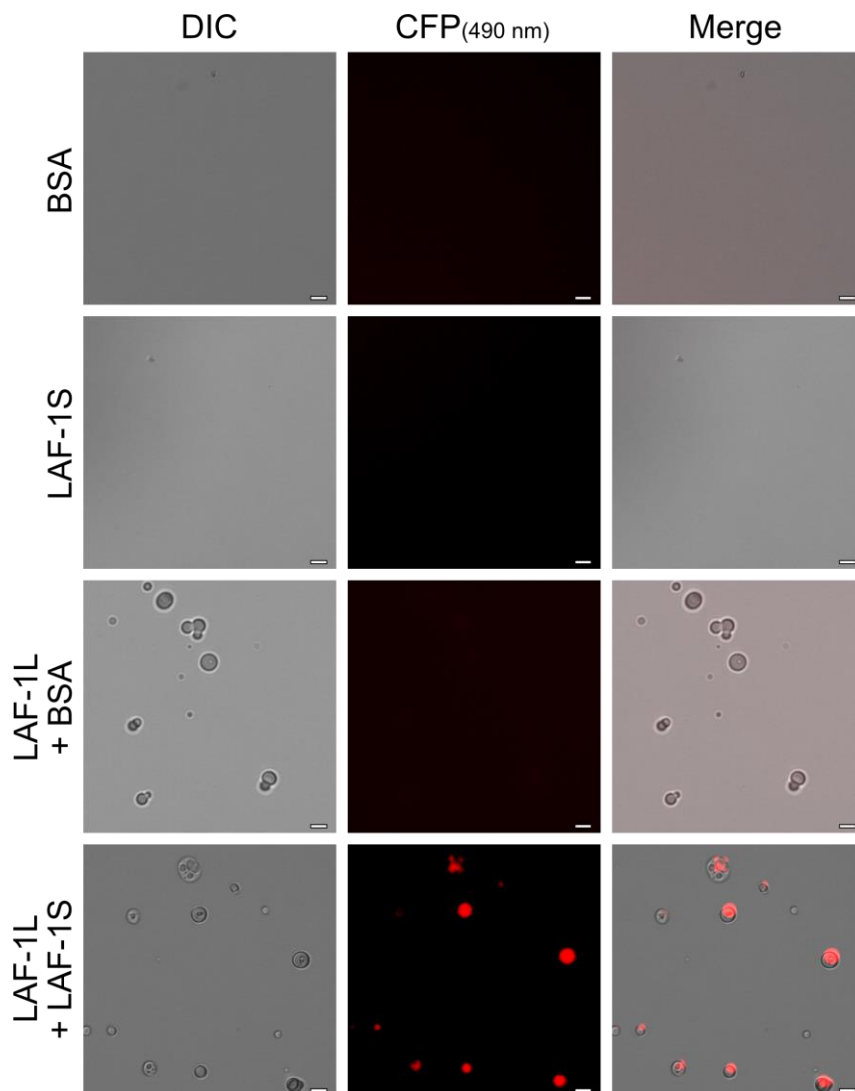


Figure 23. LAF-1S integrates into LAF-1L droplets.

Microscopical analyses of VRDye 490 fluorescently labelled LAF-1S and BSA in presence/absence of recombinant LAF-1L. Merged images represents combined DIC and CPF filter channel, background adjusted for the fluorescent signal. LAF-1L final protein concentration was 6.5 μM . LAF-1S and BSA final protein concentrations were 1.4 μM . All experiments were conducted in LAF-1L elution buffer with 500 mM NaCl after 5 minutes incubation at room temperature. The scale bar represents 10 μm .

3.4.2. LAF-1L LLPS is suppressed by eIF4E proteins

In human cells, the cap-binding protein eIF4E is a verified protein interaction partner of DDX3 (Shih et al., 2008). To investigate a potential influence of *C. elegans* eIF4E (generically abbreviated as IFE-x) protein variants on the LLPS behaviour of LAF-1, expression constructs were generated based on the LAF-1::6xHis in the pET-28+ bacterial expression vector. All five IFE-encoding ORFs were PCR amplified from cDNA laboratory's cryostock and inserted via restriction digestion to replace the LAF-1L ORF (Appendix List 5.10). Final IFE-x expression plasmids were verified by DNA sequencing and heat-shock transformed into BL21-CodonPlus (DE3)-RIL *E. coli* for protein expression.

3.4.3. Purification of *C. elegans* IFE proteins

For the first expression experiment of recombinant IFE-x proteins, 25 mL bacterial LB-media cultures were prepared. The lysis buffer contained 50 mM Tris-HCl pH 7.4, 250 mM NaCl, 10 mM imidazole, supplemented with 1x EDTA-free protease inhibitor cocktail, and 0.25 mg/mL lysozyme. Due to its efficiency, bacterial sonication lysis parameters were identical to those of the LAF-1 purification procedure. Also, induction parameters were identical to LAF-1 expression regimes and subsequently both, pellets and crude supernatants, of all five IFE-x proteins were analysed by 12% SDS-PAGE stained with Coomassie. Recombinant IFE-1 (27.8 kDa), IFE-3 (29.6 kDa), and IFE-4 (25.6 kDa) displayed significant bands in supernatant fractions corresponding to their predicted molecular weight, suggesting that a fraction of each fusion protein is soluble. By contrast, IFE-2 (27.4 kDa) and IFE-5 (24.4 kDa) had similar size bands in pellet fractions only, supernatants were free of soluble protein. Consequently, two different purification strategies were employed.

IFE-1, IFE-3, and IFE-4 purifications were initiated with 1L bacterial LB-media culture. Due to resin and experimental goal similarities, IMAC and SEC setups were identical to LAF-1 purification strategy albeit with a different subset of buffers. IFE-x wash and elution buffers contained increasing imidazole concentrations to 30 mM and 250 mM, respectively, and a 50 mM increase of NaCl in the elution buffer for easier conductive determination during IMAC and SEC. IFE-x rebuffing solution consisted of 50 mM Tris-HCl pH 7.4, 250 mM NaCl, and 10% glycerol, which was enough for protein stability during chromatography and further cryopreservation. The total yield from 1 L of bacterial LB-culture was 3-4 mg in 2 mL of IFE-x elution buffer with ~85-95% purity according to Coomassie-stained SDS-PAGE (Figure 24).

Although, aliquots of either IFE-x had no visible aggregation after the first freezing-thawing cycle at 1.0 mg/mL protein concentration, ~50% aggregation was detected after the second cycle. Moreover, a significant fraction (~40%) of recombinant IFE-1 protein was partially proteolyzed in soluble and insoluble fractions. The truncated protein could not be removed due to size and structure similarity. Expression adjustments did not change the proportion of intact and truncated forms.

To promote solubility of IFE-2 and IFE-5 recombinant proteins, a series of buffer composition optimizations were applied. The implementation of MOPS, HEPES, PBS (pH 6.2–8.0), and Tris-HCl buffer systems (pH 6.8–8.4) did not enhance the soluble recombinant protein content in the supernatant fraction after lysis. Multiple concentration adjustments of Triton X-100 (0.05–2.0%), glycerol (10–20%), MgCl₂ (5–25 mM), imidazole (0–25 mM), and NaCl (50–1000 mM) did not increase yield of soluble recombinant protein. Further attempts to change the detergent to NP-40 or Tween-20 did not help either. The best result achieved from 1L of LB was 0.3 mg of ~70% purity. Moreover, reducing the induction time from 8 to 4 hours and temperature from +16 °C to +12 °C did not increase yield, as most of the recombinant protein remained insoluble. Further attempts were rejected due to time concerns.

In parallel, an alternative approach of protein refolding was tested. Given the small size of IFE-x proteins and their AlphaFold-predicted α/β -globular structure (Jumper et al., 2021), it was assumed that the recombinant protein could reassemble its native tertiary structure without requiring additional folding molecular machinery. For each IFE-x, the denaturing buffer consisted of a 50 mM Tris-HCl pH 7.4 buffer system with 20 mM imidazole and 8M urea, which is a common chaotropic agent used for protein refolding (Cabrita & Bottomley, 2004). The input bacterial liquid culture media was downscaled to 150 mL due to the high yield of insoluble protein and the limited binding capacity (<40 mg/mL) of the IMAC column. Washed inclusion bodies (Chapter 2.3.7) were resolubilized in 40 mL IFE-x denaturing buffer, which was sufficient volume for maximal resolubilisation. The refolding procedure was done by a steady gradient replacement of IFE-x denaturing buffer from 100 to 0% by IFE-x washing buffer (Chapter 2.3.8). The total yield from 150 mL of bacterial LB-culture was 12-15 mg in 5 mL of IFE-x elution buffer with ~90-95% purity according to Coomassie-stained SDS-PAGE (Figure 24). The rebuffing procedure was identical to the native purification setup and had no identified protein aggregation. The freezing-thawing stability was similar to the natively purified IFE-1, IFE-3 and IFE-4.

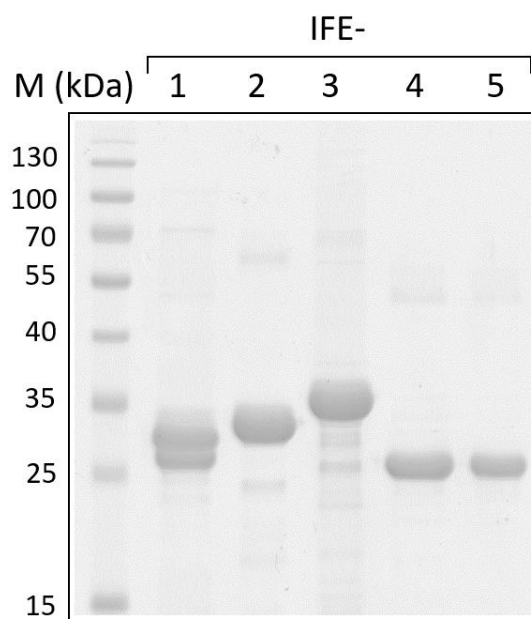


Figure 24. Five recombinant IFE protein variants of *C. elegans* were purified.

A monochrome digital scan of 1 mm Coomassie stained 12% SDS-PAGE with 10-well comb. Samples: M – 3 μ L of PageRuler protein ladder (Thermo Scientific), molecular weight assigned on the side of the image in kDa; IFE-x – 5 μ L of 1 mg/mL recombinant C-terminally 6xHis-tagged IFE-1 to IFE-5 proteins in SDS sample buffer after IMAC and SEC purifications.

3.4.4. IFE proteins affect LAF-1L LLPS

Preliminary examination of five IFE proteins did not show any signs of droplet formation over a broad range of NaCl concentrations (150–1000 mM) or during the establishment of the purification procedure (Chapter 2.3.8). The primary strategy to investigate this interaction using a far-western blot approach was rejected after multiple unsuccessful attempts ($n > 20$) (Wu et al., 2007). DIC microscopy was chosen as an alternative assay of distinguishable criteria for nonbinding proteins and with a potentially higher tolerance to weak protein-protein interactions, compared to the far-western blotting technique. This assumption was also made based on above described LAF-1S droplet integrity tests (Figure 21A). The concentration of IFE proteins used was 13 μ M, which was twice the concentration of LAF-1L protein (6.5 μ M). This decision was made to ensure a sufficient amount of IFE molecules capable of binding each LAF-1L protein in case of partial aggregation of IFE proteins, saturation of several potential LAF-1L binding sites, or the need to dimerize prior to LAF-1L binding. Furthermore, the 1:2 ratio of LAF-1L to IFE proteins kept the total protein amount similar to prior

microscopy samples of LAF-1L droplet formation in the presence of BSA or LAF-1S proteins (Figure 21).

In contrast to recombinant LAF-1L, none of the five IFE-x proteins were seen in DIC microscopy to form LLPS droplets (Figure 25), consistent with a prior absence of turbidity in protein fractions after their purification. However, under the same conditions as previous experiments performed with LAF-1S and BSA protein samples, LAF-1L in combination with any of the five IFE proteins did not show any LLPS droplets anymore (Figure 25). Such a striking difference in droplet formation potency suggests that a presumed protein-protein interaction of IFE-x proteins with LAF-1L may be able to suppresses its capability to form LLPS droplets *in vitro*.

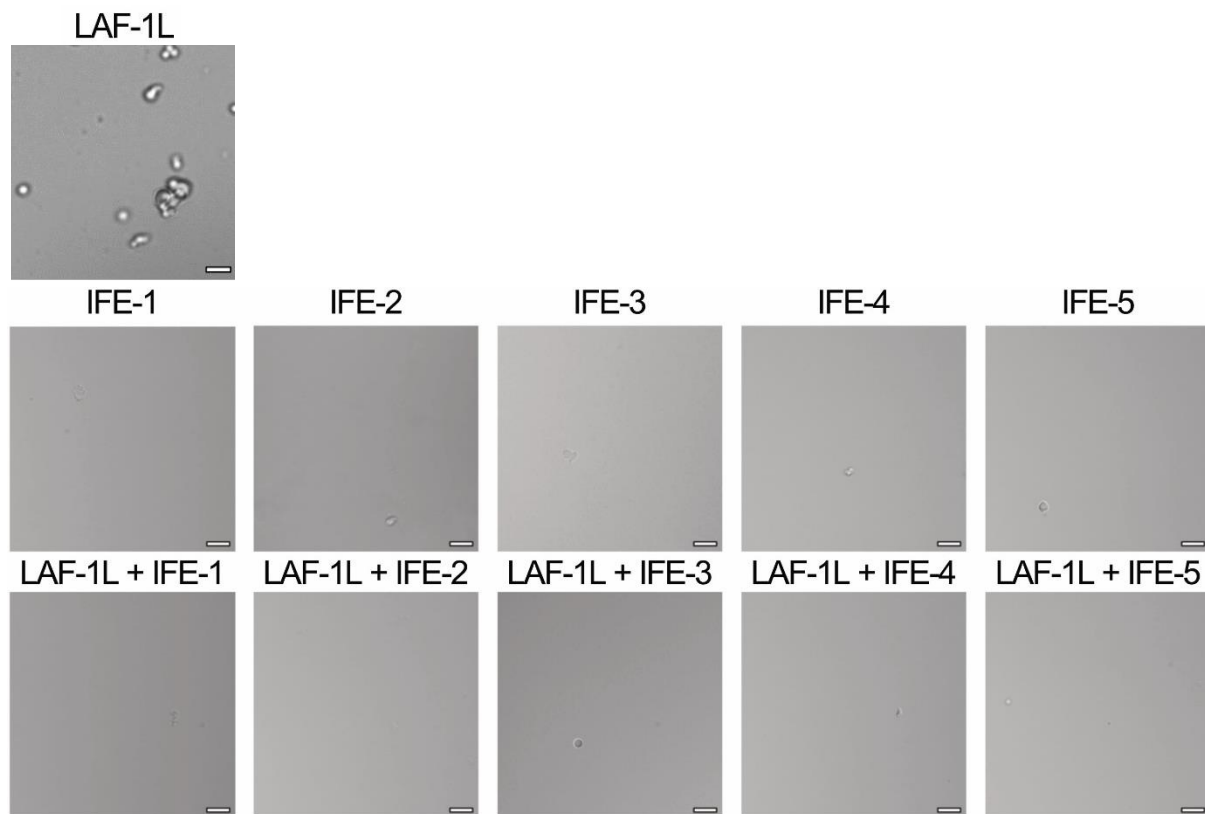


Figure 25. All five IFE-x proteins suppress LLPS of LAF-1L.

DIC microscopy images of recombinant LAF-1L only protein LLPS droplets and in the presence of recombinant IFE proteins. All experiments were conducted in LAF-1L elution buffer with 500 mM NaCl. Each sample was incubated for 5 minutes at room temperature before imaging. The concentration of LAF-1L was set to 6.5 μM , and the concentration of IFE-x proteins was 13 μM each. The scale bar represents 10 μm . Note, irregular objects on glass slides demonstrate a sharp focal plane; no LAF-1L droplets are visible.

3.4.5. LAF-1 LLPS in presence of total *C. elegans* RNA.

To investigate the impact of RNA on the LLPS behaviour of LAF-1L, a dilution series of Trizol-extracted total *C. elegans* RNA, ranging from 0 to 125 ng/ μ L, were incubated for 30 minutes at room temperature with 6.5 μ M of recombinant LAF-1L. Such incubation timeframe was sufficient for reaching maximal droplets sizes. Longer incubations had little to no effect on droplet diameter. To minimize the impact of RNA batches on experimental validity, the LLPS of LAF-1L in the presence of total RNA was conducted using aliquots generated from a mixture of three independent Trizol extractions of adult *C. elegans* nematodes.

Examinations by DIC microscopy showed a consistent (n=30) correlation between RNA concentration and droplet sizes (Figure 26). Subjectively, droplet abundance was also enhanced, but due to the low reproducibility of quantitative values and uneven distribution of droplets on the glass slide, only general conclusions regarding droplet abundance could be made. However, the general tendency of increased RNA concentration on enhancing both the quantity and size of droplets was clearly visible and reproducible throughout this research.

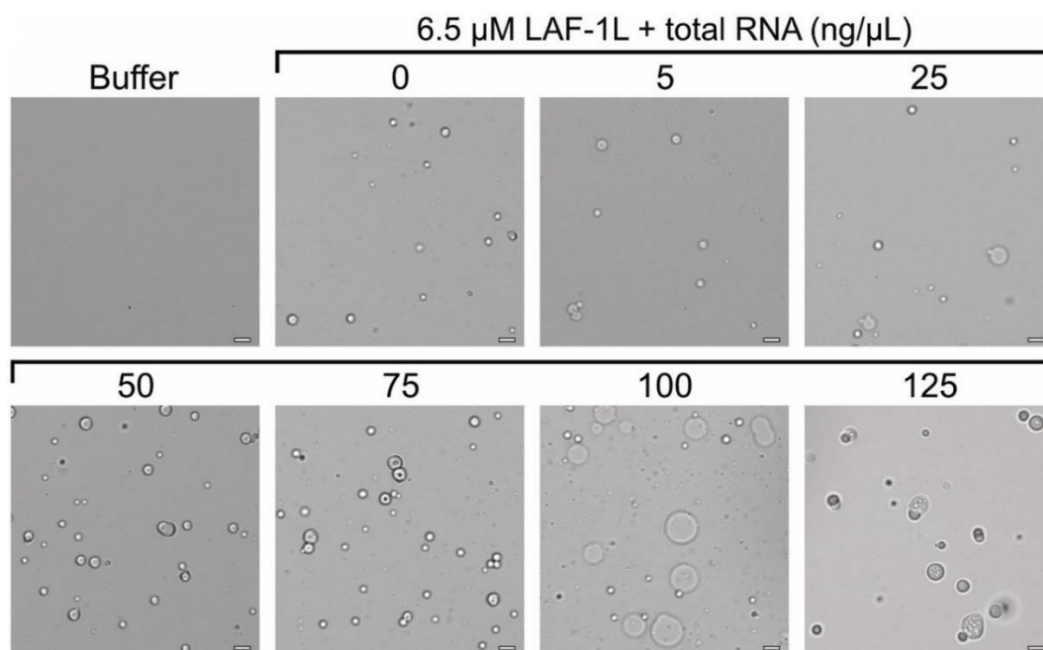


Figure 26. Total RNA reduces the dew point of LAF-1L droplets.

This series of DIC microscopy images represents recombinant LAF-1L protein LLPS droplets in presence of total RNA extracted from *C. elegans* adults. All experiments were conducted in LAF-1L elution buffer with 500 mM NaCl. Each sample was incubated for 30 minutes at room temperature before imaging. The concentration of LAF-1L was 6.5 μ M, and the concentration of total RNA was adjusted, according to its legend, in ng/ μ L units. The scale bar represents 10 μ m.

The major quantitative parameter selected for further analysis was the droplet diameter. Due to microscopy resolution, droplets below 2 μm were not taken into account. Nonetheless, this setup allowed it to reduce the impact of sample artefacts, which mostly had a diameter of less than 2 μm . Additionally, image processing of small objects had a large margin of error. The listed values were also rounded to whole numbers for ease of understanding. Such an assumption is permissible, considering the error introduced by the human factor during image processing and the resolving power of the DIC microscopy under the tested conditions.

Quantitative analyses of LAF-1L droplets demonstrates a consistent increase in droplet size from 3 ± 1 μm ($n=30$) to 13 ± 8 μm ($n=30$) in the RNA concentration range from 0 to 100 $\text{ng}/\mu\text{L}$, followed by a reduction to 10 ± 3 μm ($n=30$) at 125 $\text{ng}/\mu\text{L}$ (Figure 27). Additionally, the maximum and minimum droplet diameters were observed to increase and decrease, respectively, in a concentration-dependent manner (Figure 27). This indicates that not only the rate of droplet growth was affected by RNA, but also the potency to form new droplets was enhanced.

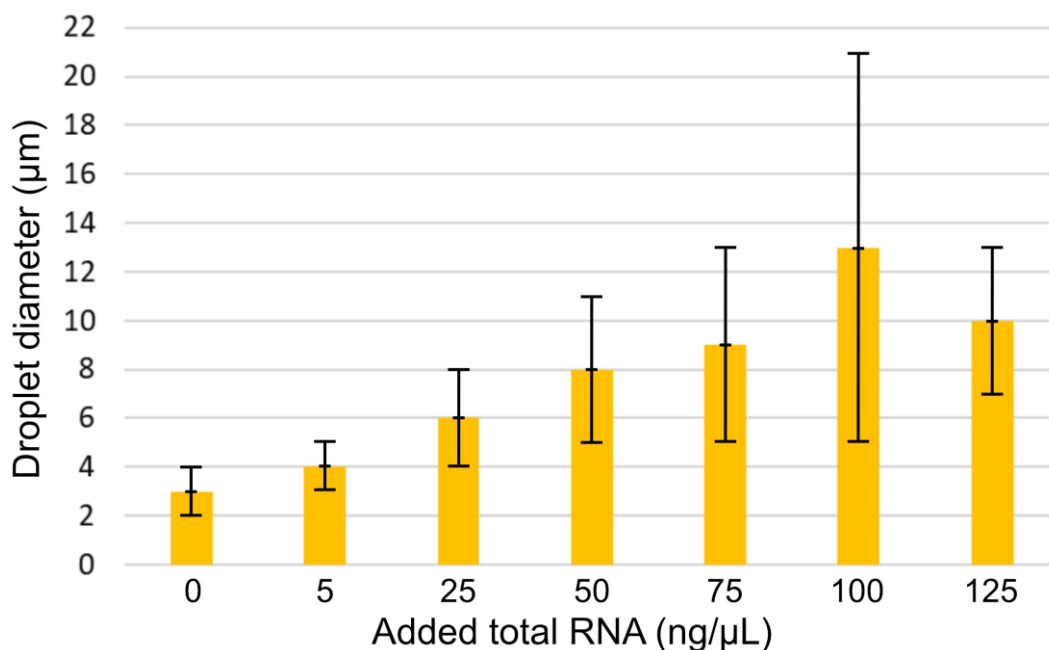


Figure 27. LAF-1L droplets size correlates with total RNA concentration.

The graph represents a quantified droplet diameter of recombinant LAF-1L protein droplets in the presence of total *C. elegans* adults RNA. All experiments were conducted in LAF-1L elution buffer with 500 mM NaCl. Each sample was incubated for 30 minutes at room temperature before imaging. The concentration of LAF-1L was 6.5 μM , and the concentration of total RNA was adjusted according to a legend in $\text{ng}/\mu\text{L}$ units. Image processing was performed using ImageJ software, and the average values and standard deviation values were calculated using a custom Python3 script. The scale bar represents 10 μm . $n=30$ droplets each.

Even though total RNA alone was unable to undergo LLPS in solution, it strongly induced changes in LAF-1L droplet morphology and abundance. This behaviour suggests that recombinant LAF-1L is capable of forming RNP droplets under favourable conditions. However, further increasing the RNA concentration to 125 ng/ μ L resulted in a reverse effect compared to the 100 ng/ μ L sample (Figure 27). This likely indicates unspecific oversaturation of RGGs with RNA phosphate backbones or protein affinity binding, leading to a loss of capability to undergo LLPS.

This experimental setup represents a simplified *in vitro* model of physiological LLPS and suggests that granule formation is driven by protein IDR domains with properties similar to LAF-1L, and further enhanced by RNA and additional proteins, as demonstrated in the LAF-1S experiments. While RNA molecules are not reported to undergo LLPS, mechanisms of granule formation might be based on nonspecific protein recognition of general structural patterns of RNA molecules, or even more specific three-dimensional folds, recognized by a given class of proteins, such as DDX3 helicases. A similar suggestion applies to proteins that are incapable of undergoing LLPS themselves but can integrate into droplets through protein-protein interactions, such as LAF-1S, or by binding RNA molecules before being recruited to droplets or granules. In either case, further investigations are needed to investigate such hypotheses.

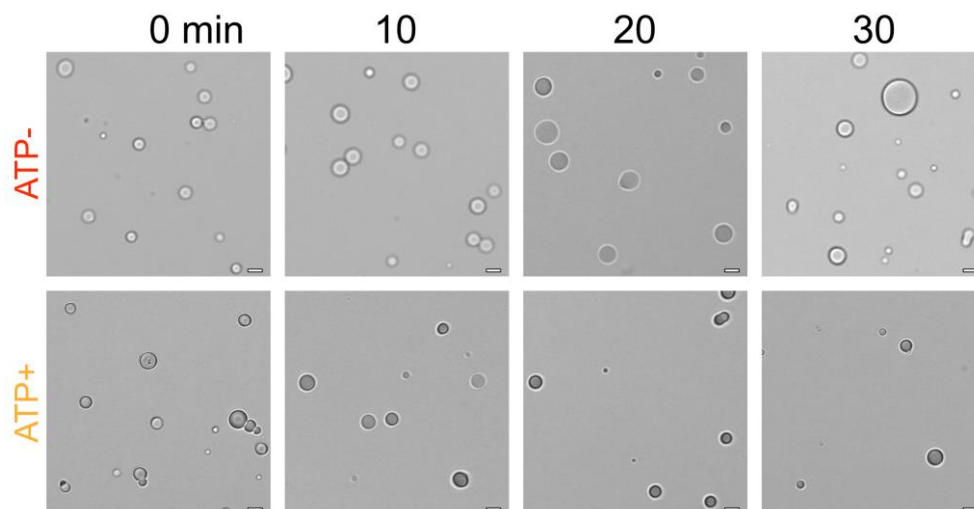


Figure 28. LAF-1L/RNA droplets do not grow in presence of ATP.

This series of DIC microscopy images represents recombinant LAF-1L protein droplets in presence of *C. elegans* total RNA with (ATP+) and without (ATP-) 25 mM of ATP. All experiments were conducted in LAF-1L elution buffer with 500 mM NaCl. Each sample was incubated for 30 minutes at room temperature before imaging. The concentration of LAF-1L was 6.5 μ M, and the concentration of total RNA was 100 ng/ μ L. The scale bar represents 10 μ m.

To characterize the impact of LAF-1L RNA-helicase activity on the LLPS of RNP granules, additional research was conducted. The previous experiment focusing on the concentration-dependent impact of total RNA on LAF-1L droplet diameter was used as a reference point. Visual LLPS documentation was performed in presence or absence of ATP over a 30-minute time period with 10-minute intervals. ATP is an essential molecule for RNA-helicase enzymatic activity, and its concentration of 25 mM was taken over from the RNA-helicase assay described below (Chapter 3.6.1), where it proved to be sufficient for supporting enzymatic catalysis. Similar to previous quantitation of droplets in DIC images, the obtained values were rounded to whole numbers for consistency.

Visual DIC examination revealed that LAF-1L droplet diameter remained relatively constant without ATP throughout the entire incubation period, while the presence of ATP enhanced droplet growth and assembly (Figure 28). Quantitative evaluation confirmed that the presence of ATP in the mixture led to a constant droplet size with an average diameter of approximately 4 μm throughout the experiment (Figure 29). In contrast, the ATP-free sample exhibited dynamic growth from $4 \pm 1 \mu\text{m}$ at the beginning to $12 \pm 10 \mu\text{m}$ ($n=30$) after 30 minutes of incubation. Samples showed any further droplet increase after 30 minutes incubation (Figure 29). Together this data suggests that RNA integration in LAF-1L droplets occurs continuously in a concentration dependent manner and can be suppressed by ATP molecules.

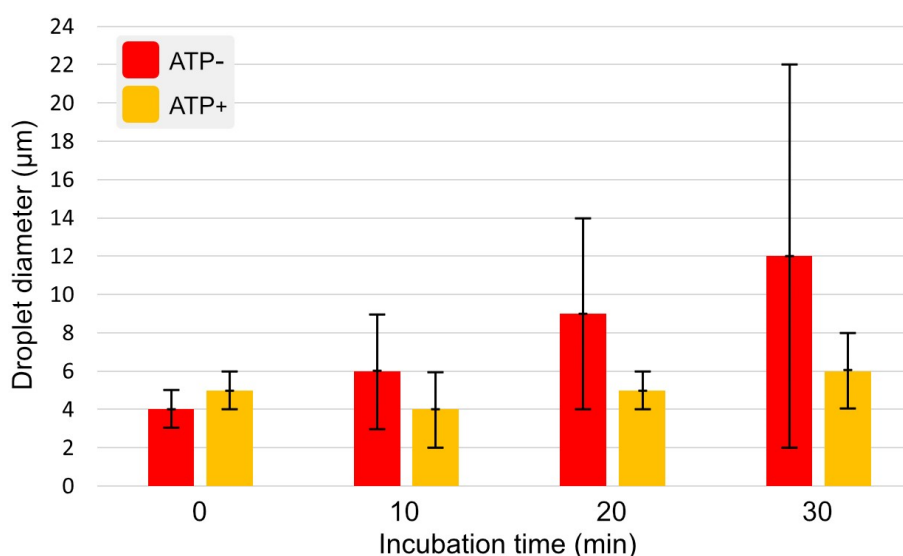


Figure 29. ATP suppresses LAF-1L/RNA droplets growth.

Graph represents a quantified droplet diameter of recombinant LAF-1L/RNA protein droplets in the presence (yellow) and absence (red) of ATP, as shown in Figure 28. Image processing was performed using ImageJ software, and the average values and standard deviations were calculated using a custom Python3 script. The scale bar represents 10 μm . $n=30$ each time point.

The final topic addressed in this chapter is the potential induction of LAF-1S LLPS by total RNA. Based on the fact that both LAF-1L and total RNA molecules have been shown to integrate into LAF-1L droplets and considering that the LAF-1S RGG is likely to have LLPS potential, a hypothesis was established that RNA may assist LAF-1S in forming droplets by combining LAF-1S RGG IDRs.

To test this hypothesis, recombinant LAF-1S and LAF-1L were separately tested in different buffer solutions, and each protein was examined individually. While LAF-1L exhibited droplet formation and growth in the presence of RNA, LAF-1S did not form any droplets in the presence of RNA (Figure 30). Attempts to adjust the NaCl concentration in the range of 100 to 500 with a step of 100 mM, as well as adjusting the RNA concentration from 25 to 125 ng/ μ L with a step of 25 ng/ μ L, did not result in any changes. This behaviour supports the previous hypothesis that DDX3 LLPS primarily depends on protein-protein interactions and cannot be induced by total RNA (Elbaum-Garfinkle et al., 2015), at least in the current experimental setup.

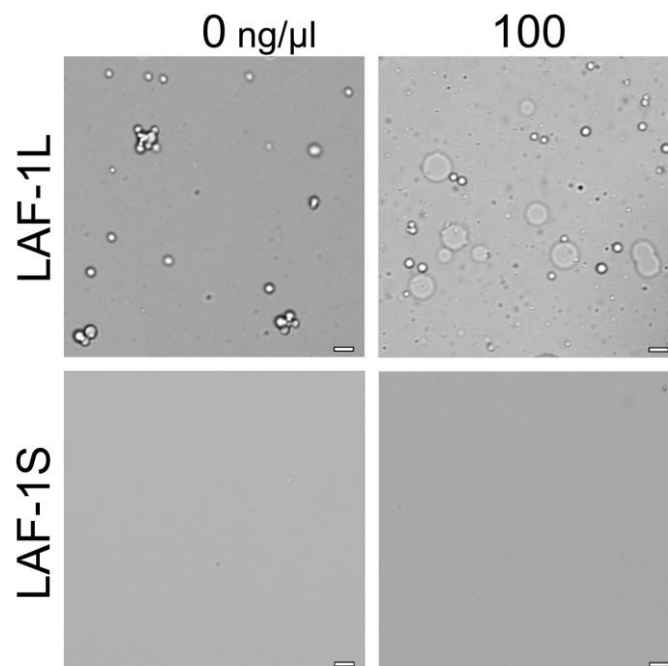


Figure 30. LAF-1S does not form droplets in presence of RNA.

This series of DIC microscopy images represents the RNA-induced enhancement of LLPS in presence of recombinant LAF-1L and no LLPS signs in presence of LAF-1S. LAF-1L experiments were conducted in LAF-1L elution buffer with 500 mM NaCl. LAF-1S experiments were conducted in LAF-1S elution buffer. Each sample was incubated for 30 minutes at room temperature before imaging. Concentrations of LAF-1L and LAF-1S were 6.5 μ M, and the concentration of total RNA was adjusted, according to the legend, in ng/ μ L units. The scale bar represents 10 μ m.

3.5. LAF-1L isomerisation SAXS studies

Primary goal of small-angle X-ray scattering (SAXS) studies was to investigate configuration of LAF-1L complex in presence and absence of RNA substrate. Ongoing state-of-the-art in DDX3 studies suggest that the enzymatically active DDX3/RNP complex contains either two- or three-unit complex (Floor et al., 2016; Song & Ji, 2019). However, both hypotheses were motivated by crystal structures and *in vitro* assays that didn't clarify whether a substrate induces complex assembly or complex forms before RNA binding (Chapter 1.1). All SAXS measurements were performed in collaboration with Dr. Maria Ott (Institute of Biochemistry, MLU).

Since SAXS requires significant amounts of protein (≥ 1 mg/mL) for sufficient scattering intensity, measured samples were solubilised in LAF-1L elution buffer which provided maximal stability of recombinant LAF-1L at 1.2 mg/mL. Such concentration was maximal for LAF-1L protein in SAXS experimental setup. Even though NaCl concentration increase to 1 M could have enhanced protein stability, salt concentration was kept at 650 mM to avoid additional dilutions and because of known LAF-1L affinity to RNA under similar conditions during RNA helicase assay. Measurements were performed for no longer than 2 hours because of continuance LAF-1L aggregation. Preliminary measurements of Trizol extracted total RNA (Figure 31) at 1,250 ng/ μ L concentration (maximal available) showed no scattering and provides a plot identical to buffer. Such observation suggested that any variations between sample plots are caused only by protein conformational changes. Moreover, background signal was excluded from samples plots for clearer comparison.

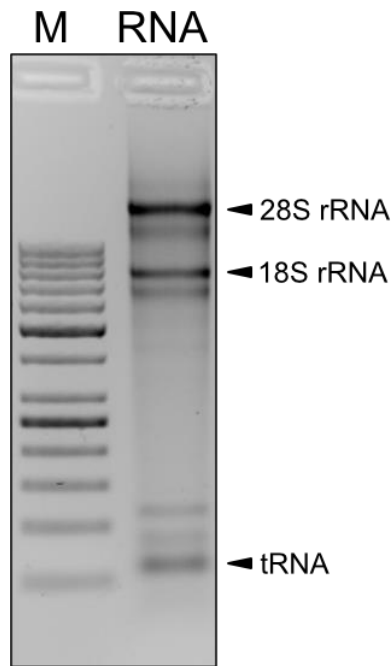


Figure 31. *C. elegans* total RNA has a stereotypical composition after Trizol extraction.

Inverted monochrome image shows a 2% agarose gel containing ethidium bromide exposed to 312 nm UV light. The samples included are as follows: M: 5 μ L of 1 kb Plus DNA Ladder marker (Thermo Scientific). RNA: 1 μ g of *C. elegans* total RNA after Trizol extraction. Major RNA species are indicated on right hand side.

LAF-1L scattering plot signals, generated in two different measurements, showed significant scattering, arguing a folded state of LAF-1L (Figure 32). Furthermore, an increase in scattering induced by total RNA indicates, implied a significant extension of the LAF-1L molecular radius from $52 \pm 1 \text{ \AA}$ to $57 \pm 3 \text{ \AA}$ (Figure 32A). At the same time, IFE-1 and IFE-3 proteins were able to enhance LAF-1L molecular radius to $54 \pm 4 \text{ \AA}$ and $54 \pm 1 \text{ \AA}$ respectively (Figures 32B and 32C). Interestingly, both tested IFE proteins induced a similar enhancement of molecular radius in LAF-1 protomer, indicating a high similarity in studied protein-protein interaction. It is worth pointing out that IFE-1 sample became partially aggregated during SAXS measurement (Figure 32B, left column), which potentially caused an increase in deviation range and scattering plot starting point.

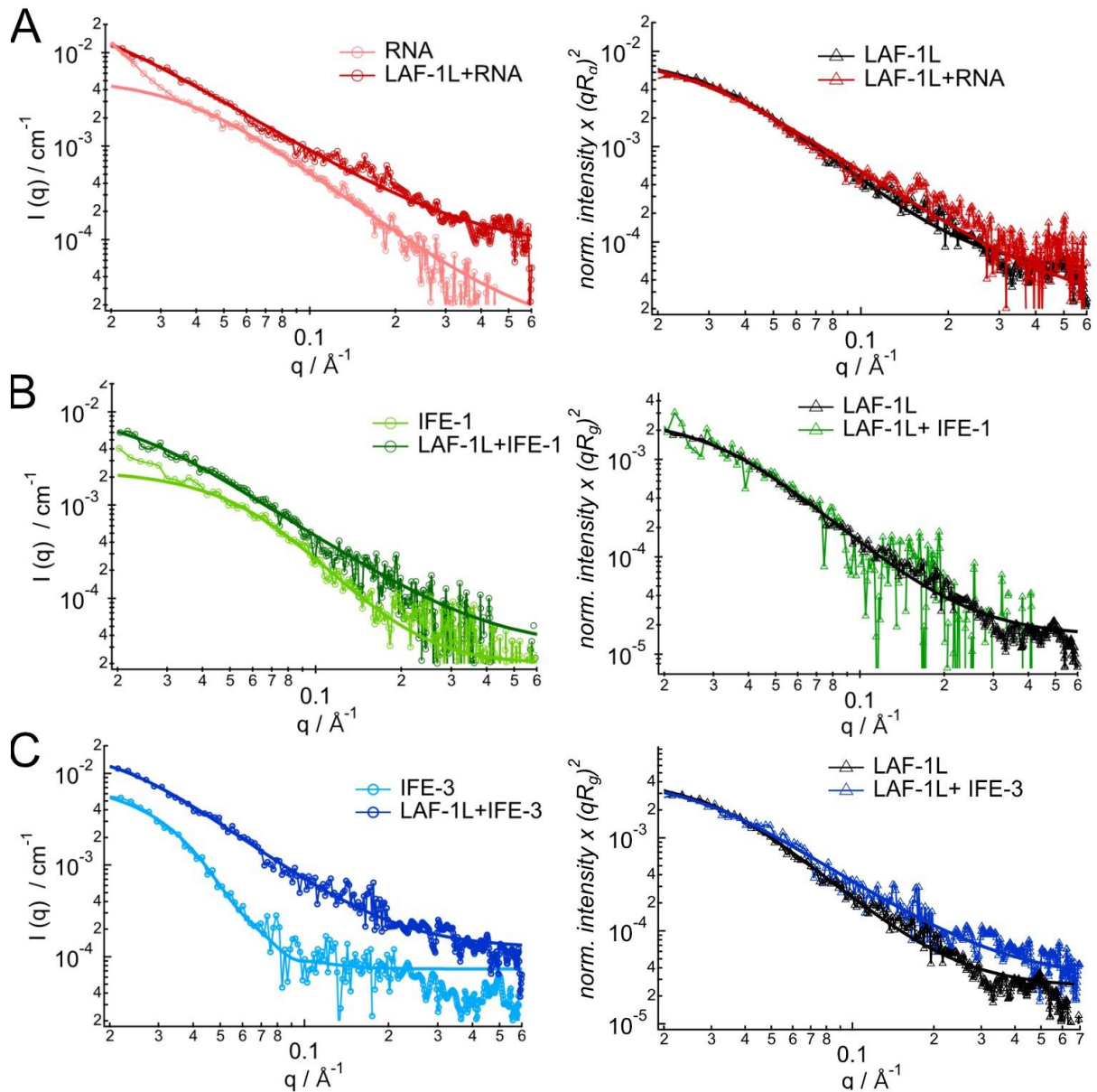


Figure 32. Total RNA and IFE proteins differently increase LAF-1L molecular radius.

Graphical representation of SAXS measurements. (left column) Scattering intensity plot of SAXS, where coordinate axes represent the intensity of scattered X-rays (y-axis) and the scattering vector (q) or momentum transfer (x-axis). (right column) Scattering intensity plots of SAXS in which interaction partner signals were subtracted from those of LAF-1 mixed samples.

Samples: LAF-1L – 1.2 mg/mL of purified recombinant LAF-1L in LAF-1L elution buffer;

A. RNA – 1.25 mg/mL of total *C. elegans* RNA extracted with Trizol; LAF-1L+RNA – 1.0 mg/mL of purified recombinant LAF-1L with 250 ng/ μ L Trizol extracted total *C. elegans* RNA in LAF-1L elution buffer;

B. IFE-1 – 1.0 mg/mL of purified recombinant IFE-1 in IFE-x elution buffer; LAF-1L+IFE-1 – 0.6 mg/mL of purified recombinant LAF-1L with 0.5 mg/mL IFE-1 in 1:1 IFE-x and LAF-1L elution buffers;

C. IFE-3 – 1.1 mg/mL of purified recombinant IFE-3 in IFE-x elution buffer; LAF-1L+IFE-3 – 0.6 mg/mL of purified recombinant LAF-1L with 0.55 mg/mL IFE-3 in 1:1 IFE-x and LAF-1L elution buffers.

Although the obtained data indicates fluctuations in the LAF-1L structure induced by both RNA and IFE proteins (Figure 33), it also highlights no changes in the LAF-1L subunits within the quaternary RNA helicase complex. This suggests that the composition of protomers remains constant, independent of the RNA substrate and IFE interactors. For the same reason, it is not possible to differentiate number of protomers in the RNA helicase complex. Such evaluation would have required scattering data of the monomeric protein state, which was not identified in any of the samples. To confirm the given assumption, the presence of oligomeric state in the tested LAF-1L protein sample was verified through an RNA helicase assay conducted in parallel (Chapter 3.6.2).

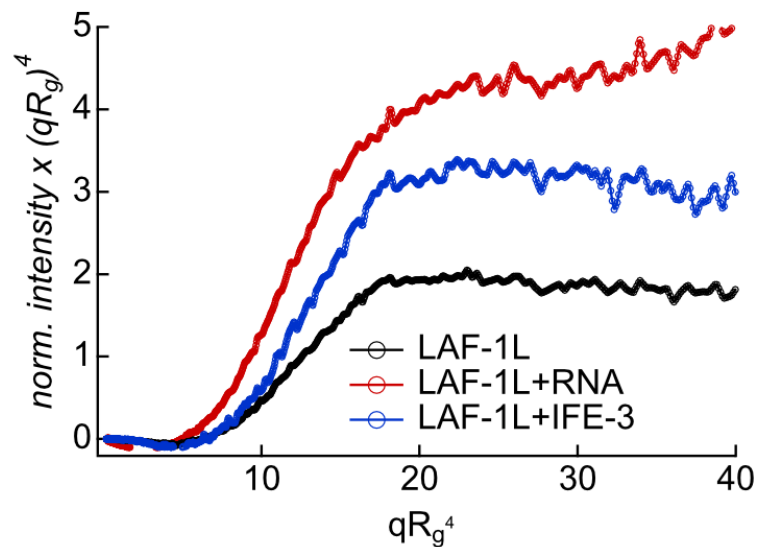


Figure 33. LAF-1L molecular radius.

Porod-Debye plot illustrates the scattering intensity (X axis) as a function of the scattering vector (Y axis) obtained from SAXS measurements of pure and mixed LAF-1 samples shown in Figure 32.

Unfortunately, a more precise evaluation of structural changes in the LAF-1L protein cannot be pursued further due to the limited resolution and time constraints of the available SAXS setup. SAXS data was generated with the help of Dr. Maria Ott (Inst. of Biochemistry & Biotechnology, MLU).

3.6. Enzymatic profile studies of LAF-1 helicase activity

The primary goal of enzymatic studies on LAF-1 was to verify and further characterize the enzymatic profile of LAF-1 as well as adjust the setup of RNA helicase assay for further studies of identified genetic mutants or contributions through IDRs. Since the long isoform of LAF-1 predominates *in vivo* (Figure 10) and shares identical helical domain structure with the short isoform (Figure 6), recombinant LAF-1L protein was selected as the main candidate for an RNA helicase assay. Moreover, to avoid artificial substrate induced bias, a complex mixture of natural RNA species were chosen as substrate for a different type of RNA helicase assay.

3.6.1. Setting up a bulk RNA helicase assay

The adapted helicase assay is based on the capability of an RNA helicase to unwind dsRNA in form of entangled RNA agglomerates upon gradient cooling from +95°C to +20°C in the presence of magnesium ions (Figure 34) (Van Treeck et al., 2018). These RNA aggregates will serve as a substrate for RNA helicases that are able to linearize inter- and intramolecular dsRNA molecules during ATP-dependent catalysis. Due to the significant difference in mass between disaggregated and entangled RNA, they can be differentiated through centrifugation (Figure 35). The separated fractions of supernatant and pellet are then subjected to 2% agarose gel electrophoresis in a TBE system with the presence of an RNA dye, followed by quantification based on the signal from the RNA dye. In this work, ethidium bromide was added to the agarose gel at a final concentration of 1 µg/mL and exposed to 312 nm UV light after electrophoresis. Although ethidium bromide is a standard DNA dye that intercalates into double helix structures, it can also associate with single-stranded RNA molecules at higher concentrations.

Two controls were introduced to validate the RNA substrate and assay (Figure 35). The positive control involved treating aggregated RNA with a temperature of +95°C for a specific duration and immediately placing it on ice. This treatment unwinds the RNA aggregates and mimics the conversion of the RNA helicase substrate. Some batches of entangled RNA showed limited disaggregation, which may be a consequence of RNA overentangling during the preparation for the helicase assay. Although the exact reason for this phenomenon was not identified, the introduction of the positive control helped in eliminating defective batches of

entangled RNA. The negative control consisted of entangled RNA particles that had neither been treated by high temperature nor RNA helicases.

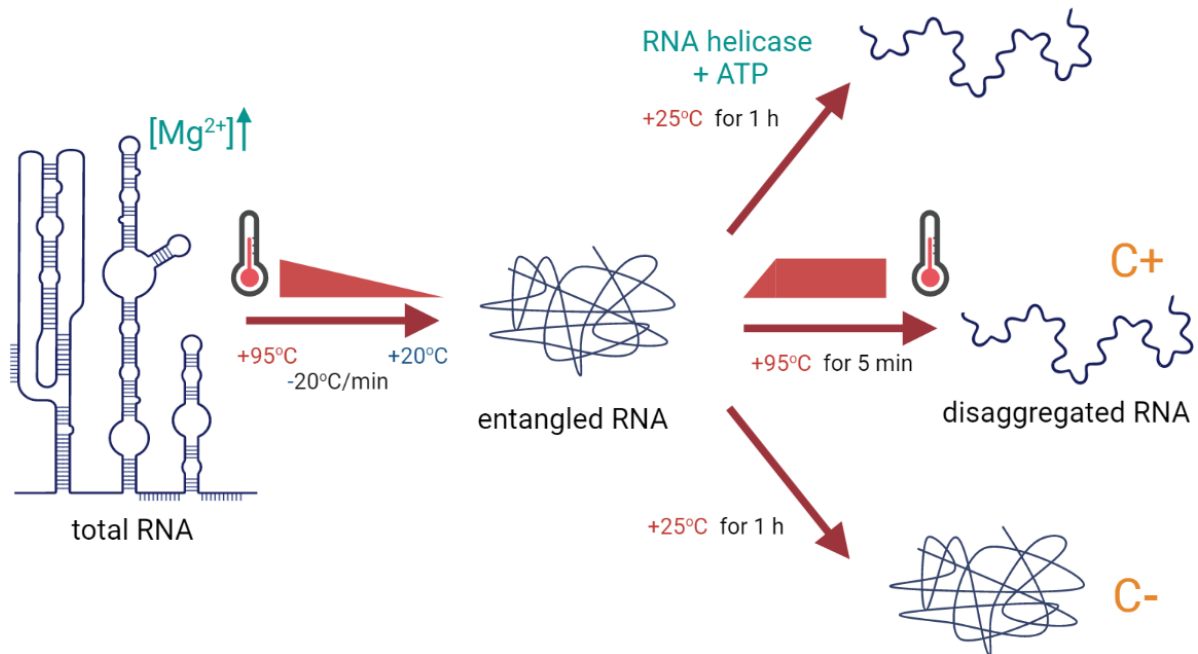


Figure 34. Schematic representation of the established bulk RNA helicase assay.

Total RNA containing some secondary structural elements are entangled into a precipitable material, when subjected to a downward heat gradient from +95 to +20°C in the presence of Mg^{2+} ions (C-). Such RNA aggregates are disentangled either by excessive heat (C+) or with the help of RNA helicases and ATP.

Trizol extraction of total RNA from *C. elegans* adult nematodes was chosen due to high yield of total RNA. However, preliminary tests revealed that such total RNA from *C. elegans* does not efficiently precipitate under conditions adjusted for total RNA from human cancer tissue culture (Van Treeck et al., 2018). Hence adjustments were necessary and primarily focused on RNA and $MgCl_2$ concentrations, as these parameters contribute the most to RNA entanglement. The final concentration for total RNA was set in the range from 50 to 250 ng/ μ L in the presence of 20 mM $MgCl_2$ instead of 5 mM original concentration. Comparing RNA distributions between pellet and supernatant fractions as well as input RNA quality control, evaluated using a 1% ethidium bromide agarose gel signal quantification, this setup allowed for approximately 75% conversion of total RNA into the aggregated form.

A series of tests determined that 250 ng of the entangled substrate was the optimal amount of RNA to be visualized on an ethidium bromide gel after partial helical unwinding in both the pellet and supernatant fractions (Figure 35). Additionally, this quantity of RNA did not result in an excessive number of overexposed pixels in RNA-dense areas, thereby reducing

the error rate during digital analysis of the final gel image. To minimize slight variations between RNA input batches, any substrate with $\leq 80\%$ solubilization in positive control heat disentangled samples were discarded. Furthermore, each subset of RNA helicase assays was performed using the same batch of tangled RNA. A typical batch quality analysis is shown in Figure 35.

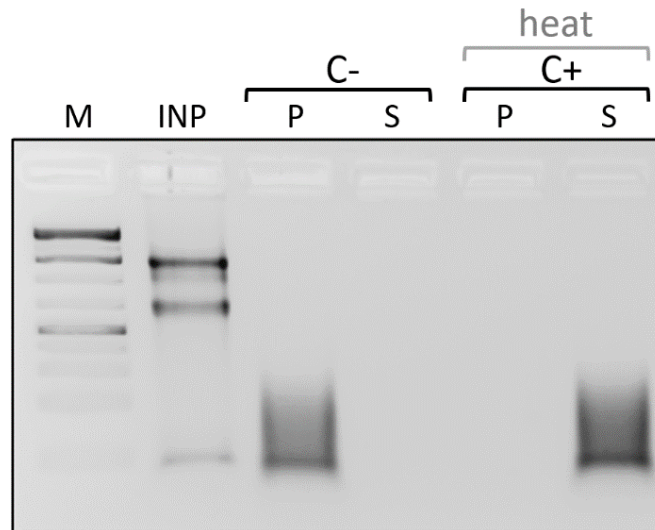
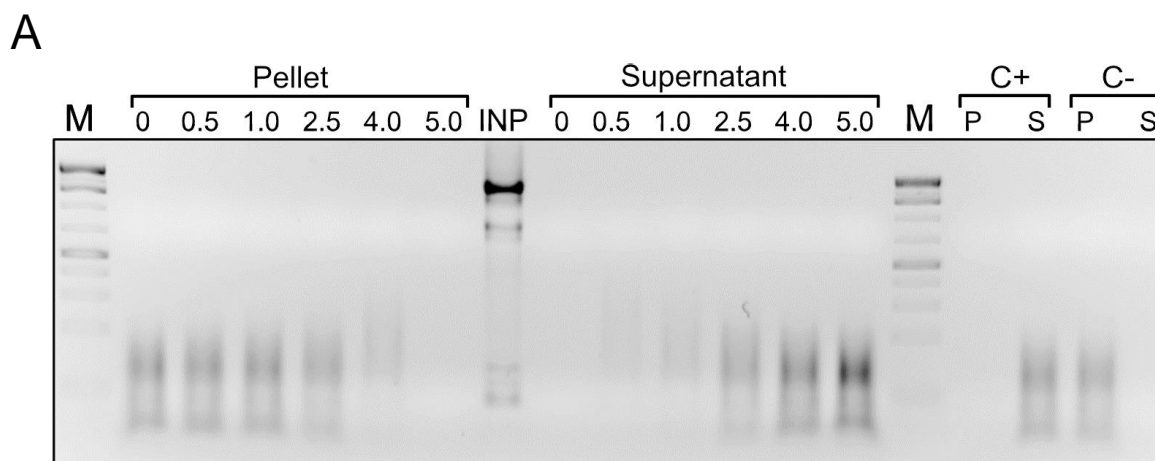


Figure 35. Quality control of entangled RNA as a substrate for RNA helicase assays.

Inverted monochrome image of a 2% agarose gel containing ethidium bromide exposed to 312 nm UV light. Samples: M: 5 μ L of 1 kb Plus DNA Ladder marker (Thermo Scientific). INP: 250 ng of Trizol-extracted *C. elegans* total RNA used as substrate input material for the RNA helicase assay. Pellet (P) and supernatant (S) samples of entangled (C-) and heat-mediated disentangled RNA (C+).

Preliminary tests demonstrated that 10 μ M of LAF-1L is capable of fully unwinding 250 ng of entangled RNA in the presence of 25 mM ATP during a 1-hour incubation at +25 $^{\circ}$ C, which is the maximal physiological temperature of *C. elegans*. The original RNA helicase assay was initially performed at +37 $^{\circ}$ C; however, due to physiological restrictions of the organism *C. elegans*, the temperature was reduced to +25 $^{\circ}$ C. Another primary test revealed that, out of six concentrations, approximately 5-6 μ M is the minimal concentration of recombinant LAF-1L required to solubilize 250 ng of entangled RNA during a 1-hour incubation at +25 $^{\circ}$ C (Figure 36). Therefore 5 μ M of enzyme was set as the maximum concentration value for enzymatic profiling of LAF-1 proteins. Contrary to the original protocol, an ATP recovery system was not required and, therefore, also not implemented.



B

| Sample | P | S | Total | P% | S% |
|--------|------------|------------|------------|--------|--------|
| 0.0 | 18,906,616 | 6 | 18,906,622 | 100.00 | 0.00 |
| 0.5 | 22,906,593 | 1,335,758 | 24,242,351 | 94.49 | 5.51 |
| 1.0 | 26,429,151 | 5,403,019 | 31,832,170 | 83.03 | 16.97 |
| 2.5 | 17,133,771 | 25,514,517 | 42,648,288 | 40.17 | 59.83 |
| 4.0 | 4,396,965 | 52,082,845 | 56,479,810 | 7.79 | 92.21 |
| 5.0 | 16,459 | 65,759,293 | 65,775,752 | 0.03 | 99.97 |
| C- | 10,876,323 | 0 | 10,876,323 | 100.00 | 0.00 |
| C+ | 0 | 22,194,753 | 22,194,753 | 0.00 | 100.00 |
| Input | 0 | 40,288,872 | 40,288,872 | 0.00 | 100.00 |

Figure 36. LAF-1L RNA helicase unwinds entangled RNA substrate in a concentration-dependent manner.

A. Inverted monochrome image of a 2% agarose gel containing ethidium bromide exposed to 312 nm UV light. M: 5 μ L of 1 kb Plus DNA Ladder marker (Thermo Scientific); INP: 250 ng of Trizol-extracted total RNA substrate used as input material for helicase assay substrate; Pellet (P) and supernatant (S) samples represent the separated entangled and unwound RNA after the RNA helicase assay with recombinant LAF-1L protein in a concentration range from 0 to 5 μ M. C+ and C- are the positive and negative controls of the RNA helicase assay substrate, respectively.

B. Image quantification of absolute and relative (in percent) pixel intensity after a series of LAF-1L dilutions in the RNA helicase assay. Pellet (P) and supernatant (S) values were taken from figure 36A.

Although the general trend of RNA abundance in the pellet and supernatant fractions showed a direct correlation with LAF-1L concentration, the absolute values varied significantly between samples (Figure 36B). This variation was presumably caused by the known property of ethidium bromide to bind RNA in a non-linear and RNA concentration-independent manner. To compensate for this effect, relative values in percentage corresponding to pellet and supernatant samples was preferred over the absolute values of total pixel density units. The

aforementioned characteristics form an additional abstraction layer, which makes the current assay a suboptimal choice for high-precision RNA helicase profiling. Rather, it should be interpreted as a universal tool for RNA helicase profiling.

The RNA distribution in the pellet and supernatant fractions was quantified based on three batches of recombinant LAF-1L RNA helicase assay samples after agarose gel electrophoresis (Figure 37). The previous observation that 5 μM of LAF-1L is the minimal quantity capable of fully unwinding a total of 250 ng of RNA substrate was confirmed. Therefore, a concentration of 5 μM of LAF-1L variants was used for further research. The graph exhibits a stereotypical sigmoidal shape with linear progression in the range of 1.0 to 4.0 μM of LAF-1L concentration.

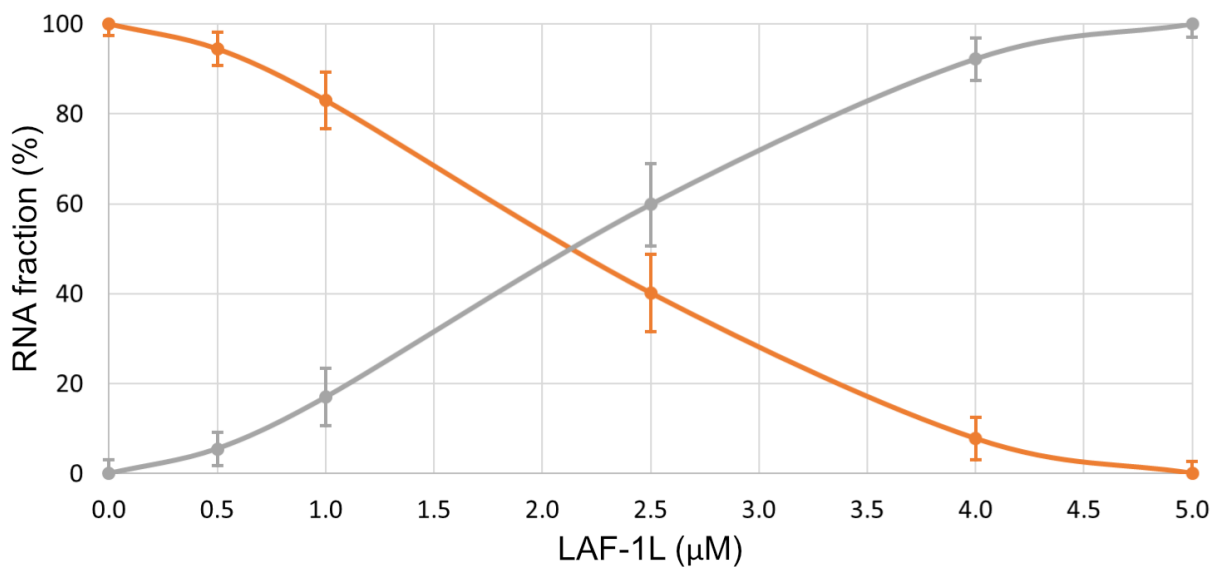


Figure 37 The progress curves of RNA substrate abundance in the pellet and supernatant fractions after the RNA helicase assay with LAF-1L protein.

This graph represents the numeric evaluations of RNA substrate abundance after the RNA helicase assay of recombinant LAF-1 protein in a concentration range from 0 to 5 μM , presented in Figure 36B. The quantification of RNA-associated ethidium bromide was performed using ImageJ software; Average values and standard deviation values were calculated using a custom Python3 script; $n=3$.

3.6.2. LAF-1L is an ATP-dependent RNA helicase

The first series of RNA helicase assays addressed the hypothesis that both long and short isoforms of LAF-1 presumably share a similar helicase profile due to their assumed identically folded DDX3 RNA helicase domain and partial sequence similarity across the N-terminal IDR, which is known for LAF-1L to possess RNA affinity (Kim & Myong, 2016). The preformed experiments showed a complete enzymatic conversion of the RNA substrate into the unwound form in both short and long LAF-1 isoform samples, paralleling the positive control (Figure 38). Since the implemented helicase assay utilizes a broad variety of entangled RNA substrates, only a similarity in total enzymatic activity can be determined without considering potential individual selectivity criteria of LAF-1L and LAF-1S.

Additional research was conducted to confirm the ATP-dependent nature of LAF-1L RNA helicase activity. The absence of ATP fully compromised the enzymatic activity of the LAF-1L protein, resulting in a distribution of RNA in the pellet and supernatant fractions that is identical to the negative control (Figure 38). This confirms the ATP dependency of LAF-1L RNA helicase enzymatic catalysis.

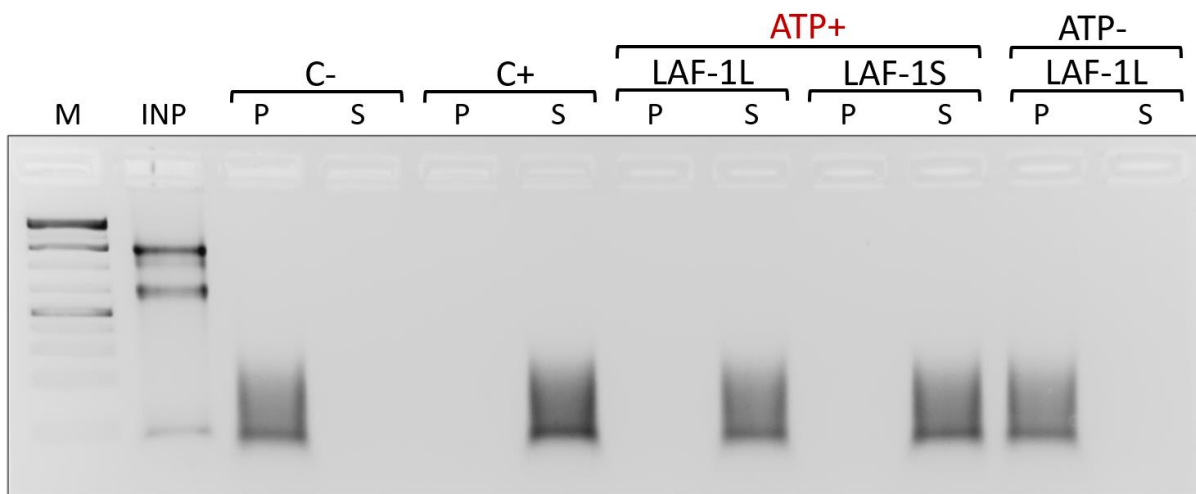


Figure 38. Both LAF-1L and LAF-1S proteins are ATP-dependent RNA helicases.

Inverted monochrome image of an ethidium bromide stained 2% agarose gel: M: 5 μ L of 1 kb Plus DNA Ladder marker (Thermo Scientific). INP: 250 ng helicase assay substrate RNA. Pellet (P) and supernatant (S) samples represent the separated entangled and unwound RNA after an RNA helicase assay was carried out in the presence of recombinant LAF-1L and LAF-1S proteins at a concentration of 5 μ M. ATP+ and ATP- labels indicate the presence or absence of 25 mM ATP in the reaction buffer, respectively. C+ and C- are the positive and negative controls of the RNA helicase assay substrate, respectively.

3.6.3. Genetically identified mutant LAF-1 proteins lack RNA helicase activity and interfere with wild-type LAF-1

Further research was conducted to investigate the documented lethal and feminizing phenotype of homozygous individuals with missense mutations in the *laf-1* locus: *q80* (R426C), *q217* (M430I), and *q267* (T434I) (Hubert & Anderson, 2009). All three *laf-1* alleles were discovered in a genetic suppression screen, displaying a dominant behaviour in a heterozygous state (Kuwabara et al., 1998). Since the *q267* mutation affects the identity of an amino acid within the SAT motif (432-434), and both *q80* and *q217* mutations are located in close proximity to it, the prevailing hypothesis suggested that each of these three mutations interferes with the biological function of the SAT motif in LAF-1. The SAT motif of DDX RNA helicases is known to mediate communication between the ATP- and RNA-binding sites by binding the γ -phosphate of ATP (De Colibus et al., 2022). To discover their mutational impact on LAF-1L proteins, RNA helicase assays were performed on recombinant mutant protein. None of the mutations showed any signs of RNA helicase activity in the standard *in vitro* setup (Figure 39). Batches that contained minor signs of enzymatic activity of mutated proteins (<25% RNA in the supernatant fraction) had a similar soluble RNA content in negative control samples and, therefore, were considered artefacts caused by less stable RNA substrates.

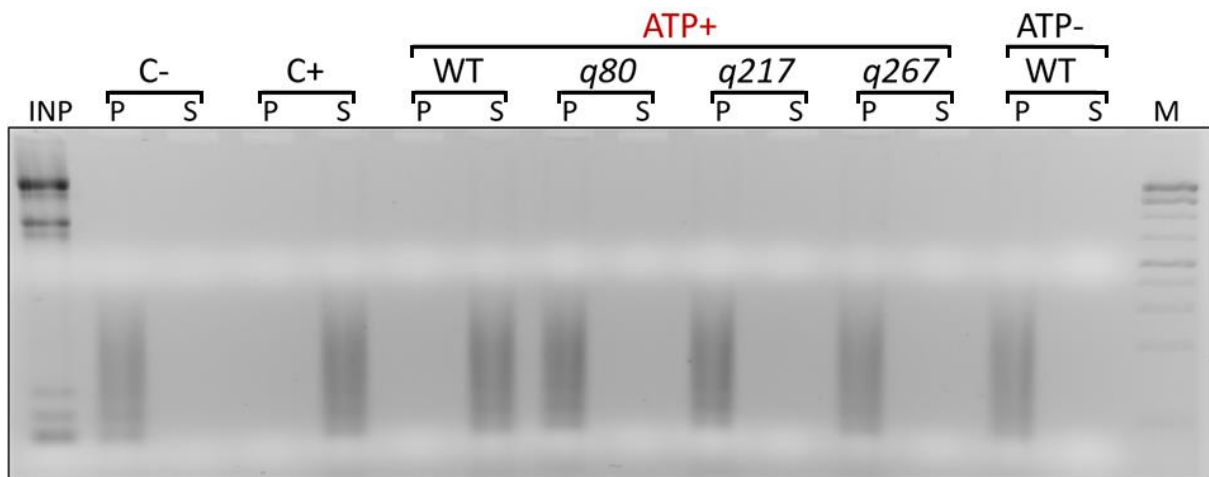


Figure 39. Genetic mutations in recombinant LAF-1L compromise RNA helicase activity.

Inverted monochrome image of a 2% agarose gel with following samples: M – 5 μ L of 1 kb Plus DNA Ladder marker (Thermo Scientific). INP – 250 ng RNA helicase assay substrate. Pellet (P) and supernatant (S) samples after the RNA helicase assay using recombinant wild type (WT) LAF-1L, *q267* mutant and BSA at a total concentration of 5 μ M. Other label as in Figure 38.

The second aspect of this research aimed at investigating the molecular mechanism behind the feminizing phenotype in heterozygous individuals with *q80*, *q217*, and *q267* mutations (Hubert & Anderson, 2009). Normally, the presence of a wild-type allele rescues the dysfunctional effect of a mutated gene, resulting in little to no phenotype in heterozygous individuals. However, in the case of *q80*, *q217*, and *q267* mutations, the phenotype is more comparable to homozygotes, suggesting that the mutated gene has an impact on the wild-type allele. To simulate the heterozygous state of the *laf-1* gene, equal concentrations of 2.5 μ M of *q267* mutated and wild-type (WT) LAF-1L proteins were combined (WT/*q267*). As a reference sample with a non-interfering protein, 2.5 μ M of LAF-1L together with 2.5 μ M of BSA (WT/BSA) was tested. This additional control should reflect the unaffected RNA helicase activity of 2.5 μ M LAF-1L at an equal protein concentration as the “hemizygote” sample. From a visual inspection of the agarose gel image, it appears that WT/BSA exhibited higher RNA helicase potency compared to the WT/*q267* sample (Figure 40).

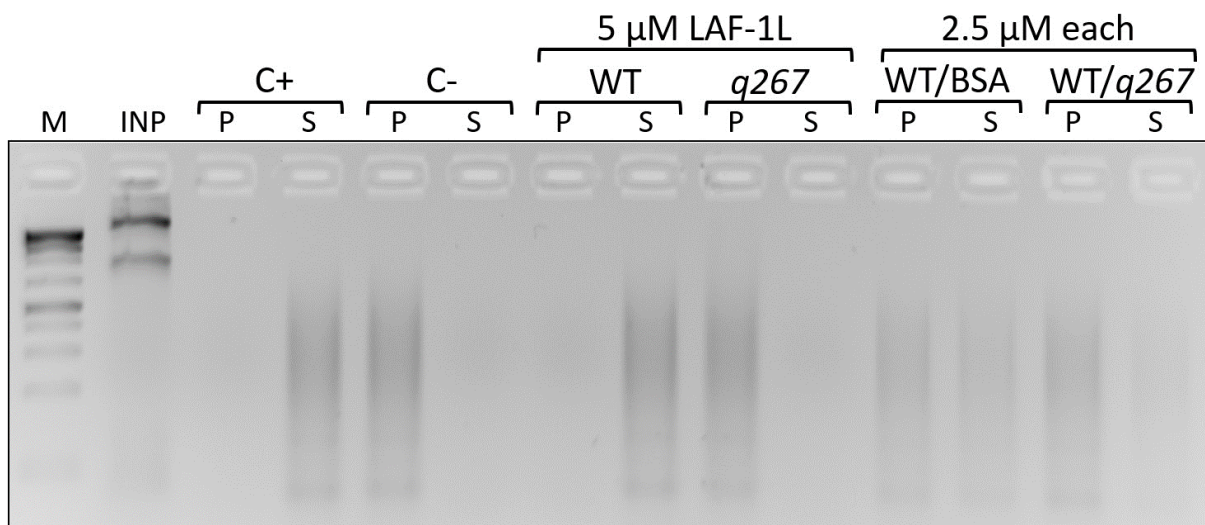


Figure 40. Wild type LAF-1L has different RNA helicase profile in the presence of BSA and the *q267* mutant.

Inverted monochrome image of a 2% agarose gel containing ethidium bromide exposed to 312 nm UV light. Samples: M - 5 μ L of 1 kb Plus DNA Ladder marker (Thermo Scientific); INP - 250 ng of Trizol-extracted total RNA used as input material for the preparation of the helicase assay substrate; Pellet (P) and supernatant (S) samples representing separated entangled or unwound RNA after the RNA helicase assay (Chapter 2.3.13) in presence of recombinant wild type (WT) LAF-1L, *q267* mutant and BSA at a total concentration of 5 μ M. Mixed samples of WT with *q267* and BSA contained 2.5 μ M pf each protein; C+ and C- are the positive and negative controls of the RNA helicase assay substrate, respectively.

A quantitative evaluation of several agarose gel images (n=3) confirmed that the average distribution of RNA in the pellet and supernatant fractions of WT/*q267* samples was 81±4% and 19±4%, respectively, under the same experimental conditions (Figure 41). In contrast, WT/BSA samples exhibited values of 48±5% and 52±5% for the pellet and supernatant fractions, respectively (Figure 41). Furthermore, the WT values were similar to those of the positive control, while *q267* mutated LAF-1L approached the values of the negative control.

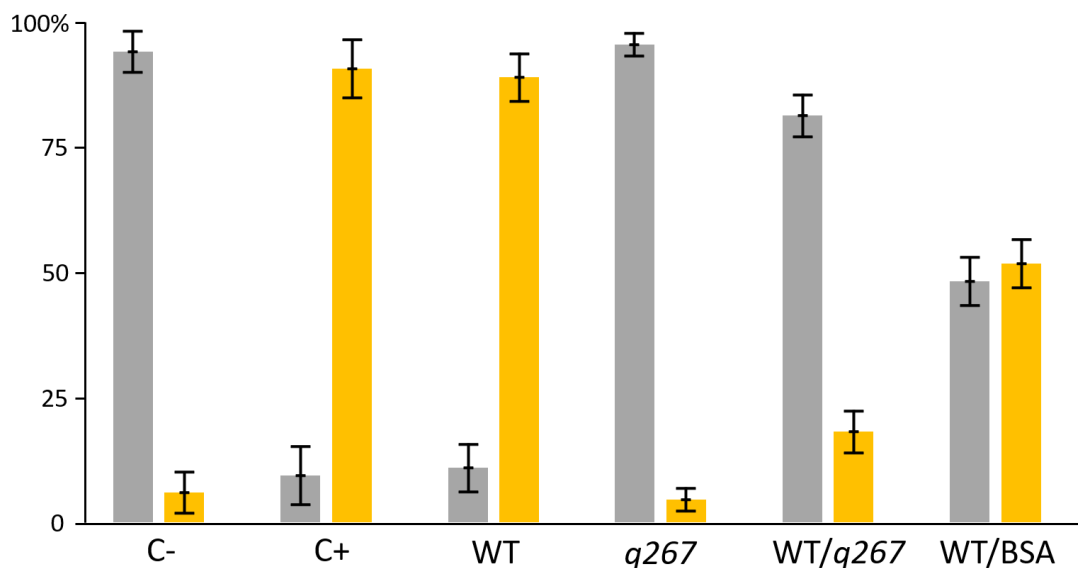


Figure 41. The *q267*LAF-1L mutant suppresses the RNA helicase activity of the wild-type protein.

This bar graph represents the average abundance of RNA in the pellet (grey bars) and supernatant (orange bars) after the RNA helicase assay using 5 μ M concentrations of wild-type LAF-1L (WT) and the *q267* LAF-1L mutant proteins, as well as 2.5 μ M mixtures of WT with *q267* and WT with BSA. Image processing of 2% agarose gels as seen in Figure 40 (n=3) was performed using ImageJ software, and the average values and standard deviation values were calculated using a custom Python3 script.

A potential mechanism for such interfering phenomena can be derived from the dimeric crystal structure of human DDX3X, which suggests the presence of two functional proteins in a dimer to catalyse the unwinding of double-stranded RNA chains (Song & Ji, 2019). In the case of dimerization involving two compromised units or a combination of one compromised and one functional unit, the assembled RNP complex is unable to unwind double-stranded RNA and either remains static or disassembles under environmental conditions (Figure 42). In this hypothetical scenario, only 25% of the dimers are predicted to be capable of catalysing RNA unwinding under ideal conditions. Considering the potential obstacles caused by interference with aggregated RNA occupied by dysfunctional dimers and previously mentioned

data processing artefacts (Chapter 3.6.1), it is suggested that this 25% prediction may be even further reduced. The obtained values of the WT/*q267* (19±4%) and WT/BSA (52±5%) supernatant fractions, along with the known crystal structure of the human ortholog of DDX3, support the presence of a valid molecular RNA helicase mechanism for LAF-1 in a suggested dimer model (Figure 42).

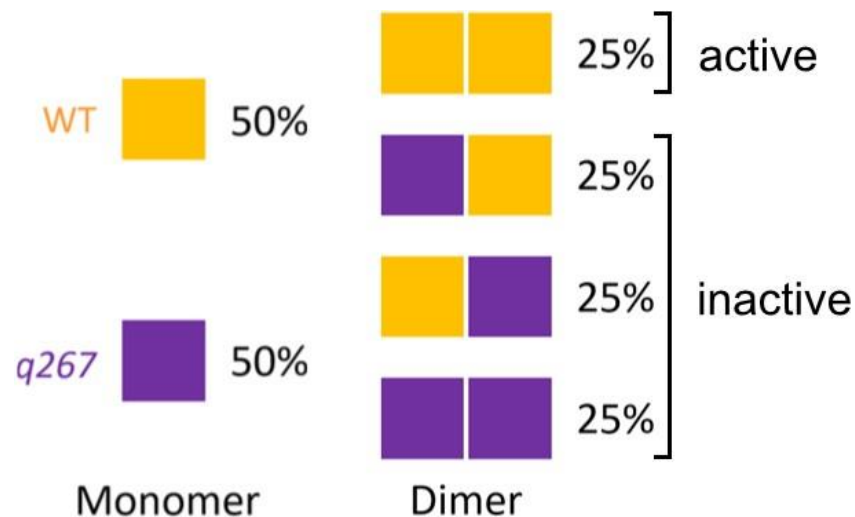


Figure 42. All dimers containing mutated protein are dysfunctional.

The schematic image of active RNA helicases in monomeric and dimeric complexes of active WT (orange) and inactive *q267* mutated (purple) LAF-1L proteins.

It is worth mentioning that trimeric and tetrameric complexes are expected to have 11% and 6% of active enzymatic units, respectively, under the suggested conditions. However, as there were no additional data points suggesting such a structural organization of LAF-1L and none of the DDX3 RNA helicases have been reported to form these types of quaternary protein complexes, this hypothesis was not further investigated.

3.6.4. mAb BW75 compromises LAF-1 activity

To investigate a potential impact of antibodies used in IP experiments on LAF-1 enzymatic activity, the RNA helicase assay was also conducted in the presence of the most prominent mAb BW75 candidate, which at the time when this research had been conducted was not known to have specificity for the folded domain of LAF-1. As a control sample, mAb BF30 of unidentified target specificity was added (Chapter 3.1.1, Figure 8). The concentrations of the antibodies were set at 1 µM, which was predicted to be sufficient for binding to 80% of

recombinant LAF-1L. Upon visual inspection, a notable difference in the distribution of the RNA substrate between the BW75 and BF30 samples, as well as the positive control was apparent in an initial experiment (Figure 43). Both mAb samples exhibited to varying degrees a negative effect on the RNA helicase activity of LAF-1L protein.

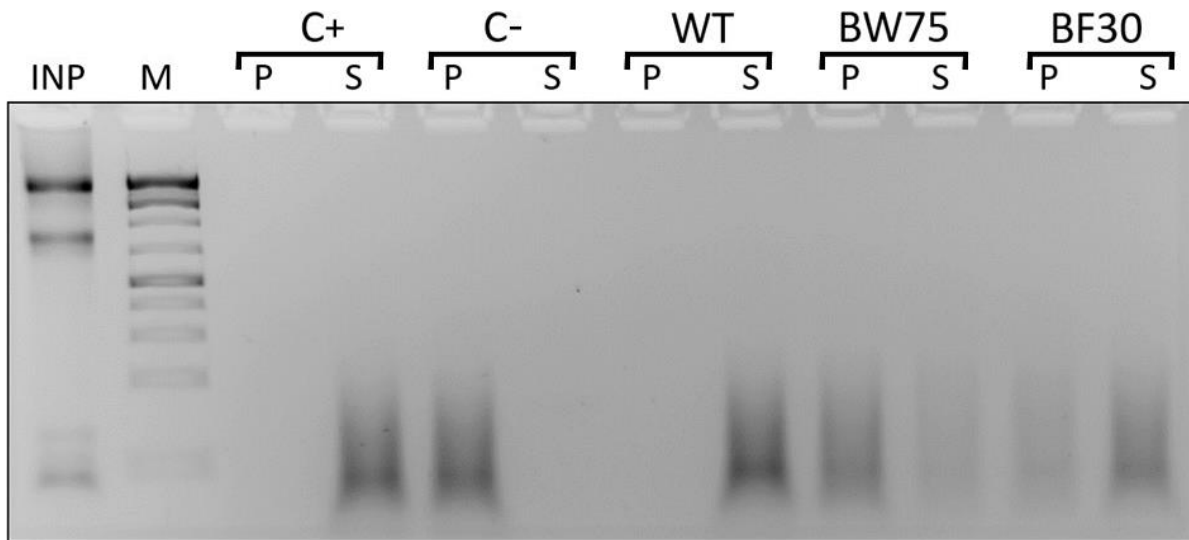


Figure 43. Anti-LAF-1 mAb BW75 partially suppresses the enzymatic activity of the LAF-1L.

Inverted monochrome image shows a 2% agarose gel containing ethidium bromide exposed to 312 nm UV light. Samples are as follows: M – 5 μ L of 1 kb Plus DNA Ladder marker (Thermo Scientific). INP – 250 ng of RNA helicase substrate. Pellet (P) and supernatant (S) samples represent the separated entangled and unwound RNA after the RNA helicase assay in the presence of recombinant wild type (WT) LAF-1L, either incubated with 0.15 mg/mL (1 μ M) of anti-LAF-1 BW75 mAb or unspecific mAb BF30. C+ and C- are the positive and negative controls of the RNA helicase assay substrate, respectively.

Image quantification from three individual experiments confirmed that RNA abundance in the pellet and supernatant fractions after RNA helicase assays in the presence of mAb BW75 was $36\pm 3\%$ and $64\pm 3\%$ ($n=3$), respectively, while mAb BF30 samples had $61\pm 5\%$ and $39\pm 5\%$, respectively (Figure 44). By contrast, the positive control and WT samples accumulated $99\pm 1\%$ in the supernatant fraction with this batch of RNA ($n=3$). This data suggests that the anti-LAF-1 mAb BW75 has an inhibitory effect on the RNA helicase activity of LAF-1L. As it targets an essential aspect of LAF-1's molecular function, it may also interfere with potential protein or RNA interaction partners that are connected to LAF-1's RNA helicase activity.

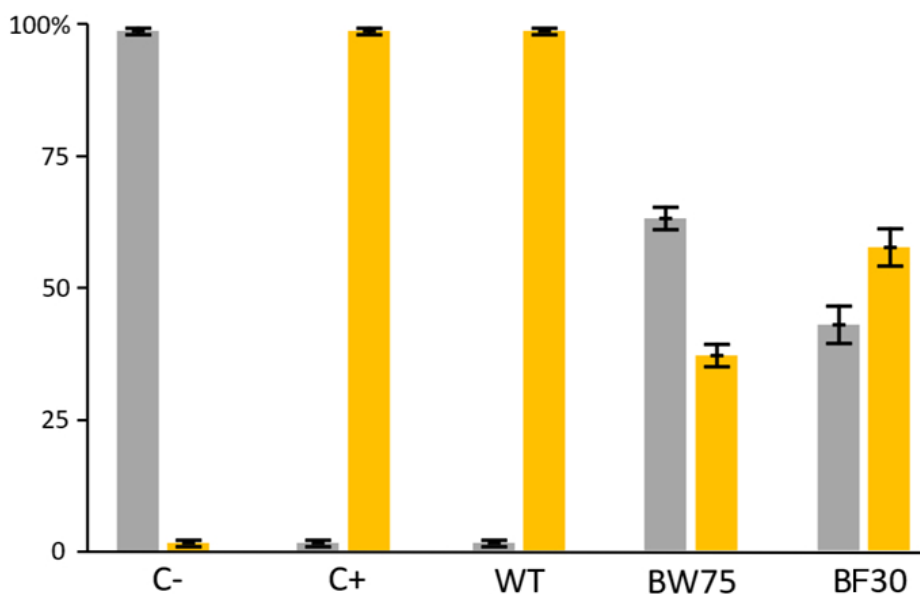


Figure 44. The Anti-LAF-1 BW75 mAb significantly compromises the helicase activity of the recombinant LAF-1L protein.

Bar graph represents the average abundance of RNA in the pellet and supernatant after the RNA helicase assay using a 5 μM concentration of wild-type LAF-1L (WT), as well as WT samples incubated with 0.15 mg/mL (1 μM) of anti-LAF-1 BW75 mAb and unspecific BF30 mAb. RNA sample values were quantified based on the RNA-associated ethidium bromide signals from 2% agarose gel electrophoresis (n=3 each). Image processing was performed using ImageJ software; average and standard deviation values were calculated using a custom Python3 script.

3.6.5. Contribution of either IDR to LAF-1L helicase activity

Further research focused on investigation of either IDR's contributions to RNA helicase activity of LAF-1L. The primary goal of investigation was to reveal an impact of IDR truncation on enzymatic activity as well as a possible effect on WT protomers in dimers, as it was shown for the *q267* mutant protein. This is why, the previous experimental setup with recombinant WT an *q267* mutant was taken as a reference point.

A first series of experiments was performed using recombinant ΔRGG ($\Delta 2\text{-}191$) LAF-1L (Figure 45). In addition to individual tests at 5 μM concentration, both protein variants were combined and tested in a mixture of 2.5 μM each. In contrast to full-length LAF-1L, N-terminal IDR-truncated LAF-1L showed little to no RNA helicase activity (Figure 45A), suggesting that the N-terminal RGG-rich IDR of LAF-1 is essential for its enzymatic helicase function. A similar reduction of helicase activity in mixed WT/ ΔRGG samples was considered to be caused

by suppression of WT LAF-1L through a truncated protein isoform in a dimer complex (Figure 45A), arguing that LAF-1L missing its RGG-IDR acts like a helicase dead molecule.

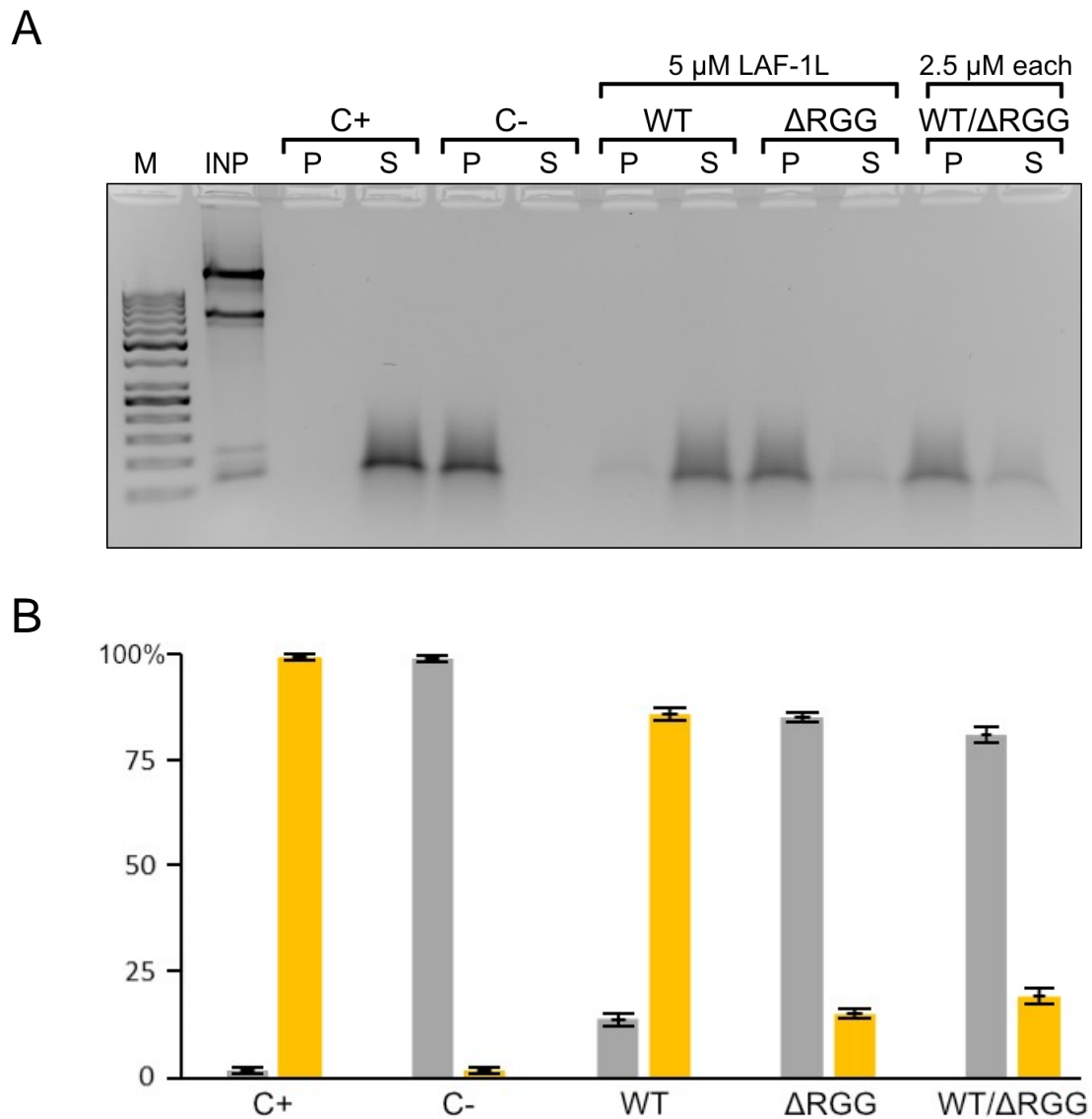


Figure 45. N-terminal RGG IDR is essential for RNA helicase activity of recombinant LAF-1L protein.

A. Inverted monochrome image of a 2% agarose gel. Samples: M – 5 μ L of 1 kb Plus DNA Ladder marker (Thermo Scientific); INP – 250 ng RNA substrate; Pellet (P) and supernatant (S) samples in presence of recombinant wild type (WT) LAF-1L and Δ RGG (Δ 2-191) LAF-1L mutant protein at a total concentration of 5 μ M. Mixed samples of WT with Δ RGG contained 2.5 μ M of each protein. Remaining labels as above (e.g. Figure 38).

B. Bar graph representing the average abundance of RNA in the pellet (grey bars) and supernatant (orange bars) after the RNA helicase assay. RNA samples were quantified based on the RNA-associated ethidium bromide signal under 312 nm UV light. Image processing was performed using ImageJ software; average and standard deviation values were calculated using a custom Python3 script, n=3 each.

Image processing of three replicates revealed a $99\pm 1\%$ transformation of the entangled RNA into a soluble form in the positive control sample (C+) (Figure 45B). At the same time, the negative control (C-) retained $99\pm 1\%$ of the RNA substrate in the pellet fraction, confirming RNA batch sustainability. The WT LAF-1 converted $86\pm 3\%$ of the substrate into a soluble form (Figure 45B), which is comparable to the amount observed previously. In contrast, the Δ RGG LAF-1L solubilized only $15\pm 2\%$ of the RNA (Figure 45B), approaching the values of the enzymatically inactive *q267* mutant. The mixed sample showed only $19\pm 4\%$ RNA-helicase linearization, with $81\pm 4\%$ of the RNA remaining insoluble. The obtained values are identical to the WT/*q267* results, making them valid comparison samples, further strengthening the conclusion that the RGG domain is essential and assists RNA helicase activity.

The smearing pattern of RNA in IDR truncated LAF-1L samples as shown in Figure 46 was less broad compared to previous samples (Figure 40). This effect was likely caused by reducing the gel runtime to 10-15 minutes at 15 V/cm on the agarose gel. While this made the pattern less visually appealing, it also made it less prone to background artefacts during the final digital image quantification. Since image quality was the main concern during the RNA-helicase assay, the agarose gel running conditions were frequently adjusted for gels that could have potentially caused distortions during pixel data collection.

After processing the RNA-helicase assay data for the recombinant Δ RGG construct, an additional research goal concerning the Δ GQ LAF-1 protein was established. Based on the 6O5F crystal structure of truncated LAF-1 in the presence of double-helix RNA both terminal IDR sequences are expected to be in close proximity to the same IDRs of a second DDX3X protomer after RNA-binding (Figure 4.B) (Song & Ji, 2019). Such a dimeric configuration suggests a potential interaction between two LAF-1 protomers might be mediated not only by the folded domain but also by one of the terminal IDR sequences.

This implies that the deletion of such an IDR should decrease the quaternary structure stability of the LAF-1 dimer, predicting a shorter lifespan for such a configuration. Conversely, native dimers with WT IDRs should have a longer duration due to the additional contribution of IDRs to complex integrity. Therefore, the study of Δ GQ (Δ 623-708) LAF-1L RNA-helicase can serve both for characterizing the GQ IDR as an RNA-helicase relevant domain and for understanding the sequence involved in LAF-1 dimer stabilization.

To achieve this, mixed samples of WT LAF-1L with truncated terminal IDRs should be further compared with inactive helicase domain (*q267*) containing WT IDR sequences. This

comparison aims to identify the least stable dimer. Any observed RNA-helicase activity above that of *q267* is predicted to indicate lower stability of dimers with truncated IDRs, resulting in a longer average duration of functional WT dimers compared to Δ IDR dimers.

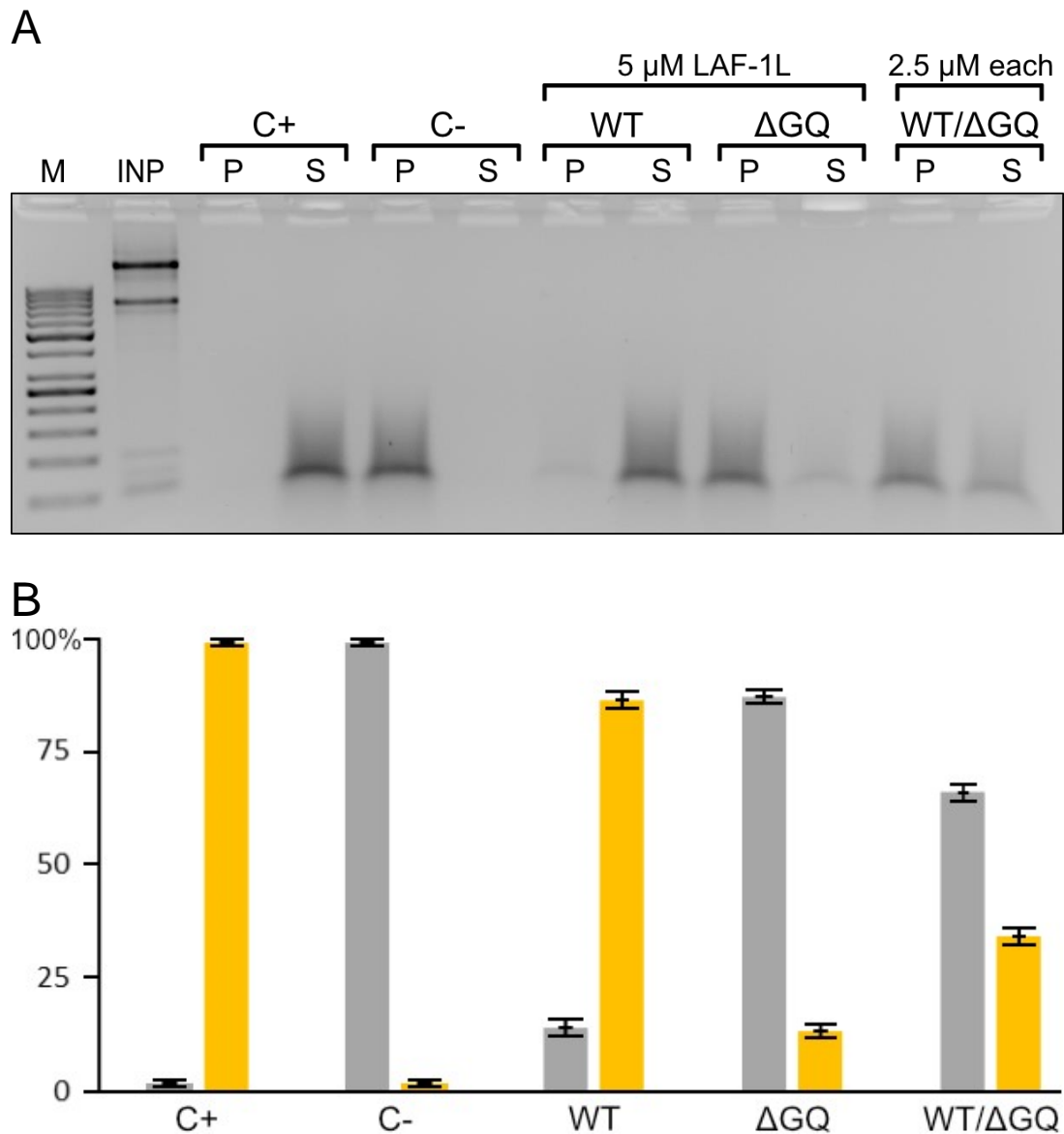


Figure 46. C-terminal GQ IDR is essential for the RNA helicase activity of recombinant LAF-1L.

A. Inverted monochrome image of a 2% agarose gel after an RNA helicase assay with recombinant wild type (WT) LAF-1L and Δ GQ (Δ 623-708) LAF-1L mutant protein at a total concentration of 5 μ M; mixed samples contained 2.5 μ M of each protein. Otherwise, samples and labels as in Figure 45.

B. Bar graph representing the average abundance of RNA in pellet (grey bars) and supernatant (orange bars) after the RNA helicase assay. Image processing was performed using ImageJ software; average and standard deviation values were calculated using a custom Python3 script, $n=3$ each.

Preliminary examination of Δ GQ LAF-1L RNA-helicase assay indicated typical distribution of RNA in control samples, as well as WT sample (Figure 46). On the contrary, Δ GQ LAF-1L sample demonstrated predominant accumulation of RNA in pellet fraction, similar to Δ RGG LAF-1L, indicating loss of activity.

Quantitative gel evaluation of the Δ RGG samples revealed a substantial RNA accumulation in the supernatant for the positive control ($99\pm 1\%$) and a comparable amount of substrate in the pellet fraction for the negative control (Figure 46). Here it is worth noting that both experimental subsets in Figures 46 and 47 were conducted using the same RNA substrate batch, allowing a direct comparison of each protein activity to each other. The WT LAF-1L successfully unwound $87\pm 3\%$ of the entangled RNA, which is consistent with the typical behaviour of this protein sample. In contrast, the Δ GQ LAF-1L demonstrated only a $16\pm 3\%$ conversion of the RNA substrate, indicating a high similarity in remaining RNA-helicase activity to the Δ RGG LAF-1 variant, which disentangled $15\pm 2\%$ of the RNA. Both are close to the values of *q267* LAF-1 and can therefore be seen as strongly compromised RNA helicases.

However, a significant distinction between the Δ RGG and Δ GQ LAF-1 truncations emerged in the mixed samples with WT protein. The Δ GQ/WT combination still converted $34\pm 4\%$ of the substrate, whereas the Δ RGG/WT sample converted only $19\pm 4\%$, resulting in twice the amount of untangled RNA present in the supernatant fraction for the Δ GQ/WT combination. This data suggest that a dimer composed of Δ GQ LAF-1L and FL-LAF-1L retains partial RNA helicase activity. Nonetheless, taken together, both IDRs are important for LAF-1's RNA helicase activity.

The RNA-helicase assay's final aspect to be considered is the slight accumulation of RNA in either the pellet or supernatant fraction, while the predominant fraction displays varying distribution. This behaviour is primarily contingent on the specific RNA batch, rendering such an artefact poorly reproducible. As an illustrative instance, one might consider the case of the WT LAF-1L sample, which exhibited RNA-helicase efficiency ranging from an average of 99% (Figure 46) to 87% (Figure 41), depending on the experimental conditions. An additional influential factor to keep in mind is the presence of any type of protein within the sample. Such a protein is likely to interact with the RNA in a nonspecific manner, potentially leading to the observed RNA behaviour.

Lastly, a comparative series of DIC microscopy experiments was conducted to investigate whether each RNA-helicase deficient LAF-1 variant is able to form LLPS droplets

in vitro. All proteins were tested under buffer conditions identical to the protein stocks used for the previous LLPS assays, but the protein concentration was increased from 6.5 μM to 13.0 μM to enhance droplet diameter. Neither LAF-1S nor the BSA sample exhibited any signs of LLPS, while LAF-1L formed droplets (Figure 47). These observations are consistent with previous findings above (Figure 30). Also, all three LAF-1L variants with a single missense mutation in the helicase core formed droplets that were indistinguishable from WT LAF-1L. Interestingly, only the ΔGQ LAF-1L truncated variant was capable of forming droplets, unlike the ΔRGG LAF-1 sample, which remained free of droplets. Altogether, these data of tested LAF-1 variants confirmed the previously suggested theory that RGG IDR of LAF-1L plays a critical role in droplet formation (Elbaum-Garfinkle et al., 2015). The obtained data also suggest that partial truncation, as seen in the LAF-1S isoform, of the aforementioned region is sufficient to fully suppress LLPS and that RNA helicase inactive LAF-1L is not compromised in LLPS.

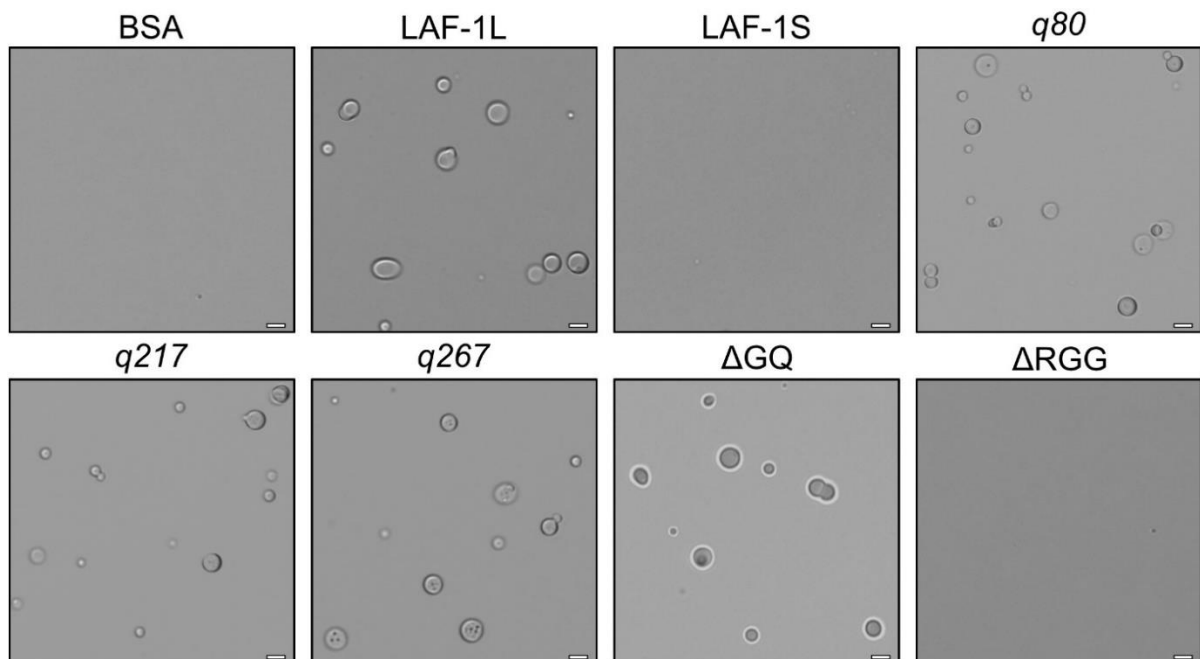


Figure 47. Only the RGG IDR is essential for LLPS of LAF-1L.

This series of DIC microscopy images represents purified recombinant LAF-1 variants (Chapter 3.2) and BSA. Each sample was incubated for 5 minutes at room temperature before imaging. LAF-1L, q80, q217, q267, ΔGQ and ($\Delta\text{623-708}$) LAF-1L variants and BSA were incubated in LAF-1L elution buffer with 500 mM NaCl. ΔRGG ($\Delta\text{2-191}$) and LAF-1S variants were incubated in LAF-1S elution buffer. Concentrations of each protein is 13 μM . The scale bar represents 10 μm . Note, irregular objects on glass slides demonstrate a sharp focal plane; no LAF-1L droplets are visible in the BSA, LAF-1S, or ΔRGG LAF-1L sample.

3.7. Attempts to identify components of LAF-1 RNPs

3.7.1. Immunoblot affinity purification of anti-LAF-1 polyclonal rabbit sera

Purified polyclonal rabbit sera were used to diversify the LAF-1 binding epitopes in IP and WB assays. The sera were induced by recombinant LAF-1L::GST protein obtained from resolubilisation of inclusion bodies washed in a 2% SDS solution. Maintenance, induction, and serum extraction of host rabbits were outsourced to the MPI-CBG Antibody Facility (Dresden). To avoid the enrichment of anti-GST antibodies during purification, recombinant LAF-1::6xHis protein was used for immunoblot affinity purification.

At the start of this research, two sera were already available in the laboratory cryostock and referenced by the previously given identifiers 32978 and 328800. Although both unpurified sera showed minimal cross-reactivity to worm proteins in WB analyses (Figure 8), they could not be further used for WB due to a high nonspecific membrane sorption, causing significant visual artefacts during fluorescence detection. Additionally, they could not be used for IP due to significant sorption of nonspecific antibodies on protein G magnetic beads, resulting in a low enrichment of LAF-1.

The original strategy involved generating an affinity FPLC column by crosslinking recombinant LAF-1 protein with NHS-activated (N-hydroxy succinimide) sepharose resin. However, efficient NHS-coupling requires a high protein content (≥ 3 mg/mL), a buffer system without amino groups ($-NH_2$), and a low detergent content. Despite several attempts (Chapter 3.2), these conditions could not be achieved. The best affinity column generated contained 0.8 mg of protein in 1 mL of NHS-activated resin.

Preliminary purification experiments indicated that the current FPLC anti-LAF-1 affinity column had a capacity of 0.2 mg of anti-LAF-1 purified polyclonal (pAb) per cycle. Achieving a sufficient yield of purified pAb would have required over 20 purification cycles. Considering time constraints and high material usage, a decision was made to adapt the immunoblot affinity purification strategy (described in Chapter 2.3.9). Therefore, after all elution steps, all fractions were evaluated by WB analysis and documented (Figure 48).

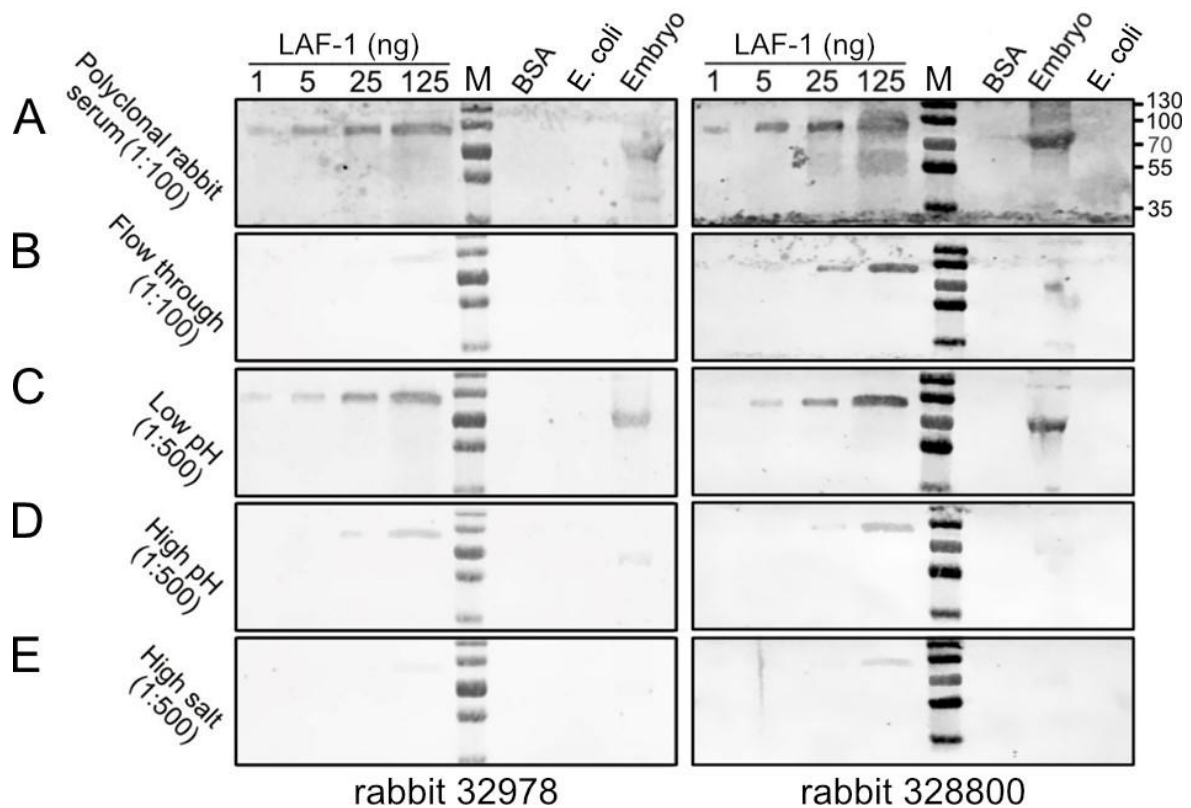


Figure 48. Two polyclonal rabbit sera were purified using immunoblot affinity purification.

This series of monochrome chemiluminescence images of WB nitrocellulose membranes was probed with immunoblot affinity purification fractions of polyclonal rabbit sera 32978 and 328800, along with IRDye 680RD goat anti-rabbit IgG secondary antibody (1:1000). Samples include: M – 3 μ L of PageRuler protein ladder (Thermo Scientific), with molecular weights assigned in kDa; LAF-1 – 1 to 125 ng of recombinant C-terminus 6xHis full-length LAF-1L purified inclusion bodies; BSA – 125 ng of BSA calibration standard (Thermo Scientific); *E. coli* – 2.5 μ g of total OP50 lysate; Embryo – 2.5 μ g of total N2 *C. elegans* strain multistage embryonic lysate. n = 5.

- A. Raw sera used for immunoblot affinity purification (1:100).
- B. Leftover sera after immunoblot affinity purification (1:100).
- C. pAbs eluted with acidic antibody elution buffer (1:500).
- D. pAbs eluted with basic antibody elution buffer (1:500).
- E. pAbs eluted with high salt antibody elution buffer (1:500).

Using the immunoblotting purification procedure, the average yield from 1 mL of 32978 serum was approximately 1.3 mL of purified pAb with a concentration of 2.3 mg/mL. This concentration was sufficient for WB analysis at a 1:1000 dilution. After four purification cycles, the purification strips retained most of the anti-LAF-1 binding capacity. No protein aggregation was observed during dialysis rebuffing.

The average yield from 1 mL of 328800 serum was 1.6 mL of purified pAb with a concentration of 1.4 mg/mL. This concentration was sufficient for WB analysis at a 1:650

dilution. However, during the dialysis procedure, the 328800 purified serum partially aggregated, which may explain the significantly lower antibody yield compared to the final output of 32978 serum. Similar aggregation behaviour was also observed in a freshly thawed aliquot of 328800 serum from the cryostock, which reduced the reusability of the purification strips even after centrifugation and filtration procedures (Chapter 2.3.9). After the second purification cycle, the membranes irreversibly lost approximately 90% of their binding capacity. Additionally, a small fraction of anti-LAF-1 antibodies from the 328800 serum remained in the flow-through fraction even after several incubations with immunoblotting membranes. The reason for this behaviour remains unknown. Both sera had a similar distribution pattern and specificity in all elution fractions, but due to lower yield and high aggregation potency of 328800 serum, 32978 purified pAb stock was primarily used for further IP and WB assays.

3.7.2. LC-MS/MS of *C. elegans* embryo samples

The ultimate goal of the LC-MS/MS experiments was to identify upon pulldown potential protein interactors of the LAF-1 protein in the germ line. As the antibodies used in this study cannot distinguish between the long and short isoforms of LAF-1 protein, both proteins were labelled as LAF-1. However, prior to this the immediate goal was to quantify the fraction of LAF-1 in the proteome, to distinguish potential LAF-1 isoforms, and to establish the proteome of early embryos, which were planned to be used as starting material for Immunoprecipitation experiments. Early embryos (≤ 128 -cell stage) represent the lowest ratio of somatic to germ line cell biomass throughout the *C. elegans* life cycle.

Preliminary single-replica experiments were conducted to determine the appropriate quantity of *C. elegans* embryos for LC-MS/MS analysis. A list of 42 stage-specific proteins of *C. elegans*, including LAF-1, was selected as germline and somatic developmental markers (Appendix 5.12). Calibration samples were prepared by extracting 10, 50, and 250 thousand N2 embryos (Chapter 2.3.17). DIC microscopy examination (Chapter 2.3.18) identified 83% of the embryos as being at the ≤ 128 -cell stage. Smaller embryo quantities were not tested due to complexity during the maintenance of lower aliquots. Ten thousand embryos were sufficient for LC-MS/MS analysis, containing 37 identified marker proteins (Appendix 5.12). Five marker proteins were not identified in any of the three tested aliquots, which may be explained

by a lack of unique peptides in their structure or low embryonic expression. The exact reasons were not further investigated.

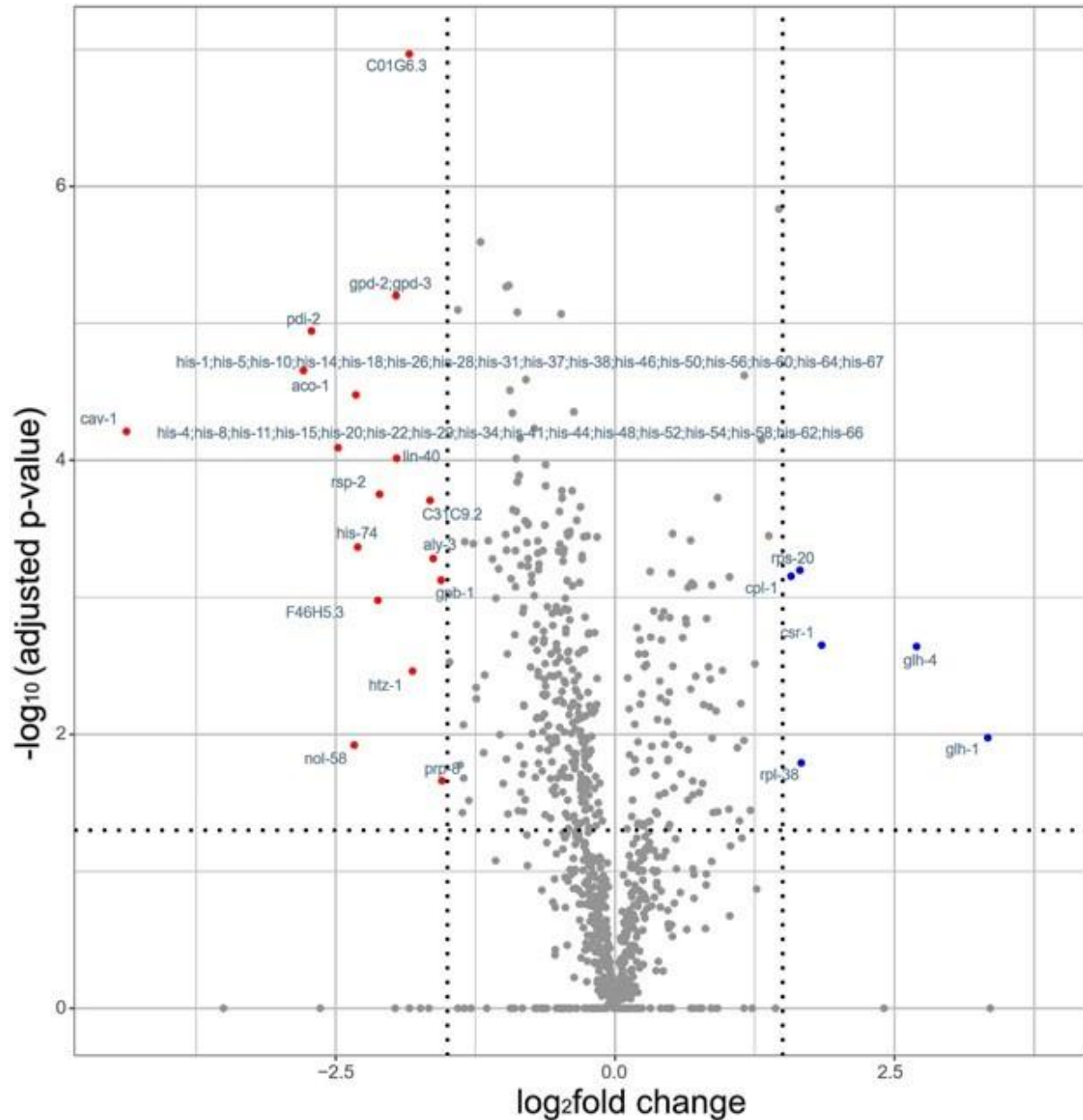


Figure 49. Early and late *C. elegans* embryos accommodate enriched and depleted protein pools.

Volcano plot of LC-MS/MS analysis of *C. elegans* protein abundance in early stage comparing to late stage embryonic samples; Significance criteria: $\log_2 > 1.3$, adjusted p-value < 0.05 ; Blue marks: enriched proteins; Red marks: depleted proteins; Grey marks: protein values that don't meet the significance criteria; n=4.

Further LC-MS/MS analysis identified that the total *C. elegans* early-stage embryo proteome consisted of approximately 4800 individual proteins (*C. elegans* genome contains approximately 20,000 protein-coding genes). LAF-1 was shown to occupy the 430th abundance ranking position with a $0.028 \pm 0.003\%$ (n=4) total proteome share.

To discover proteome differences between early (≤ 128 -cell embryos) and late stages (> 128 -cell embryos) of *C. elegans* embryogenesis and possible variations in LAF-1 expression throughout nematode egg stage development, a comparative analysis between two embryonic batches was conducted. DIC microscopy examination (Chapter 2.3.18) identified that 57% of embryos were at the bean or later developmental stage and 6% were at the ≤ 128 -cell stage. Early-staged *C. elegans* embryonic proteomes contained six reliably higher abundant proteins and at least 17 depleted proteins (Figure 49). The LAF-1 expression pattern was not statistically significantly different in the tested *C. elegans* egg staged embryogenesis samples. Early-stage enriched proteins were germline development regulators (CSR-1, GLH-1, GLH-4), yolk nutrients extractor CPL-1, and two ribosomal subunit proteins (RPS-20, RPL-38). Late-stage enriched proteins were poorly characterized proteins (C01G6.3, C31C9.2), macro-energetic metabolism-associated proteins (GPD-2, GPD-3, ACO-1), cell signalling proteins (CAV-1, GPB-1), developmental regulators (RSP-2, HTZ-1), RNA processing proteins (ALY-3, PRP-8, LIN-40, NOL-58), histone proteins (a broad variety of peptides representing histones from HIS-1 to HIS-74 were identified), and the protein disulphide isomerase PDI-2.

3.7.3. LAF-1 immunoprecipitation experiments

The primary objective of the LAF-1 immunoprecipitation (IP) was to identify the native protein interaction partners of LAF-1 using LC-MS/MS analysis. Given that the results of an IP heavily rely on the characteristics of the chosen antibody, several essential criteria were established for potential candidates. The selected antibodies needed to exhibit affinity toward both the long and short isoform ($\Delta 40-106$) of LAF-1 while avoiding interference with evolutionarily conserved sequences found in other members of the DDX3 RNA helicase protein family.

From the available antibodies, the anti-LAF-1 BW75 mouse monoclonal antibody had already undergone testing for recognition of both long and short isoforms, and it had been shown not to bind to VBH-1, the second DDX3 family member in *C. elegans* (as discussed in Chapter 3.1.1). Consequently, this antibody was identified as the primary candidate for LAF-1

IP. However, it had also been found to partially inhibit LAF-1's enzymatic activity (Chapter 3.6.3). Therefore, as an alternative antibody source, pooled elutions of purified anti-LAF-1 rabbit 32978 sera were chosen. This alternative had the potential advantage of recognizing multiple epitopes and had previously demonstrated sufficient LAF-1 recognition (Figures 8 and 47).

Further investigation was carried out to explore the lack of affinity of the monoclonal antibody (mAb) BF30 to LAF-1. This antibody was employed as a negative control in both IP and helicase assays. Since it had not been previously tested for LAF-1 recognition, concerns arose regarding potential artefacts that might impact subsequent research. Western blot (WB) analysis revealed no observable signal from the secondary antibodies for all tested LAF-1 variants (Figure 8B).

As the operational time for LC-MS/MS was limited, the initial step in implementing the LAF-1 IP assay involved determining the approximate quantities of LAF-1 protein in the IP samples using WB analysis, which had lower sensitivity (5-10 ng) compared to LC-MS/MS (<1 ng). Protein G magnetic beads (ThermoFisher) were chosen as the matrix for the IP assay due to their high affinity for mouse IgG1, IgG2a, IgG2b, IgG3, and total rabbit immunoglobulins. The alternative option of protein A magnetic beads (ThermoFisher) was also tested but ultimately rejected due to their similar binding capacity for anti-LAF-1 antibodies and lower stock volume. To ensure an adequate amount of biomaterial for LC-MS/MS analysis (10,000 embryos), the quantity of material for the IP was increased to 20,000±1,500 embryos.

As previously described, 19 mAbs against LAF-1 had been generated for WB and immunohistochemistry assays (Szczepaniak 2021). Among these characterised mAbs, four were chosen for IP validation due to their known affinity for the RGG IDR domain of LAF-1. In order to assess the background sorption on the IP matrix, an additional negative control was included using the mAb BF30, which showed no affinity to *C. elegans* proteins in WB analysis with total adult nematode lysates (Figure 8B). The initial estimation for the amount of immunoglobulins required for a single IP reaction was 6 µg, but this was later reduced to 3 µg based on empirical data (Figure 50). According to the manufacturer's datasheet, 10 µL of magnetic beads were needed for this quantity of antibodies. To prevent possible dissociation of the antibody from the protein G magnetic beads and to minimize the presence of protein G and antibody in the elution samples, an additional DMP crosslinking step was introduced. This step was carried out following the manufacturer's guidelines with minor modifications (Chapter

2.3.10). For WB analysis, proteins were eluted by incubating the magnetic beads with 10-15 μ L of 2x SDS SB for 15 minutes at +95°C with brief vortexing every 2-3 minutes. LC-MS/MS samples were provided to the collaborating lab of Carla Schmid (ZIK HALOmem, Institute of Biochemistry and Biotechnology, MLU) in the uneluted form for proteolytic digestion on the bead prior to analysis. This change in elution strategy improved the quantity and diversity of IP protein peptides, thereby enhancing intensity based absolute quantification (iBAQ) signal intensities.

Although all four mAbs were capable of recognizing LAF-1 in WB and immunohistochemistry assays, with minor variations in background signals, only BW75 mAb exhibited nearly complete reduction of the LAF-1 signal in the supernatant flow-through fraction and a significant enrichment in IP elution samples (Figure 50). None of the other tested monoclonal immunoglobulins demonstrated such promising results. Therefore, BW75 mAb emerged as the best and sole candidate for further LC-MS/MS analysis of IP LAF-1 and its interaction partners. Other candidates from the anti-LAF-1 mAb library were not tested due to their previously characterized low affinity or high background signal, which could potentially have a negative impact on the further evaluation of IP content. Based on image signal processing via ImageJ, the percentage of LAF-1 enrichment in the BW75 IP ranged from 83% to over 95%, depending on the batch and image capturing settings.

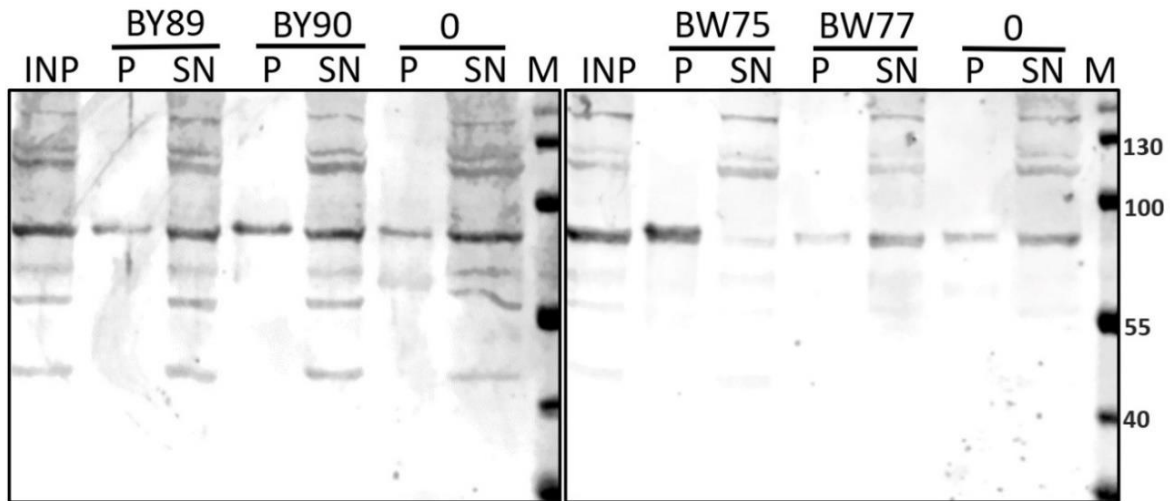


Figure 50. Only one out of the four tested mAbs is suitable for LAF-1 IP.

Monochrome fluorescence scan of a WB nitrocellulose membrane probed with immunoblot affinity purification fractions of the 32978 polyclonal rabbit serum and IRDye 680RD goat anti-rabbit IgG secondary antibody (1:1000). Samples: M – 3 μ L of PageRuler protein ladder (Thermo Scientific), with molecular weights assigned in kDa; INP – 20 μ g of total extract of *C. elegans* N2 strain multistage embryonic lysate; 0 – control IP performed with mAb BF30 of unidentified specificity; BY89, BY90, BW75, BW77 – anti-LAF-1 mAb used for IP; P – 50% of SDS SB eluted protein from IP beads; SN – 10 μ L of supernatant after IP reaction from 20,000 N2 embryos lysed in 100 μ L with a total protein concentration of 2 mg/mL. n = 5.

The second LAF-1 IP strategy was developed based on purified polyclonal antibody serum. This setup was motivated by the potential artefacts caused by the high selectivity of epitopes in mAb IP experiments, which may reduce the abundance of binding partners relying on the specified epitope during protein-protein interaction with LAF-1. The 32978 purified rabbit serum was selected as the most prominent and only candidate based on serum purification outcome (Chapter 3.7.1). The amount of immunoglobulins used for a single IP magnetic bead preparation was upscaled to 4 μ g compared to the mAb samples, to compensate for potential protein impurities left after serum purification. The DMP crosslinking of protein G in complex with pAb was performed identically to the mAb magnetic beads. The IP efficiency of the pAb magnetic beads was tested on 20,000 embryonic lysates under standardized conditions. The quantification of WB signal showed that the IP efficiency was approximately 85% of the total lysate LAF-1, depending on the batch and image capturing settings (Figure 51).

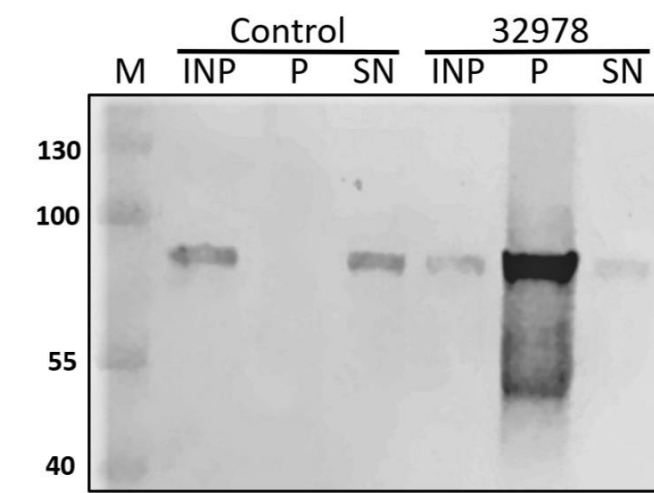


Figure 51. The purified polyclonal rabbit serum 32978 is suitable for LAF-1 IP.

Monochrome fluorescence image of a WB nitrocellulose membrane probed with immunoblot affinity purification fractions of polyclonal rabbit serum 32978 and IRDye 680RD goat anti-rabbit IgG secondary antibody (1:1000). Samples are: M – 3 μ L of PageRuler protein ladder (Thermo Scientific) with assigned molecular weights in kDa; INP – 20 μ g of total N2 *C. elegans* strain multistage embryonic lysate; Control – IP performed with mAb BF30 as a negative control; 32978 – combined anti-LAF-1 purified polyclonal rabbit antibodies used for IP; P – 50% of eluted protein from IP beads with SDS SB; SN – 15 μ L of supernatant after IP reaction from 20,000 N2 embryos lysed in 150 μ L with a total protein concentration of 1.3 mg/mL. n = 5.

Interestingly, a minor fraction of LAF-1 from the total lysate was not pulled down in both mAb and pAb IP experiments, even after doubling the volume of IP magnetic beads. This behaviour was reproducibly observed in every IP experiment and could not be eliminated by intensifying the biomass grinding or extending the IP incubation duration. The quantification of LAF-1 abundance should not be taken solely at face value since the final image accumulates typical artefacts associated with WB, including nonlinear recognition of different protein concentrations by primary and secondary antibodies, as well as fluorescent signal capturing artefacts caused by oversaturated pixels and the strong impact of image exporting conditions on signal densities.

To discover LAF-1 interaction partners, an immunoprecipitation with anti-LAF-1 monoclonal antibody was subjected to LC-MS/MS analysis. The mAb IP protein G beads contained the BW75 clone. IP with protein G beads crosslinked with BF30 mAb was used as a negative control (Chapter 3.1.1). Protein G and IgG peptides were not considered during the final table data analysis. The average content of LAF-1 in the protein IP samples was $6.184 \pm 0.434\%$ according to relative iBAQ (n=4), which was the highest fraction among *C. elegans* proteins. The LAF-1 protein content in the negative IP control was $0.017 \pm 0.003\%$

(n=4), confirming the validity of the implemented control (Figure 52). The anti-LAF-1 mAb IP achieved ~221-fold enrichment compared to the raw *C. elegans* embryonic lysate LC-MS/MS analysis.

Additionally, multiple proteins from several protein families were identified, including yolk lipoproteins (VIT-1, VIT-2, VIT-3, VIT-4, VIT-5, VIT-6), heat-shock proteins (HSP-1, HSP-60, DAF-21), cytoskeleton components (TBA-1, TBA-2, TBB-2, ACT-1, ACT-2, ACT-3, ACT-4, ACT-5), macroenergetic metabolism-associated proteins (ATP-1, ATP-2, ENOL-1, MDH-2), developmental regulators (NAP-1, RACK-1, NASP-2, PAR-5), ubiquitin ligases (UBQ-1, UBQ-2), translation factors (IFF-1, EEF-1B.2, EEF-2), transcription factor ICD-1, big and small ribosomal subunit proteins (RLA-1, RPA-0, RPA-2, RPL-3, RPL-4, RPL-5, RPL-6, RPL-7, RPL-7A, RPL-8, RPL-9, RPL-17, RPL-18, RPL-30, RPS-1, RPS-3, RPS-4, RPS-10, RPS-14, RPS-18, RPS-22), and nascent polypeptide-associated complex protein ICD-2 (Figure 52).

The results of the helicase assay suggested that the BW75 antibody had a partial inhibitory effect on LAF-1 helicase activity (Chapter 3.6.4). To avoid potential negative effects of the reduced helicase activity on the stability of LAF-1 complexes with interaction partners, a new set of LC-MS/MS analyses was performed using purified rabbit 32978 anti-LAF-1 serum for IP samples. The average content of LAF-1 in the protein IP samples was $4.937 \pm 0.381\%$ (n=4) according to relative iBAQ, which was the highest fraction among *C. elegans* proteins. Anti-LAF-1 pAb IP achieved approximately 176-fold enrichment compared to raw *C. elegans* lysate LC-MS/MS analysis, which was less efficient than the 221-fold enrichment observed in mAb IP. Due to the significantly lower LAF-1 enrichment efficiency of pAb IP and high similarity in precipitated protein patterns, the mAb IP results were considered further due to their better enrichment and higher protein diversity. However, the secondary goal of confirming the existence of the short LAF-1 isoform (LAF-1S) was not achieved due to inadequate peptide coverage in the RGG IDR.

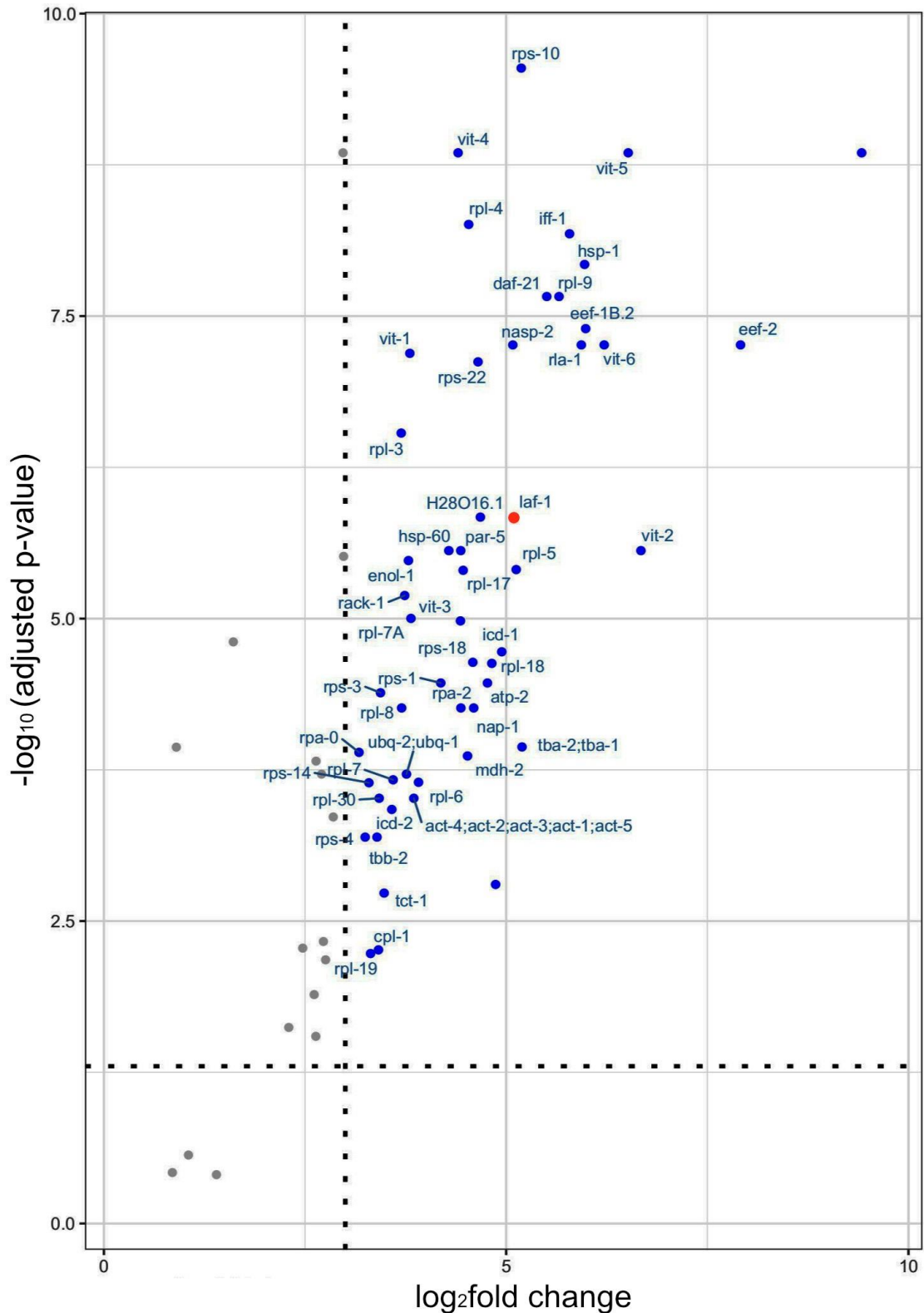


Figure 52. Anti-LAF-1 mAb IP samples contain multiple enriched proteins.

Volcano plot of LC-MS/MS analysis of *C. elegans* proteins enriched in anti-LAF-1 mAb IP samples; Enrichment criteria: $\log_2 > 3.0$, adjusted p-value < 0.05 ; Red mark: LAF-1; Blue marks: protein values that meet enrichment criteria; Grey marks: protein values that don't meet the enrichment criteria; n=4;

4. Discussion

4.1. LAF-1 activity is represented by two protein isoforms

Alternative splicing is an important mechanism of gene expression regulation to diversify the proteome, often leading to protein isoforms with specialized functions. While different genomes encode several DDX3 orthologs from individual genes, such as human DDX3X and DDX3Y (Kim et al., 2001) no case of protein isoform from a single *DDX3* locus had been described to date. Hence, the primary goal of this work on LAF-1S research was to substantiate the existence of LAF-1S protein, as cDNA clones obtained by RT-PCR do not prove further translation of the identified mRNA. Shortly after the confirmation of the LAF-1S isoform by this work (in August 2022), the UniProt database file of LAF-1 (D0PV95) was updated with the new isoform, D0PV95-2. It exactly matches the LAF-1S-specific truncation of $\Delta 41-105$ in the RGG IDR. During the writing stage of this PhD thesis (August 2023), the new isoform D0PV95-2 was labelled as "Curated" without any further reference to the source of such a datapoint.

Even though LC-MS/MS analyses of embryonic lysates or LAF-1 IP material failed to identify peptides specific to LAF-1S, a combination of IEF and WB confirmed the presence of LAF-1S during early embryonic stages (≤ 128 cells). Unlike continuous LAF-1L expression, L1 and further life cycle stages showed no visible signal of LAF-1S, arguing either for its absence or minor expression levels during postembryonic development. Due to sensitivity limitations of WB, it cannot be excluded that LAF-1S is present in postembryonic stages. However, the dramatic shift from LAF-1S to LAF-1L as the predominant isoform of LAF-1 in postembryonic stages suggests a difference in biological function or a more favourable need of LAF-1S during early embryogenesis. Taken into account that early-stage embryos have a lower ratio of germline to somatic cells, LAF-1S may even be enriched in the embryonic germ cell lineage, making it a presumed tissue-specific variant of LAF-1. While this hypothesis cannot be confirmed yet, as extracting sufficient germline biomass for WB analysis is not technically possible, it would also imply that *laf-1S* mRNA is a maternally donated transcript to the embryonic germ line to aid early embryonic expression. This argument is based on young adult animals not expressing LAF-1S protein and that zygotic transcription starts late in early embryos. Despite uncertainty regarding whether LAF-1S is specific to distinct embryonic

stages, the germ cell lineage, or both, the fact of its existence is intriguing and should be investigated further with respect to a potential unique role in P granule dynamics.

DDX3 proteins are known ATPases that unwind dsRNA (Song & Ji, 2019). Characterization of RNA helicase activity revealed no overt difference between LAF-1S and LAF-1L, suggesting a high degree of enzymatic similarity. While this might be expected from sharing an identical central helicase core region, substrate-specific differences are beyond the capability of the established bulk RNA helicase assay, as it lacks a defined RNA substrate molecule with structural specificity, typical of other reported helicase assays (Marecki et al., 2021). Instead, the presented assay is more suitable for characterizing overall RNA helicase activity, as it is not confined to a single and often artificially designed substrate. Furthermore, numerous studies suggested as potential substrates for human DDX3 a large and diverse set of transcripts with no sequence similarity (Calviello et al., 2021; Franca et al., 2007; Soto-Rifo et al., 2012), supporting that this work's RNA substrate choice is insightful to study enzymatic properties of LAF-1 isoforms. Irrespective of yet undefined RNA specificity among LAF-1 isoforms, the comparable RNA substrate conversion efficiency of entangled total RNA mixtures argues that both isoforms are capable of catalysing different types of RNA molecules. Given current data, LAF-1S is a bona fide RNA helicase with a similar activity range compared to LAF-1L.

RGG regions in DDX3 RNA helicases are known to possess RNA affinity (Kim & Myong, 2016). LAF-1S differs from LAF-1L only in its N-terminal RGG region by amino acids 41-105 (highlighted in more detail in Chapter 4.2 below). Therefore, it is likely that this N-terminal truncation in LAF-1S has an effect on RNA substrate recognition. However, in the established RNA helicase assay no effect on enzymatic activity was detected, arguing that much more detailed kinetic studies would have to be conducted. Also, additional research on RNA helicase activity with specific substrates would be required to reveal potential differences in enzymatic characteristics among LAF-1 isoforms. In addition, RNA affinity measurements should be carried out to complement such analyses. Based on the obtained data, it is possible to conclude that both isoforms are active RNA helicases *in vivo*, presumably with a similar, if not identical, enzymatic profile.

The most unexpected discovery during the investigation of LAF-1S was a significant difference in behaviour during recombinant protein purification. In comparison to LAF-1L, truncation of the RGG IDR drastically changed the behaviour of LAF-1S *in vivo*, rendering all

LAF-1L purification buffers unsuitable. A new subset of buffers was identified that supported purification of soluble LAF-1S and suppressed protein aggregation. Surprisingly, this buffer failed to induce liquid-liquid phase separation of LAF-1S although it did not for LAF-1L, arguing that LLPS is an isoform intrinsic and specific behaviour. As the N-terminal IDR of LAF-1 is known to drive LLPS (Elbaum-Garfinkle et al., 2015; Wei et al., 2017), a truncation by approximately 33.5% is likely to reduce the LLPS potential of the RGG IDR (further discussed in more detail in Chapter 4.2 below). Achieving LLPS of LAF-1L required precise calibration of buffer conditions, and additional adjustments to all buffers may therefore be necessary to find an appropriate composition for LAF-1S LLPS *in vitro*, as demonstrated for proteins with similar-sized RGG IDRs (Qamar et al., 2018; Schuster et al., 2018). Nonetheless, the observed difference in LLPS potency suggests that specific variations in the N-terminal IDRs among LAF-1L and LAF-1S may affect subcellular localization, favouring granular or free cytoplasmic localization. Since LAF-1S is a recent discovery, the subcellular localization of this LAF-1 isoform still needs to be characterized.

4.2. RNA-helicase activity is the essential function of LAF-1

LAF-1 was cloned based on previously identified genetic *laf-1* lesions that suppressed a sex determination phenotype, induced by translational gain-of-function (*gf*) alleles of *fem-3* (Hubert & Anderson, 2009). While suppression of exclusive spermatogenesis in *fem-3(gf)* hermaphrodites to self-fertile animals was dependent on a heterozygous *laf-1(-/+)* state, homozygous *laf-1(-)* alleles exhibited a not yet further analysed larval arrest phenotype (Goodwin et al., 1993). Based on LAF-1 homology to other DDX3 helicases and the molecular lesions associated with three *laf-1* alleles in the central helicase domain, it was suggested that they affect enzymatic activities of LAF-1 (Hubert & Anderson, 2009). However, neither of the three missense mutations, *q80* (R426C), *q217* (M430I), or *q267* (T434I), had yet been characterized at the molecular level.

In the established RNA helicase assay, all three LAF-1L mutant isoforms exhibited a negligible amount of entangled RNA conversion to soluble and presumably linearized or less structured molecules. This confirms that each of the introduced amino acid exchanges critically compromises the enzymatic activity of LAF-1, and as all three are located in the central domain, both LAF-1 isoforms would be equally affected *in vivo*. Their severe impact on RNA helicase activity is likely caused by a reduction in molecular functions of the conserved Walker

domain motif III (also known as the SAT motif), which is known in other DDX proteins to be responsible for both ATP binding and hydrolysis during RNA unwinding (De Colibus et al., 2022). Based on these findings and connected to *laf-1*'s essential roles *in vivo*, it can be concluded that RNA helicase activity represents the primary molecular role of LAF-1 as a developmental regulator in the soma and germ line. Importantly, as none of the missense mutations prevent LAF-1L droplet formation *in vitro*, it can also be concluded that RNA helicase activity is likely not a prerequisite for P granule formation in germ cells.

These discoveries strongly resonate with the traditional biochemical dogma that protein structure determines function, as each biologically relevant mutation resides in the Walker domain. However, this work also provides evidence that either flanking IDR plays a pivotal role in assisting the enzymatic functionality of LAF-1. A deletion of the entire RGG IDR or the GQ IDR led to a similar reduction in helicase activity of the remaining polypeptides, Δ RGG LAF-1 or Δ GQ LAF-1L, respectively. The impact on RNA helicase activity is as severe as the *q267* (T434I) missense mutation in the helicase domain of the full-length protein, enforcing an emerging theory that the N-terminal RGG IDR is just as important for helicase function as the C-terminal GQ IDR.

Although the detailed molecular mechanism through which either region contributes to this enzymatic activity remains to be elucidated, several observations suggest that they may—at least in part—differ from each other. On the one hand, the RGG IDR by itself has a proven generic RNA affinity but the GQ IDR has not (Ozdilek et al., 2017; this work). On the other hand, the RGG IDR is necessary and sufficient for LLPS *in vitro* but the GQ IDR has no role in LLPS (Elbaum-Garfinkle et al., 2015; this work). While the current research doesn't definitively ascertain the minimum sufficient size of the RGG IDR for LAF-1, LAF-1S did not experience any downregulation of its enzymatic activity, arguing that elimination of a portion of the RGG IDR to a certain length is acceptable, whereas a complete removal of the N-terminal IDR is not tolerated. While it remains unclear whether RNA recognition by the RGG IDR is mediated uniformly across the entire sequence or whether it has a site-specific nature, results from the bulk RNA helicase assay align well with this work's LLPS data points. DIC microscopy of LAF-1L's LLPS in the presence of RNA indicates that, compared to LAF-1S LLPS, RNA binding is enhanced by the longer RGG IDR of LAF-1L independently from its folded helicase domain. Assuming that RNA may serve as an electrostatic rod, guiding the substrate to the central helicase domain, this data could support a model in which the helicase domain itself may lack sufficient RNA affinity to effectively recruit and retain the RNA

substrate for subsequent unwinding activity. Consequently, additional assistance from the RGG IDR may be essential. However, this model does not explain how LAF-1S manages to perform its RNA helicase activity. Therefore, it is more likely that both the RGG and GQ IDR help to stabilize the Walker domain or to communicate potential interactions between the two flexible IDRs of the same DDX3 molecule or among protein dimers.

Until this point, the RNA helicase activity of LAF-1 has primarily been discussed as a singular unit, without considering its quaternary structure. Intriguingly, a series of published crystal structures argues that DDX3 proteins form oligomers (Floor et al., 2016; Song & Ji, 2019). However, none of these studies used full-length DDX3 proteins, instead they all characterized fragments trimmed down to the helicase core, lacking most of their flanking IDRs. Nonetheless, combined with the heterozygote-specific suppression phenotype in *C. elegans*, resulting from the aforementioned *laf-1* single point mutations, it is important to consider protein-protein interactions within the DDX3 population as critical contributors to RNA helicase activity, further improving our understanding of DDX3's molecular mechanisms.

The results of the bulk RNA helicase assay, derived from combining wild-type (WT) and *q267* mutant LAF-1L isoforms, shed light on various aspects of DDX3's organization. Firstly, acquired data points support a dimeric arrangement of LAF-1 protein molecules, as indicated by the approximately 25% unwinding of an RNA substrate predicted for the dimeric state. Heteromeric protomers are likely to possess nearly identical protein structures, rendering them equally stable to homomeric dimers. Secondly, it is evident that a single dysfunctional (mutant) unit is enough to compromise the function of a second functional (WT) molecule in the dimer. This phenomenon explains why heterozygote individuals manifest a spectrum of developmental defects even in the presence of wild-type LAF-1 isoforms and contrasts to the proposed monomeric mechanism of fly Belle (Liao et al., 2019). The consideration of LAF-1's quaternary structure and its impact on RNA-helicase activity adds a new dimension to our understanding of its function and its role in developmental processes.

A similar approach was also employed to differentiate the impact of each IDR truncations on LAF-1 dimer stability. While in isolation each Δ IDR isoform exhibited inactive RNA-helicase activity, yet in equimolar mixtures with full-length LAF-1L each IDR truncation demonstrated a different negative effect on the full-length (FL) protein. The Δ RGG variant had a similar effect compared to that of the *q267* mutant, indicating that both of these LAF-1

versions possess stable oligomerization characteristics, akin to native WT LAF-1. By contrast, the Δ GQ/FL mixture was capable of converting twice the amount of entangled RNA substrate compared to the Δ RGG/FL or *q267*/WT samples. This phenomenon could be a result of reduced stability of non-functional Δ GQ/FL dimers compared to functional FL/FL dimers, rendering Δ GQ LAF-1L a less potent inhibitor of a FL LAF-1L protomer than a Δ RGG LAF-1L. Consequently, as Δ GQ/FL dimers decrease, FL/FL dimers increase. This evidence suggests that the GQ IDR primarily plays a role in stabilizing LAF-1 dimers rather than being involved in RNA recognition, a function of the RGG IDR. The absence of the GQ IDR diminishes dimer longevity and rigidity, both of which are vital for RNA unwinding catalysis. As the identical GQ IDR is present in both LAF-1L and LAF-1S proteins, it can also be concluded that the GQ IDR carries out its functionality in the same manner for both isoforms. Evidently, both terminal IDR regions contribute to LAF-1's central role as an RNA helicase, each contributing in its own specific way to trigger RNA unwinding and to assemble into higher order LLPS structures.

4.3. LAF-1 LLPS behaviour depends on molecular environment

DDX3 RNA helicases have been documented to enrich *in vivo* in liquid-liquid phase separated RNP granules (Elbaum-Garfinkle et al., 2015). In germ cells, LAF-1L is a known component of P granules and phase separates *in vitro* in an RGG-dependent manner (Elbaum-Garfinkle et al., 2015). Previous work suggested that the RGG IDR of LAF-1 is a main contributor to LLPS *in vitro* and that this low complexity region is even sufficient for droplet formation. While the impact of certain buffer contributions had been noted before, this research expanded on this previous work, extended it to mutant LAF-1 isoforms, LAF-1S and diverse interactors of LAF-1, including RNA and additional proteins (discussed in depth in the next Chapter 4.4).

To study LLPS aspects of numerous LAF-1L isoforms, buffer conditions were established under which it was possible to induce LLPS of LAF-1L, preventing it from immediate aggregation due to high protein concentrations. Consistent with previous works (Elbaum-Garfinkle et al., 2015), the range of established buffer conditions was narrow, suggesting that a specific composition of molecular environment is required for an RGG N-terminus IDR to noncovalently interact with each other. This composition suppressed over-compacted protein agglomerates typically observed under low NaCl concentrations and maintained individual proteins in solution at high salt concentrations. In this respect,

optimisation experiments of salt concentrations were most beneficial, leading to a most significant enhancement of protein yield in LLPS state during optimisations of recombinant LAF-1L purification. Moreover, a further increase of NaCl concentration to 1M totally diminished LAF-1L droplets *in vitro*, which argues that electrostatic interactions between N-terminal RGG IDRs are likely to be the major driver of LAF-1L LLPS under tested conditions (Figure 53A). Such interactions can potentially occur between amino acid residues with opposite charge in RGG IDR that are evenly distributed throughout the whole length of IDR.



Figure 53. N-terminal RGG IDR of LAF-1 contains clusters of polar and non-polar amino acid residues.

Distribution of amino acid residues in RGG IDR of LAF-1L color-coded based on their biophysical properties. Amino acids missing in LAF-1S are between brackets. Numbering is according to full length LAF-1L.

- A.** Positively (red) and negatively (blue) charged residues.
- B.** Hydrophobic (orange) and hydrophilic (green) residues.

LLPS dynamics of LAF-1L can be described as a dynamic system in which the difference between assembled and disassembled noncovalent interactions between RGG IDRs regulates the prevalence and intensity of LLPS. A positive ratio of such interactions enhances LLPS and further over-compactisation results by dense crowding of IDR's. Contrary to this, a negative ratio leads to a decrease in droplet size and number until total dissociation. It is likely that discovered LAF-1L buffer conditions had slightly positive dynamics at 500 mM NaCl, which allowed to preserve LLPS stage at 6.5 μ M LAF-1L concentration for sufficient amount of time (up to 1 hour) to conduct experiments. Meanwhile, 1000 mM NaCl fully compensated most of IDR-mediated interactions, preventing LLPS, whereas 650 mM had minimal intensity of droplet formation under tested conditions. Obtained data suggest that droplet size and dynamics could be manipulated in real time by adjustment of ions concentrations. As tested

salt concentrations are above physiological levels of *C. elegans*, it is very likely that organic ion molecules are involved in granules dynamics regulation *in vivo*.

Next to electrostatic interactions, hydrophobic interactions may also contribute to LLPS *in vitro* (Das et al., 2020). The calculated theoretical grand average of hydropathicity (GRAVY) of LAF-1L N-terminal IDR is -1.737, predicting it to be a slightly hydrophobic sequence capable of additional compactisation through hydrophobic interactions between non-polar amino acidic clusters present in RGG IDR (Figure 53B). Even though hydrophobic interactions were here identified to be a secondary contributor to LLPS of LAF-1L, as the LAF-1L elution buffer required at least 0.1% nondenaturing detergent Triton X-100, these low amounts were sufficient for destabilisation of non-polar clusters to prevent formation of over-compact protein aggregates. A further increase of Triton X-100 to higher concentration than 0.1% did not contribute to enhanced recombinant LAF-1L protein solubility or droplet stability, probably because most non-polar clusters were already saturated. The here established buffer conditions were able to maintain a sufficient amount of multivalent interactions between multiple N-terminal IDRs of LAF-1L proteins to keep them in a LLPS state. Moreover, the low theoretical aliphatic index value of 12.88, combined with AlphaFold structure predictions of LAF-1L RGG IDR (Jumper et al., 2021), allow to speculate that N-terminal IDR interactions are highly adaptable and have no constant site specificity due to ongoing dimensional rearrangements. This theory is also supported by LAF-1S isoform studies indicating lack of interactions for LLPS but not for RNA recognition.

While salt concentrations are rather homeostatic in an organism, the amount of available protein may be subject to change. LAF-1L protein concentration itself was discovered as an additional factor regulating droplet formation. At least 2.6 μM of LAF-1L were necessary to trigger LLPS at 500 mM NaCl. This behaviour suggests that active ions of buffer are not abundant enough to saturate all RGG IDR charges, therefore, leading to a dramatic increase of N-terminal interprotein interactions, enhancing LAF-1L droplet formation. A similar concentration-dependent LLPS of LAF-1 may also occur *in vivo*. Previous immunomicroscopic studies of *C. elegans* embryos using the pan-LAF-1 mAb BW75 documented that somatic cells contain LAF-1 mostly in a free cytoplasmic form, while cells of the germ lineage additionally had phase-separated LAF-1 enriching in P granules (Elbaum-Garfinkle et al., 2015). Presented *in vitro* data of this work also suggests that expressional upregulation of LAF-1 in germ cells may act as LLPS drivers *in vivo* as an additional biological

mechanism of granule induction. How abundance changes between somatic and germ cell lineages in early embryos may occur needs to be investigated further.

Based on published *in vivo* data, different types of physiological granules are enriched in different kind of RNA molecules (Brangwynne et al., 2009; Updike & Strome, 2010). This is why additional experiments were conducted to investigate a possibility of co-LLPS of RNA with LAF-1L *in vitro*. Across a range of 0 to 125 ng/ μ L final concentration of total RNA and 6.5 μ M of LAF-1L in LAF-1L elution buffer, droplets proportionally grew from 3 ± 1 μ m at 0 ng/ μ L RNA to 14 ± 8 μ m at 100 ng/ μ L and begun slightly to decrease in diameter to 10 ± 3 μ m at 125 ng/ μ L. This continued growth suggests that LAF-1L droplets are able to accumulate RNA in a concentration dependent manner. Moreover, the observed extension of droplet diameter suggests that RNA molecules are able to enhance LAF-1L droplet growth, in addition to inducing formation of new droplets, which explains the observed abundance of small droplets in samples. However, the observed reduction in average diameter at 125 ng/ μ L of RNA may be a consequence of over-saturation of RGG IDRs by RNA phosphate backbones and a partial loss of LAF-1L granule integrity. Such affinity of LAF-1Ls' RGG IDR to RNA is likely determined by its high content in arginine residues, which is known to form highly stable electrostatic interactions with phosphate (Woods & Ferre, 2005). Additionally, IDRs and RNA are flexible molecules that may assist mutual compensatory three-dimensional adjustments. It remains unclear whether all RNA molecules or only a fraction of them is capable to co-LLPS with LAF-1L. Because of that, additional experiments are still required to clarify a potency of each RNA population to be recruited into LAF-1L droplets.

As LAF-1L helicase activity is dependent on ATP hydrolysis, it was important to clarify whether LAF-1L enzymatic activity is able to modulate droplet formation in presence of RNA-induced ATPase activity. As a starting point served conditions with 100 ng/ μ L of total RNA at 6.5 μ M LAF-1L, where droplet size was the biggest. In the presence of 25 mM ATP, average droplet diameters insignificantly increased from 5 ± 1 μ m to 6 ± 2 μ m over 30 minutes incubation at room temperature, while droplets in ATP-free samples grew from 4 ± 1 μ m to 12 ± 10 μ m under same conditions. This behaviour suggests that the active RNA helicase domain of LAF-1L prevents RNA to co-LLPS with LAF-1L droplets. It remains unclear how much of the RNA from the total extract is capable of integrating into the droplets, suggesting that only a fraction of RNA with specific molecular features is recruited into RNP droplets. As the RNA helicase activity is dependent on ATP, it is possible to speculate that only RNA molecules with double-stranded structural features can be recruited to RNA granules through binding to LAF-1L RNA

helicase domains. Activation of the RNA-helicase domain through ATP hydrolysis is expected to induce loss of double-stranded regions and subsequent exclusion from RNP granules. The further recruitment to RNP droplets occurs after the reformation of double-stranded helices, which takes a certain period of time. This described lifecycle forms a dynamic ATP-dependent equilibrium that may establish a constant LAF-1L droplet size throughout the experimental time scale. Nevertheless, it is possible that the concentration of 25 mM ATP is sufficient to suppress RNA co-LLPS with LAF-1L as it was shown for several kinds of granules to act as a hydrotrope (Aida et al., 2022; Dang et al., 2023; Patel et al., 2017). In this respect, experiments with non-cleavable ATP analogues and kinase dead mutants LAF-1 (e.g. *q267*) should be carried out to investigate a combined influence of RNA-ATP on droplet formation.

Taken together, presented data suggest that biophysical principles underlying LAF-1L protein droplets and RNP droplet organisation are affected by LAF-1L concentration, ATP accessibility, content of ions, polar and hydrophobic molecules as well as proteins capable to co-LLPS, like LAF-1S, or specific LLPS suppressors, such as IFE proteins (discussed in detail in Chapter 4.4 below). Speed of LLPS is directly proportional to the difference of association and dissociation of non-covalent multivalent intermolecular interactions between RGG IDRs, providing a highly dynamic and flexible scenario for protein and RNP LLPS studies *in vitro*. Presented discoveries can also be extrapolated to RNA granules as they are known to be affected by similar biophysical parameters *in vivo* (Brangwynne et al., 2009), giving more insights on their organisation principles and molecular regulatory mechanisms under different conditions. Nevertheless, additional research needs to be conducted for creation of a valid model capable to predict droplet behaviour under specific conditions.

Lastly, as yet another LLPS parameter, a previously suggested model speculated that an increase in entropy is capable of reducing frequency and duration of intermolecular interactions (Dignon et al., 2019). Unfortunately, attempts to identify differences in droplet size in temperature ranging from +16 °C to +25 °C didn't show any significant difference. Any further expansion of the temperature range is difficult to comprehend of such heat impact *in vivo* as *C. elegans* has a very narrow temperature optimum around +20 °C and a 4 to 5-degree shift is already the borderline viable temperature for *C. elegans*.

4.4. LAF-1 as a P granule component and potential translational regulator

DDX3 helicases have been suggested to participate in multiple stages of mRNA biogenesis (Linder & Jankowsky, 2011). In the cytoplasm, DDX3 RNA helicase activity has been linked to posttranscriptional mRNA regulation and is suggested to aid the translational initiation process (Lee et al., 2008). In this respect, DDX3 helicases are proposed to assist scanning of the 43S pre-initiation complex by unwind dsRNA structures in the 5'UTR of mRNAs (Calviello et al., 2021). How DDX3 proteins might be recruited to this process is less well understood and one prevalent model in the field resides on an interaction with the cap-bound translation initiation factors (Shih et al., 2008; Soto-Rifo et al., 2012). Due to a conserved eIF4E-binding motif within the RGG IDR of all investigated DDX3 RNA helicases, a model has been proposed in which DDX3 binding to eIF4E might exert a translational regulatory role (Lee et al., 2008; Shih et al., 2012). However, these studies primarily relied on colocalization with DDX3 in subcellular compartments or proteins expressed in extracts and had not been recapitulated via a direct physical protein-protein interaction of purified protein components. Therefore, to gain insights into LAF-1's molecular roles in posttranscriptional RNA regulation, this work characterized its predicted interaction with recombinant eIF4E orthologs and attempted to co-purify eIF4Es and additional RNP components associated with mRNA regulation by immunoprecipitation from embryo extracts.

All five *C. elegans* eIF4E proteins were purified in this work to assess a potential physical interaction with LAF-1 in solution. With the exception of IFE-5, IFE-1 to IFE-4 possess a short N- and C-terminal IDR of ~15-35 amino acids in length and none of them phase separated as judged superficially by a lack of turbidity of the protein solution after purification/resolubilisation, and more detailed by missing droplet formation at the level of DIC microscopy in LAF-1L LLPS buffer conditions. Consistent with available crystal structures of mammalian eIF4E orthologs and AlphaFold predictions of either *C. elegans* eIF4E protein, performed SAXS measurements of IFE-1 and IFE-3 suggest that eIF4E proteins adopt a globular fold in solution. As its respective IDRs fail to support LLPS *in vitro*, eIF4E protein are likely not initiators of RNA granule formation. Nonetheless, eIF4Es are found *in vivo* in RNA granules, presumably by their ability to adhere to mRNAs that themselves are part of RNA granules (Huggins et al., 2020).

The morphology of LAF-1L droplets can be influenced by protein binding partners such as LAF-1S. Based on this finding, a similar experimental setup was employed to investigate LAF-1L LLPS in the presence of recombinant IFE-x proteins. In contrast to BSA or LAF-1S, a complete suppression of LAF-1L droplet formation was observed in the presence of either IFE-x protein. This data suggests a specific interference of each IFE-x on LAF-1L LLPS and is consistent with a proclaimed physical interaction between DDX3 RNA helicases and eIF4E proteins. As LLPS of LAF-1L is mediated in large parts by its N-terminal RGG IDR and the predicted eIF4E-binding motif resides in this region, it is tempting to speculate that eIF4E proteins bind to the RGG IDR of LAF-1 and thereby inhibit multivalent LAF-1L/LAF-1L interactions to suppress droplet formation. According to SAXS measurements, LAF-1L entities increase in volume when associating with IFE-1 or IFE-3, but no indication of stable complex formation was identified. Unfortunately, initial attempts to reveal IFE-x/LAF-1L interactions using the technique of far-western blotting failed and co-immunoprecipitation from worm extracts have been also unsuccessful to validate this interaction. However, together these data support the following emerging picture, the presumed physical interaction among eIF4E and DDX3 proteins might be based on very weak affinities and that the LLPS assay is a more suited test for such weak interactions.

To gain further insights into how LAF-1 may contribute to RNA granule dynamics and posttranscriptional mRNA regulation, an IP enrichment protocol for LAF-1 proteins was developed and optimized to precipitate the total LAF-1 pool along with potential interactors. Since no LAF-1 binding partners were known at that time and antibodies to eIF4Es were not available to the lab, LC-MS/MS was selected as an advanced technique capable of identifying a broad range of proteins in complex mixtures (Jensen et al., 2021). Next to some other proteins, the LC-MS/MS analysis of IP material from *C. elegans* embryonic lysate revealed an enrichment of one translation initiation and two translation elongation factors as well as 21 proteins from both ribosomal subunits, compared to unspecific mAb IP. While none of these proteins have yet been confirmed with a complimentary technique and unspecific co-purifications are possible, this data may suggest that LAF-1 is part of mRNAs that are actively translated. This interpretation would be consistent with previous reports on human DDX3 assisting the subunit joining process (Geissler et al., 2012) and more recently, specifically binding to the 18S ribosomal RNA of the small ribosomal subunit near the mRNA entry channel during late stages of translation initiation (Calviello et al., 2021).

Unfortunately, none of the *C. elegans* orthologs of eIF4E were identified in the LC-MS/MS analysis. It is possible that the fraction of ribosomal complexes at the initiation stage was insufficient for identification during the LC-MS/MS experiments due to the shorter duration of the initiation stage compared to the elongation and termination phases of translation, as well as suboptimal IP conditions. Alternatively, the affinity between eIF4Es and LAF-1 may also be too low to maintain in the chosen buffer conditions or to survive this experimental procedure, as discussed above. Moreover, this interaction is anyways envisioned to be very transient in nature. eIF4E's promote translation initiation by binding to eIF4G to form the cap-binding complex that assists in further recruitment of the charged 43S ribosomal subunit. With regards to binding to eIF4E, DDX3 and eIF4G would stand in competition to each other, as both are expected to use their eIF4-binding motif to interact with a designated binding surface on eIF4E. Hence, to promote cap-complex assembly on the mRNA, the affinity of DDX3 should not be able to constantly outcompete eIF4G recruitment. While these mechanistic details are key to our understanding on how DDX3 may contribute to translational regulation of mRNAs with structured 5'UTRs, they remain enigmatic and an important topic for further research.

A side aspect to enzymatic activity but probably relevant for RNP purifications is the observation that the mAb BW75 partially interfered with LAF-1's RNA helicase activity, potentially biasing the immunopurification procedure. Based on the location of the epitope near the ATP-binding loop of the central helicase domain, it is conceivable to assume that the antibody may either compete with ATP binding, or alternatively, influences the mobility of the RGG IDR when in close proximity to the Rossmann-like tertiary fold of the LAF-1 helical core, restricting dimerization. This assumption aligns with the fact that RNA unwinding by a DDX3 helicase necessitates a three-dimensional rearrangement of the folded domains, and the N-terminus RGG IDR might interact with the RNA phosphate backbone (Chong et al., 2018). Any hindrance to this physical flexibility could potentially disrupt enzymatic catalysis and consequently may affect RNP composition or favour specific RNPs during the IP procedure. It should be also noted that a minor inhibitory effect of the mAb BF30 antibody on LAF-1's enzymatic activity was observed, which remains unexplained. This small but noticeable effect could either be attributed to an uncharacterized affinity of mAb BF30 towards the RNA substrate or the nonspecific binding of tangled RNA to the monoclonal antibody, possibly unrelated to LAF-1L. Further investigation is required to unravel the intricate details of this interaction and mAb BW75's impact on LAF-1's RNA-helicase activity.

Taken together, all data of this work combined allows to present a speculative working hypothesis on the dynamic behaviours of LAF-1 *in vivo*, existing in both a non-granular soluble and a granular LLPS state, to promote translation in the cytosol and mRNA storage in P granules, respectively. At the molecular level, LAF-1 is a dimeric ATP-dependent RNA helicase, utilizing its RGG-IDR to enhance RNA affinity and its GQ-IDR to couple dimer activities. Both IDRs assist the central ATPase domain in unwinding intra- or intermolecularly formed structured elements of RNA molecules. These features appear to be essential to mRNAs with structured 5'UTRs to be translated in the cytosol. Stem-loop structures are typical substrates for DEAD-box RNA helicases, which can recognize them in a sequence-unspecific manner. While ribosomes are capable with the help of eIF4A-type RNA helicases to efficiently unwinding RNA during the elongation step (Takyar et al., 2005), a 5' UTR stem-loop can impede ribosome recruitment during the initiation stage (Kozak, 1990). This is where LAF-1 becomes an essential molecule that linearizes the 5' UTR stem-loop, facilitating scanning of the 43S pre-initiation complex. During the translation elongation phase, LAF-1 may stay associated with the 40S subunit to assist potential reinitiation by repeatedly unwinding reformed 5' UTR stem-loops, and/or in helping to reattach IFE proteins to the mRNA cap to maximize the translation of specific mRNA in need of constant assistance. In return, cap-bind IFE's may strongly interfere with LAF-1's tendency to drive RNA-promoted LLPS, keeping mRNAs in the cytosol. This may further be enhanced, by readily available ATP molecules, which may suppress RNA-mediated LLPS of LAF-1 and fuel its helicase activity.

Whereas interactions with IFE-x and ATP interfere with LLPS, multivalent RGG-mediated interactions among LAF-1L protein interactions and in parallel occurring non-specific RNA binding affinities are promoting LLPS, tipping the balance and shifting a fraction of LAF-1 into P granules, where it also maintains the integrity of P granule RNPs. Consistent with this, a reduction of LAF-1 in early embryonic germ cells, affected accumulation of the major P granule component PGL-1 (Elbaum-Garfinkle et al., 2015). P granules are rich in translationally inactive mRNAs (Wang & Seydoux, 2014), and an IFE-mediated interaction with LAF-1 may trigger a release of these mRNAs from RNA storage. This IFE-induced shift from P granules to the cytosol is potentially capable of reducing the presence of LAF-1 in RNA granules and decreasing the potential for droplet formation *in vivo* through a specific association with its N-terminus RGG IDR. Consequently, a fraction of LAF-1 RNP complexes may be released into the cytoplasm, where an ATP-dependent helical catalytic event triggers the dissociation of linearized RNA from LAF-1 dimers. Consistent with the negative effect of

ATP on LAF-1L/RNP droplet growth it would have to be assumed that P granules are predominantly free of ATP. Unwound mRNAs would then become accessible to the 43S pre-initiation complex, promoting translation. A potential difference between the two isoforms of LAF-1 remains at this point highly speculative and may reflect difference in the balance between LLPS and non-LLPS states of LAF-1 isoforms, potentially relevant during early embryogenesis.

All general principles summarized in the above sketched hypothetical model on LAF-1 dynamics may very well generically apply to all DDX3 RNA helicases in other systems. DDX3 proteins are versatile posttranscriptional RNA regulators, assisting preservation, accumulation, and structural reorganization of a limited population of mRNA molecules to be eventually translated. Moreover, the cellular population of DDX3 RNA helicases maintain a homeostatic balance between a granular LLPS and cytosolic non-LLPS state. Certain developmental or physiological circumstances tip this balance towards a predominant granular state e.g. upon stress, but this is reversible. Such flexible dynamics between these states appear to be facilitated by the many intrinsic molecular features of DDX3-specific RNA-binding and RNA helicase activities, all governed and integrated by its unique IDRs that flank a central Walker domain fold that becomes an active ATPase upon dimerization on an RNA substrate. Like in *C. elegans*, DDX3 RNA helicases are essential regulators of organismal development and cellular homeostasis. Despite these prevalent roles, however, further research is necessary to clarify its mechanistic roles as a posttranscriptional RNA regulator and to elucidate its own regulating, which is likely not limited to eIF4Es but also other yet to be discovered interactors.

5. Appendixes

5.1. List of equipment

| Unit | Manufacturer | Cat.No. |
|--|-------------------|-----------------|
| 10 mL Stainless Steel Grinding Jar | Retsch | 01.462.0236 |
| 5417R Refrigerated Centrifuge | Eppendorf | 17483-10 |
| 5810R Benchtop Centrifuge | Eppendorf | 5811000015 |
| A-4-62 Swing Bucket Rotor | Eppendorf | 022638351 |
| C0650 Fixed-Angle Conical Tube Rotor | Beckman Coulter | 364670 |
| Electroporation Cuvettes | Bio-Rad | 1652082 |
| Electroporator Eporator | Eppendorf | E4309000035 |
| F2402H Biocontainment Rotor | Beckman Coulter | 361171 |
| F-45-30-11 Rotor | Eppendorf | 17483-51 |
| Fluorescence Motorized Microscope DM6 B | Leica | DM6B |
| Imaging System Odyssey XF | LI-COR | 2802 |
| IPGphor Strip Holder 7 cm | Amersham | 80-6416-11 |
| Isoelectric Focusing System Ettan IPGphor II | Amersham | 80-6414-02 |
| Microvolume Spectrometer Colibri | Titertek-Berthold | 312010 (Biozym) |
| Mini-PROTEAN Tetra Cell | Bio-Rad | 165-8001 |
| Mini-Trans-Blot Cell | Bio-Rad | 170-3935 |
| Mixer Mill MM 301 | Retsch | 20.741.0001 |
| NGC Discover 100 Chromatography System | Bio-Rad | 7880010 |
| NGC Fraction Collector with Racks | Bio-Rad | 17002070 |
| Plus Gel Electrophoresis Unit with Combs | Thermo Fisher | 15845541 |
| Rocker 2D digital | IKA | 0004003000 |
| SmartBlock 1.5 mL | Eppendorf | 460-0222 |
| Sonotrode UW70 | Bandelin | UW70 |
| T100 Thermal Cycler | Bio-Rad | 1861096 |
| ThermoMixer C | Eppendorf | 460-0223 |
| The Allegra X-30R Benchtop Centrifuge | Beckman Coulter | B06322 |
| Ultrasonic Bath with Heating (RK100H) | Sonorex | 3230 |
| Ultrasonic homogeniser Sonopuls GM70 | Bandelin | GM70 |
| UV Gel Documentation System | Vilber Lourmat | BIO-VISION-3026 |

5.2. List of FPLC columns and matrixes

| Unit | Manufacturer | Cat. No. |
|---------------------------------|--------------|--------------|
| EconoFit Profinity IMAC Columns | Bio-Rad | 12009298 |
| ENrich SEC 650 | Bio-Rad | 7801650 |
| HiLoad 26/600 Superdex 200 | Cytiva | GE28-9893-36 |
| HisTrap IMAC Columns | Cytiva | 17524701 |

5.3. List of chemicals and materials

| Unit | Manufacturer | Cat. No. |
|---|-------------------|--------------|
| 1 kb Plus DNA Ladder | Thermo Fisher | 10787018 |
| 2-Mercaptoethanol | SERVA | 39563.01 |
| 3 M Sodium acetate solution pH 5.0 | SERVA | 39572.01 |
| Acetic acid | Millipore | 1.00063.1011 |
| Acetone | Sigma-Aldrich | 32201 |
| Acrylamide/Bis solution (19:1) | SERVA | 10681.01 |
| Agar | ROTH | 5210.2 |
| Agarose | ROTH | 5210.02 |
| Ammonium persulfate | AppliChem | 5M012857 |
| Ammonium thiocyanate | ROTH | 4477.1 |
| Aqua-Phenol pH 4.5 | ROTH | A980.2 |
| ATP | SERVA | 10920.02 |
| Bacto™ Peptone (GIBCO) | Thermo Fisher | 211677 |
| Bovine Serum Albumin Standard (2 mg/mL) | Thermo Fisher | 23209 |
| Bromophenol blue | Thermo Fisher | A18469.18 |
| CaCl ₂ | ROTH | CN92.1 |
| Carbenicillin | Diagonal | 195092.005 |
| CHAPS | Sigma-Aldrich | 75621-03-3 |
| Chloramphenicol | SERVA | 16785.02 |
| Chloroform | Millipore | 1.07024.2500 |
| Cholesterol | SERVA | 17101 |
| Coomassie Brilliant Blue R-250 Dye | SERVA | 17525 |
| Cycloheximide | SERVA | 10700 |
| D(+)-Glucose Monohydrate | ROTH | 6780.2 |
| Dimethyl pimelimidate dihydrochloride (DMP) | Sigma-Aldrich | 8388 |
| DTT (Fermentas) | Thermo Fisher | R0861 |
| Dynabeads Protein A | Thermo Fisher | 10001D |
| Dynabeads Protein G | Thermo Fisher | 10003D |
| EconoFit Profinity IMAC Columns | Bio-Rad | 12009298 |
| EDTA | ROTH | 8040.2 |
| EDTA-free Protease Inhibitor Cocktail | Roche Diagnostics | 11836170001 |
| EGTA | ROTH | 3054.2 |
| Ethanol | ROTH | P075.5 |
| Ethanolamine | Sigma-Aldrich | E9508-100ML |
| Ethidium Bromide | ROTH | 2218.2 |
| Filter paper for blotting | Whatman | 3030917 |
| Formamide | Qbiogene | B043302 |
| Glycerol | VWR | 19J044109 |
| Glycine | Sigma-Aldrich | 33226-1KG |
| Guanidinium thiocyanate | ROTH | 0017.1 |
| HCl (37%) | ROTH | 9277.2 |
| Horse serum (GIBCO) | Thermo Fisher | 16050122 |
| HPE IPG Overlay | SERVA | 43397 |
| HPE IPG strip buffer | SERVA | 43368 |
| Imidazole | AppliChem | 1Q014057 |
| Iodoacetamide | SERVA | 26710.02 |
| IPG BlueStrip 3-10 / 7 cm | SERVA | 43001.01 |
| IPTG | SERVA | 26600.06 |
| Isopropanol | AppliChem | 6P011742 |
| Kanamycin | ROTH | T832.2 |
| KCl | ROTH | HN02.3 |
| KH ₂ PO ₄ | ROTH | 3904.3 |
| Lysozyme | SERVA | 28263.02 |
| MgCl ₂ | Millipore | 1.05833.1000 |
| MgSO ₄ | Millipore | 1.05886.1000 |

| | | |
|--|--------------------|--------------|
| MnCl ₂ | ROTH | T881.3 |
| Na ₂ HPO ₄ | ROTH | P030.3 |
| NaCl | ROTH | HN00.3 |
| NaOH | ROTH | 6771.1 |
| Nitrocellulose membrane, 0.45µm | GE Healthcare | A10021531 |
| Orange G | AppliChem | A1404.0025 |
| PageRuler prestained protein ladder | Thermo Fisher | 26616 |
| RiboLock RNase Inhibitor | Thermo Fisher | EO0382 |
| Skimmed milk powder (TSI) | REWE | 023078 |
| Slide-A-Lyzer Dialysis Cassettes (10K) | Thermo Fisher | 66380 |
| Sodium azide (NaN ₃) | SERVA | 30175.01 |
| Sodium borate (Na ₂ B ₄ O ₇ · 10H ₂ O) | Merk/Sigma-Aldrich | B9876-500G |
| Sodium dodecyl sulfate (SDS) | SERVA | 20765.03 |
| Sodium Hypochlorite Solution | Supelco | 1.05614.2500 |
| TEMED | Thermo Fisher | 17919 |
| Tetracycline | ROTH | HP63.1 |
| Trichloroacetic acid (TCA) | Merk/Sigma-Aldrich | T6399 |
| Tris base | ROTH | 4855.4 |
| Triton X-100 | Merk/Millipore | 1.08603.1000 |
| Tryptone | AppliChem | 0A011675 |
| Tween-20 | SERVA | 37470.01 |
| Urea | ROTH | 3941.1 |
| Vivaspin 2 PES Centrifugal Concentrator | Sartorius | VS0201 |
| Xylene cyanol | Merk/Sigma-Aldrich | X4126-10G |
| Yeast extract | MP Biomedicals | 103303 |

5.4. List of kits

| Unit | Manufacturer | Cat.No. |
|--|---------------|-----------|
| BCA Protein Assay Kit (RAC) | Thermo Fisher | 23250 |
| Coomassie Plus (Bradford) Assay Kit | Thermo Fisher | 23236 |
| Gibson Assembly Cloning Kit | NEB | E5510S |
| VRDye 490 Protein Labelling Kit | LI-COR | 928-49040 |
| Wizard Plus Minipreps DNA Purification Kit | Promega | A7510 |
| Wizard SV Gel and PCR Cleanup Kit | Promega | A9281 |

5.5. List of enzymes

| Unit | Manufacturer | Cat.No. |
|--------------------------------------|--------------|---------|
| EcoRI-HF | NEB | R3101S |
| HindIII-HF | NEB | R3104S |
| NcoI-HF | NEB | R3193S |
| Phusion High-Fidelity DNA Polymerase | NEB | M0530L |
| Q5 High-Fidelity DNA Polymerase | NEB | M0491L |
| T4 DNA Ligase | NEB | M0202L |
| T4 Polynucleotide Kinase | NEB | M0201L |
| Taq DNA Polymerase | NEB | M0273L |

5.6. List of enzymatic buffers and its components

| Unit | Manufacturer | Cat.No. |
|--|--------------|---------|
| Phusion DMSO | NEB | B0515A |
| Phusion GC Buffer Pack | NEB | B0519S |
| Phusion HF Buffer Pack | NEB | B0518S |
| Phusion MgCl ₂ solution | NEB | B0510A |
| Q5 High GC Enhancer | NEB | B9028A |
| Q5 Reaction Buffer Pack | NEB | B9027S |
| rCutSmart Buffer | NEB | B6004S |
| Standard Taq Reaction Buffer Pack | NEB | B9014S |
| T4 DNA Ligase Reaction Buffer | NEB | B0202S |
| T4 Polynucleotide Kinase Reaction Buffer | NEB | B0201S |

5.7. List of antibodies

| ID | Type | Dilution | Host | Specificity | Origin |
|-----------|---------------------|----------|--------|----------------|-------------|
| 328800 | 1° pAb | 1:500 | Rabbit | LAF-1(L+S) | MPI-CBG |
| 329787 | 1° pAb | 1:500 | Rabbit | LAF-1(L+S) | MPI-CBG |
| 926-32210 | 2° pAb, IRDye 800CW | 1:1000 | Goat | Mouse IgG | LI-COR |
| 926-32211 | 2° pAb, IRDye 800CW | 1:1000 | Goat | Rabbit IgG | LI-COR |
| 926-68071 | 2° pAb, IRDye 680RD | 1:1000 | Goat | Rabbit IgG | LI-COR |
| BF30 | 1° mAb | 1:1000 | Mouse | Not identified | MPI-CBG |
| BW75 | 1° mAb | 1:1000 | Mouse | LAF-1(L+S) | MPI-CBG |
| BW77 | 1° mAb | 1:1000 | Mouse | LAF-1 | MPI-CBG |
| BY89 | 1° mAb | 1:1000 | Mouse | LAF-1 | MPI-CBG |
| BY90 | 1° mAb | 1:1000 | Mouse | LAF-1 | MPI-CBG |
| B-5-1-2 | 1° mAb | 1:10000 | Mouse | tubulin | Merk: T5168 |

5.8. List of primers

| ID | Sequence | purpose |
|---------|---|------------|
| CE06351 | ttaagaaggagatataaccatgGAATCCAATCAATCCAATAAC | cloning |
| CE06352 | acggagctcgaattcggatccTTTGTTAGCAGCCGGATCTCA | cloning |
| CE06353 | AGTGGCGAGCCCGATCTTCCC | sequencing |
| CE06354 | ATTGTGAGCGGATAACAATTC | sequencing |
| CE06359 | GCAGCCGATCTCACTGTTTTC | sequencing |
| CE06360 | CGGTTTCAGGCAAAACGGCCGC | sequencing |
| CE06365 | ACAATTTGAACGTGAAAAACA | sequencing |
| CE06366 | TACGTTACCGTATTGGCCGC | sequencing |
| CE06552 | CATGGTATATCTCCTTCTTAAAGT | cloning |
| CE06553 | AATTCGAGCTCCGTCGACAAGCTT | cloning |
| CE06554 | aaggagatataccatgTCAGATTCTGAAATAGCATTTGAG | cloning |
| CE06555 | cgacggagctcgaattGACGGCGGATTTCTCGGCCACTGG | cloning |
| CE06556 | aaggagatataccatgTCCGAAGAACCAGTCGCAGCTCCT | cloning |
| CE06557 | cgacggagctcgaattAGTGGCTGGTGTGGCAGGAGTCTC | cloning |
| CE06558 | aaggagatataccatgAGCACATCCGTAGCGGAAAAACAAA | cloning |
| CE06559 | cgacggagctcgaattAGGAGTTGGGGTGGCTGGAGAAGT | cloning |
| CE06560 | aaggagatataccatgGAAGCTGAAACGTCAACTCAGGAA | cloning |
| CE06561 | cgacggagctcgaattTTTGCAGATATTTTTAGTAGTATG | cloning |
| CE06562 | aaggagatataccatgACTGAATTGACGACACCCATCTAT | cloning |
| CE06563 | cgacggagctcgaattGACGATGGATTTCAATGAAAATTT | cloning |
| CE06581 | ATTACCGCTATGTTTTCAGC | cloning |
| CE06582 | ACATTCTTCTTTGGACGGCATA | cloning |
| CE06583 | TTTTCAGCGACGTTCCCGAAAG | cloning |
| CE06584 | AATAGCGGTAATGCGTTCTTCT | cloning |
| CE06585 | TTCCCGAAAGAAATCCAGCTG | cloning |
| CE06586 | AATCGCTGAAAACATAGCGGTA | cloning |
| CE06792 | GGCGGTATCGTCGC | cloning |
| CE06793 | CATGGTATATCTCCTTCTTAAAGTTAA | cloning |
| CE06794 | GGCGGTGGCGGTGGCGGTGGCAATCG | cloning |
| CE06795 | ACCGCCCGCACCGCCGCGACGGTC | cloning |
| CE06796 | GGTAGTGGCCGTTCTACAATAAC | cloning |
| CE06797 | GTTGTAACCACGGTCTTCATAATTACGATC | cloning |
| CE06798 | TTTTCCGGCCAACCTGTCAGGTATCAAC | cloning |
| CE06799 | GCGGTTGTCGCTGCCTTCA | cloning |
| CE06903 | CATCTTCTTCCACCCAGACGA | cloning |
| CE06904 | AAAAACGCTCGTACCTGATGGA | cloning |
| CE07085 | AGCAGATGCAGCTGC | cloning |
| CE07086 | GGCGGTGGCAATCG | cloning |
| CE07156 | CGTGATGAACGCATTGAACAGGAACTG | cloning |
| CE07157 | CATGGTATATCTCCTTCTTAAAGTTAAACAAAATTATTC | cloning |
| CE07158 | AAGCTTGCGGCCGCACTCGAGCACCACCACCAC | cloning |
| CE07159 | CAGCCAATCCGGCAGTTCTGATTTGCTTCCACGATCAG | cloning |

5.9. List of primer combinations to clone new LAF-1 expression plasmids

| Construct name | Modification | Forward primer | Reverse primer |
|------------------------|-------------------|----------------|----------------|
| 6xHis::LAF-1L (WT) | G477E fix | CE06903 | CE06904 |
| LAF-1L(WT)::6xHis | C-term. 6xHis | CE06351 | CE06352 |
| LAF-1L(q80)::6xHis | R426C | CE06581 | CE06582 |
| LAF-1L(q217)::6xHis | M430I | CE06583 | CE06584 |
| LAF-1L(q267)::6xHis | T434I | CE06585 | CE06586 |
| LAF-1S::6xHis | Δ41-105 of LAF-1L | CE07085 | CE07086 |
| LAF-1L ΔRGG::6xHis | Δ2-191 | CE07156 | CE07157 |
| LAF-1L ΔGQ::6xHis | Δ623-708 | CE07158 | CE07159 |
| 6xHis::LAF-1L Δ2-51 | Δ2-51 | CE06792 | CE06793 |
| 6xHis::LAF-1L Δ50-101 | Δ50-101 | CE06794 | CE06795 |
| 6xHis::LAF-1L Δ102-151 | Δ102-151 | CE06796 | CE06797 |
| 6xHis::LAF-1L Δ152-201 | Δ152-201 | CE06798 | CE06799 |

5.10. List of primer combinations to clone IFE-x expression constructs

| Construct name | Size (aa) | Forward primer | Reverse primer |
|-------------------|-----------|----------------|----------------|
| pET-28b+ backbone | 0 | CE06552 | CE06553 |
| IFE-1::6xHis | 250 | CE06554 | CE06555 |
| IFE-2::6xHis | 247 | CE06556 | CE06557 |
| IFE-3::6xHis | 267 | CE06558 | CE06559 |
| IFE-4::6xHis | 231 | CE06560 | CE06561 |
| IFE-5::6xHis | 220 | CE06562 | CE06563 |

5.11. List of *C. elegans* strains

| Strain | Genotype | Reference |
|--------|---|-------------|
| N2 | Wild type – isolate Bristol | CGC |
| EV1280 | <i>laf-1(ef117) / qC1[dpy-19(e1259ts) glp-1(q339) nIs189 [myo-2::gfp]] III line 171-7 [Short only] 2x backcrossed</i> | unpublished |
| EV1324 | <i>laf-1(ef127) / qC1[dpy-19(e1259ts) glp-1(q339) nIs189[myo-2::gfp]] III line A34-14-5 [Long only]</i> | unpublished |

5.12. LC-MS/MS results of 42 selected protein markers of embryonic stage

| Gene | iBAQ | relative iBAQ | Seq. coverage | Score | Intensity |
|---------------|-----------|---------------|---------------|--------|-------------|
| <i>car-1</i> | 31541000 | 4.54314E-05 | 24.6 | 208.88 | 1608600000 |
| <i>cgh-1</i> | 458410000 | 0.000660291 | 70 | 323.31 | 11460000000 |
| <i>deps-1</i> | 34181000 | 4.92341E-05 | 30.2 | 35.116 | 1093800000 |
| <i>glh-1</i> | 2774000 | 3.99565E-06 | 20.2 | 29.808 | 97089000 |
| <i>glh-1</i> | 2774000 | 3.99565E-06 | 20.2 | 29.808 | 97089000 |
| <i>glh-2</i> | 16758000 | 2.41381E-05 | 17.7 | 85.206 | 653560000 |
| <i>glh-4</i> | 3795500 | 5.46701E-06 | 18.5 | 32.853 | 261890000 |
| <i>gls-1</i> | 5877400 | 8.46577E-06 | 6.4 | 12.331 | 182200000 |
| <i>laf-1</i> | 194950000 | 0.000280805 | 47.5 | 323.31 | 8188100000 |
| <i>mex-3</i> | 2675200 | 3.85334E-06 | 13 | 7.0121 | 53505000 |
| <i>mex-5</i> | 1178800 | 1.69794E-06 | 7.9 | 3.7333 | 20040000 |
| <i>mex-6</i> | 1671000 | 2.4069E-06 | 6.6 | 2.2343 | 26736000 |
| <i>nmy-1</i> | 23497000 | 3.38449E-05 | 39.1 | 323.31 | 2443700000 |
| <i>nmy-2</i> | 76155000 | 0.000109693 | 51.9 | 323.31 | 9062400000 |
| <i>nos-1</i> | 73866000 | 0.000106396 | 56.6 | 124.62 | 1846600000 |
| <i>nos-2</i> | | | | | |
| <i>nos-3</i> | 2257200 | 3.25126E-06 | 8.8 | 15.112 | 69973000 |
| <i>ntl-1</i> | 3185800 | 4.5888E-06 | 13.6 | 4.5622 | 57345000 |
| <i>ntl-2</i> | 6374000 | 9.18107E-06 | 4.1 | 6.9682 | 70114000 |
| <i>ntl-3</i> | 13024000 | 1.87597E-05 | 11.1 | 11.962 | 351660000 |
| <i>ntl-5</i> | | | | | |
| <i>ntl-9</i> | 91348000 | 0.000131577 | 44.8 | 76.771 | 1278900000 |
| <i>pab-1</i> | 755180000 | 0.001087756 | 67 | 323.31 | 24921000000 |
| <i>pab-2</i> | 68658000 | 9.88945E-05 | 41.9 | 208.16 | 2265700000 |
| <i>panl-2</i> | 2169200 | 3.1245E-06 | 7.7 | 26.873 | 119310000 |
| <i>par-1</i> | 22520000 | 3.24377E-05 | 28.2 | 190.66 | 968360000 |
| <i>par-2</i> | | | | | |
| <i>par-3</i> | 389750 | 5.61393E-07 | 1.8 | 3.0961 | 27672000 |
| <i>par-4</i> | 4774600 | 6.8773E-06 | 14.9 | 12.806 | 85943000 |
| <i>par-6</i> | 21760000 | 3.1343E-05 | 33.3 | 18.29 | 326400000 |
| <i>pgl-1</i> | 65786000 | 9.47577E-05 | 47 | 114.95 | 2960400000 |
| <i>pgl-3</i> | 31876000 | 4.5914E-05 | 37.5 | 165.8 | 1243200000 |
| <i>pos-1</i> | 4119000 | 5.93298E-06 | 11 | 5.432 | 61784000 |
| <i>rde-2</i> | 0 | 0 | 1 | 2.3933 | 0 |
| <i>rde-4</i> | 33285000 | 4.79435E-05 | 31.7 | 39.305 | 499280000 |
| <i>rde-8</i> | 774150 | 1.11508E-06 | 13.6 | 3.0665 | 14709000 |
| <i>rde-12</i> | 38325000 | 5.52031E-05 | 38.1 | 248.43 | 2069600000 |
| <i>spn-2</i> | | | | | |
| <i>spn-4</i> | 2040400 | 2.93898E-06 | 7.7 | 4.7014 | 40809000 |
| <i>vbh-1</i> | 116670000 | 0.000168051 | 50.3 | 226.2 | 3616700000 |
| <i>wago-1</i> | 27913000 | 4.02057E-05 | 32.5 | 167.97 | 1367700000 |
| <i>wago-4</i> | 22821000 | 3.28712E-05 | 30.3 | 67.616 | 1163900000 |

Proteins that were not identified or have insignificant peptide coverage labelled in orange. *laf-1* labelled in green. Relative intensity based absolute quantifications (iBAQ) were determined relative to the sum of all identified peptides.

6. References

- Abdelhaleem, M. (2005). RNA helicases: regulators of differentiation. *Clin Biochem*, 38(6), 499-503. <https://doi.org/10.1016/j.clinbiochem.2005.01.010>
- Aida, H., Shigeta, Y., & Harada, R. (2022). The role of ATP in solubilizing RNA-binding protein fused in sarcoma. *Proteins*, 90(8), 1606-1612. <https://doi.org/10.1002/prot.26335>
- Albarqi, M. M. Y., & Ryder, S. P. (2022). The role of RNA-binding proteins in orchestrating germline development in *Caenorhabditis elegans*. *Front Cell Dev Biol*, 10, 1094295. <https://doi.org/10.3389/fcell.2022.1094295>
- Angus, A. G., Dalrymple, D., Boulant, S., McGivern, D. R., Clayton, R. F., Scott, M. J., Adair, R., Graham, S., Owsianka, A. M., Targett-Adams, P., Li, K., Wakita, T., McLauchlan, J., Lemon, S. M., & Patel, A. H. (2010). Requirement of cellular DDX3 for hepatitis C virus replication is unrelated to its interaction with the viral core protein. *J Gen Virol*, 91(Pt 1), 122-132. <https://doi.org/10.1099/vir.0.015909-0>
- Argon, Y., & Ward, S. (1980). *Caenorhabditis elegans* fertilization-defective mutants with abnormal sperm. *Genetics*, 96(2), 413-433. <https://doi.org/10.1093/genetics/96.2.413>
- Benjamini, Y., & Hochberg, Y. (1995). Controlling the False Discovery Rate - a Practical and Powerful Approach to Multiple Testing. *Journal of the Royal Statistical Society Series B-Statistical Methodology*, 57(1), 289-300. <https://doi.org/DOI> 10.1111/j.2517-6161.1995.tb02031.x
- Botlagunta, M., Vesuna, F., Mironchik, Y., Raman, A., Lisok, A., Winnard, P., Jr., Mukadam, S., Van Diest, P., Chen, J. H., Farabaugh, P., Patel, A. H., & Raman, V. (2008). Oncogenic role of DDX3 in breast cancer biogenesis. *Oncogene*, 27(28), 3912-3922. <https://doi.org/10.1038/onc.2008.33>
- Brangwynne, C. P., Eckmann, C. R., Courson, D. S., Rybarska, A., Hoege, C., Gharakhani, J., Julicher, F., & Hyman, A. A. (2009). Germline P granules are liquid droplets that localize by controlled dissolution/condensation. *Science*, 324(5935), 1729-1732. <https://doi.org/10.1126/science.1172046>
- Brenner, S. (1973). The genetics of behaviour. *Br Med Bull*, 29(3), 269-271. <https://doi.org/10.1093/oxfordjournals.bmb.a071019>
- Brenner, S. (1974). The genetics of *Caenorhabditis elegans*. *Genetics*, 77(1), 71-94. <https://doi.org/10.1093/genetics/77.1.71>

- Byerly, L., Cassada, R. C., & Russell, R. L. (1976). The life cycle of the nematode *Caenorhabditis elegans*. I. Wild-type growth and reproduction. *Dev Biol*, *51*(1), 23-33. [https://doi.org/10.1016/0012-1606\(76\)90119-6](https://doi.org/10.1016/0012-1606(76)90119-6)
- Cabrita, L. D., & Bottomley, S. P. (2004). Protein expression and refolding--a practical guide to getting the most out of inclusion bodies. *Biotechnol Annu Rev*, *10*, 31-50. [https://doi.org/10.1016/S1387-2656\(04\)10002-1](https://doi.org/10.1016/S1387-2656(04)10002-1)
- Calviello, L., Venkataramanan, S., Rogowski, K. J., Wyler, E., Wilkins, K., Tejura, M., Thai, B., Krol, J., Filipowicz, W., Landthaler, M., & Floor, S. N. (2021). DDX3 depletion represses translation of mRNAs with complex 5' UTRs. *Nucleic Acids Res*, *49*(9), 5336-5350. <https://doi.org/10.1093/nar/gkab287>
- Chao, C. H., Chen, C. M., Cheng, P. L., Shih, J. W., Tsou, A. P., & Lee, Y. H. (2006). DDX3, a DEAD box RNA helicase with tumor growth-suppressive property and transcriptional regulation activity of the p21waf1/cip1 promoter, is a candidate tumor suppressor. *Cancer Res*, *66*(13), 6579-6588. <https://doi.org/10.1158/0008-5472.CAN-05-2415>
- Chen, Y. P., Tang, L. L., Yang, Q., Poh, S. S., Hui, E. P., Chan, A. T. C., Ong, W. S., Tan, T., Wee, J., Li, W. F., Chen, L., Ma, B. B. Y., Tong, M., Tan, S. H., Cheah, S. L., Fong, K. W., Sommat, K., Soong, Y. L., Guo, Y., . . . Ma, J. (2018). Induction Chemotherapy plus Concurrent Chemoradiotherapy in Endemic Nasopharyngeal Carcinoma: Individual Patient Data Pooled Analysis of Four Randomized Trials. *Clin Cancer Res*, *24*(8), 1824-1833. <https://doi.org/10.1158/1078-0432.CCR-17-2656>
- Chong, P. A., Vernon, R. M., & Forman-Kay, J. D. (2018). RGG/RG Motif Regions in RNA Binding and Phase Separation. *J Mol Biol*, *430*(23), 4650-4665. <https://doi.org/10.1016/j.jmb.2018.06.014>
- Chuang, J. H., & Li, H. (2004). Functional bias and spatial organization of genes in mutational hot and cold regions in the human genome. *PLoS Biol*, *2*(2), E29. <https://doi.org/10.1371/journal.pbio.0020029>
- Consortium, C. e. S. (1998). Genome sequence of the nematode *C. elegans*: a platform for investigating biology. *Science*, *282*(5396), 2012-2018. <https://doi.org/10.1126/science.282.5396.2012>
- Cordin, O., Banroques, J., Tanner, N. K., & Linder, P. (2006). The DEAD-box protein family of RNA helicases. *Gene*, *367*, 17-37. <https://doi.org/10.1016/j.gene.2005.10.019>
- Cordin, O., Tanner, N. K., Doere, M., Linder, P., & Banroques, J. (2004). The newly discovered Q motif of DEAD-box RNA helicases regulates RNA-binding and helicase activity. *EMBO J*, *23*(13), 2478-2487. <https://doi.org/10.1038/sj.emboj.7600272>

- Dang, M., Li, T., & Song, J. (2023). ATP and nucleic acids competitively modulate LLPS of the SARS-CoV2 nucleocapsid protein. *Commun Biol*, 6(1), 80. <https://doi.org/10.1038/s42003-023-04480-3>
- Das, S., Lin, Y. H., Vernon, R. M., Forman-Kay, J. D., & Chan, H. S. (2020). Comparative roles of charge, pi, and hydrophobic interactions in sequence-dependent phase separation of intrinsically disordered proteins. *Proc Natl Acad Sci U S A*, 117(46), 28795-28805. <https://doi.org/10.1073/pnas.2008122117>
- De Colibus, L., Stunnenberg, M., & Geijtenbeek, T. B. H. (2022). DDX3X structural analysis: Implications in the pharmacology and innate immunity. *Curr Res Immunol*, 3, 100-109. <https://doi.org/10.1016/j.crimmu.2022.05.002>
- Dignon, G. L., Zheng, W., Kim, Y. C., & Mittal, J. (2019). Temperature-Controlled Liquid-Liquid Phase Separation of Disordered Proteins. *ACS Cent Sci*, 5(5), 821-830. <https://doi.org/10.1021/acscentsci.9b00102>
- Elbaum-Garfinkle, S., Kim, Y., Szczepaniak, K., Chen, C. C., Eckmann, C. R., Myong, S., & Brangwynne, C. P. (2015). The disordered P granule protein LAF-1 drives phase separation into droplets with tunable viscosity and dynamics. *Proc Natl Acad Sci U S A*, 112(23), 7189-7194. <https://doi.org/10.1073/pnas.1504822112>
- Epling, L. B., Grace, C. R., Lowe, B. R., Partridge, J. F., & Enemark, E. J. (2015). Cancer-associated mutants of RNA helicase DDX3X are defective in RNA-stimulated ATP hydrolysis. *J Mol Biol*, 427(9), 1779-1796. <https://doi.org/10.1016/j.jmb.2015.02.015>
- Fairman-Williams, M. E., Guenther, U. P., & Jankowsky, E. (2010). SF1 and SF2 helicases: family matters. *Curr Opin Struct Biol*, 20(3), 313-324. <https://doi.org/10.1016/j.sbi.2010.03.011>
- Floor, S. N., Condon, K. J., Sharma, D., Jankowsky, E., & Doudna, J. A. (2016). Autoinhibitory Interdomain Interactions and Subfamily-specific Extensions Redefine the Catalytic Core of the Human DEAD-box Protein DDX3. *J Biol Chem*, 291(5), 2412-2421. <https://doi.org/10.1074/jbc.M115.700625>
- Franca, R., Belfiore, A., Spadari, S., & Maga, G. (2007). Human DEAD-box ATPase DDX3 shows a relaxed nucleoside substrate specificity. *Proteins*, 67(4), 1128-1137. <https://doi.org/10.1002/prot.21433>
- Frezal, L., & Felix, M. A. (2015). C. elegans outside the Petri dish. *Elife*, 4. <https://doi.org/10.7554/eLife.05849>
- Gebauer, F., & Hentze, M. W. (2004). Molecular mechanisms of translational control. *Nat Rev Mol Cell Biol*, 5(10), 827-835. <https://doi.org/10.1038/nrm1488>

- Geissler, R., Golbik, R. P., & Behrens, S. E. (2012). The DEAD-box helicase DDX3 supports the assembly of functional 80S ribosomes. *Nucleic Acids Res*, *40*(11), 4998-5011. <https://doi.org/10.1093/nar/gks070>
- Goodwin, E. B., Hofstra, K., Hurney, C. A., Mango, S., & Kimble, J. (1997). A genetic pathway for regulation of tra-2 translation. *Development*, *124*(3), 749-758. <https://doi.org/10.1242/dev.124.3.749>
- Goodwin, E. B., Okkema, P. G., Evans, T. C., & Kimble, J. (1993). Translational regulation of tra-2 by its 3' untranslated region controls sexual identity in *C. elegans*. *Cell*, *75*(2), 329-339. [https://doi.org/10.1016/0092-8674\(93\)80074-o](https://doi.org/10.1016/0092-8674(93)80074-o)
- Gotze, M., Dufourt, J., Ihling, C., Rammelt, C., Pierson, S., Sambrani, N., Temme, C., Sinz, A., Simonelig, M., & Wahle, E. (2017). Translational repression of the *Drosophila* nanos mRNA involves the RNA helicase Belle and RNA coating by Me31B and Trailer hitch. *RNA*, *23*(10), 1552-1568. <https://doi.org/10.1261/rna.062208.117>
- Gururajan, R., Perry-O'Keefe, H., Melton, D. A., & Weeks, D. L. (1991). The *Xenopus* localized messenger RNA An3 may encode an ATP-dependent RNA helicase. *Nature*, *349*(6311), 717-719. <https://doi.org/10.1038/349717a0>
- Han, Y., & Yang, H. (2020). The transmission and diagnosis of 2019 novel coronavirus infection disease (COVID-19): A Chinese perspective. *J Med Virol*, *92*(6), 639-644. <https://doi.org/10.1002/jmv.25749>
- Hellen, C. U. T. (2018). Translation Termination and Ribosome Recycling in Eukaryotes. *Cold Spring Harb Perspect Biol*, *10*(10). <https://doi.org/10.1101/cshperspect.a032656>
- Hinnebusch, A. G. (2014). The scanning mechanism of eukaryotic translation initiation. *Annu Rev Biochem*, *83*, 779-812. <https://doi.org/10.1146/annurev-biochem-060713-035802>
- Hinnebusch, A. G., Ivanov, I. P., & Sonenberg, N. (2016). Translational control by 5'-untranslated regions of eukaryotic mRNAs. *Science*, *352*(6292), 1413-1416. <https://doi.org/10.1126/science.aad9868>
- Hubbard, E. J., & Greenstein, D. (2005). Introduction to the germ line. *WormBook*, 1-4. <https://doi.org/10.1895/wormbook.1.18.1>
- Hubert, A., & Anderson, P. (2009). The *C. elegans* sex determination gene *laf-1* encodes a putative DEAD-box RNA helicase. *Dev Biol*, *330*(2), 358-367. <https://doi.org/10.1016/j.ydbio.2009.04.003>
- Huggins, H. P., Subash, J. S., Stoffel, H., Henderson, M. A., Hoffman, J. L., Buckner, D. S., Sengupta, M. S., Boag, P. R., Lee, M. H., & Keiper, B. D. (2020). Distinct roles of two

- eIF4E isoforms in the germline of *Caenorhabditis elegans*. *J Cell Sci*, 133(6). <https://doi.org/10.1242/jcs.237990>
- Hunt, P. R. (2017). The *C. elegans* model in toxicity testing. *J Appl Toxicol*, 37(1), 50-59. <https://doi.org/10.1002/jat.3357>
- Ihry, R. J., Sapiro, A. L., & Bashirullah, A. (2012). Translational control by the DEAD Box RNA helicase belle regulates ecdysone-triggered transcriptional cascades. *PLoS Genet*, 8(11), e1003085. <https://doi.org/10.1371/journal.pgen.1003085>
- Iost, I., Dreyfus, M., & Linder, P. (1999). Ded1p, a DEAD-box protein required for translation initiation in *Saccharomyces cerevisiae*, is an RNA helicase. *J Biol Chem*, 274(25), 17677-17683. <https://doi.org/10.1074/jbc.274.25.17677>
- Jarmoskaite, I., & Russell, R. (2011). DEAD-box proteins as RNA helicases and chaperones. *Wiley Interdiscip Rev RNA*, 2(1), 135-152. <https://doi.org/10.1002/wrna.50>
- Jensen, P., Patel, B., Smith, S., Sabnis, R., & Kaboord, B. (2021). Improved Immunoprecipitation to Mass Spectrometry Method for the Enrichment of Low-Abundant Protein Targets. *Methods Mol Biol*, 2261, 229-246. https://doi.org/10.1007/978-1-0716-1186-9_14
- Jiang, L., Gu, Z. H., Yan, Z. X., Zhao, X., Xie, Y. Y., Zhang, Z. G., Pan, C. M., Hu, Y., Cai, C. P., Dong, Y., Huang, J. Y., Wang, L., Shen, Y., Meng, G., Zhou, J. F., Hu, J. D., Wang, J. F., Liu, Y. H., Yang, L. H., . . . Chen, S. J. (2015). Exome sequencing identifies somatic mutations of DDX3X in natural killer/T-cell lymphoma. *Nat Genet*, 47(9), 1061-1066. <https://doi.org/10.1038/ng.3358>
- Johnstone, O., Deuring, R., Bock, R., Linder, P., Fuller, M. T., & Lasko, P. (2005). Belle is a *Drosophila* DEAD-box protein required for viability and in the germ line. *Dev Biol*, 277(1), 92-101. <https://doi.org/10.1016/j.ydbio.2004.09.009>
- Jones, P. A. (2012). Functions of DNA methylation: islands, start sites, gene bodies and beyond. *Nat Rev Genet*, 13(7), 484-492. <https://doi.org/10.1038/nrg3230>
- Jumper, J., Evans, R., Pritzel, A., Green, T., Figurnov, M., Ronneberger, O., Tunyasuvunakool, K., Bates, R., Zidek, A., Potapenko, A., Bridgland, A., Meyer, C., Kohl, S. A. A., Ballard, A. J., Cowie, A., Romera-Paredes, B., Nikolov, S., Jain, R., Adler, J., . . . Hassabis, D. (2021). Highly accurate protein structure prediction with AlphaFold. *Nature*, 596(7873), 583-589. <https://doi.org/10.1038/s41586-021-03819-2>
- Kamath, R. S., Fraser, A. G., Dong, Y., Poulin, G., Durbin, R., Gotta, M., Kanapin, A., Le Bot, N., Moreno, S., Sohrmann, M., Welchman, D. P., Zipperlen, P., & Ahringer, J. (2003).

- Systematic functional analysis of the *Caenorhabditis elegans* genome using RNAi. *Nature*, 421(6920), 231-237. <https://doi.org/10.1038/nature01278>
- Keiper, B. D., Lamphear, B. J., Deshpande, A. M., Jankowska-Anyszka, M., Aamodt, E. J., Blumenthal, T., & Rhoads, R. E. (2000). Functional characterization of five eIF4E isoforms in *Caenorhabditis elegans*. *J Biol Chem*, 275(14), 10590-10596. <https://doi.org/10.1074/jbc.275.14.10590>
- Khan, F. R., & Mcfadden, B. A. (1980). A Rapid Method of Synchronizing Developmental Stages of *Caenorhabditis-Elegans*. *Nematologica*, 26(2), 280-282. <https://doi.org/10.1163/187529280x00189>
- Khong, A., & Parker, R. (2020). The landscape of eukaryotic mRNPs. *RNA*, 26(3), 229-239. <https://doi.org/10.1261/rna.073601.119>
- Kim, Y., & Myong, S. (2016). RNA Remodeling Activity of DEAD Box Proteins Tuned by Protein Concentration, RNA Length, and ATP. *Mol Cell*, 63(5), 865-876. <https://doi.org/10.1016/j.molcel.2016.07.010>
- Kim, Y. S., Lee, S. G., Park, S. H., & Song, K. (2001). Gene structure of the human DDX3 and chromosome mapping of its related sequences. *Mol Cells*, 12(2), 209-214. <https://www.ncbi.nlm.nih.gov/pubmed/11710523>
- Kimble, J., & Crittenden, S. L. (2007). Controls of germline stem cells, entry into meiosis, and the Sperm/Oocyte decision in *Caenorhabditis elegans*. *Annual Review of Cell and Developmental Biology*, 23, 405-433. <https://doi.org/10.1146/annurev.cellbio.23.090506.123326>
- Kozak, M. (1990). Downstream secondary structure facilitates recognition of initiator codons by eukaryotic ribosomes. *Proc Natl Acad Sci U S A*, 87(21), 8301-8305. <https://doi.org/10.1073/pnas.87.21.8301>
- Kutscher, L. M., & Shaham, S. (2014). Forward and reverse mutagenesis in *C. elegans*. *WormBook*, 1-26. <https://doi.org/10.1895/wormbook.1.167.1>
- Kuwabara, P. E., Okkema, P. G., & Kimble, J. (1998). Germ-line regulation of the *Caenorhabditis elegans* sex-determining gene *tra-2*. *Dev Biol*, 204(1), 251-262. <https://doi.org/10.1006/dbio.1998.9062>
- Kuznicki, K. A., Smith, P. A., Leung-Chiu, W. M., Estevez, A. O., Scott, H. C., & Bennett, K. L. (2000). Combinatorial RNA interference indicates GLH-4 can compensate for GLH-1; these two P granule components are critical for fertility in *C. elegans*. *Development*, 127(13), 2907-2916. <https://doi.org/10.1242/dev.127.13.2907>

- Laemmli, U. K. (1970). Cleavage of structural proteins during the assembly of the head of bacteriophage T4. *Nature*, 227(5259), 680-685. <https://doi.org/10.1038/227680a0>
- Lai, M. C., Lee, Y. H., & Tarn, W. Y. (2008). The DEAD-box RNA helicase DDX3 associates with export messenger ribonucleoproteins as well as tip-associated protein and participates in translational control. *Mol Biol Cell*, 19(9), 3847-3858. <https://doi.org/10.1091/mbc.e07-12-1264>
- Lane, D. (1988). Enlarged family of putative helicases. *Nature*, 334(6182), 478. <https://doi.org/10.1038/334478a0>
- Langdon, E. M., Qiu, Y., Ghanbari Niaki, A., McLaughlin, G. A., Weidmann, C. A., Gerbich, T. M., Smith, J. A., Crutchley, J. M., Termini, C. M., Weeks, K. M., Myong, S., & Gladfelter, A. S. (2018). mRNA structure determines specificity of a polyQ-driven phase separation. *Science*, 360(6391), 922-927. <https://doi.org/10.1126/science.aar7432>
- Lasda, E. L., & Blumenthal, T. (2011). Trans-splicing. *Wiley Interdiscip Rev RNA*, 2(3), 417-434. <https://doi.org/10.1002/wrna.71>
- Lee, C. S., Dias, A. P., Jedrychowski, M., Patel, A. H., Hsu, J. L., & Reed, R. (2008). Human DDX3 functions in translation and interacts with the translation initiation factor eIF3. *Nucleic Acids Res*, 36(14), 4708-4718. <https://doi.org/10.1093/nar/gkn454>
- Lennox, A. L., Hoye, M. L., Jiang, R., Johnson-Kerner, B. L., Suit, L. A., Venkataramanan, S., Sheehan, C. J., Alsina, F. C., Fregeau, B., Aldinger, K. A., Moey, C., Lobach, I., Afenjar, A., Babovic-Vuksanovic, D., Bezieau, S., Blackburn, P. R., Bunt, J., Burglen, L., Campeau, P. M., . . . Sherr, E. H. (2020). Pathogenic DDX3X Mutations Impair RNA Metabolism and Neurogenesis during Fetal Cortical Development. *Neuron*, 106(3), 404-420 e408. <https://doi.org/10.1016/j.neuron.2020.01.042>
- Levy, T., Siper, P. M., Lerman, B., Halpern, D., Zweifach, J., Belani, P., Thurm, A., Kleefstra, T., Berry-Kravis, E., Buxbaum, J. D., & Grice, D. E. (2023). DDX3X Syndrome: Summary of Findings and Recommendations for Evaluation and Care. *Pediatr Neurol*, 138, 87-94. <https://doi.org/10.1016/j.pediatrneurol.2022.10.009>
- Liao, S. E., Kandasamy, S. K., Zhu, L., & Fukunaga, R. (2019). DEAD-box RNA helicase Belle posttranscriptionally promotes gene expression in an ATPase activity-dependent manner. *RNA*, 25(7), 825-839. <https://doi.org/10.1261/rna.070268.118>
- Liao, S. E., & Regev, O. (2021). Splicing at the phase-separated nuclear speckle interface: a model. *Nucleic Acids Research*, 49(2). <https://doi.org/10.1093/nar/gkaa1209>

- Linder, P. (2006). Dead-box proteins: a family affair--active and passive players in RNP-remodeling. *Nucleic Acids Res*, *34*(15), 4168-4180. <https://doi.org/10.1093/nar/gkl468>
- Linder, P., & Jankowsky, E. (2011). From unwinding to clamping - the DEAD box RNA helicase family. *Nat Rev Mol Cell Biol*, *12*(8), 505-516. <https://doi.org/10.1038/nrm3154>
- Mamiya, N., & Worman, H. J. (1999). Hepatitis C virus core protein binds to a DEAD box RNA helicase. *J Biol Chem*, *274*(22), 15751-15756. <https://doi.org/10.1074/jbc.274.22.15751>
- Marecki, J. C., Byrd, A. K., & Raney, K. D. (2021). Identifying RNA Helicase Inhibitors Using Duplex Unwinding Assays. *Methods Mol Biol*, *2209*, 53-72. https://doi.org/10.1007/978-1-0716-0935-4_4
- Marsh, E. K., & May, R. C. (2012). *Caenorhabditis elegans*, a model organism for investigating immunity. *Appl Environ Microbiol*, *78*(7), 2075-2081. <https://doi.org/10.1128/AEM.07486-11>
- Merz, C., Urlaub, H., Will, C. L., & Luhrmann, R. (2007). Protein composition of human mRNPs spliced in vitro and differential requirements for mRNP protein recruitment. *RNA*, *13*(1), 116-128. <https://doi.org/10.1261/rna.336807>
- Mittag, T., & Parker, R. (2018). Multiple Modes of Protein-Protein Interactions Promote RNP Granule Assembly. *J Mol Biol*, *430*(23), 4636-4649. <https://doi.org/10.1016/j.jmb.2018.08.005>
- Miyoshi, H., Dwyer, D. S., Keiper, B. D., Jankowska-Anyszka, M., Darzynkiewicz, E., & Rhoads, R. E. (2002). Discrimination between mono- and trimethylated cap structures by two isoforms of *Caenorhabditis elegans* eIF4E. *EMBO J*, *21*(17), 4680-4690. <https://doi.org/10.1093/emboj/cdf473>
- Montpetit, B., Thomsen, N. D., Helmke, K. J., Seeliger, M. A., Berger, J. M., & Weis, K. (2011). A conserved mechanism of DEAD-box ATPase activation by nucleoporins and InsP6 in mRNA export. *Nature*, *472*(7342), 238-242. <https://doi.org/10.1038/nature09862>
- Nicola, P., Blackburn, P. R., Rasmussen, K. J., Bertsch, N. L., Klee, E. W., Hasadsri, L., Pichurin, P. N., Rankin, J., Raymond, F. L., Study, D. D. D., & Clayton-Smith, J. (2019). De novo DDX3X missense variants in males appear viable and contribute to syndromic intellectual disability. *Am J Med Genet A*, *179*(4), 570-578. <https://doi.org/10.1002/ajmg.a.61061>

- Oh, S., Flynn, R. A., Floor, S. N., Purzner, J., Martin, L., Do, B. T., Schubert, S., Vaka, D., Morrissy, S., Li, Y., Kool, M., Hovestadt, V., Jones, D. T., Northcott, P. A., Risch, T., Warnatz, H. J., Yaspo, M. L., Adams, C. M., Leib, R. D., . . . Cho, Y. J. (2016). Medulloblastoma-associated DDX3 variant selectively alters the translational response to stress. *Oncotarget*, 7(19), 28169-28182. <https://doi.org/10.18632/oncotarget.8612>
- Orsborn, A. M., Li, W., McEwen, T. J., Mizuno, T., Kuzmin, E., Matsumoto, K., & Bennett, K. L. (2007). GLH-1, the *C. elegans* P granule protein, is controlled by the JNK KGB-1 and by the COP9 subunit CSN-5. *Development*, 134(18), 3383-3392. <https://doi.org/10.1242/dev.005181>
- Ozdilek, B. A., Thompson, V. F., Ahmed, N. S., White, C. I., Batey, R. T., & Schwartz, J. C. (2017). Intrinsically disordered RGG/RG domains mediate degenerate specificity in RNA binding. *Nucleic Acids Res*, 45(13), 7984-7996. <https://doi.org/10.1093/nar/gkx460>
- Padmanabhan, P. K., Ferreira, G. R., Zghidi-Abouzid, O., Oliveira, C., Dumas, C., Mariz, F. C., & Papadopoulou, B. (2021). Genetic depletion of the RNA helicase DDX3 leads to impaired elongation of translating ribosomes triggering co-translational quality control of newly synthesized polypeptides. *Nucleic Acids Res*, 49(16), 9459-9478. <https://doi.org/10.1093/nar/gkab667>
- Patel, A., Malinowska, L., Saha, S., Wang, J., Alberti, S., Krishnan, Y., & Hyman, A. A. (2017). ATP as a biological hydrotrope. *Science*, 356(6339), 753-756. <https://doi.org/10.1126/science.aaf6846>
- Pelletier, J., & Sonenberg, N. (2019). The Organizing Principles of Eukaryotic Ribosome Recruitment. *Annu Rev Biochem*, 88, 307-335. <https://doi.org/10.1146/annurev-biochem-013118-111042>
- Phillips, C. M., & Updike, D. L. (2022). Germ granules and gene regulation in the *Caenorhabditis elegans* germline. *Genetics*, 220(3). <https://doi.org/10.1093/genetics/iyab195>
- Protter, D. S. W., & Parker, R. (2016). Principles and Properties of Stress Granules. *Trends Cell Biol*, 26(9), 668-679. <https://doi.org/10.1016/j.tcb.2016.05.004>
- Protter, D. S. W., Rao, B. S., Van Treeck, B., Lin, Y., Mizoue, L., Rosen, M. K., & Parker, R. (2018). Intrinsically Disordered Regions Can Contribute Promiscuous Interactions to RNP Granule Assembly. *Cell Rep*, 22(6), 1401-1412. <https://doi.org/10.1016/j.celrep.2018.01.036>

- Putnam, A. A., Gao, Z., Liu, F., Jia, H., Yang, Q., & Jankowsky, E. (2015). Division of Labor in an Oligomer of the DEAD-Box RNA Helicase Ded1p. *Mol Cell*, 59(4), 541-552. <https://doi.org/10.1016/j.molcel.2015.06.030>
- Qamar, S., Wang, G., Randle, S. J., Ruggeri, F. S., Varela, J. A., Lin, J. Q., Phillips, E. C., Miyashita, A., Williams, D., Strohl, F., Meadows, W., Ferry, R., Dardov, V. J., Tartaglia, G. G., Farrer, L. A., Kaminski Schierle, G. S., Kaminski, C. F., Holt, C. E., Fraser, P. E., . . . St George-Hyslop, P. (2018). FUS Phase Separation Is Modulated by a Molecular Chaperone and Methylation of Arginine Cation- π Interactions. *Cell*, 173(3), 720-734 e715. <https://doi.org/10.1016/j.cell.2018.03.056>
- Riva, V., Garbelli, A., Casiraghi, F., Arena, F., Trivisani, C. I., Gagliardi, A., Bini, L., Schroeder, M., Maffia, A., Sabbioneda, S., & Maga, G. (2020). Novel alternative ribonucleotide excision repair pathways in human cells by DDX3X and specialized DNA polymerases. *Nucleic Acids Res*, 48(20), 11551-11565. <https://doi.org/10.1093/nar/gkaa948>
- Rocak, S., & Linder, P. (2004). DEAD-box proteins: the driving forces behind RNA metabolism. *Nat Rev Mol Cell Biol*, 5(3), 232-241. <https://doi.org/10.1038/nrm1335>
- Saito, M., Hess, D., Eglinger, J., Fritsch, A. W., Kreysing, M., Weinert, B. T., Choudhary, C., & Matthias, P. (2019). Acetylation of intrinsically disordered regions regulates phase separation. *Nat Chem Biol*, 15(1), 51-61. <https://doi.org/10.1038/s41589-018-0180-7>
- Samir, P., Kesavardhana, S., Patmore, D. M., Gingras, S., Malireddi, R. K. S., Karki, R., Guy, C. S., Briard, B., Place, D. E., Bhattacharya, A., Sharma, B. R., Nourse, A., King, S. V., Pitre, A., Burton, A. R., Pelletier, S., Gilbertson, R. J., & Kanneganti, T. D. (2019). DDX3X acts as a live-or-die checkpoint in stressed cells by regulating NLRP3 inflammasome. *Nature*, 573(7775), 590+. <https://doi.org/10.1038/s41586-019-1551-2>
- Schroder, M., Baran, M., & Bowie, A. G. (2008). Viral targeting of DEAD box protein 3 reveals its role in TBK1/IKKepsilon-mediated IRF activation. *EMBO J*, 27(15), 2147-2157. <https://doi.org/10.1038/emboj.2008.143>
- Schuller, A. P., & Green, R. (2018). Roadblocks and resolutions in eukaryotic translation. *Nat Rev Mol Cell Biol*, 19(8), 526-541. <https://doi.org/10.1038/s41580-018-0011-4>
- Schuster, B. S., Reed, E. H., Parthasarathy, R., Jahnke, C. N., Caldwell, R. M., Bermudez, J. G., Ramage, H., Good, M. C., & Hammer, D. A. (2018). Controllable protein phase separation and modular recruitment to form responsive membraneless organelles. *Nat Commun*, 9(1), 2985. <https://doi.org/10.1038/s41467-018-05403-1>

- Sengoku, T., Nureki, O., Nakamura, A., Kobayashi, S., & Yokoyama, S. (2006). Structural basis for RNA unwinding by the DEAD-box protein Drosophila Vasa. *Cell*, *125*(2), 287-300. <https://doi.org/10.1016/j.cell.2006.01.054>
- Sharma, D., Putnam, A. A., & Jankowsky, E. (2017). Biochemical Differences and Similarities between the DEAD-Box Helicase Orthologs DDX3X and Ded1p. *J Mol Biol*, *429*(23), 3730-3742. <https://doi.org/10.1016/j.jmb.2017.10.008>
- Shen, P., Yue, Y., & Park, Y. (2018). A living model for obesity and aging research: *Caenorhabditis elegans*. *Crit Rev Food Sci Nutr*, *58*(5), 741-754. <https://doi.org/10.1080/10408398.2016.1220914>
- Shen, P., Yue, Y., Zheng, J., & Park, Y. (2018). *Caenorhabditis elegans*: A Convenient In Vivo Model for Assessing the Impact of Food Bioactive Compounds on Obesity, Aging, and Alzheimer's Disease. *Annu Rev Food Sci Technol*, *9*, 1-22. <https://doi.org/10.1146/annurev-food-030117-012709>
- Shih, J. W., Tsai, T. Y., Chao, C. H., & Wu Lee, Y. H. (2008). Candidate tumor suppressor DDX3 RNA helicase specifically represses cap-dependent translation by acting as an eIF4E inhibitory protein. *Oncogene*, *27*(5), 700-714. <https://doi.org/10.1038/sj.onc.1210687>
- Shih, J. W., Wang, W. T., Tsai, T. Y., Kuo, C. Y., Li, H. K., & Wu Lee, Y. H. (2012). Critical roles of RNA helicase DDX3 and its interactions with eIF4E/PABP1 in stress granule assembly and stress response. *Biochem J*, *441*(1), 119-129. <https://doi.org/10.1042/BJ20110739>
- Smith, J., Calidas, D., Schmidt, H., Lu, T., Rasoloson, D., & Seydoux, G. (2016). Spatial patterning of P granules by RNA-induced phase separation of the intrinsically-disordered protein MEG-3. *Elife*, *5*. <https://doi.org/10.7554/eLife.21337>
- Snijders Blok, L., Madsen, E., Juusola, J., Gilissen, C., Baralle, D., Reijnders, M. R., Venselaar, H., Helsmoortel, C., Cho, M. T., Hoischen, A., Vissers, L. E., Koemans, T. S., Wissink-Lindhout, W., Eichler, E. E., Romano, C., Van Esch, H., Stumpel, C., Vreeburg, M., Smeets, E., . . . Kleefstra, T. (2015). Mutations in DDX3X Are a Common Cause of Unexplained Intellectual Disability with Gender-Specific Effects on Wnt Signaling. *Am J Hum Genet*, *97*(2), 343-352. <https://doi.org/10.1016/j.ajhg.2015.07.004>
- Song, H., & Ji, X. (2019). The mechanism of RNA duplex recognition and unwinding by DEAD-box helicase DDX3X. *Nat Commun*, *10*(1), 3085. <https://doi.org/10.1038/s41467-019-11083-2>

- Soto-Rifo, R., Rubilar, P. S., Limousin, T., de Breyne, S., Decimo, D., & Ohlmann, T. (2012). DEAD-box protein DDX3 associates with eIF4F to promote translation of selected mRNAs. *EMBO J*, *31*(18), 3745-3756. <https://doi.org/10.1038/emboj.2012.220>
- Soulat, D., Burckstummer, T., Westermayer, S., Goncalves, A., Bauch, A., Stefanovic, A., Hantschel, O., Bennett, K. L., Decker, T., & Superti-Furga, G. (2008). The DEAD-box helicase DDX3X is a critical component of the TANK-binding kinase 1-dependent innate immune response. *EMBO J*, *27*(15), 2135-2146. <https://doi.org/10.1038/emboj.2008.126>
- Spike, C., Meyer, N., Racen, E., Orsborn, A., Kirchner, J., Kuznicki, K., Yee, C., Bennett, K., & Strome, S. (2008). Genetic analysis of the *Caenorhabditis elegans* GLH family of P-granule proteins. *Genetics*, *178*(4), 1973-1987. <https://doi.org/10.1534/genetics.107.083469>
- Strome, S., & Wood, W. B. (1982). Immunofluorescence visualization of germ-line-specific cytoplasmic granules in embryos, larvae, and adults of *Caenorhabditis elegans*. *Proc Natl Acad Sci U S A*, *79*(5), 1558-1562. <https://doi.org/10.1073/pnas.79.5.1558>
- Szczepaniak, K. (2021). Developmental Roles of DDX3 Helicase LAF-1 [PhD thesis]. *PhD thesis*. <https://doi.org/https://d-nb.info/1231917350/34>
- Takyar, S., Hickerson, R. P., & Noller, H. F. (2005). mRNA helicase activity of the ribosome. *Cell*, *120*(1), 49-58. <https://doi.org/10.1016/j.cell.2004.11.042>
- Updike, D., & Strome, S. (2010). P granule assembly and function in *Caenorhabditis elegans* germ cells. *J Androl*, *31*(1), 53-60. <https://doi.org/10.2164/jandrol.109.008292>
- Valentin-Vega, Y. A., Wang, Y. D., Parker, M., Patmore, D. M., Kanagaraj, A., Moore, J., Rusch, M., Finkelstein, D., Ellison, D. W., Gilbertson, R. J., Zhang, J., Kim, H. J., & Taylor, J. P. (2016). Cancer-associated DDX3X mutations drive stress granule assembly and impair global translation. *Sci Rep*, *6*, 25996. <https://doi.org/10.1038/srep25996>
- Van Treeck, B., Protter, D. S. W., Matheny, T., Khong, A., Link, C. D., & Parker, R. (2018). RNA self-assembly contributes to stress granule formation and defining the stress granule transcriptome. *Proc Natl Acad Sci U S A*, *115*(11), 2734-2739. <https://doi.org/10.1073/pnas.1800038115>
- Venkataramanan, S., Gadek, M., Calviello, L., Wilkins, K., & Floor, S. N. (2021). DDX3X and DDX3Y are redundant in protein synthesis. *RNA*, *27*(12), 1577-1588. <https://doi.org/10.1261/rna.078926.121>

- Wang, J. T., & Seydoux, G. (2014). P granules. *Curr Biol*, 24(14), R637-R638. <https://doi.org/10.1016/j.cub.2014.06.018>
- Watts, J. L., & Ristow, M. (2017). Lipid and Carbohydrate Metabolism in *Caenorhabditis elegans*. *Genetics*, 207(2), 413-446. <https://doi.org/10.1534/genetics.117.300106>
- Wei, M. T., Elbaum-Garfinkle, S., Holehouse, A. S., Chen, C. C., Feric, M., Arnold, C. B., Priestley, R. D., Pappu, R. V., & Brangwynne, C. P. (2017). Phase behaviour of disordered proteins underlying low density and high permeability of liquid organelles. *Nat Chem*, 9(11), 1118-1125. <https://doi.org/10.1038/nchem.2803>
- Wolf, N., Priess, J., & Hirsh, D. (1983). Segregation of germline granules in early embryos of *Caenorhabditis elegans*: an electron microscopic analysis. *J Embryol Exp Morphol*, 73, 297-306. <https://www.ncbi.nlm.nih.gov/pubmed/6683746>
- Woods, A. S., & Ferre, S. (2005). Amazing stability of the arginine-phosphate electrostatic interaction. *J Proteome Res*, 4(4), 1397-1402. <https://doi.org/10.1021/pr050077s>
- Wu, Y., Li, Q., & Chen, X. Z. (2007). Detecting protein-protein interactions by Far western blotting. *Nat Protoc*, 2(12), 3278-3284. <https://doi.org/10.1038/nprot.2007.459>
- Yarunin, A., Harris, R. E., Ashe, M. P., & Ashe, H. L. (2011). Patterning of the *Drosophila* oocyte by a sequential translation repression program involving the d4EHP and Belle translational repressors. *RNA Biol*, 8(5), 904-912. <https://doi.org/10.4161/rna.8.5.16325>
- Yedavalli, V. S., Neuveut, C., Chi, Y. H., Kleiman, L., & Jeang, K. T. (2004). Requirement of DDX3 DEAD box RNA helicase for HIV-1 Rev-RRE export function. *Cell*, 119(3), 381-392. <https://doi.org/10.1016/j.cell.2004.09.029>

Acknowledgement

I would like to express my sincere gratitude to my scientific advisor, Christian R. Eckmann, for his scientific inspiration, expertise, and continuous encouragement. I am also thankful to the members of my research team for their spirit, collaboration, and valuable insights. Their personalities and dedication were essential for the research. I would like to express special appreciation to Robin Selle for his community management and consulting.

Furthermore, I would like to acknowledge the financial support provided by DFG and RTG2467. Without their funding, this project would not have been possible. Moreover, I am thankful to all RTG2467 members for a productive and enjoyable time that we spent together. I want to express special gratitude to RTG2467's head and coordinator, Andrea Sinz and Claudia Spielmann, for their constant mental and administrative support during the most crucial periods, which frequently occurred.

Additionally, I would like to express my gratitude to my academic collaborators, Maria Ott and Marie Alfes, whose scientific supervision and expertise became an integral part of this thesis. Of course, I cannot forget to acknowledge my thesis advisors, Jochen Balbach and Carla Schmidt, who drastically expanded my outlook and understanding of science.

Finally, I want to express my gratitude to my family for sharing all the difficulties during this endeavour. You are priceless.

Eidesstattliche Erklärung

Hiermit erkläre ich, dass ich die vorliegende wissenschaftliche Arbeit selbständig und ohne fremde Hilfe verfasst habe. Ich erkläre weiterhin, dass andere als die von mir angegebene Quellen und Hilfsmittel nicht benutzt und die den benutzten Werken wörtlich oder inhaltlich entnommenen Stellen als solche kenntlich gemacht wurden.

Mit dieser Arbeit bewerbe ich mich erstmals um die Erlangung des Doktorgrades.

Halle (Saale),

Oleksandr Sorokin

Curriculum vitae

Personal details

Name: Oleksandr Sorokin
Sex: Male
Nationality: Ukrainian

Education

09/2019 – 08/2023 **PhD Student (RTG2467)**
Martin Luther University Halle-Wittenberg
Halle (Saale), Germany

2014 – 2016 **Master in Biochemistry**
Taras Shevchenko National University of Kyiv
Kyiv, Ukraine

2010 – 2014 **Bachelor in Biology**
Taras Shevchenko National University of Kyiv
Kyiv, Ukraine

2000 – 2010 **General secondary education**
Gymnasium № 117 named after Lesya Ukrainka
Kyiv, Ukraine

Halle (Saale),

Oleksandr Sorokin